The Investigation, Development and Optimisation of Global Laser Diagnostics for Combustion and Related Flow Applications

Andrew Michael Shand

A thesis submitted for the degree of:
DOCTOR OF PHILOSOPHY

Submitted to:

THE UNIVERSITY OF WARWICK

in

March 1996

AEA Technology,
Harwell, UK.

NUMEROUS ORIGINALS IN COLOUR

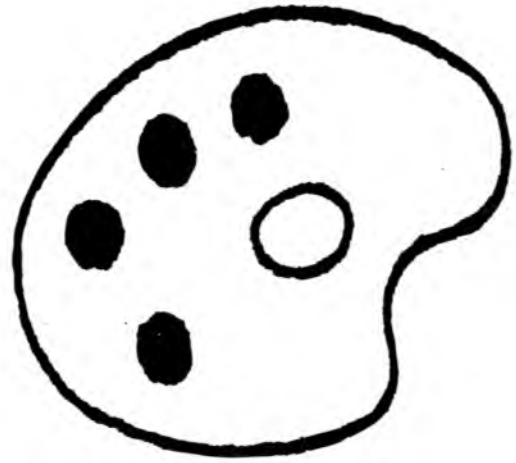

Summary

This thesis explores global, or whole-field, optical diagnostics for combustion and related flow applications. Global optical diagnostics are becoming increasingly popular as an efficient way of measuring an entire flow field at one time.

Conventional mechanical and optical point measurement techniques are first discussed and their limitations described. A variety of global optical diagnostics for visualisation, anemometry and film thickness measurement are then assessed. A summary of light scattering from particles is included, together with their behaviour when present in a flow. Suitable lasers and cameras for global diagnostics are also discussed.

A family of global techniques have been reviewed in this thesis. Examples are presented to illustrate the strengths and limitations which make different techniques appropriate for different types of flow.

A detailed description of a particle image velocimetry (PIV) system has been made. An example application is presented, showing how it can be used to aid the study of a simulated IC engine block flow. A comparison of the PIV data with laser Doppler anemometry data and computational fluid dynamics data is then made.

Global optical techniques are then applied to two combustion applications; diesel fuel sprays and pulverised coal furnaces. Laser sheet illumination is applied to semi-industrial scale coal furnaces for what is believed to be the first time. Development of the techniques and optimisations made to them for these applications are described.

Finally the current experimental challenges and future application of global optical diagnostics have been reviewed.

Contents

Table of Figures

List of Tables

Acknowledgements

I would like to thank the United Kingdom Atomic Energy Authority for financially supporting this work and providing experimental and computational facilities.

I would like to thank Dr. Peter Ereaut for his constant advice, moral support and regular technical collaboration. I also owe a great deal of thanks to all of the other members of the Combustion Centre at Harwell Laboratory, but in particular the support and guidance of Dr. John Sykes and Dr. Fraser Old.

From Warwick University I would like to thank Dr. Peter Bryanston-Cross for technical advice and academic support.

I would also like to thank the staff of the International Flame Research Foundation and RISØ Laboratory for use of their coal furnace facilities, and the other collaborating laboratories without whom this work would not have been possible.

Finally, I would like to show my appreciation to Anne-Marie Beech and my parents for their patience, support and understanding throughout this period of work.

Declaration

The work described in this thesis was undertaken as part of several applied research programmes at Harwell Laboratory. All experimental and computational work was performed by the author, except where stated below.

Computational fluid dynamics (CFD) calculations, experimental rig design and construction for the engine coolant flow measurements were carried out by Mr. Ian Postlethwaite and Mr Malcolm Sandford of Lotus Engineering Ltd. Interpretation of the engine coolant CFD results was also carried out by these two workers.

Diesel fluorescence spectra measurements were undertaken by Dr. Andrew Astill. Coal furnace imaging measurements at NEI, IFRF and RISØ laboratories was undertaken by the author with the help of Dr. Peter Ereaut and the staff of these institutions. Interpretation of the IFRF coal furnace light sheet images was undertaken with the help of Dr. Jacques Dugué.

Parts of Chapters 2, 3, 4 and 5 have formed the basis for a number of UKAEA technical reports and the following presentations.

- Presentation at the *International Conference on Fringe Analysis*, Loughborough, organised by the Fringe Analysis Special Interest Group, April 1989.
- Presentation at the *International Conference on Applied Optics and Opto-Electronics*, Nottingham, organised by the Institute of Physics, September 1990.
- Presentation at the *International Symposium on Experimental and Numerical Flow Visualisation*, Atlanta, organised by the American Society of Mechanical Engineers, December 1991.
- Presentation at the *International Conference on Optical Methods and Data Processing in Heat and Fluid Flow*, London, April 1992.
- Presentation at the *International Conference on Combustion in Engines: Technology, Applications and the Environment*, London, organised by the Institute of Mechanical Engineers, November 1993.

The VISIFLOW PIV analysis software is now marketed internationally by AEA Technology and its appointed representatives. At the time of writing, it is in use with over 50 research groups.

1. Introduction

1.1 Overview

Modern environmental and efficiency concerns require increasingly sophisticated technology to optimise and improve existing combustion technologies. An important combustion parameter is flow behaviour, so combustion flow diagnostic techniques are becoming increasingly important.

Global techniques are particularly useful for studying complex and/or transient flow fields. These are advancing rapidly as a result of advances in the areas of lasers, imaging and computing. This thesis explores the development and optimisation of global techniques for two particular combustion applications; fuel sprays and coal furnaces.

This first chapter discusses the nature of the two combustion applications. The second chapter describes the global optical diagnostics developed or improved as part of this study. The third chapter discusses analysis methods developed for particle image velocimetry, leading to the VISIFLOW PIV software package. The fourth chapter discusses the application of global diagnostics to fuel sprays. The fifth chapter discusses the application of global diagnostics to coal furnaces. The sixth chapter then summarises the findings, and additionally describes future improvements and potential new techniques that may be possible in this area.

1.2 Introduction to applications

1.2.1 The diesel engine

The diesel engine, which for many years has provided motive power for cars, transport vehicles, ships and various industrial processes, works on a simple cycle. Each cycle comprises a sequence of sucking in air, rapidly compressing this air to a high pressure and temperature, and then injection of liquid fuel with atomisation, evaporation and rapid combustion. Extraction of useful work from movement of the piston is followed by expulsion of exhaust gases and induction of a new charge of air for the next cycle.

The diesel cycle contrasts to that of the spark ignition engine, where a more volatile fuel is mixed with air and vaporises before entering the cylinder. The movement of the piston then compresses the mixture somewhat, and a spark is used to initiate combustion. The faster

combustion process allows higher speed operation and a greater output power than an equivalent compression ignition engine. Lower compression ratios are necessary in the petrol engine to prevent pre-ignition. Pre-ignition leads to vibration, noise and in severe cases, engine damage. The lower compression ratios and the lower energy density of petrol compared to diesel tends to yield a poorer economy.

The originator of the diesel engine is usually given as Dr. Rudolf Diesel, and the principle the engine uses is based on his hypothesis first published as "Theory and Construction of an Economical Thermal Motor". The essential part of which reads:

> "Motive work by means of heated air ... compressed to so high a degree, that by the expansion subsequent to the combustion the air is cooled to about atmospheric temperature, and that into this quantity of air, after its compression, fuel is gradually introduced ... At this compression the temperature becomes so high that the fuel employed is spontaneously ignited when it comes into contact with the compressed air."

The modern high speed diesel engine owes much of its growth to the small high pressure fuel pump and the associated injection nozzles. Robert Bosch designed the first pump which was capable of providing the required high pressure, together with an accurately regulated quantity of fuel at a precise time relative to the position of the piston within the cylinder. As a result of this development, the diesel engine has rapidly become the power unit of choice for many applications. The precise design and consequent behaviour of this injection system have a major impact of the overall efficiency and performance of the diesel engine.

Direct/indirect injection designs

Diesel engines are either of direct or indirect injection designs. Indirect injection systems have a divided combustion chamber, with some form of pre-chamber in which the fuel is injected, and a main chamber with the piston and valves. Direct injection systems spray the fuel directly into the cylinder itself. A simplified schematic of a direct injection engine cylinder is shown in Figure 1.

For direct injection designs, the key requirement is rapid mixing of the fuel and air to accelerate the combustion process. This is accomplished through careful design of the air

motion and fuel injection. The most important air motion in direct injection engines is swirl (the ordered rotation of air about the cylinder axis). Swirl can be induced by masking the inlet valves, and by design of the inlet passage.

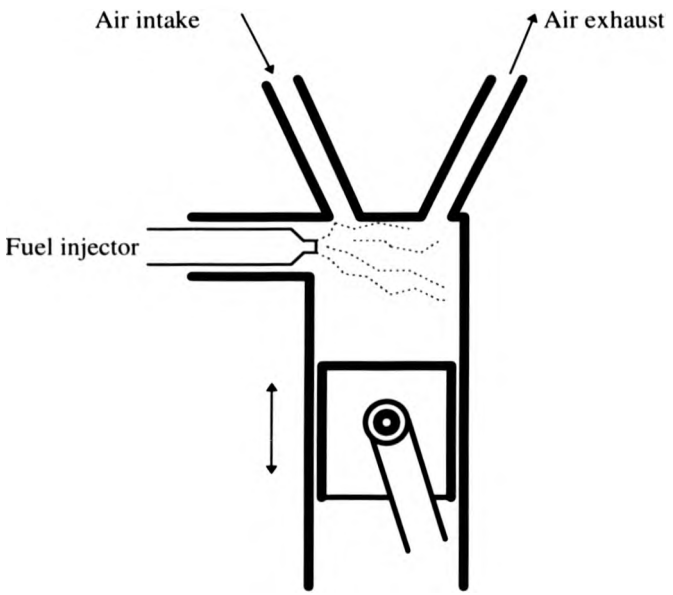

Figure 1. Direct diesel injection

The purpose of a divided combustion chamber in the indirect injection design is to speed up the combustion process, in order to increase the engine output by increasing engine speed. The small pre-chamber uses heat-resistant inserts with a low thermal conductivity. The inserts are quickly heated up by the combustion process and this then helps to reduce the ignition delay. The fuel is injected and impinges on the combustion chamber insert, the jet breaks up and the fuel evaporates. During initial combustion the burning air/fuel mixture is ejected into the main chamber, so generating a lot of turbulence. This ensures rapid combustion in the main chamber. A simplified schematic of an indirect injection engine cylinder is shown in Figure 2.

The direct and indirect designs each have their advantages and limitations. The indirect design permits rapid combustion and thus allows small engines to run at higher speed with larger power outputs. This makes it ideal for use in cars, where flexibility is important. However, the pre chamber requires additional compression work and there is a corresponding loss during

expansion also, with the result that the mechanical efficiency of the engine suffers. This generally results in a lower fuel economy for indirect injection engines.

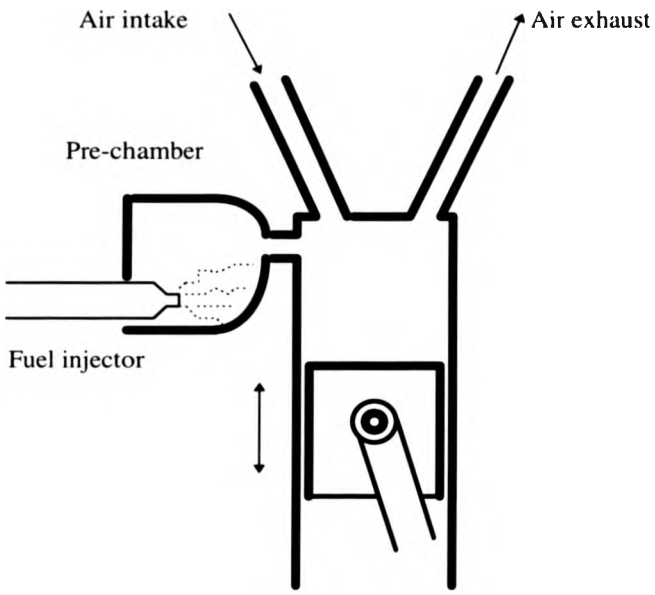

Figure 2. Indirect diesel injection

Fuel injection

The high injection pressure in conjunction with a small nozzle hole diameter ensures that the injected diesel fuel undergoes rapid and efficient atomisation as it issues from the injector. The mean droplet diameter of a typical diesel spray is a few tens of microns. Air temperatures in the combustion chamber approach the critical temperature of fuel so that droplets evaporate rapidly and the major portion of the spray is in the gaseous form. At lower injection pressures and/or temperatures, atomisation is less effective than under combustion conditions, and both liquid ligaments and large droplets are expected. The precise nature of the inner regions of the spray is poorly understood at present due to the high concentration of droplets, which acts to effectively obscure flow features.

The requirements for the injection system are accurate fuel metering, a rapid increase of pressure at the nozzle so that injection conditions are reached quickly, and at the end of the injection period a rapid reduction of pressure to avoid any after-dribbling of fuel from the

nozzle with consequent fuel waste, smoky exhaust, carbon deposit and choking-up of the spraying orifices.

Many different designs of spraying nozzles have been introduced, their construction and action being varied to suit different types of engine and forms of combustion chamber. Usually, the nozzle uses some form of needle valve that closes under a spring load when not spraying. When the fuel pressure reaches a certain value, the needle is forced open and injection takes place. The advantage of the needle valve is mechanical simplicity, but the precise timing and quantity of injection is set only by the fuel pressure/time profile. This can limit accurate control available over the injection process. Frankl et al [1] describe an electronic injector which accumulates fuel near the nozzle and uses a high speed solenoid to open and close a valve in the nozzle. Electronic control of injection timing and duration can thus be accomplished independently of varying injection pressure. This approach may find increasing application in the future, although at the present time the needle valve is still used in virtually all injectors.

Nozzles are either of the multi-orifice or single orifice type, the former often being employed to give better dispersion of the fuel, for direct injection engines. In direct injection engines, the nozzle orifices are positioned and angled so that the fuel spray is directed onto specific regions of the cylinder bowl.

Direct injection engines are widely used for industrial purposes, and larger automotive applications. Their fuel economy advantages are now driving their utilisation in small automotive applications, where increasing emphasis will be needed on injection system design and combustion chamber geometry and flow to make them viable.

Combustion in a diesel engine involves a series of complex physical and chemical processes. If the many aspects of these processes are to be fully understood various experimental and analytical techniques need to be applied. Air/fuel mixing characteristics have long been recognised as crucial to understanding combustion and heat release in diesel engines. In recent years considerable progress has been made in modelling of fuel sprays, and this work has been assisted by various experimental techniques, increasingly including optical techniques.

Considerable effort is being expended in improving the performance of direct injection diesel engines. The potential for higher efficiency is a major consideration in the modern drive for improved fuel consumption and reduced environmental impact. In the warm-up phase of

running of current direct injection engines, the low temperatures mean that the injected fuel spray will tend to directly impinge on the cylinder and piston walls, rather than rapidly vaporise. This is illustrated in Figure 3. Consequently, this spray-wall interaction is an important factor in the combustion process.

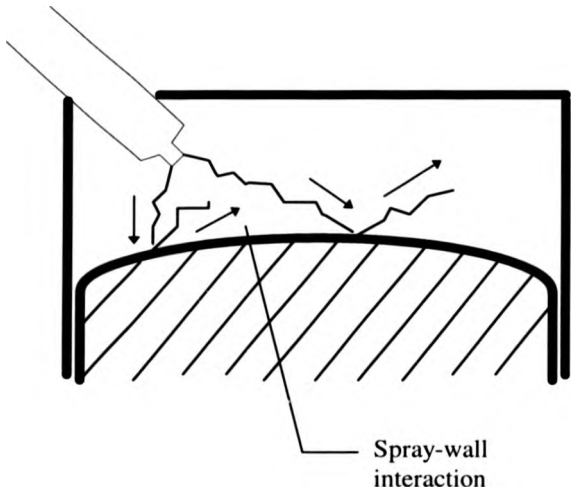

Figure 3. Spray-wall interaction

A major aim of the experimental work discussed here was improving our capability of understanding of the spray wall impingement behaviour. The development of techniques for studying the impinging spray, and the behaviour of the resulting wall liquid film is discussed.

Behaviour of diesel wall films

In small direct injection diesel engines, as the engine speed increases the fuel spray tends to impinge on the wall of the combustion chamber. This is a result of the small distance between the injector and the walls and the finite delay between injection and combustion. This interaction with the wall is thought to have a significant effect on fuel vaporisation and mixing, on the subsequent combustion efficiency and on pollutant formation.

Physical phenomena, such as atomisation and evaporation, are very important controls of combustion and auto-ignition in diesel engines. These physical processes must be understood if future diesel engines are to be designed which are fuel efficient and produce little pollution.

Computational fluid dynamics will provide important models for considering the in-cylinder air motion, spray behaviour and mixing in future engines. However, in any flow simulation, a detailed knowledge of the atomisation, evaporation, interaction with walls and re-atomisation of the diesel spray will be essential to fully realise the potential of such advanced theoretical models.

An important aspect of the interaction between a diesel spray and a wall is that droplets may strike the solid wall, stick and form an unsteady film. The spatial-temporal structure of the film depends on the thermal environment in the vicinity of the wall as well as the velocity and size characteristics of the liquid phase of the in-flowing jet. The penetration of droplets into the film results in the release of droplets of a different size class into the wall jet.

In particular, the formation of wall films in piston bowls is important as it affects the evaporation and re-atomisation of fuel droplets. Evidence has been found linking the formation of wall films with increased soot emission. Rao et al [2] describe measuring increasing particulate emissions under engine conditions where the injected spray impinges against a wall. Near to the wall, the local fuel/air ratio will consequently be very high, leading to flame quenching. This results in incomplete combustion, and high emissions. It is, therefore, necessary to study the mechanism by which these films are deposited and to quantify their thickness as a function of time. To be at all representative of a real engine, these measurements must be made at realistic engine pressures and temperatures - that is, inside a high temperature/high pressure cell, with the spray impinging on a hot wall.

Spray surface impingement with many droplets and droplet-surface interaction has been traditionally difficult to analyse, and aspects of the droplet wall interaction have been investigated with impingement of isolated droplets onto hot surfaces [3] [4]. Zhang and Gogos [5] have examined the vapour layer between the droplet and the surface and the corresponding surface temperature, known as the Leidenfrost temperature and shown that it can affect heat transfer and evaporation dramatically. The state of the environment surrounding the droplet is a key factor so that the evaporation and heat transfer rates can be higher in dry air than in a saturated atmosphere [6]. The mechanism of impaction on the film is rather different from impaction in a non-wetting state, in that the droplets coalesce with the wetting film only if they expel and rupture the intervening air-vapour film [7] [8].

Naber and Reitz [9] consider three numerical models for tracking droplets after wall impingement, namely,

1. the stick model - droplets that reach the wall stick to the wall

2. the reflect model - droplets that reach the wall reflect specularly

3. the jet model - droplets move tangentially to the surface after impingement.

They report that the jet model produced the best results. Wang and Watkins [10] discuss a CFD model developed for predicting diesel spray impaction. Their wall impaction and modified drop collision models are somewhat empirical, but achieve considerable success in predicting impaction behaviour. They describe the development of wall sprays - droplets first arriving at the wall form a cushion and those that come later, pushed by others behind them then move along the cushion. Thus the wall spray gets thicker as later droplets catch up and collide over those in the front.

1.2.2 Coal furnaces

Coal is a major fuel in the world economy. Uses include power generation, industrial process heating and domestic heating. In the UK, pulverised coal combustion is the dominant method of electricity generation, accounting for over 50 % of generating capacity. This is a historical consequence of the large reserves of coal within the island.

Coal combustion can produce significant environmental pollution. The combustion process can produce high levels of nitrogen oxides (NOX), sulphur oxides (SOX), carbon monoxide and dioxide and particulates. Due to its widespread application, coal combustion emissions are a significant world-wide environmental hazard, causing such phenomena as smog and acid rain and potentially global warming.

Recent legislation is now requiring considerable reductions in emissions from coal plant. This drives research promising to enable both new and existing furnaces to produce less emissions. Increasing energy costs, the "greenhouse effect" supposedly resulting from CO_2 emissions, and finite coal stocks are driving increasing efficiency.

Addition of gas cleaning technology (such as flue gas de-sulphurisation) to the output of existing coal furnaces can reduce emissions, but not increase efficiency. However, this

approach is not an ideal solution, as it does not cure the emission problem, but merely relieves its symptoms, while being very expensive. A better approach is to redesign the cause of the emissions - the furnace itself.

The basic principle of operation of a typical large coal furnace is fairly simple. The furnace consists of a box or cylinder lined with an insulating material. This insulator, known as a refractory lining is usually made from a heat proof ceramic. A flue is situated at one end of the furnace, often leading to a tall chimney (stack). At the other end of the furnace, pulverised coal is injected into a burner. Pieces of coal from storage are fed into one or more mills which pulverise the coal into fragments. The coal is then often mixed with air in a fluidised bed, creating a coal/air mixture which can be pumped into the furnace like a liquid.

Within the coal burner, the coal is further mixed with air to dilute it ready for combustion. As each coal particle enters the furnace and is heated, it begins to burn. The particle undergoes de-volatisation, followed by char burnout. The furnace is designed so that the particle is completely combusted before leaving the furnace. The remnant of the particle is ash. This ash either leaves via the flue, or stays within the furnace, often forming a troublesome slag on the refractory surface.

Coal combustion is not naturally self-supporting. External heating, usually from an oil or gas burner is required to initiate the coal combustion. Once the furnace reaches its operating temperature (sometimes several days), the refractory lining of the furnace absorbs combustion radiation and re-radiates sufficient of it back into the main volume to sustain further combustion, obviating the need for external heating.

The design of the coal burner varies considerably from furnace to furnace. A popular approach is to use an annular design, with air streams on either side of the coal stream. Swirl is usually introduced into the air stream to increase mixing of the coal and air prior to combustion. The part of the furnace in the region of the burner is known as the quarl. Here the geometry expands from the small burner diameter to the larger diameter of the main furnace. The design of the burner, and the geometries of the quarl and main furnace can have a significant effect on the efficiency and emissions of the furnace. However, optimisation of these parameters is still largely empirical, due to the complex interactions involved in the combustion process.

For the last thirty years, the measurement techniques used in gas, oil and coal flames at semi-industrial scale (thermal input of 1 MW or higher) have consisted mainly of sampling techniques for temperature, gas composition, solid composition and heat transfer measurements. Although flame aerodynamics plays an important part in the combustion process, flow field diagnostics have remained difficult to apply because of the high flame temperature, turbulence level and particle loading.

The industrial coal furnace is a difficult and hostile environment for flow diagnostics. The large size, typically several metres in diameter, means that diagnostics need a long working distance. The high coal particle loading can cause abrasion of measurement probes and obscure the flow from view. The high temperatures (up to around 2000 °C) can cause damage to many designs of probe.

1.3 Existing techniques for flow measurement

Techniques for flow measurement will be broken down here into two main types; mechanical and optical. Mechanical techniques rely on the flow affecting the physical characteristics of some sort of sensor, while optical techniques use the effect of the flow on some optical characteristic of an interrogating light beam.

Important characteristics of a flow that can be measured include velocity, pressure, temperature, species concentration, and particulate concentration. Only the first and last of these will be covered in detail in this study, together with measurement of the thin liquid films caused by a spray impinging onto a surface. The rest of this section describes techniques for anemometry, flow pressure measurement, temperature measurement, species measurement and film thickness measurement.

1.3.1 Mechanical flow anemometry techniques

There are a number of different physically intrusive, or mechanical anemometry techniques. Each technique is particularly useful in specific applications [11].

Differential pressure anemometry

A major group of flow anemometry techniques uses differential pressure measurement. The Pitot-static tube is the most widely used and reliable differential pressure probe for flow

measurement. This probe has two pressure taps, indicating the static P_S and stagnation or total pressure P_T in the flow. Bernoulli's equation then gives

$$P_T = P_S + \frac{1}{2}\rho_0 U^2 \tag{1}$$

The difference between the static and stagnation pressures gives the local fluid velocity:

$$U = \sqrt{\frac{2(P_T - P_S)}{\rho_0}} \tag{2}$$

Measurement of the pressure differential therefore gives the time-averaged flow velocity at the position of the probe. The simple two hole Pitot tube, giving one component velocity measurements can be extended to more components using a more complex design with multiple holes.

Thermal anemometry

Another important group of anemometers relies on sensing the changes in heat transfer from a small, electrically heated sensor exposed to the fluid motion. A simple and widely used sensor uses a very thin heated metal wire (typically a few microns in diameter) exposed to the flow, and is known as a hot-wire anemometer. As the flow velocity increases, the heat loss from the wire increases. This heat loss can be measured from the change in resistance of the wire, typically using a constant-temperature bridge circuit. Assuming a linear relation between temperature and resistance, the resistance R of the sensor can be represented as

$$R = R_r\left[1 + \alpha(T_m - T_r)\right] \tag{3}$$

where R_r is the resistance at reference temperature T_r, T_m is the average sensor temperature and α is the temperature coefficient of resistance.

The relationship between heat loss (and thus probe resistance) and flow velocity is complex and very non-linear, and a thermal probe always requires calibration in a range of flows of known velocities.

Many other flow velocity measuring techniques exist, including momentum based designs such as the turbine and cup anemometers.

The application of mechanical anemometers to combustion applications

To measure velocity in a moving fluid, the ideal instrument should

1. Have high accuracy
2. Cause no flow intrusion
3. Have a good frequency response to allow flow transients to be followed
4. Measure a wide velocity range
5. Have a small physical size to give good spatial resolution
6. Measure all three velocity components, and detect flow reversal
7. Be easy to operate
8. Be low in cost

Each measuring technique has advantages and limitations, making it more or less suitable for different applications.

Pitot tubes are often fairly bulky (several mm or cm), especially for multi-component velocity measurement. This limits them to large-scale flows, where their size has a negligible intrusive effect on the flow field. They also have a poor frequency response (<1 Hz), making them only applicable to time-averaged velocity measurement.

Hot-wire probes are very small, giving good spatial resolution. They have a low thermal inertia, giving an excellent frequency response, with measurements to several hundred kHz easily obtainable. This allows rapid flow transients to be measured. Their main limitations are their fragility, and their sensitivity to contamination. Other limitations are that the probe needs detailed calibration before use, normal configurations usually limit the turbulence intensity that can be measured accurately, and heat loss from the sensor can be caused by other factors than convection into the flow, such as interactions with walls, giving rise to errors.

Accuracy of these mechanical anemometry techniques is very dependent on the type of flow being measured, but velocity data within one percent of the true velocity can be readily

obtained with some applications. Resolution of 1 part in 10,000 is easily accomplished using hot-wire anemometry [11].

The use of the above mechanical techniques for the combustion applications of coal furnaces and diesel fuel sprays have been limited. The particle laden nature and fluctuating temperature of both these flow types precludes the delicate hot-wire technique.

In gas flames, the Hubbard five-hole Pitot probe can be used for measurement of the total velocity vector. In swirling flows, however, measurements are very inaccurate as a result of the very high velocity fluctuations encountered in the flame region and in the central recirculation zone shear layer. Therefore use of the Hubbard probe is usually limited to simple non-reversing flows, with a low turbulence.

In coal flames, the high particle loading generally precludes the use of Pitot type techniques. Attempts have previously been made to design probes less sensitive to hole blockage, but these probes remain difficult to use and crude in accuracy. Until recently, flow mapping in coal flames has been done using an acetylene probe. This probe contains a water cooled tip which supports a small pre-mixed air/acetylene flame. This flame is deflected by the flow and so acts as a 'flag', revealing the flow direction. Although simple, application of this method is time consuming since it is a single point measurement technique and requires traversing the flag-probe to different positions in the furnace.

Diesel fuel is normally injected into diesel engines under pressures of the order of 10^8 N/m^2. This high pressure, and the small injector hole size (typically 0.3 mm) produces a short duration spray and high droplet velocities and momenta. Flow measurement of diesel fuel sprays has not been possible using the mechanical techniques described above. The high momentum of the spray acts to rapidly damage or destroy any mechanical sensor. Also, the small size of a typical automotive diesel spray means that any mechanical probe is highly intrusive; its presence significantly modifying the spray flow field. Flow mapping has only been possible using indirect methods. For instance, volume flow rate can be deduced from measuring the changes in the feed line pressure with time, together with weighing the total quantity of liquid emitted per injection.

The inherently non-intrusive nature of optical flow techniques promises to circumvent the major problems with measuring in these hostile combustion environments. These optical techniques are outlined in the next section.

1.3.2 Optical anemometry techniques

Optical techniques for flow measurement rely on illuminating the flow in some way, and then detecting a change in the characteristics of the light which has interacted with the flow. This change can be in the frequency, intensity, phase or polarity of the light scattered. In many cases, the light can be generated and then detected at a significant distance from the flow. The insubstantial nature of a light ray means that for most applications, the light has no effect on the flow field.

Optical techniques for flow measurement can be sub-divided into four main groups, based on elastic or inelastic scattering, absorption or non-linear optical processes. These groups of techniques can refer to particles suspended in the fluid, or to the fluid itself. The techniques discussed in this thesis are based on elastic scattering, with the exception of laser-induced fluorescence (inelastic scattering).

An important requirement of optical measurement is optical access. Light needs to enter a flow, interact with it in some way, and then exit the flow for detection. This optical access is a significant limitation for many applications, precluding optical techniques where the flow is opaque. Also, flows fully enclosed within a vessel require some form of transparent window(s) for introducing and removing the light.

Laser Doppler anemometry

For anemometry, the main optical technique is laser Doppler anemometry (LDA) (e.g. [12]). This relies on light undergoing a Doppler frequency shift as it is scattered from small seeding particles moving within the flow. Laser light is used because it is monochromatic and coherent. The frequency shift of the light scattered by a particular particle can be related to the particle velocity by

$$\nu_s = \frac{\mathbf{v} \cdot (\hat{\mathbf{r}} - \hat{\mathbf{s}})}{\lambda} \qquad (4)$$

where ν_s is the frequency shift, λ is the wavelength of the incident light, $\mathbf{v}$ is the velocity of the scattering particle, $\hat{\mathbf{r}}$ is the scattering direction and $\hat{\mathbf{s}}$ is the incident light direction. Thus velocities in different flow directions can be measured by adjusting the incident and/or scattering directions. The frequency shift is thus linearly proportional to the flow velocity.

The Doppler frequency shift is very small (typically around 0.4 MHz per m/s, where $\hat{\mathbf{r}}$ and $\hat{\mathbf{s}}$ are nearly parallel) relative to the basic frequency of the light which is of the order 10^{14} Hz. Consequently, direct detection of the Doppler shift is usually only possible in high speed flows. Optical heterodyne detection (optical mixing) is thus used to subtract the basic light frequency, leaving only the Doppler shift frequency.

Several methods of accomplishing the optical mixing are possible, the most common being the dual-beam approach. This illuminates a scattering particle with two light beams, propagating in two different directions. The beams are focused to intersect in a region, referred to as the measurement volume. Moving particles passing through the measurement volume scatter light with a varying intensity (Doppler burst signal). The frequency of the intensity variation is proportional to the particle velocity. Signal processing can be used to measure this burst frequency and thus compute the particle velocity. The burst frequency can be directly related to the particle velocity via the precise dual beam geometry, with no calibration needed. Velocity is measured for discrete particles, and when a number of measurements are made over a pre-set time period, time-averaged velocities can be computed, together with other statistical quantities such as turbulence intensity.

The LDA dual beam method is clearly a point measurement technique, with the velocity measured within a small probe volume. This has advantages and disadvantages; the spatial resolution of the technique is high, while measurement of an entire flow field requires often lengthy traversing. As well as the long acquisition time, this traversing means that only steady flows can be measured across their whole field.

Transient, unsteady flows such as fuel sprays can be measured only with difficulty using LDA, by making repeated measurements on a number of successive sprays with only a low number of Doppler bursts per injection, building up a suitably detailed velocity time-history to give useful statistics, and then traversing the measuring volume.

Recent application of the LDA technique for velocity measurements in semi-industrial scale flames has resulted in a significant improvement in flame aerodynamic characterisation. The LDA technique can provide accurate, quantitative measurement of the flow mean velocity and velocity fluctuations at well-defined spatial positions. The LDA technique has now been demonstrated at semi-industrial scale in gas, oil and coal flames [13]. LDA has also been applied to transient fuel sprays. Such applications are described further in later chapters.

The rapid transient nature of a diesel fuel spray (typically 3 ms duration and 250 m/s exit velocity) and the high momentum of the spray require that non-intrusive and thereby optical techniques are used. The high optical density within the spray (as a result of absorption and multiple scattering) makes even these flow diagnostics difficult. Optical transmissivities of only a few percent are likely.

Other point measurement optical anemometry techniques

Other optical techniques related to LDA are laser two spot, and phase Doppler anemometry (PDA). Laser two spot (L2S) [14] uses a pair of closely spaced parallel light beams, and signal processing to measure the time of flight of particles between the two beams. L2S is often used for high speed flows such as those in transonic wind-tunnels, where the signal processing bandwidth required for the previously described dual beam LDA technique is too high.

PDA [15] [16] uses the same beam generation optics as LDA, but with two detectors rather than one. The two detectors are sited so that they receive light scattered at known, different angles to the incident beam. Calculations from Mie scattering theory (described in the next chapter) show a phase difference between these two optical beams, which is for spherical particles directly proportional to the diameter of the particle. Knowledge of the refractive index of the particle allows the size to be calculated from the phase shift. Thus, both the velocity (using conventional LDA signal processing) and particle diameter can be determined. This technique is thus useful in many spray applications where the particle size distribution against particle velocity is an important characteristic. As for LDA, it's application is restricted by signal processing speed limitations to slower flows.

Another useful optical technique for flow measurement is the forward diffraction (or Malvern) technique, e.g. [17]. This measures the Airey (Bessel function) forward diffraction pattern from a spherical particle. The spacing of the diffraction fringes is dependent on the diameter of

the particle. The Malvern technique uses a collimated beam passing through the flow, and then focused onto an annular silicon detector. Processing of the fringe signal falling onto the detector can determine the average particle diameter within the illuminated volume of the flow. The main disadvantages of this technique are the lack of spatial resolution, due to the signal integration along the whole illuminating beam path, and the need for optical access for the entry and exit of the collimated beam.

In order to complement the local measurements obtainable with LDA and other related techniques, there is thus a strong need for techniques which can provide global information on transient fuel/air mixing behaviour, film thickness and on the near-burner-zone flow field. This need leads to the development of global, or whole-field optical techniques. These are described in the next chapter.

1.3.3 Flow pressure measurement techniques

Pressure can be measured mechanically using a variety of means. The liquid barometer uses the height of a supported column of liquid such as mercury (with a vacuum above it), to indicate absolute pressure. In the aneroid barometer, a metal bellows containing a vacuum expands or contracts according to variations in pressure. This movement is transmitted via a suitable linkage to a pointer.

The manometer is a device that uses columns of a liquid to measure the difference in pressure between a certain point and the atmosphere, or between two different points. A common type employs a "U-tube" set in a vertical plane.

Other methods utilise the elastic deformation of a solid. These include the Bourdon gauge, and the piezo-electric gauge.

No optical method has been found to measure flow pressure fully non-invasively. However, mechanical techniques utilising the compression of an optical fibre are now beginning to find application.

1.3.4 Flow temperature measurement techniques

The temperature of a point in a flow can be measured mechanically using a thermocouple. These can be made on a very small scale, thereby causing only little disturbance to the flow

field, and a high spatial resolution. Making the sensor small also increases the speed of response to temperature transients, although the measurement is still an integration over time.

The temperature of a flow can be measured optically using coherent anti-Stokes Raman spectroscopy (CARS) [18]. This measures the change in the Raman spectrum of a majority species (such as nitrogen) within the flow. The Raman spectrum is excited at the intersection of three laser beams (two 'pump' beams at one wavelength and a third 'probe' beam at a different wavelength). The intensity and wavelengths of the various peaks of the Raman spectrum can be pre-computed for a range of temperatures, and these can then be fitted to the experimentally measured spectra to yield temperatures. Pulsed lasers are used, giving temperature measurement for an instant of time.

1.3.5 Flow species measurement techniques

The concentration of a particular chemical species can be measured spectroscopically. For combustion applications, species of interest are generally gaseous. The greater the partial pressure of the specie of interest, the greater the intensity of its excited spectum. Species concentration can be obtained by measuring the intensity of the Raman spectrum, recorded as for CARS, but light levels are generally low, and species concentration sensitivity is of the order 1000 parts per million (ppm). More commonly, laser induced fluorescence spectroscopy (LIF) [18] is used. Fluorescence is the spontaneous emission of radiation from an upper energy level which has been previously excited. In LIF, a pump laser is used to excite the required specie, and the fluorescence produced is then detected. The laser wavelength is tuned to excite the chosen atom or molecule at one of its known electronic absorption wavelengths, and a spectrometer is tuned to one of its known fluorescencing wavelengths. A wide variety of species, including OH, CH, CN, NH and NO have been studied using LIF. Fluorescence light levels can be significant, and high sensitivities of <1 ppm are achievable. With accurate knowledge of such factors as the radiative decay rate, the fluorescence wavelength, the collection solid angle, the sample volume and the light collection efficiency, LIF measurements can be calibrated to give quantitative species concentrations.

1.3.6 Film thickness measurement techniques

A number of approaches have been used to study and to measure liquid films. Both temporal development and quantitative thickness information is required. The technique(s) used should

give good temporal resolution, allowing a number of measurements during and after the spray injection event.

A good spatial resolution is also desirable, allowing fine detail in the film to be discerned. For the small automotive type diesel spray application studied here, this spatial resolution should ideally be in the mm range or better. The range of film thickness to be measured was unknown before commencing work, but was expected to be a few tens of microns. High absolute thickness measurement accuracy is not essential, but good accuracy mapping temporal change is important.

Film thickness measurement techniques can be broken down into mechanical, electrical and optical methods.

Mechanical film thickness measurement

Mechanical techniques are generally simple. One method is to use a micrometer gauge which is screwed in so that the end of the measuring rod first approaches and then just touches the liquid surface. This technique gives a direct measure of the film thickness in microns. However, potential accuracy is low as it is difficult to control the exact moment that the metal rod touches the liquid, and it may not be clear when this has occurred. Surface tension effects are important. Mechanical uncertainties tend to limit the technique to relatively thick films, i.e. >100 microns. This technique is adequate for static films on a test surface, but the inherent intrusiveness and slow speed means that it is unsuitable for dynamically measuring a real spray impingement.

Electrical film thickness measurement

Electrical techniques rely on a change in the electrical environment of a immersed sensor as a liquid film thickness changes. Several electrical characteristics can be studied, including conductance and capacitance.

Conductance sensors measure the change in resistance between two metallic contacts immersed in a liquid film. The thickness of the film determines the effective resistance seen by the junction; as the thickness changes, the resistance across the contacts should also change. The resistance of the sensor can be measured by an electrical bridge circuit. The suitability of

the conductance sensor is dependent on the conductivity of the liquid itself. Liquids with high conductivity allow high sensitivity and give good accuracy.

The sensor can be small as point metal contacts can be used. This gives a good spatial resolution as there is little averaging of thickness over the sensor area. However, little success in diesel film measurement has been reported using this technique [19]. The normal conductivity of typical diesel fuel is very low, and this leads to unacceptably poor sensor sensitivity and accuracy. A number of additives had been tried, in an attempt to increase conductivity, but were found to be needed in high concentration, which suggests a significant modification of the pure fuel physical and chemical characteristics.

Capacitance sensors measure the capacitance of two metallic contacts, again immersed in the liquid film. The liquid forms the dielectric of the resulting capacitor and so should have a low conductance to minimise the leakage across the junction. As the film thickness increases, the capacitance also increases. Gover and Ereaut [20] describe measurements of cylinder bowl film thickness using a 4 mm square capacitance sensor as part of an electronic oscillator. As the capacitance measured by the sensors changes, so the frequency of the oscillators also changes. The authors report that this method allows rapid measurement of the small capacitances involved, thereby giving a high temporal resolution. Five sensors and associated circuits were miniaturised and fitted inside a piston. Infra red links were made to an external system, allowing measurements under engine motoring conditions.

The sensitivity of the capacitance sensor is dependent on the dielectric strength of the liquid. The sensitivity can be improved by increasing the area of the sensor, thereby increasing its capacitance, although reducing the spatial resolution achievable.

The main disadvantages of the capacitance technique are the need to install sensor(s) on the surface of interest, and extract signals from them. Also, the spatial resolution is limited by the size of the sensor.

Optical film thickness measurement

Optically based film thickness measurement techniques offer the advantage of non-intrusive measurement and several approaches are possible.

Ozdemir [21] describes a film thickness measurement technique based on optical interference. A laser beam is focused onto the liquid film through a transparent window in the surface. Reflected light from the window/liquid interface and that passing through the film and reflected from the liquid/air interface interfere together and this interfering light can be imaged onto a detector and measured. If the film thickness changes, the path length of the light ray passing through the film also changes and thus the phase between the two interfering rays. This phase change causes a change in the intensity. Ozdemir describes using a standard LDA signal processor to measure this intensity variation which is similar to a Doppler burst signal. The LDA signal processor measures the frequency of variation of intensity, from which can be calculated the rate of change in thickness of the liquid film.

The main disadvantage of this interference technique is that the actual film thickness cannot be measured directly, but can only be inferred by integrating the rate of change of film thickness. This requires the assumption of no film being present at the start of the measurement interval. Clearly, knowledge of the film thickness itself becomes less accurate as time goes on, due to the accumulation of measurement error.

Another optical approach for film thickness measurement is to exploit laser induced fluorescence. Diesel fuel is rich in aromatic organic compounds which readily fluoresce when excited by laser light. This fluorescence is generally in the 450 - 550 nm range (blue-green). If a laser is focused onto the diesel fuel through a window in the surface, the diesel will fluoresce and the intensity of this fluorescence light is dependent on the length of the path through the liquid. The film thickness can thus be determined by measuring the fluorescence intensity. This measurement is made by focusing the laser to a spot and then imaging this spot onto a detector such as a PMT. The technique has been applied mainly for in-cylinder lubricant film measurement [22] [23] [24] [25] [26] [27].

The main disadvantage of the above LIF technique is that the intensity of fluorescence in diesel has a strong temperature dependence. This means that local film temperature and its thickness cannot be uncoupled from the results. Consequently, a new technique was developed, which did not use the intensity of the fluorescence. This will subsequently be referred to as the "length of line" technique. Further discussion of this technique can be found in chapter 4.

The existing LIF and new length of line techniques have a number of limitations, primarily that they only measure thickness at a single point, or at best along a line. Ideally, the film measurement technique should provide global information on the entire spray "footprint" with high temporal and spatial resolution. In addition, the technique should be capable of being employed in high temperature and pressure environments, preferably inside a real engine with a curved impingement bowl. A new technique for global film thickness measurement based on total internal reflection is proposed in the next chapter.

2. Global Optical Techniques

As previously discussed, mechanical, and LDA and other similar optical point measurement techniques are only of limited use for the combustion applications of coal furnaces and fuel sprays. For an analysis of the spatial structure of the flow field, a scan through different locations is necessary. In these non-stationary flows, however, this is unsatisfactory because an instantaneous measurement at all flow locations would be necessary. Techniques that render the instantaneous velocity field over an extended region in space are therefore required - quantitative whole-field or global methods. A number of these global optical techniques have now been developed, but with only limited development and application to these combustion flows to date.

The most significant global optical techniques are discussed in the chapter, together with the other main parameters that need to be considered for successful application of these techniques. The main factors associated with these global optical techniques are Mie scattering theory, flow seeding, the illuminating laser, recording media and image processing.

2.1 Global Optical Techniques

2.1.1 Schlieren/shadowgraphy

Shadowgraphy and Schlieren [28] are probably the simplest techniques for whole-field flow visualisation. Both techniques measure the changes in refractive index of the flow medium (usually gaseous), and thus do not require scattering from seed particles suspended in the flow.

For shadowgraphy, the flow is illuminated from behind (not necessarily using a laser) and a screen is placed in front of the flow. A camera is focused on the screen, as shown in the schematic of Figure 4. When the density gradient of the flow medium is the same in all points of the plane P, light rays are deflected by the same angle, and the screen remains uniformly illuminated. Illumination changes appear only when there are changes in the refractive index-gradient. The shadowgraph method sensitivity is then proportional to the second derivative of refractive index with respect to distance.

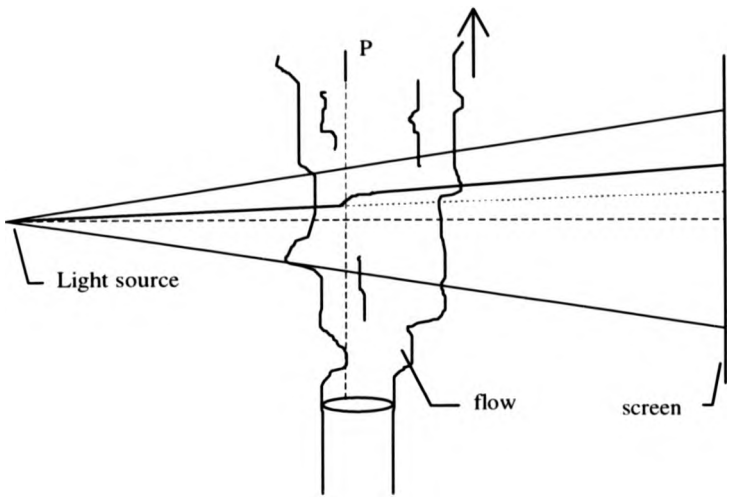

Figure 4. Schematic of the Shadowgraphy Techniques

In the Schlieren technique, the flow is again illuminated from behind and a screen placed in front of the flow. This is illustrated in Figure 5. A lens L1 images the light source placed at the focus of a field lens L2. The flow is then illuminated with the collimated light beam. A second field lens L3 on the other side of the flow then focuses the light, which then goes onto the screen to form an image. This configuration gives equivalent results to the above shadowgraph technique. If apertures (Schlieren diaphragms) such as knife edges are now introduced into the focal planes of the two field lenses, D1 and D2, they can act as filters (in the Fourier plane) if their position is carefully adjusted. The filter removes half of the Fourier spectrum, while letting the d.c. frequency and other half through unchanged. Small changes in the refractive index of the flow are thus revealed. The sensitivity of the Schlieren technique is considerably higher than for shadowgraphy, and is proportional to the first derivative of refractive index with respect to distance.

Both shadowgraphy and Schlieren are relatively insensitive to refractive index changes, and are usually used where the index gradient is high, typically for shock and flame phenomena. At low speeds, a flow is incompressible, and no deviation occurs. At higher speeds, a flow becomes compressible and the density of the fluid begins to vary. Although flows are never completely incompressible, density changes for speeds less than Mach 0.1 are negligible (< 1 %), and thus this sets the lower limit above which Schlieren measurements are possible for isothermal flows.

Both techniques integrate through the flow, and localisation of flow features is thus made difficult.

A laser is not necessary for either of these techniques, but it can be useful in increasing the detail of the screen image. Also, a pulsed laser allows the structure of high speed flows to be frozen, and thus revealed.

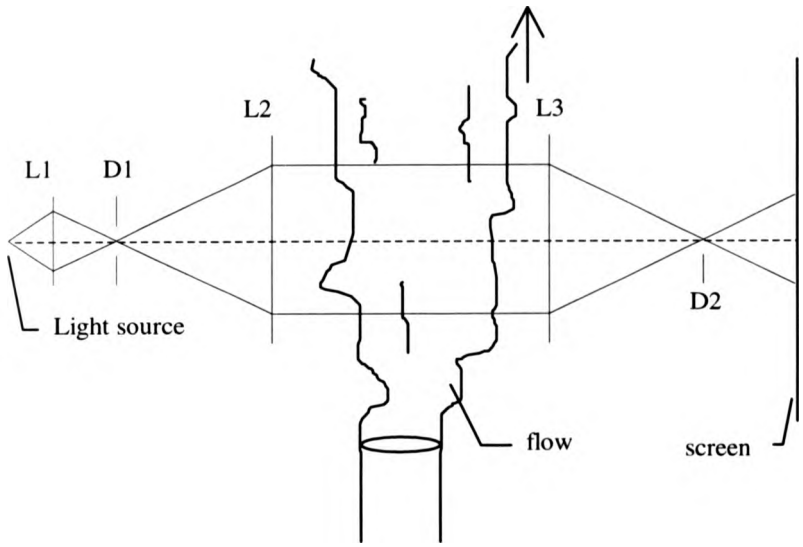

Figure 5. Schematic of the Schlieren Technique

2.1.2 Light sheet illumination

Light sheet illumination (LSI) relies on expanding a light beam in one direction, to form a thin sheet of light. Particles moving within the flow scatter this light, and can be imaged by a camera viewing along a perpendicular direction to that of the sheet. LSI is a simple but powerful technique for *visualising* the behaviour of a flow. It is a global, whole-field technique because the whole of the flow (or rather a plane within it) is imaged simultaneously. The technique reveals the instantaneous global distribution of the seeding particles, and how it changes with time [29].

A light sheet can be generated using a conventional light source and a simple slot. As the slot is made more narrow, a high intensity light source becomes necessary as most of the light is discarded. Also, the incoherent polychromatic nature of the light means that it diverges

rapidly. This makes such a light sheet suitable only for small flows of a few cm diameter. A significant problem with high power light sources is that significant heat is generated at the same time. This heat can be sufficient to affect the flow, and thus render this optical technique intrusive.

A better light source for sheet generation is a laser. This can generate intense light, with little or no associated heating of the flow field. Also, the monochromatic light is easy to focus into a defined illumination pattern. A light sheet extending for several metres can easily be generated using a laser.

The laser sheet generation can be accomplished in several ways, depending on whether a c/w or pulsed laser is used. For c/w lasers, a rotating segmented polygonal mirror can be used. Here the rotation of the mirror surfaces cause the reflected beam to scan to and fro. The scanning beam is then introduced into the flow, and causes a plane to be illuminated. A focusing lens is usually used before the rotating mirror to reduce the thickness of the sheet, and thereby increase the spatial selectivity of the technique. If the change in the flow is small over the period of beam scan, then an effectively instantaneous image of the flow is produced. This scanning LSI technique makes efficient use of laser beam power - the entire power of the beam falls on the particle being illuminated (although only for a short time). A schematic for the scanning LSI technique is shown in Figure 6.

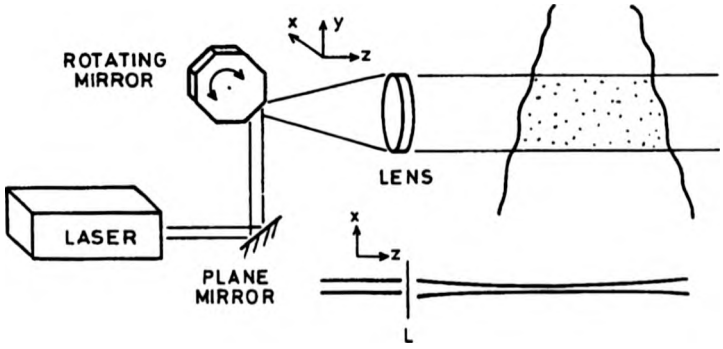

Figure 6. Light sheet generation using a rotating mirror

The other main approach for generating a light sheet is to use cylindrical optics. If a converging lens is used, the laser beam focuses and then diverges into a plane. This is suitable for low power c/w lasers, but for high power pulse lasers, the power density at the focus is often sufficient to ionise air, strongly reducing the resultant power. To avoid this problem, a diverging cylindrical lens which does not bring the beam to a focus should be used. A schematic for this is shown in Figure 7.

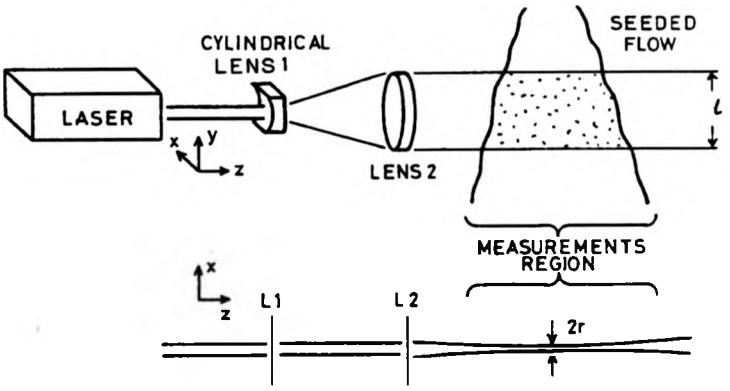

Figure 7. Light sheet generation using a cylindrical lens

Using a scanning mirror or cylindrical lens produces a diverging light sheet. Thus the intensity of the illuminated plane of the flow field will vary significantly as the sheet diverges, reducing the quality of the visualised flow image. This can be overcome by using only the central region of a large sheet, where the intensity variation is minimal. Alternatively, a collimating spherical or cylindrical lens can be used to correct the diverge of the light sheet. However, the collimating lens then needs to be the same size as the required light sheet. For larger flow applications, this means large diameter optics which can be difficult and expensive to obtain. Another approach is to use an off-axis parabolic mirror.

If a c/w laser is used with cylindrical optics, a c/w light sheet will be generated. This is often suitable for showing streamlines of seed particles moving in the flow, but most flow features will be blurred significantly, when integrating over the imaging camera's often significant exposure time. A common method of generating a pulsed light sheet from a c/w laser is to use a shutter (mechanical or liquid crystal), or an acousto-optic modulator (Bragg cell).

In addition to the light sheet forming optics, one or more converging spherical lenses are usually used to focus the sheet to form a waist. If the incident light beam is considered to have a Gaussian intensity distribution, the minimum waist of the sheet can be calculated using:

$$2w_0 = \left(\frac{4\lambda}{\pi}\right)\left(\frac{F}{D}\right) \tag{5}$$

where $2w_0$ is the beam waist diameter, λ is the wavelength, F is the focal length of the lens and D is the diameter illuminated on the lens by the beam. Equation (5) assumes all geometric distortions are negligible. So, for a beam with an input diameter of 4 mm, the sheet thickness at 1 m from a spherical lens of focal length 1 m is 170 μm. In reality, a laser beam is often not a pure Gaussian and the lens is not aberration free, and so the sheet thickness can be expected to be typically several times thicker than this.

The three methods of generating a pulsed sheet are thus shuttered c/w laser with cylindrical optics, scanned c/w laser and pulsed laser with cylindrical optics. A variety of laser types and optical systems were available at the commencement of this work. The sheet method was chosen according to the following calculations.

The exposure level associated with an illuminated particle varies depending on the method chosen. The exposure of a tracked particle to laser light, here defined as

$$E = \int_0^T I(t)\,\mathrm{d}t \tag{6}$$

where I is the light incident on the particle and T is the duration of exposure, depends on a combination of parameters. To record particle tracks, exposure times must be relatively long; to "freeze" particle images, the exposure times must be short, so $T << d/u$ where d is the particle diameter and u is the particle speed. For a c/w laser with cylindrical optics, the incident light intensity in the sheet, averaged over the illuminated area, is given by

$$I = \frac{P}{2 \cdot l \cdot r} \tag{7}$$

where P is the laser beam power, l is the sheet width and $2r$ is the waist thickness. The residence time of the particle within an observed portion of the light sheet is given by d/u, if

the condition for a "frozen" image is that the particle moves no more than its diameter during the exposure.

So, for the c/w illuminated sheet this results in an average overall exposure E_{CW} of

$$E_{CW} = \frac{P}{2 \cdot l \cdot r} \cdot \frac{d}{u} \tag{8}$$

Similarly, for scanned illumination, the average intensity of the scanning beam is given by

$$I = \frac{P}{\pi r^2} \tag{9}$$

The effective exposure time is now also dependent on the scan velocity v_b and the size $2r$ of the scanning beam and is given by

$$(d + 2r) \Big/ |v_b \pm u| \tag{10}$$

where ± indicates the possible limits with the scan velocity opposite (+) or with (-) that of the particle. In practice, $v_b >> u$ and $2r >> d$ is chosen so that

$$E_{SC} = \frac{P}{\pi r^2} \cdot \frac{2r}{v_b} \tag{11}$$

The mean scan velocity is derived from the rotating mirror as $v_b = R \cdot n \cdot l$ where R is the speed of rotation, n is the number of facets, and l is the sheet width as before. The time-averaged illumination is more homogeneous over the whole width than the c/w sheet. However, the observed flow field may not be considered as instantaneous due to the finite time which the beam takes to complete its traverse and in which time the flow may have changed. Unless $v_b >> u$, the scan period must be taken into account. This factor aside, many images may conveniently be recorded with a single camera exposure.

Typical commercially available mirrors have between 8 and 32 facets and can rotate at up to approximately 250 revolutions per second. An 8-facet mirror can therefore provide 2000 scans/second. A comparison of effective exposure levels for the c/w and scanned (sc) systems

can be made by considering a 40 μm particle travelling at 40 m/s within a sheet 100 mm wide and 0.5 mm thick. Then

Now, for a pulsed laser and cylindrical optics, all of the laser energy is released in a single, extremely short (effectively infinitely short) pulse. The exposure energy is thus simply

$$E_{PL} = \frac{E}{2 \cdot l \cdot r} \tag{12}$$

where E is the energy per pulse. If a pulse rate of 1 Hz is assumed and the same total average power and flow conditions as before, then $E_{PL} = 10^6 E_{CW}$. Thus relative exposures are much higher than either the c/w or scanned methods.

In summary, the disadvantage of using a c/w laser, cylindrical optics and a shutter or AOM is that much of the laser power is not used - it is discarded for the (long) time period when the shutter is closed. So scanned c/w or pulsed illumination should be used. The main disadvantage of scanned illumination is that the illumination is not-instantaneous, and the flow structure may change over the period of the scan. Scanning is therefore only suitable for slow flows.

It is therefore clear that where possible, a pulsed laser should be used. This maximises the light intensity incident on the flow seeding particles, and allows smaller particles to be used, which follow the flow better.

LSI is particularly useful for the rapid characterisation of a flow. It reveals the global distribution of seeding particles within a flow, and how this changes with time. Regions of rapid change in seed concentration indicate strong mixing, often an important flow parameter. If multiple LSI images are recorded, development of flow features such as vortices can be tracked.

2.1.3 Particle image velocimetry

As described, LSI is very useful for visualising a flow field. However, it only produces flow images, which are purely qualitative by their nature. These images are therefore difficult to use as a quantitative flow diagnostic.

Particle image velocimetry (PIV) (e.g.[30] [31] [32] [33]) is an extension of LSI to give quantitative global velocity data. It relies on a light sheet as for LSI, but using two or more pulses of laser light. This is illustrated in Figure 8. Now, seed particles moving within the illuminating sheet scatter light to produce multiple images on the camera recording medium. These multiple images represent the time development of the particle position, and can be linked together to form a record of its movement. The magnitude and direction of the displacement between the multiple images can be used to calculate the particle velocity, assuming the time separation between the laser pulses is known.

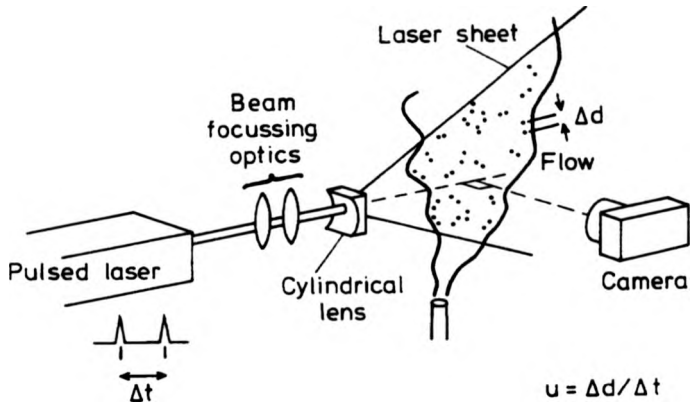

Figure 8. Particle image velocimetry

Multiple images are recorded for each of the seed particles moving within the illuminated flow plane, giving velocity information for the whole area. Velocity information can be derived from the flow image manually, using an enlarged photograph, pen and sharp eye, joining pairs of particles where the matching is clear. However, for many flow images, there can be several thousand multiple imaged particles and a manual approach to image analysis is not feasible. Automated analysis methods are becoming available and being developed further, and are discussed in more detail in the next chapter.

The nature of the velocity data derived from PIV is rather different to that derived from the previously described LDA technique. LDA and related techniques produce time-resolved data for a single measurement point, allowing *time-averaged* velocities to be determined. PIV produces velocity data across an entire measurement plane, but the data is integrated only over the time between the multiple laser pulses. For many flows this time may be only a few

microseconds. Thus PIV velocity data can usually be considered as *instantaneous*. For a unsteady flow, there can be significant differences between the mean and instantaneous flow velocity at any one point in space. Thus it is not usually valid to directly compare LDA and PIV data.

There are two types of PIV image, using either single and two image frames. In the former, the image is illuminated with two or more pulses. In the later, each of the frames is illuminated with a single pulse. The optimum spacing of these multiple pulses is dependent on the flow speed. Typically for a flow speed of 10 m/s and a photographic recording, a suitable displacement is around 0.1 - 1 mm. This gives a time spacing of 10 - 100 μs. For two-frame PIV, these framing rates (10 - 100 kHz) are difficult to achieve, and consequently, PIV images are usually recorded on single frames.

It is possible to derive time history data from PIV by recording a sequence of flow images, spaced in time. However, it is usually not practical to record more than a few tens of images, thus giving only poor statistical information for such quantities as the temporal velocity mean and its deviation.

2.1.4 Backlighting

Backlighting relies on expanding a pulsed laser beam and illuminating the flow from behind. The laser light can be either diffusely scattered from a suitable surface such as a piece of white card or ground glass screen, or passed directly through the flow. Features such as spray droplets will then give shadow images which can be recorded by a suitable camera. Multiple pulsing of the laser can be performed as for PIV, encoding velocity information in the multiple particle images.

Backlighting gives flow images similar to LSI/PIV, but additionally, the shapes of the particles are recorded in their silhouette images. This means that particle sizes can be determined by using image processing to measure the area of their silhouettes. The technique is equally suitable for non-spherical particles, such as coal particles, unlike other sizing techniques such as forward diffraction and PDA.

An advantage of the backlighting technique is that only relatively low laser power is needed, as a result of the direct nature of the illumination. Forward scattering of light is considerably stronger than in the perpendicular direction needed for LSI.

The main disadvantage of the technique is that it integrates through the flow, thereby losing some definition of flow structure. The recording camera also only records fully sharp images in its plane of focus. Particles out of the focal plane are blurred but still contribute to the image, causing a reduction in contrast of the intended flow plane. The technique can be considered to give flow images similar to the LSI technique, but with a much less sharply defined measurement plane.

Out of focus, blurred particles give incorrect results when measuring image diameters for particle sizing. The blurred particles appear bigger than their true focused size, skewing the measured size distribution. The sizing algorithm can be modified to check for sharp edges to particle images (thereby focused), at the expense of additional complexity and processing time. Considerable experimentation may be needed to find a suitable criterion to separate blurred particle images from suitably sharp images.

Backlighting can only be used to size or classify particle shapes that are sufficiently large that their images occupy multiple pixels on the image recording medium. Otherwise there is no image "area" that can be measured. Thus for a 1000 x 1000 pixel image, and a field of view of 1 x 1 cm, particles with a diameter larger than about 50 microns can be studied.

Another disadvantage of backlighting is that it is suitable only for flows with a high transmissivity. This is because particle image contrast decreases as transmitted light decreases. Thus dense flows with a high particle concentration pose a problem.

2.1.5 Holography

Holography, invented by Gabor [34], relies on the interference between two or more temporally coherent waves (object and reference beams) to produce a fringe pattern on a recording medium (such as a high resolution photographic plate). The technique can be used to record a three-dimensional volume of a moving flow (e.g. [35]).

A number of optical configurations can be used, to suit the flow conditions, including off-axis and in-line techniques. A volume within the flow is illuminated and, if a pulsed laser is

employed, three dimensional images of particles moving within the entire volume can be recorded. If the laser is double pulsed each particle will result in a pair of images being recorded. Velocity information is encoded as for PIV but now all three components are recorded. In practice, the ability to determine the depth (z co-ordinate) of the particle image is almost always less than for its x and y co-ordinates, and thus the derived z component of velocity is usually less accurate than the other two components.

Variations in the refractive index within the illuminated flow volume can be recorded by making a double exposure hologram, with and without the moving flow. On reconstruction, the two object beams interfere, giving a fringe pattern, modulated by the optical path changes imparted by the refractive index variation of the flow. This technique is known as holographic interferometry, and can be used to study density variations within a flow e.g. [36].

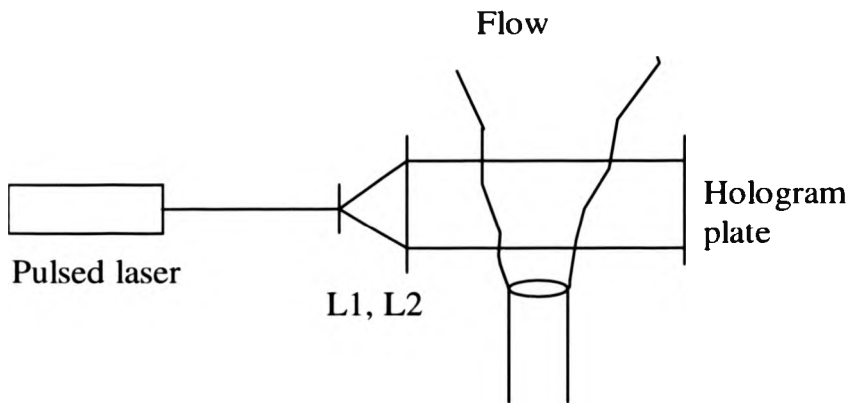

Figure 9. The in-line holographic configuration

The in-line (or Fraunhöfer) technique uses a single beam which is passed through the flow[37]. Scattered light from the particles (object beam) interferes with the un-deviated light (reference beam) to form the hologram. A schematic is shown in Figure 9. Successful recording relies on an unattenuated reference beam and hence negligible optical absorption within the flow. It is therefore only suitable for flows with low particulate numbers. The size of the volume must be smaller than the laser coherence length. Typical laser coherence lengths range from fractions of millimetres (Cu vapour laser), to several hundred metres (single-mode Argon ion). In practice, the upper size limit of the flow is often set by unwanted local phase decorrelation by

refractive index gradients occurring between a particular point in the flow and the hologram recording.

The off-axis technique uses two or more beams (angularly separated) to form the hologram, and so does not require the flow to be fully transparent to the reference beam [38]. A schematic is shown in Figure 10. The two beams which are coherent with respect to each other, are generated using a beam splitter (BS). The amplitudes of the separate object and reference beams can now be varied independently, thereby allowing the hologram fringe visibility to be adjusted. The extra exposure control over the visibility of the fringe pattern interference pattern offered by the use of two beams allows optimisation of the hologram efficiency (brightness) and signal to noise ratio. Also, phase objects in the flow, such as enclosing pipe work which would otherwise distort the in-line reference beam, can be included. However, the off-axis technique is more complicated optically, and has a theoretically poorer resolution limit. The laser coherence length generally needs to be higher than for the in-line configuration for a given size of flow.

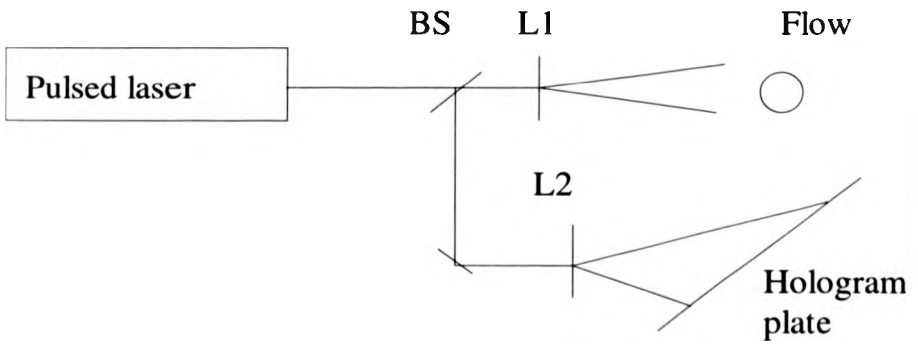

Figure 10. The off-axis holographic configuration

Trolinger et al [39] applied holographic imaging and interferometry to the study of individual combusting coal particles in flight. They found that off-axis holography appeared to give a slightly lower image resolution than the in-line technique, but gave images that were lower in noise and easier to view.

2.1.6 Laser induced fluorescence

As explained previously, a laser can be tuned to excite a particular energy band transition in the material of interest. The intensity of the resulting fluorescence can then be related to the concentration or temperature of the material.

Within a flow, the laser illumination can be focused to a point, or formed into a sheet as for LSI described previously. Thus a planar visualisation of the distribution of a particular species can be achieved. Quantitative species concentration may also sometimes be determined if the LIF measurement is carefully calibrated.

Many flow species have been measured using LIF including OH [40] and NO [41]. If the concentration of the species is known across the flow, flow temperature can be determined or visualised instead [42] [43].

2.1.7 The TIR film thickness technique

A new technique is proposed which differentiates fully the liquid in contact with the wall, reveals the entire wall film structure, is able to be calibrated for quantitative thickness, and has the potential (as will be discussed) of showing the temporal development of the spray with good resolution [44]. This technique is referred to as the total internal reflection (TIR) technique.

When an optical ray meets an interface between two media at an incident angle greater than the critical angle, θ_c total internal reflection occurs. The critical angle can be computed from the refractive indexes, n_1 and n_2 of the two media using Snell's Law:

$$\sin\theta_c = \frac{n_2}{n_1} \tag{13}$$

Clearly, if a change in refractive index of one of the media occurs, the critical angle will change.

Consider an optical plate and a collimated light beam introduced into the plate in such a way as to illuminate the surface, from within, at an incident angle slightly greater than the critical angle. The light suffers total internal reflection. If a film of liquid is present on the surface, the

critical angle increases to greater than the incident angle, total internal reflection does not occur, and light is transmitted into the film.

Furthermore, if the liquid is able to fluoresce by illumination of the incident light, then this fluorescence may be viewed through the plate and recorded using a camera. Provided saturation is avoided, the intensity of the fluorescence will be dependent on the film thickness and may be calibrated for quantitative measurement. Figure 11 shows a schematic of the principle of the complete TIR technique.

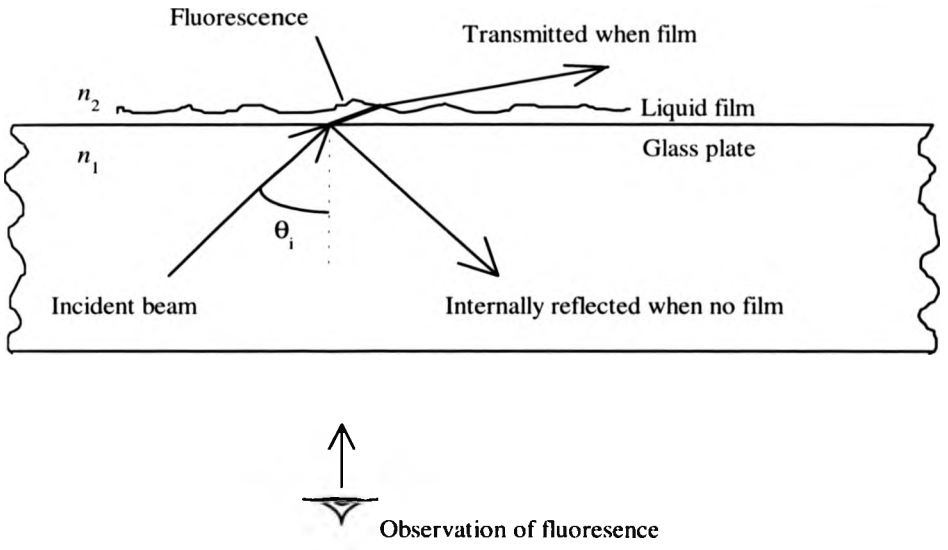

Figure 11. Schematic of the TIR film thickness measurement technique

This technique has several potential advantages over the previously described mechanical and optical film thickness measurement techniques. Mechanical techniques are intrusive, often affecting the film. For electrical techniques, it is difficult to extract the measured film thickness data from a realistic combustion application, such as a confined and enclosed engine cylinder. All of the existing techniques measure film thickness only at a point, or integrate over the area of a sensor. The TIR technique promises global film measurement. Application of the TIR technique is discussed in Chapter 4.

2.2 Global optical diagnostic parameters

For successful application of global optical diagnostics, a number of parameters need to be optimised. These are flow seeding, illuminating laser and the medium used for recording the image.

2.2.1 Flow seeding

Flow diagnostics such as LSI/PIV, backlighting and holography rely on light scattered from seed particles. In many cases, the particles are naturally present in the flow, i.e. diesel sprays and pulverised coal furnaces. However, where naturally occurring particles are not present, or are unsuitable, artificial particles need to be added to the flow and they must be carefully chosen. The particles used are selected according to the amount of scattered light required, and the characteristics of the flow itself. The intensity and directional dependence of the light scattered by an illuminated seed particle is a function of the shape, size and refractive index of the particle, and the surrounding medium. The equations relating scattering intensity to these parameters are derived from Mie Theory. This is discussed in depth by van de Hulst [45].

Mie theory

Mie theory tells us that when a particle is illuminated by light of wavelength, λ, and intensity, I_0, the light intensity which reaches a point at a distance, R, and in the direction, θ,ϕ, from the particle is,

$$I_s(\theta,\phi) = I_0 \frac{S^2(\theta,\phi)}{k^2 R^2} \tag{14}$$

where the wave-number, $k = \frac{2\pi}{\lambda}$

and S is the scattering matrix for the particle,

$$S = \begin{bmatrix} S_2 & S_3 \\ S_4 & S_1 \end{bmatrix} \tag{15}$$

Each element of S is a complex function of the particle dimensions as well as of θ and ϕ. For spherical homogeneous particles, S is diagonal with $S_3 = S_4 = 0$.

When the particle is detected by a physical sensor, the scattered light is collected over a solid angle, and the total power scattered by the particle is given by,

$$P_S = R^2 \int I_S(\theta,\phi)\, d\Omega \tag{16}$$

where $d\Omega$ is the solid angle,

$$d\Omega = \sin\theta d\theta d\phi \tag{17}$$

The result of this integration is,

$$P_s = I_0\, C_S(\theta,\phi) \tag{18}$$

where C_S is called the *scattering cross-section.*

For small spherical particles, where the diameter is much smaller than the wavelength of the light $\left(d/\lambda < 0.1\right)$, the full Mie equation can be simplified and Rayleigh theory then applies. Now $I_S \propto d^4/\lambda^4$.

For large particles (>5 μm), the scattered light can be considered as coming from a large evenly illuminated disk, and so $I_S \propto d^2$ (the so-called geometric scattering range). Scattering is more or less independent of wavelength, unless the particles themselves are large and selectively absorbing.

For particles with sizes in between the Rayleigh and geometric ranges, the relationship is more complex, and the full Mie theory has to be used to calculate scattering intensity. This is the transitional scattering range. Equation (14) cannot be solved analytically, but has to instead be approximated numerically. This can be performed to any desired level of accuracy using a digital computer, and has been computed by a number of workers. Adrian and Yao [46] show that the transitional behaviour occurs for particles with sizes approximately in the 1 - 10 micron range.

Seed particle behaviour in a flow

Another important characteristic of a seed particle is the degree to which it follows the flow medium of interest. Only the shadowgraphy, Schlieren and holographic interferometry techniques measure the flow medium - the other techniques are measuring the seed particles. It is therefore necessary to check that fluid and particle velocities are similar. There are two main causes of differences in seed and medium velocities.

If the particle density and fluid density are different, this causes a gravitationally induced velocity that can be calculated from an appropriate drag law. The other main difference results from inertial delay when the particle is accelerated. Hjemfelt and Mockros [47] give an analysis of the other (usually smaller) factors affecting particle velocity.

The equation of motion for a spherical particle relative to an infinite fluid was first derived by Basset[48] by balancing the acceleration forces on the particle and a stationary displaced fluid. This can be converted to a form applying to a moving fluid by considering the instantaneous velocity of the particle relative to the fluid[49]:

$$\frac{\pi d^3}{6}\rho\frac{\mathrm{d}\mathbf{u}}{\mathrm{d}t} = -3\pi\mu d\mathbf{v} + \frac{\pi d^3}{6}\rho_F\frac{\mathrm{d}\mathbf{u_F}}{\mathrm{d}t} - \frac{1}{2}\frac{\pi d^3}{6}\rho_F\frac{\mathrm{d}\mathbf{v}}{\mathrm{d}t} - \frac{3}{2}d^2\sqrt{(\pi\mu\rho_F)}\int_{t_0}^{t}\frac{\mathrm{d}\mathbf{v}}{\mathrm{d}t'}\frac{\mathrm{d}t'}{\sqrt{t-t'}} \quad (19)$$

where ρ, ρ_F are the particle and fluid densities,

μ is the fluid dynamic viscosity,

$\mathbf{v} = \mathbf{u_F} - \mathbf{u}$ is the velocity difference between fluid and particle.

The four terms on the right hand side of equation (19) represent respectively the Stokes drag force, the pressure gradient force on the fluid, the fluid resistance to an accelerating sphere, and the drag force associated with unsteady motion. Equation (19) is valid only within the following assumptions:

- homogeneous, time-invariant turbulence
- particles smaller than turbulence micro-scale
- Stoke's drag law applies (spherical particles)
- particle is always surrounded by the same fluid molecules
- no interaction between particles

Now, for particles suspended in gases, $\sigma = \rho/\rho_F \approx 10^3$, and provided that the Stokes number,

$$\mathbf{N}_S \equiv \sqrt{\frac{\nu}{\omega d^2}} \tag{20}$$

where ω is the frequency of the turbulent fluctuations, is greater than about 8 [50], then equation (19) reduces to,

$$\frac{\mathrm{d}\mathbf{u}}{\mathrm{d}t} + \frac{18\upsilon}{d^2\sigma}\cdot\mathbf{v} = 0 \tag{21}$$

where $\upsilon = \mu/\rho_F$ is the fluid kinematic viscosity.

This equation assumes a pure drag force obeying Stoke's law. This can now be solved giving,

$$\mathbf{u} = \mathbf{u}_F + (\mathbf{u}(0) - \mathbf{u}_F)e^{-t/\tau} \tag{22}$$

where

$$\tau = \frac{\sigma d^2}{18\upsilon} \tag{23}$$

Here τ is the response (relaxation) time of the seed particle to changes in the fluid velocity. If the fluid turbulent fluctuations are considered sinusoidal, then the frequency response is given by [47],

$$\omega = \frac{\sqrt{\left(1/\eta^2\right) - 1}}{2\pi\tau} \tag{24}$$

where η is the particle oscillation amplitude divided by that of the fluid. If a criterion for particles following the flow of $\eta > 0.95$ is set, then particles must satisfy

$$d^2 < \frac{0.94\nu}{\omega\sigma} \tag{25}$$

A useful concept for selecting seed particles is the aerodynamic diameter, defined as $d_a^2 = \sigma d^2$. This is the equivalent diameter of a particle, were it to have unit density (1000 kgm^{-3}). Particles with equivalent aerodynamic diameter respond equally well to fluctuations in fluid velocity.

For air flows at ambient conditions, $\sigma \approx 833$ and $\nu \approx 1.5 \times 10^{-5}$ m^2/s. So, if it is required that particles respond to fluctuations of up to 1 kHz, equation (25) indicates that they must have an aerodynamic diameter of less than 4.1 microns. Particle sizes for liquid flows can be considerably larger.

Limitations of laser intensity, particularly when expanded into a large sheet, mean that particles larger than the ideal size often need to be used, at the expense of some loss of flow tracking (apparent as a particle lag).

Choice of seed particle

For optimum results, seed particles should ideally be:

- small (to follow the flow accurately)
- mono-disperse (all particles to behave identically)
- spherical (to scatter light independently of orientation)
- stable - both physically and chemically (for use at high temperatures and in reactive environments)
- low density relative to fluid (to minimise any settling out)
- highly reflective - white preferably (for maximum light scatter)
- non hazardous (potential inhalation)
- cheap (large flows may require considerable quantities of seed)

In practice, no seed material has all of these properties, and the choice for a particular flow application is a compromise. The seeding requirements for global diagnostics are similar to those of LDA, and particles intended for this are often employed. Many different materials are

available, including TiO_2, smoke, oil drops, BN, He bubbles, glass beads (micro-balloons), flour, milk and latex spheres. All of these materials have been successfully used in flow measurement.

2.2.2 Lasers

Many materials will lase, and consequently a considerable number of different types of laser are available for application to flow measurement. However, only a small number of these lasers are actually used in practice, each a compromise of a performance and expense.

Desirable laser characteristics for flow imaging

As previously described, a pulsed laser is most suitable for LSI, PIV, backlighting and holography. The pulsed illumination provides the most efficient imaging of moving seed particles. High pulse energy is needed to illuminate small particles, and to allow use of high resolution (and usually insensitive) recording media.

Pulse duration should be short to freeze particle motion, and to allow high speed flows to be studied. For LSI/PIV, particles should not move more than about their diameter during the pulse exposure. So for 1 μm particles moving at 100 m/s, the pulse duration should be approximately 10 ns or less. For holography, particles should ideally not move more than about $\lambda/10$. A long coherence length and therefore a narrow bandwidth is necessary for holography. A coherence length greater than the flow volume is needed. However, as pulse duration decreases, coherence length also decreases, reducing the suitability of the laser for holography.

The wavelength of the laser light should be short. As previously discussed, the efficiency of light scattering from particles increases as the wavelength decreases. From this, the wavelength should be as short as possible. However, if the wavelength is short enough to mean ultra-violet light, then a number of problems occur. Optics and imaging lenses need to be made of silica, for high transmissivity, which increases costs. The main disadvantage is that the light is non-visible - optical alignment and camera focusing becomes much more difficult. It is also important to match the detector wavelength response to the laser wavelength.

For multiple pulse techniques, an ability to provide these multiple pulses is obviously necessary. For high speed flow measurement, rapid pulsing is necessary. For a flow speed of

100 m/s, inter-pulse separations of a few μs are typically needed. It is also important that the pulse-to-pulse stability is good, so that pulse intensity is similar, to maximise matching between particle images. Timing jitter (variation in pulse-to-pulse time separation) should also be low to minimise uncertainty in velocity measurement. Easy synchronisation of the laser pulsing to the recording camera framing rate is also important.

Other useful features are that the laser is portable, and can therefore be moved easily from one flow application to another, often in a different building. In conjunction with this, air rather than water cooling means that installation time is reduced, and the laser can be used where mains water is not available. High efficiency in the conversion of electrical input energy to light output means that single-phase mains power can be used, again easing the installation time and laboratory requirements.

Eye-safe output is useful, allowing the laser to be used without safety precautions. Unfortunately, eye-safe lasers (Class 1) are either very low power (< 1 mW), and/or have a long (infra-red) wavelength. For sufficient illumination of medium and large-scale flows, high power (Class 4) lasers are necessary.

Finally, the laser should preferably be inexpensive. This is often the main factor in the choice of laser. Most suitable lasers require a significant capital investment, and it is often necessary to make best use of an existing laser within a laboratory, rather than purchase an optimum type.

Potential lasers for global diagnostics

The most suitable lasers for flow measurement are first described, followed by the lasers used in the flow studies reported here.

Although there are many different lasers, only a few are suitable for flow measurement. At the low-end, the helium-neon (HeNe) laser has found some application. This cheap c/w laser produces red light at 633 nm, but is usually only available at low powers of 0.1-30 mW. For small scale flows (a few mm in diameter), this may be sufficient.

The argon ion laser is another c/w design, but can produce much higher output powers than HeNe. It produces light at two main wavelengths, 488 nm (cyan) and 514 nm (green). Power outputs of several tens of watts are possible.

The ruby laser was the first laser invented, and is still finding application. It produces pulses of deep red light at 694 nm, and can provide output energies of 10 J or more when used in an oscillator-amplifier configuration. A significant disadvantage is that the pulse repetition rate is low, often many seconds or minutes between pulses. This means that configuring the optical system is difficult, and multiple imaging of time-varying flows is not possible.

The NdYAG laser can be used in c/w or pulsed operation. It produces pulses of near infra-red light at 1064 nm, and can provide pulse energies of up to 1 J (oscillator only - higher with amplifier).

The copper-vapour laser is a pulsed design that can be operated at repetition rates as high as 40 kHz. It produces light at 511 nm (green) and 578 nm (yellow). Output powers up to 120 W (average) are possible.

Increasingly the semi-conductor diode laser will find application. Similar in power to the HeNe (although increasing rapidly all the time), it is very efficient in converting electrical energy to light. Light quality is infra-red and often poor quality, with the output strongly diverging. A major improvement has been to use a hybrid NdYAG/diode design, with the diode acting as an efficient coupled pump for the NdYAG crystal.

The lasers used in these flow studies were an NdYAG laser, an argon ion laser and a copper vapour laser.

NdYAG Laser

The NdYAG laser is a solid-state design and can operate in a c/w or pulsed mode. As previously described, a pulsed laser is best suited for LSI and PIV. At the commencement of these flow studies, existing commercially available NdYAG designs were not considered optimal for PIV, so a custom version was designed and purchased. The Spectron NdYAG purchased is described below, with a schematic shown in Figure 12. This laser was used as the "work-horse" for these flow studies.

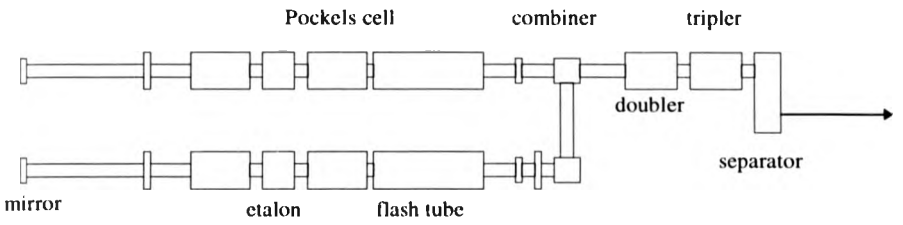

Figure 12. Schematic of NdYAG laser

Conventional close coupled high voltage flash tubes are used to excite the NdYAG material, which lases in the near infra-red at 1064 nm. The flash tubes can be fired repeatedly, enabling a variable pulse repetition rate of 0-40 Hz. A dual loop water cooling system uses de mineralised water in the closed loop primary, in direct contact with the laser rod and flash tubes, and a secondary circuit taking water on demand from the mains supply.

An active Q-switch is used, consisting of a Pockel's cell mounted within the laser cavity. The Pockel's cell uses a single crystal of Potassium Dideuterium Phosphate (KD_2PO_4 or KD^*P) which acted to modulate the polarisation of the beam. This polarisation modulation is used as a high speed shutter with the addition of a crossed polariser. The Q-switch acts to spoil the lasing output until triggered, allowing the population inversion to build up further, thus concentrating the normal lasing pulse (approximately 200 µs duration) into a much shorter pulse (15 ns duration) of much higher peak intensity. A pinhole (1 mm diameter) is used inside the cavity to eliminate many of the multi-modes normally associated with NdYAG excitation , and thereby improve the quality and reduce the diameter of the beam without appreciably reducing the maximum output power.

Plane dielectric mirrors are used to define the laser cavity. These mirrors are designed to handle the high peak powers present during the laser pulse without damage. The rear reflector has 100 % reflectance, while the front reflector is only partly reflecting, to allow the output to be coupled.

A single convex spherical lens is used inside the laser cavity to act as a collimating telescope. The power of this telescope is adjustable to compensate for the change in beam characteristics which occur if the pulse repetition rate is changed significantly (i.e. from 1 Hz to 25 Hz). The cause of this change in beam collimation is due to a change in temperature of the NdYAG rod

itself. Most NdYAG designs use an unstable resonator cavity rather than a telescope, which although more efficient, is suitable for only a narrow range of repetition rates.

The laser consists of two oscillators as described above, with full duplication of power supplies and controls. The cavities are mounted in parallel on an Invar sub-chassis for increased stability against temperature and vibrational effects. The output beams from the two cavities are combined by deflecting one of the beams by 90° and using a polarising beam splitter/combiner. The deflection mirror is adjusted so that the two beams are accurately superimposed, and follow the same path out of the beam splitter. This is important to ensure the two subsequently generated light sheets are also properly superimposed.

The use of two separate cavities means that double pulse light sheets are easily generated, with a very flexible time separation, and easy control of the relative pulse intensities. An alternative two pulse design would be to use a single cavity, but to trigger the Q-switch partially and then later fully, both within the single main pulse population inversion. This approach has the advantages of simplicity and lower cost, but only a limited range of pulse separation would be available (typically 50-150 μs), and control of the relative pulse intensities can be difficult.

The combined laser beams are then passed through a frequency doubler crystal (again KD^*P). This deliquescent crystal was mounted in a temperature controlled oven (39° C) for stable operation and protection against water vapour ingress. The output of the laser was measured to be approximately 250 mJ for each of the two pulses in the infra-red, and 75 mJ at 532 nm, the frequency doubled wavelength (green). This gives a net conversion efficiency of 30 %. The frequency doubled light is then separated from the remaining fundamental light using a simple prism. This fundamental light is then not needed and is dumped. Increased laser power could be produced if required using additional laser rods to act as amplifiers for the existing oscillators.

The laser in its initial form was used for LSI and PIV. Later, another non-linear crystal was fitted to allow addition of fundamental and second harmonic photons, giving third harmonic photons (355 nm). This allowed the laser to be used for laser induced fluorescence (LIF) studies. Also, etalons were purchased, which when inserted into the cavities of the two oscillators, increased the coherence length to approximately 40 cm. This allowed the laser to be used for holographic recording.

Argon ion laser

The argon ion laser used for these studies was an Innova 90-5. This provides 5 W of multi-line output. Three-phase mains power is needed together with mains water cooling.

For these studies, it was used for holographic reconstruction. The normal multi-line cavity rear mirror was replaced by a mirror/prism combination. This changed the laser to single colour operation (514 nm) and reduced the output power to 2.5 W. A solid glass etalon was then added to reduce the line bandwidth to a single mode, and thus increase the coherence length to some 200 m. The etalon was placed in an electrical oven with better than 0.01 °C stability. The etalon was then temperature tuned for maximum output power. It was found that after a warm-up period, a single mode, and a constant output power of 1.0 W could be maintained for several hours.

Copper vapour laser

The copper vapour laser is a rather less common design to the previously described lasers. It is based on the lasing of copper atoms in the vapour phase. The main differentiating feature is the high pulse repetition rate available.

The laser used here was an Oxford Lasers CU10 model. This provides 10 W of light, 65 % at 510 nm, 35 % at 578 nm. Copper metal (electrical grade) is first placed inside a glass tube, insulated with a thick layer of alumina. The air inside is first evacuated using a vacuum pump, and then replaced by low pressure neon (approximately 40 mBar). A pulsed 5 kV electrical discharge (switched by a radar thyratron) is then struck across the length of the tube. The neon acts as a buffer gas, transferring energy from the discharge to the copper atoms. The discharge is then repeated at a high repetition rate of between 2 and 40 kHz. Over a period of around an hour, the 1.5 kW energy input causes the copper to first melt, then vaporise, and finally lase. Laser pulse duration is approximately 40 ns.

The laser tube produces a multi-mode beam some 50 mm in diameter. Thus, larger diameter (and more expensive) steering and focusing optics are required than for the other lasers described here. Beam quality is not particularly high, and it diverges more than the other laser types described. However, (average) output power is high, although the high repetition rate means that individual pulse energy (up to approximately 2 mJ) is much lower than that

available from NdYAG. The laser efficiency is also high, with only single-phase electrical input required. Cooling is by forced air circulation.

Synchronising the laser pulse to a camera is straightforward, as the light output occurs directly in response to the input electrical pulse. This allows the repetition rate to be varied easily. The laser was used in conjunction with high speed camera for these flow studies, allowing high framing rate imaging.

2.2.3 Recording media

Assuming the flow has been adequately seeded and laser illumination produces an acceptable image, then this image must be detected and recorded for later analysis. This means a camera and compatible recording method. The main available techniques are discussed, and the most suitable then chosen for these flow studies.

There are two main methods of recording a flow image, based on photographic or electronic technologies. The photographic approach has been available for many years, while the video technique has only recently become competitive in terms of resolution and price.

Photography

Photography is based on the physical and chemical changes that occur in certain silver salts when exposed to light. The salts are immobilised on a plastic base which is chemically developed after exposure. After development, the silver is left behind in greater or less amounts dependent on the exposure it received. The density of the silver remaining causes changes in transmissivity of the film. The silver forms "grains" of random shapes and sizes. These grains determine the resolution of the image. The response of the film to light is non-linear.

The sensitivity of photographic film is strongly dependent on the size of the grains. As the grains are made larger, the film becomes more sensitive to light. The sensitivity of photographic film is measured on the ASA and DIN scales. As the grain size increases, the resolution and contrast range of the film decreases. Thus film sensitivity (speed) and resolution are inversely related. So for example, to achieve high resolution and a fine contrast, one would use a 50 ASA film, while in low light conditions, one would use a 1000 ASA film and get characteristically "grainy" images.

In many flow applications, where the flow size is large and/or the laser is low-powered, the light exposure is limited, and a fairly high speed film (400 ASA) is usually needed. For this type of film, a resolution of around 100 line pairs/mm is typical. This refers to the highest resolution that can be resolved from a calibrated test chart.

Video

Video recording now relies almost entirely on the charge coupled device (CCD). Until recently, video cameras used a variety of vidicon designs (equivalent to a cathode ray display tube working in reverse) to sense the input image. Modern video cameras instead use a CCD as the light sensing element. This consists of a silicon surface, divided up into a large number of small insulated "pits". Light falling on the silicon causes charge to build up in these pits as a result of the photoelectric effect. Discharge channels are built into each pit and allow the charge to be moved across the CCD on demand (end of exposure). The charge is shuffled from one pit to another until it is read off from the CCD. The charge associated with each pit is in linear proportion to the light flux on the pit, integrated over the period of exposure. Thus the electrical read-out signal represents the light distribution received across the CCD surface, with each pit acting as an image pixel.

Commercial CCDs are available in a range of sizes, typically described as half inch, 2/3 inch and one inch. (although the actual light sensitive area is rather smaller). The image resolution is determined by the number and size of the pixels. The vast majority of currently available CCDs are designed with around 700 x 500 pixels, each some 10 - 20 microns square. These particular values are a result of the intended application - the PAL (CCIR) and NTSC domestic television formats. The PAL format specifies 625 image lines at 25 Hz, while the NTSC format specifies 525 lines at 30 Hz. Both formats are interlaced, with two fields of alternating image lines added together to form the full frame. The large size of the television market means that the cost of these CCDs is very reasonable. The camera output can be conveniently viewed on a standard television monitor.

Higher resolution CCDs are available, but at considerably higher cost. At the time of writing, resolutions of up to 2000 x 2000 pixels are readily available, fully integrated into camera designs. Signal bandwidth limitations within the CCD silicon chip limit the readout data rate to 10 MHz or so (for a single output channel). This means that as the number of pixels increases,

the image framing rate tends to decrease. Thus these high resolution cameras are slow-scan devices with frequencies of a few Hz. The main disadvantage of these cameras is that their non-standard image format cannot be viewed on a standard monitor.

Other recording methods

Holography is usually performed using photographic materials. The fringe modulation is high and usually requires high resolution (thousands of lp/mm) and therefore slow (<0.01 ASA) film.

One alternative to film is the use of thermoplastic materials. These use materials which physically deform when exposed to light. The modified surface relief of the material can be used to diffract light and thus reconstruct the hologram. The main advantage of thermoplastic materials is that they do not require any chemical processing - the hologram can be reconstructed instantly. Also, the hologram can be erased and re-recorded simply by heating the material. The main disadvantage of thermoplastics is their relative insensitivity. Typical exposure levels are around 100 times greater than film to achieve the same fringe visibility. This usually precludes their application to recording flow images, where scattered light levels are low.

Comparison of photography and video

Photographic and video cameras are both used to record images of the flow of interest. However, their relative performances are considerably different. For flow imaging cameras, there are four main factors of interest, namely framing rate, resolution, intensity response, and spectral response. Framing rate and resolution have already been covered above.

The response of film and CCD to light is quite different. The response of film to changing exposure levels is complex. As light exposure increases, the processed film image density increases. A typical film response is shown in Figure 13 [51]. Film density is a logarithmic measure of how much light is absorbed by the film negative when viewed (e.g. 0.0≡100%, 1.0≡10%, 2.0≡1% transmittance). It can thus be seen that the film response is non-linear. Film has a minimum density irrespective of exposure. When exposure exceeds a minimum level, then the film begins to respond. As exposure increases further, the film density increases until the film is saturated (fully black).

In contrast to film, a CCD responds linearly to exposure. When the light level is above the minimum illumination of the CCD (8 micro-lux for Kodak MEGAPLUS 1.4 [52]), then the response is accurately linear (0.4% [52]). When the exposure exceeds a certain level (55 dB dynamic range [52]), the CCD will saturate, and often "bloom". This is where the charge from one pixel site leaks into its neighbours, creating spurious image artefacts. The sensitivities for typical CCD's and films are similar. For example, Kodak TMAX-100 film and the Kodak MEGAPLUS 1.4 CCD camera both have an equivalent film speed of 100 ASA.

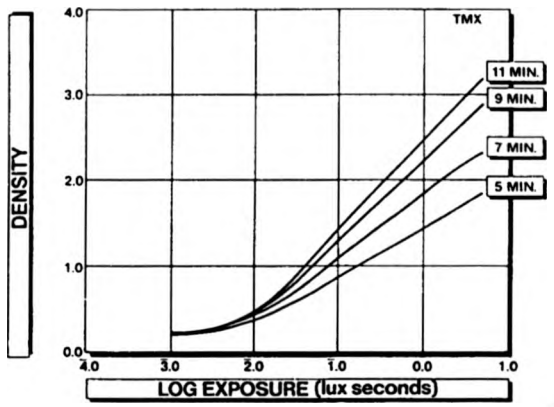

Figure 13. Exposure response for Kodak TMAX-100 film

Spectral response of film and CCD is again different. Typical responses at different wavelengths are shown in Figure 14 and Figure 15 for film and CCD respectively. CCD's have an extended response into the infra-red, and a rapidly curtailed response in the ultra-violet. CCD chips can be specified with a special (fluorescent) coating to extend their sensitivity into the near ultra-violet. Film can be purchased with enhanced infra-red sensitivity, but most brands generally fall off sharply towards 700 nm. The response of film to ultra-violet and shorter wavelengths is generally good (specialised x-ray films are available).

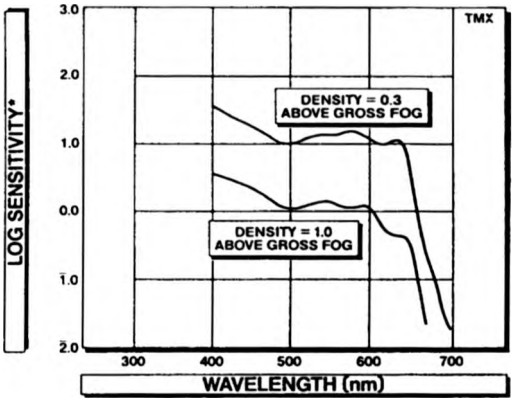

Figure 14. Spectral response for Kodak TMAX-100 film

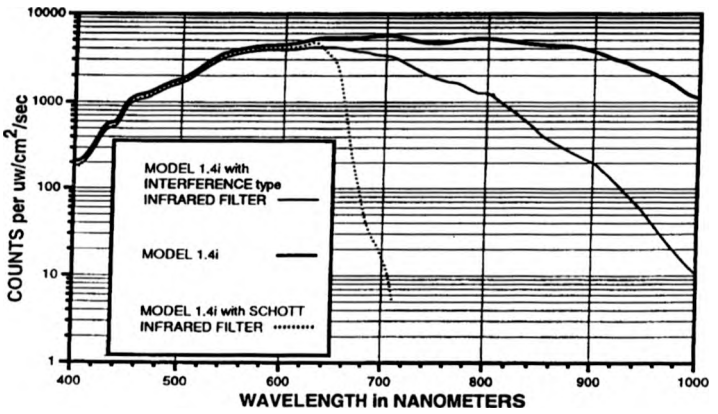

Figure 15. Spectral response for Kodak MEGAPLUS 1.4 CCD camera

2.3 Image processing

2.3.1 Overview

Flow images are inherently qualitative - they are easy to assimilate visually by the human eye and brain, but difficult to analyse quantitatively An image needs to be *digitised* if it is to be analysed by a computer. This image digitisation is performed by a frame grabber. This consists

of a fast analogue to digital converter (ADC) and a bank of computer memory. The analogue video signal is digitised and then stored, before being transferred to a host computer for further processing. The UK/European video standard is PAL (625 interlaced lines, 25 frames per second), which if digitised at 768 x 512 pixels (picture elements) and 8 bits per pixel, requires a conversion sampling rate of around 12 MHz, and storage space of 384 kB per frame.

The image is now in the form of a numerical array within the computer memory. It can be manipulated in many ways to extract a variety of information. Processing operations fall in four basic groups: algebraic operations, geometric operations, filtering and transforming, and feature recognition [53].

Algebraic processing operations consider each pixel separately, with no interaction with its neighbours. Examples are look-up table (LUT) modifications for enhancing image contrast and brightness through the use of false colours and shades to represent particular image intensity values. Also, image arithmetic (such as addition and subtraction) is often used for averaging several frames of a changing image scene or for removing the effect of an unwanted background to emphasise the subject. Both of these techniques are applied here to flow images, and are described in Chapter 5.

Geometric processing operations are similar to algebraic processing methods in that pixels interact only with themselves, but now can change spatial position as a result of the operation. An example is image warping: this is where the image is interpolated onto a new pixel grid, so that distortions can be added or removed. This can be used to compensate for viewing through a refracting medium such as a curved surface, or to change the perspective from one viewing angle to another.

Filtering and transforming techniques modify the image by replacing pixels with the result of an arithmetic operation on the surrounding pixels. Filtering operations are used to remove noise from an image, or to emphasise detail, such as edges of objects. Filtering is performed by convoluting the image with a filter mask, for example, a low pass filter (for smoothing and noise reduction), can be implemented by convoluting the image with this simple mask;

$$\begin{matrix} 1 & 1 & 1 \\ 1 & 1 & 1 \\ 1 & 1 & 1 \end{matrix}$$

and similarly a high pass (Laplacian) filter;

$$\begin{matrix} -1 & -1 & -1 \\ -1 & 8 & -1 \\ -1 & -1 & -1 \end{matrix}$$

This type of filter is useful for edge and point detection, and enhancing image sharpness. More complex filters using adaptive masks are also available [54]. The high pass filter is used to generate the contour images shown in Chapter 5.

Transforming operations are similar to filtering, but are generally more complex. They are used for more advanced image processing. An example is the Fourier transform, which converts the image into the spatial frequency domain. This is discussed further in the PIV analysis chapter.

The final group of operations is feature recognition. These operations use intensity thresholding to produce groups of pixels with the same intensity, corresponding to objects in the original image. The connectivity of these groups of pixels is then examined to identify each discrete object. Various parameters can then be derived for each object, such as its position in the image, its size (area in pixels) and shape. Feature recognition is used in the particle tracking algorithm described in the PIV analysis chapter.

2.3.2 Implementation of image processing

The processing algorithms described above are all useful for flow diagnostics. Implementation of these algorithms can be performed in a number of ways.

Where processing time must be minimised, such as in real-time applications where all of the processing must be carried out within one frame time (40 ms for PAL), hardware based processing is often used. Here, customised circuit logic is designed for operations such as filtering, transforming and recognition. Clearly, this is inflexible, and requires a fixed design. The cost and time needed to implement a hardware solution can be high.

Where ultimate speed is not needed, a PC based solution is preferable. PC and related imaging hardware is low cost, and a wide variety is readily available. A bus mounted frame grabber expansion card digitises the video signal, transferring the data to the host processor memory space. The PC CPU can then process the image data as required.

When rapid implementation is needed, a command interpreter/macro based software tool can be used. Here, a sequence of standard image processing functions can be combined to perform the required task.

For these flow studies, a PC based solution was used, and custom-written software was written using the 'C' programming language. This offered good structuring together with highly efficient (and therefore fast) code. Software algorithms were written with the intention of re-usability in mind, so algorithms were coded to be of general application. Descriptions of processing software for specific flow applications follow in the next chapters.

3. Development of a PIV Analysis System

The previous chapter introduced the particle image velocimetry technique. This chapter discusses methods of PIV analysis, and goes on to detail the software developed as part of these flow studies. The application of this software to the processing of PIV images of the cooling water flow around a model IC engine block is then described.

3.1 PIV analysis methods

There are two main approaches to PIV analysis. These are correlation analysis, and particle tracking analysis. The first analyses a region of the flow image, and determines the average displacement of the particle field. The second analyses the positions of the individual particles and then attempts to match them with their respective multiple images. Each technique has advantages and disadvantages, and is relevant to particular kinds of PIV flow image. Both of these approaches can be used to study single frame or two-frame PIV images (as discussed in the previous chapter).

3.1.1 Correlation analysis

Correlation analysis involves *correlating* one region of the flow image against another region. Movement of the flow region is revealed in its correlation. Correlation analysis makes use of Fourier theory. This is outlined below.

Fourier theory

The complex function $\mathbf{h}(t)$ can be transformed:

$$\mathbf{H}(f) \equiv \int_{-\infty}^{\infty} \mathbf{h}(t) e^{2\pi f t} \mathrm{d}t \qquad (26)$$

The complex function $\mathbf{H}(f)$ is the *Fourier transform* of $\mathbf{h}(t)$ and represents a transformation of the time variable, t, to the frequency variable, f.

This is reversible; the original function can be retrieved by computing the inverse transform:

$$\mathbf{h}(t) = \int_{-\infty}^{\infty} \mathbf{H}(f) e^{-2\pi j t} df \tag{27}$$

In shorthand notation, the Fourier transform can be represented:

$$\mathbf{h}(t) \Leftrightarrow \mathbf{H}(f) \tag{28}$$

Using the same Fourier transform, a function of a spatial (or displacement) variable can be transformed to a function of a spatial frequency variable. Distance is analogous to time as spatial frequency is analogous to frequency in transform space.

The Fourier transform of a function with a single variable, or dimension, can be extended to multi dimensional functions:

$$\mathbf{H}(f_1, f_2) = \int_{-\infty}^{\infty} \int_{-\infty}^{\infty} \mathbf{h}(t_1, t_2) e^{2\pi(f_1 t_1 + f_2 t_2)} dt_1 dt_2 \tag{29}$$

The (cross-) correlation between two functions, $\mathbf{g}(t)$ and $\mathbf{h}(t)$, is defined;

$$\mathrm{Corr}(\mathbf{g}, \mathbf{h}) = \int_{-\infty}^{\infty} \mathbf{g}(\tau + t)\mathbf{h}(\tau) d\tau \tag{30}$$

The correlation measures the degree of similarity between the two functions g and h. The operation can be visualised as laying the two functions over each other, moving one relative to the other and then checking for similarity. Where the two functions are similar, the correlation has a high value.

The correlation can be computed using the Fourier transform:

$$\mathrm{Corr}(\mathbf{g}, \mathbf{h}) \Leftrightarrow \mathbf{G}(f)\mathbf{H}^*(f) \tag{31}$$

where $\mathbf{H}^*$ is the complex conjugate of $\mathbf{H}$. This is the *Correlation Theorem*.

The auto-correlation is simply the correlation of the function with itself:

$$\mathrm{Corr}(\mathbf{g}, \mathbf{g}) \Leftrightarrow |\mathbf{G}(f)|^2 \tag{32}$$

The auto-correlation of a function can thus be computed by computing its Fourier transform, squaring the modulus of this complex function to obtain the power spectrum, and then inverse transforming this real function.

This auto-correlation can be thought of as "overlapping" the function with itself. If the function has a periodic nature, then the auto-correlation will have a strong signal at the same place as the periodic displacement. The auto-correlation of $\mathbf{g}(t)$ in effect compares the function with its value at some other $t=\tau$, $\mathbf{g}(t+\tau)$.

Correlations can be extended to two (or more) dimensions in the same way as for the Fourier transform. If the auto-correlation of a PIV image region is computed, then any dominant image displacements resulting from multiple particles will yield a strong signal in the correlation plane at the same value as the displacement. This dominant displacement for the region can be converted into an average velocity for the region. This is the basis of using correlation computation for PIV analysis.

Auto-correlation is used only for single-frame PIV images [55], while cross-correlation is usually used for two-frame PIV [56]. All of the flows studied here are relatively fast, and available cameras did not have a high enough framing rate to allow two-frame PIV recording. Thus, all PIV correlation work has been concentrated on the single-frame auto-correlation approach.

In practice, the two dimensional auto-correlation of a region of a PIV image results in at least three signal peaks. The strongest peak comes from the un-shifted image - this is the d.c. component, and its strength represents the overall intensity of the image. The other two peaks are mirror images of each other and represent the dominant displacement of the region. The directional ambiguity inherent in PIV is thus represented by these two peaks - the velocity direction vector is known, but not its sign.

In summary then, analysis of a PIV frame can be carried out by breaking the image down into regions and computing the auto-correlation function of each region. This auto-correlation function is then searched for the strongest correlation signal. This represents the dominant spatial displacement and the *average* particle velocity for the image region can then be computed from this.

The auto-correlation function can be computed in a number of different ways. The most obvious way is direct computation. When the function, h, is sampled at a number of discrete values rather than being a continuous function, the Fourier transform in equation (26) becomes the discrete Fourier transform (DFT):

$$H_n \equiv \sum_{k=0}^{N} h_k e^{\frac{2\pi i k n}{N}} \tag{33}$$

where h_n is sampled at N regularly spaced points.

The DFT can be calculated numerically, and so can be performed by a digital computer. As before, the two dimensional DFT is:

$$H_{n,m} = \sum_{l=0}^{M} \sum_{k=0}^{N} h_{k,l} e^{\frac{2\pi i k n}{N}} e^{\frac{2\pi i l m}{M}} \tag{34}$$

This can be separated so that it can be performed by applying 1-D DFTs on the rows of the data, followed by 1-D DFTs on the columns of the data. The DFT requires of the order N^2 operations, and is therefore increasingly computationally intensive as N increases. The *Fast Fourier Transform* (FFT) [57] is a computer algorithm for the efficient computation of the DFT and reduces the computation to order $N \log_2 N$ operations. This is a significant reduction, particularly for large N and for multi-dimensional transforms.

Computation of the auto-correlation function for a region of a PIV image requires two, two-dimensional Fourier transforms, and is therefore numerically intensive, requiring a large-scale computation, even using the FFT algorithm. Different PIV analysis methods have therefore been found to reduce the computational burden.

Optical/computational analysis

A popular method with many workers is to use a hybrid optical/numerical computation [58]. This method was the first used for PIV analysis, deriving from laser speckle velocimetry [59].

A PIV photograph is printed as a transparency and mounted so that it is illuminated by a low powered laser beam. A lens is then used to focus the illuminated region onto a screen. If the screen is positioned at the focal length of the lens, the lens acts as a optical Fourier processor,

converting the illuminated region of the photograph to the power spectrum of its Fourier transform, on the screen. This technique is illustrated in Figure 16.

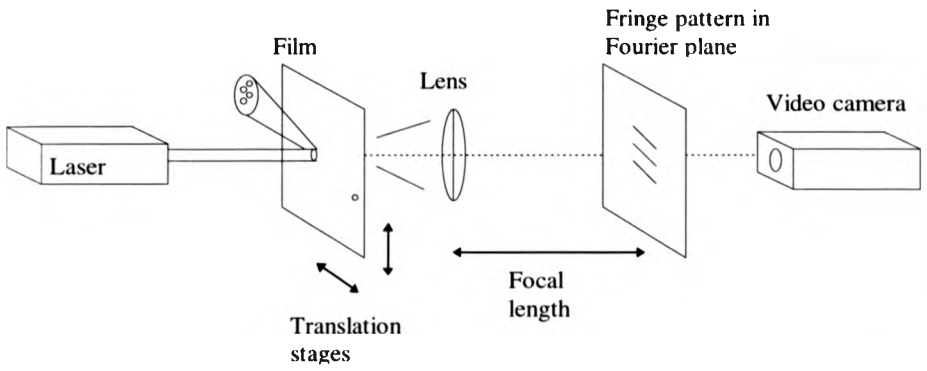

Figure 16. Schematic of opto-computational PIV analysis

If multiple particle images are present, then a fringe pattern is displayed on the screen. The fringes are perpendicular to the displacement direction and their spacing is inversely proportional to the displacement. This is analogous to the familiar Fraunhöfer/Young's fringes experiment, but now the two slits are replaced by the double particle images.

The fringe pattern produced still requires further analysis, generally by digital computer. Several computational methods have been used, grouped into one and two dimensional methods.

The fringe pattern has first to be acquired by the computer. This is done by imaging the pattern onto a video camera and then digitising the video signal using a frame grabber. This converts the analogue image into a numerical array held in computer memory.

The simple one dimensional methods require the operator to define the direction of the fringes using some sort of graphical device such as a cursor. The computer then determines the spacing of the fringes along the defined direction, and hence the particle velocity. The fringe spacing can be found by directly examining the defined line data for "peaks" and "troughs" [60]. A more robust way is to compute a 1-D FFT along the line and look for the dominant spatial frequency. More elaborate methods dispense with the need for manual determination of the fringe direction, by analysing along several 1-D directions [59].

One dimensional fringe analysis methods are computationally efficient, but vulnerable to noisy fringes. Fringes produced from experimentally derived PIV images are often difficult to see, as a result of speckle noise from the interrogating laser, and interference from neighbouring particles. The 1-D techniques are most reliable when there is a large number of clear fringes in the image. Two dimensional techniques are generally more robust. Several methods have been used, but with general agreement that 2-D FFT and auto-correlation are the most robust [61]. It is interesting that the result of applying an FFT to the Young's fringe pattern is the same as the direct auto-correlation described later. Here, one of the FFTs is performed optically and the other electronically.

Once the auto-correlation signal peaks have been located, the PIV photograph must be moved to another position, for the next velocity vector to be determined. This can be carried out by mounting the photograph on a two axis motorised translation stage, usually controlled by the computer performing the fringe analysis.

Fully optical analysis

Fully optical analysis is based on the opto-computational method described above, but replaces the electronic stage with a further optical Fourier transform stage, so that the auto-correlation is computed wholly optically. This has the advantage of utilising effectively instantaneous optical processing, which unlike numerical analysis, is independent of image resolution.

The obvious design of using two converging lenses, one for each transform, while attractively simple is unfortunately not suitable. The problem is that the second Fourier transform has to be performed on the power spectrum of the optical signal from the first transforming lens. The simple two lens design passes the amplitude *and* phase information to the second transforming lens, the output image of which is effectively the same as the original image. What is required is some way of discarding the phase information. Several techniques have been proposed for this [62] [63]. One way is to use an optically addressable spatial light modulator (SLM). Here the first transform output (the Young's fringe pattern) is imaged onto the SLM. This SLM is used to modulate a second laser beam which is then transformed again. This results in the autocorrelation, which can be imaged. A schematic for this design is shown in Figure 17.

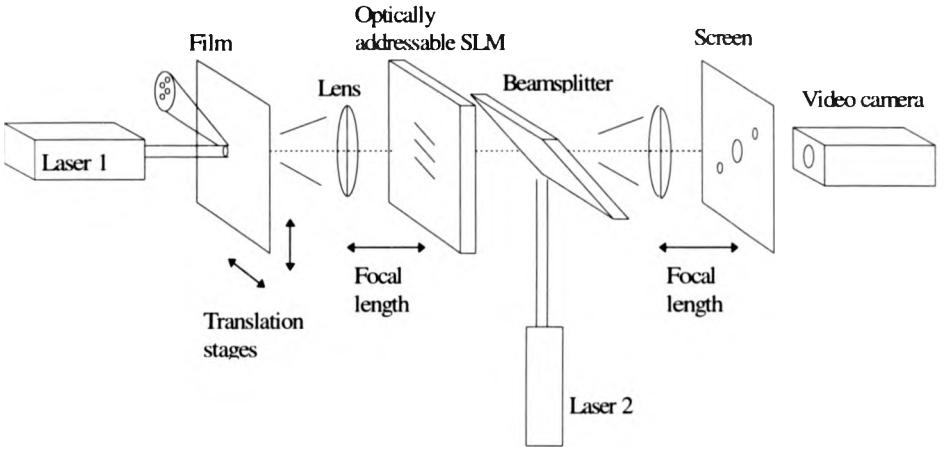

Figure 17. Schematic of a typical all-optical PIV analysis system

The optically derived autocorrelation image must then be inspected to find the position of the main signal peaks. This has generally been done by imaging onto a video camera and then digitising and analysing the image by a computer. The peaks are located by searching through the image and finding the position of the brightest pixels. This is the only numerical processing used in this analysis method.

Fully numerical analysis

The two methods described above each have their advantages and limitations. The opto-computational method is relatively simple to implement and with an efficient fringe analysis algorithm is reasonably rapid. The fully optical method has the potential for very high speed analysis, and a simplified computer based component.

These optical methods are somewhat sensitive to the type of photographic film being imaged. The coherent nature of the interrogating laser means that the fringe pattern has a speckle pattern superimposed on it which can obscure the fringes. The intensity of the speckles is partly dependent on the film transmission characteristics, while the speckle size is inversely related to the aperture size of the imaging optics.

The opto-computational method still requires considerable computation, especially when a robust fringe analysis method is chosen to analyse noisy fringes. At best, this hybrid method only saves around half of the computation of a full numerical analysis.

The processing time for the fully optical technique is currently limited by the electronic steps which are still required. The SLM or holographic system has a finite response time, and the processing computer also requires a finite time to acquire the video image and locate the auto-correlation signal peaks. Also, this approach is difficult to implement, and requires a complex and expensive optical arrangement. Another limitation is the need to traverse the negative between each vector. If this is done mechanically, this traverse time (typically 100 ms or more) is often the main limitation on the processing speed. Mao et al [64] describe an alternative optical traversing system that overcomes this problem.

Both of these optical methods require the PIV photograph to be printed as a positive image to reduce the phase noise associated with transmission through the negative and reduce the contribution of the d.c. peak to the auto-correlation result [65]. This requirement for a positive image requires an extra processing step, adding to the time delay between recording the image and obtaining numerical results.

The alternative to the two optical methods is fully numerical analysis [66]. This requires the simplest experimental apparatus, namely some form of image projection system so that regions of the photographic negative can be imaged by a video camera. The computational requirement is high though, and a high speed computer is to be preferred.

Now, the camera is focused on a region of the flow image. The grabbed image is then transformed using a 2D FFT, giving the fringe pattern as for the hybrid opto-electronic method. The power spectrum of this fringe pattern is then transformed again to give the auto-correlation function.

The main advantages of this method are flexibility and simplicity. The optical system is very simple, and incoherent light can be used to illuminate the flow photograph. This removes the speckle pattern often seen with laser illumination and also gives an eye-safe system. The fully computational nature means that analysis parameters, such as interrogation area and resolution can be easily varied, without the need for changing the optical configuration. As the original flow image is available, the resulting velocity vector can be overlaid directly upon it, and thus easily visually matched to particular features within the flow.

As the PIV image is now converted directly to a video signal, this allows a variety of non-photographic image sources to be substituted. Video cameras can be used to record a flow directly, giving an on-line processing capability.

Optimisation of auto-correlation analysis

For optimum results using the auto-correlation method, a number of flow parameters, such as the particle image diameter, minimum and maximum particle image displacements and seeding density need to be adjusted. Keane and Adrian [67] discuss this in detail, but their main findings are as follows.

For seed particle image diameters that do not tend to zero, the correlation peak position is shifted towards lower values (velocities). Keane and Adrian indicate that the particle image diameter should thus not exceed one tenth of the interrogation region diameter. Above this size, the error in determining peak position exceeds 1%. However, as the particle diameter increases, the (bias) error in determing the correlation peak position decreases, due to increased number of pixels making up the peak. A particle diameter to pixel size ratio of 2-4 is recommended [68].

The maximum measurable particle image displacement is one half of the interrogation region diameter. However, as the particle image displacement increases, the height of the correlation peak relative to the noise background tends to reduce and the probability of correct detection therefore also decreases. Keane and Adrian recommend a maximum displacement of one quarter of the region diameter, although the work discussed here limits displacements to one third of the region diameter in order to not reduce the velocity dynamic range adversely.

The minimum measurable particle image displacement is one particle image diameter. However, at this small separation, any uncertainties in measuring the correlation centroid position are significant and the velocity computed thus highly inaccurate. A minimum displacement of two image diameters is thus recommended.

If the flow field has a significant velocity gradient, then the area of each correlated region must be made sufficiently small so that the velocity is effectively constant across the region. Otherwise, the changing velocity field will be averaged across the region. Keane and Adrian suggest the criterion,

$$M|\Delta \mathbf{u}|\Delta t / d < 0.05 \qquad (35)$$

where M is the image magnification, $\Delta \mathbf{u}$ is the maximum variation in velocity across the interrogation region and d is the diameter of the interrogation region.

However, if the region area is made too small, then it is likely that there will be few or no particle image pairs present. This will increase the tendency of the analysis to be affected by spurious cross-correlations, thus increasing the number of incorrectly determined velocity vectors. This process is illustrated in Figure 18. Keane and Adrian suggest a seeding density of at least 7 particle image pairs per interrogation region to minimise the incorrect choice of vector.

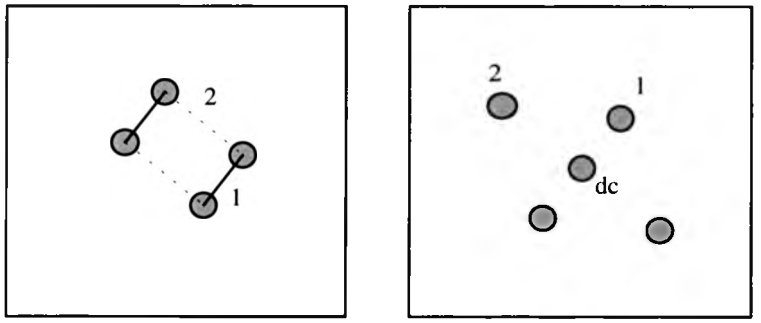

Particle images in interrogation Auto-correlation peaks

Figure 18. Illustration of spurious PIV correlation

The size of the d.c. component in the auto-correlation function has a significant effect on the dynamic range and accuracy achievable by PIV analysis. This is shown in Figure 19. If the d.c. peak is large, a large mask has to be applied to remove it, thereby limiting the minimum velocity that can be determined. Also, a large d.c. peak will shift the position of nearby peaks, causing a loss of accuracy. The d.c. peak is large when there is a significant average intensity in the image, when compared to the degree of periodicity. Therefore, if the particle image diameters are large, and/or the image background is bright, the d.c. peak will be pronounced. A large d.c. peak means that a large mask is needed to remove it and this consequently limits the minimum velocity that can be measured, thereby reducing the dynamic range attainable.

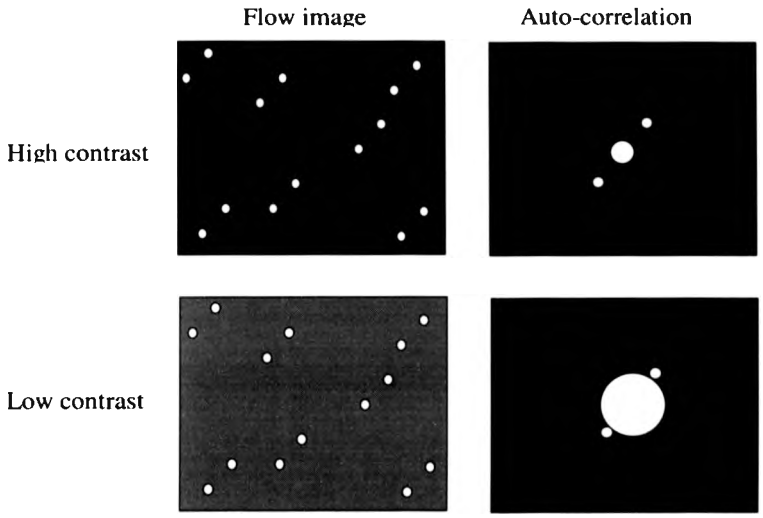

Figure 19. Effect of the d.c. component of the PIV auto-correlation on analysis

3.1.2 Particle tracking analysis

The correlation analysis methods described above analyse rectangular regions of the PIV image to identify average displacement of the particle field. This approach has a number of advantages and disadvantages. The main advantage is that the method is robust when the PIV image is noisy. If the noise is randomly distributed through the image plane, such as film grain noise, the effect on the auto-correlation function is simply to raise the background level, relative to the main signal peaks. As long as the main signal peaks are visible above this noise background, then the analysis is unaffected.

Particle tracking analysis methods take a different approach to the correlation based methods. They rely on identifying the actual positions of the particle images. This is done by first thresholding the image and then using object analysis to identify particles from groups of connected pixels. The centroids of these particle images can then be computed, and the data formed into a list.

The different methods then take the list of co-ordinate data and attempt to match the respective multiple images of each particle, thus computing velocity vectors for the flow field.

The simplest approach to particle tracking takes the first particle image from the list and then searches through the remainder of the list to find the nearest neighbouring image. The two images are then matched together to determine the velocity vector for this particular particle. The two matched particle images are then eliminated from the list and the process repeated, to match all of the remaining images. This method works as long as the seeding particle density is low so that no particle tracks overlap each other. If any tracks overlap, then matching will occur between separate particles and incorrect velocities will be computed.

More advanced methods use this simple approach, but in addition apply various parameters to the tracking process to increase the probability of differentiating particles from the background, and in matching a particle image with its associated repeated image (e.g. [69] [70] [71] [72] [73]).

Tracking methods can also yield the size (area) of the individual particle images. This size information can be used to differentiate between different sized seeding particles. As the LSI illumination is directed at the side of the particle, the brightness of the scattered light is not directly linked to particle size, but brighter particles are generally larger than darker ones, allowing a qualitative differentiation. However, most light sheets do not have a "top-hat" intensity profile, and hence particles situated at different depths through the sheet will scatter more or less light. This reduces the value of the potential qualitative size information. Alternatively, if the particles are mono-disperse, the apparent particle image size/brightness could possibly be used to determine the position of the particle within the depth of the sheet, and thus determine three-component velocities.

The behaviour of correlation and particle tracking methods is dependent on the seeding density and quality of the flow PIV image. For low seeding densities, particle tracking is preferable, with reliability improving as the density decreases. At higher densities, some incorrect particle matching is likely and correlation starts to become attractive. At still higher densities, where there are always several particle pairs in an interrogation region, correlation is the best technique, due to its superior noise tolerance.

In practice, seeding density is dependent on the type of flow application. High speed (transonic) gas flows usually have a very low seeding density, due to the difficulty of introducing and dispersing sufficient material. Low speed liquid flows can be seeded easily,

allowing a high particle concentration to be established. For flows between these extremes, the choice of analysis method is less clear, and usually depends on other factors, such as the degree of noise present, or the complexity of the flow. Many tracking methods assume a simple overall flow velocity trend, so that matching probabilities can be increased. Where a flow does not have a dominant flow direction, such as in a recirculation, then it is often necessary to supply the tracking algorithm with some existing knowledge of the flow behaviour.

3.2 Implementation of a PIV analysis system

The PIV analysis system was developed over a considerable time period, and gradually evolved in terms of functionality and usability. The processing hardware and software are described separately below.

3.2.1 PIV processing system hardware

The PIV analysis system has been designed around the IBM compatible range of personal computers (PC's). These are now very common in most academic and industrial research and development environments. A modern PC offers a very good price/performance ratio compared to the main alternatives, namely UNIX workstations and Apple Macintosh computers.

The original PIV analysis system (then known as HarPIV) was first conceived in 1988, and due to the limited computer power available, was based on the opto-electronic method described above. Limited available funds and a short time-scale did not permit the fully optical method to be developed. The simplicity and limited hardware of the opto-electronic method was attractive. Equipment already present within the laboratory was utilised, giving a rapid, low cost solution.

A probe Helium-Neon laser was used to illuminate a small area (approximately 1 mm^2) of the positive flow image transparency. The laser beam was then passed through a converging spherical lens. This lens acted as an optical Fourier transform processor, and a diffusing screen placed in its diffraction plane gave a fringe pattern, with an intensity equivalent to the power spectrum of the Fourier transform of the original probed image area. The fringe pattern on the screen was imaged by a Siemens CCD camera using a macro lens.

The CCD video signal from the camera was passed to a BM901 dedicated image processor controlled by an IBM AT micro computer. The digitised fringe pattern was analysed by computing the two-dimensional auto-correlation, giving the fringe spacing and angle. This was then related to the flow velocity of the probe area as previously described. Using the host 6 MHz 80286 processor (with 80287 maths co-processor), each velocity vector could be determined in approximately 90 seconds (64 x 64 pixel Fourier transform). A typical 1000 vector field could thus be computed in approximately 25 hours.

This analysis time was found to be excessive as it was often found necessary to change the analysis parameters after a processing run, and then repeat it. For example, the probe laser beam diameter must be larger than the maximum spacing of the multiple images, and its intensity set such that fringes have sufficient intensity to be visible without saturating the camera. Also, the separation between the analysed vectors needs to be such that flow velocity structures are resolved. A circular mask often needed adjustment to fully obscure the unwanted undiffracted probe beam from the fringe pattern, and thus not dominate the auto-correlation image.

The long analysis time meant that this procedure was very unwieldy. It was also found that the interrogating laser beam tended to produce poor quality fringes from experimental data (for the reasons described earlier). The optical interrogating beam was found to be rather inflexible, as it was often necessary to change its diameter, to cope with flow photographs with a variety of different spacing between the multiple images. For these reasons, an improved hardware system was conceived.

The modified processing hardware can be broken down into a number of components, notably the host computer, an array processor, a frame grabber, a video camera and a two axis motorised translation system. The camera and translation stages were used as a film interrogation system. A schematic of the system is shown in Figure 20, and a photograph of the system, mounted in a portable trolley in Figure 21.

Computer

The host computer consists of the central processor and a number of other assorted devices. A Compaq 386/33 computer was used initially for the system. The central processor was an Intel i386 micro-processor chip. 16 MB of 32 bit memory were attached to the main processor, and

addressed through an interleaved memory architecture. The i386 was used together with a i387 floating point maths co-processor. The combination offered approx. 10 million instructions per second (MIPS), and was the most powerful PC processor available at the time of this experimental work. Other compatible devices in the Intel family now range from the 16 bit i286 chip, through the i386 to the i486 and Pentium which both offer a built in floating point maths co-processor. Current state of the art PC processor power (Pentium 133 MHz) is considerably greater than 100 MIPS.

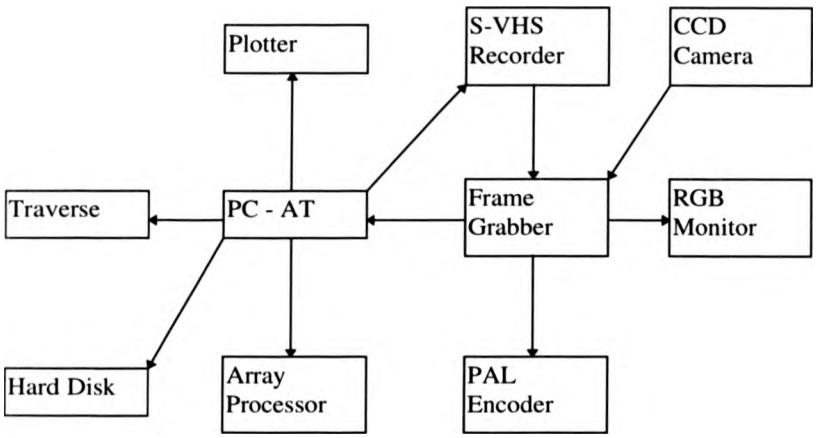

Figure 20. Schematic of PIV analysis system

A 16-bit ISA bus was used in the computer to link the central processor to the other processing elements. This bus ran at 8 MHz and allowed data transfer at up to approximately 5 MBytes/second. Higher speed transfer could have been achieved, if required, using a MCA or EISA bus architecture (40 MBytes/second).

A Fujitsu 256 MB hard disk was used, controlled by an Adaptec SCSI controller. The hard disk provided ample storage for programs and data, with fast access (12 ms average) and a high transfer rate (up to 5 MB/second).

Figure 21. Photograph of PIV analysis system

Frame grabber

A Data Translation DT3852 frame grabber was used for image acquisition. This board uses a Texas Instruments 40 MHz 34020 graphics processor running a TIGA (Texas Integrated Graphical Architecture) environment. The 34020 processor was used to control all aspects of frame acquisition and manipulation. An analogue to digital converter enabled analogue video data to be digitised at up to 20 MHz. 1 MB of high speed video acquisition memory was provided. This combination allowed for acquisition of sequential image frames of up to 1024 x 1024 8-bit pixels and at full real-time framing rates. The flexible nature of the design allowed for easy adjustment of the acquisition resolution. The acquisition resolution was generally set to 768 x 512 pixels, and the digitised rate set to 15 MHz, giving square pixels and hence a 1:1 aspect ratio. This was found to be the optimum setting for CCIR (PAL) signals (625 lines, 50 Hz interlaced). 4 MB of auxiliary memory was provided on the board, storing the graphics driver code and also permitting a sequence of several frames to be acquired and stored. A display memory of 1 MB of fast video RAM allowed displays of up to 1024 x 768 x 256 colours.

The frame grabber was also used as the main host graphical display. When running MS-DOS, a video pass-through mode was used, with the host VGA providing the 640 x 480 x 16 colour display through a connecting interface, and the grabber inactive. When running Windows, an

overlay plane was defined, consisting of 4 bits (16 colours) of the 1024 x 768 display memory. The TIGA system was used to provide a display driver at this resolution for running Windows programs, thus acting as the main display. In this configuration, a transparent overlay "keying" colour could be set, allowing the live acquired image, and Windows display to be viewed simultaneously on-screen. Another advantage of using the TIGA driver was the accelerated Windows graphical display over the standard VGA display, with high speed drawing of graphical objects such as windows, icons and menus, and faster rendering of bitmap images.

A 17 inch Taxan 875 monitor was used for display. This is a large multi-frequency design, permitting the high resolution image and Windows display to be clearly seen. The high scan frequency (70 Hz) and non-interlaced format were found to be very ergonomic, with no perceived flicker.

Array processor

A Data Translation DT2878 array processor was used for floating point acceleration. This board uses a 50 MHz AT&T DSP32C processor, and provides highly accelerated floating point maths with a peak performance of 25 million floating points operations per second (MFLOPS). The processor uses a highly optimised digital signal processing (DSP) architecture to enable intensive, repeated computation such as vector (array) arithmetic and tightly structured, looping algorithms (such as FFT's) to be executed efficiently. 2 kB of on-chip fast static RAM, and 4 MB of on-board dynamic RAM permitted the DSP processor to execute a 512 x 512 complex 2-D FFT in 3.3 seconds.

The array processor and frame grabber were connected together using the DT-CONNECT dedicated external data bus. This asynchronous bus offered a higher speed transfer (10 MB/second) than the standard AT-bus, and also allowed the host processor to perform other tasks while the transfer was underway.

Film interrogation system

A Sony XC/77RRCE video camera was used to acquire the image data. This provided a standard formatted CCIR video signal. The video camera used a 1/2 inch charge coupled device (CCD) sensor, with a resolution of 756 x 581 pixels (each 11 µm square). CCDs have a

number of advantages over conventional vidicon designs, including a linear intensity response, good robustness, small size, and freedom from geometric distortion.

A Bausch and Lomb MonoZoom-7 microscope lens was attached to the camera C mount and used to image the PIV photographic record. The lens was a fixed focus (though the working distance was adjustable over a few mm's) design, and with the 2X objective lens, provided a working distance of 36 mm. Its zoom action permitted the object to image plane magnification to be varied continuously from 0.9X to 6.3X, giving a field diameter varying from 10 - 1.43 mm. After some initial minor adjustment, the magnification could be varied without affecting the image focus. This allowed easy variation of the correlation interrogation area.

An Ealing Electro Optics incandescent lamp was used as the illumination source for the photograph. The 6V 20W quartz halogen lamp was mounted in a lamp house, behind a square of 6 mm white plastic material. This white plastic acted as an effective diffusing screen, providing a constant incoherent bright background illumination for the photograph.

A Time and Precision Ltd. linear stage system was used to translate the PIV photograph. A three axis design was used, with the Y and Z axes linked to stepper motors. The X axis was manually controlled with a travel of 500 mm and a screw pitch of 2 mm, and allowed the separation between the back light, photograph and camera to be readily adjusted. The Y and Z axes had a travel of 130 mm and a lead screw pitch of 1 mm. The 400 step per revolution stepper motor allowed a minimum step of 2.5 µm. The two stepper motors were controlled by a Digiplan IF1 device. This automatically provided the necessary acceleration and deceleration profiles, and allowed the motors to run at up to 50000 steps/second, giving a maximum linear speed of 120 mm/s. The IF1 was connected to the host computer through an RS232 interface. Its command language allowed easy computer control, with simple commands such as "X1000@10$" used to represent movement of the X axis by 1000 steps, at 10000 steps per second. The controller permitted simultaneous interpolated movement of the X and Y axes, thus reducing the time to reach a specified position. Limit switches were fitted to prevent the motors from stalling at the ends of slide travel. Datum switches were also fitted, to allow return to a known absolute position. These operated on the Hall effect, and allowed repeatable positioning to 2 µm.

A custom designed mount was used to hold the photograph. The holder consists of a black anodised aluminium frame, with a pane of optical glass attached. Another frame with a pane of glass was attached to the first, using two knurled screws. An accurately machined ledge under one of the frames allowed for the slide to be supported horizontally. The design of the holder allowed for the mounting of a wide range of photographic materials of different sizes and thickness, from glass mounted and un-mounted 35 mm slides and strips of film, to 4 x 5 inch negatives. The design is shown in Figure 22.

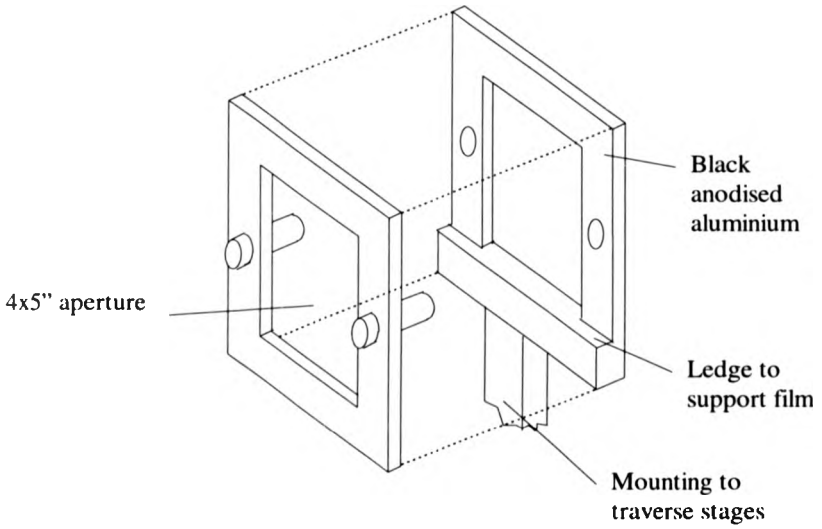

Figure 22. Design of PIV film holder

3.2.2 PIV processing software

Initial version

This software was initiated by the author in 1988. At that time it was very simple in nature, and consisted of a small MS-DOS program written in the C language. This design was chosen for its easy and rapid implementation.

The frame grabber was controlled through a library of access functions, enabling operations such as look up table selection, image acquisition and image transfer to host computer memory to be performed. This "HarPIV" software was a menu based design, and enabled a photographic positive print to be analysed by the hybrid optical/electronic processing method

described above. A 2D FFT was used to convert the fringe pattern into the auto-correlation pattern. With the then available computing hardware, the program required a long time to analyse more than a few vectors.

In addition to the slow processing time, the software was somewhat constrained by the MS-DOS operating environment. The program was limited to 640 kB of memory access (for both program code and image data), and 64 kB memory segments (16 bit segment base and offset registers) as a result of the 16-bit MS-DOS. The program was also not very portable, meaning that it was limited to operating with a particular graphical display, Logitech mouse and Hewlett-Packard pen plotter.

HarPIV in use

In use, the HarPIV software did give reasonable results, but it was found to be somewhat limited. Figure 23 shows a typical output plot from the program. This output was generated from a PIV photograph of a small nebuliser air jet seeded with water droplets which were approximately 10 µm in diameter.

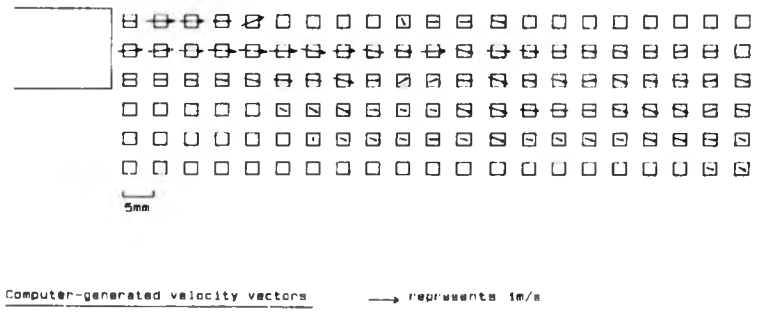

Figure 23. HarPIV output plot

The opto-computational method was found to be rather sensitive to the quality of the PIV negative. Fringes of poor visibility were recorded. The problem was found to be greatest when illuminating the contact printed transparency. This was thought to be a result of the contact print being made with poor focus and contrast. It was found to be very difficult to reliably maintain the precise particle image focus required for PIV. Therefore, for development of the

black and white film, a reverse processing method was used. This converted the negative film directly into a positive film, thus eliminating the need for contact printing of the negative.

It was decided to improve the PIV software to make it faster and more flexible. It was also thought necessary to make it more graphical in nature in order to aid the user interaction with the analysed velocity vector dataset.

The opto-computational method was dropped in favour of the more flexible fully numerical method. The indirect nature of the opto-computational interrogation and analysis means that the software does not get to see the original image, only the auto-correlation of the illuminated region. This meant that it was difficult to relate particular flow features to the vector map. The numerical method with its direct imaging meant that the original image could be overlaid onto the vector map. This would allow particular flow velocity features to be matched easily to actual physical features, such as rig inlets and outlets, and wall boundaries.

PIV software under Windows

Microsoft Windows 3.0 was chosen as a suitable graphical environment to host the modified PIV analysis program, now renamed as VISIFLOW. This Windows environment had then recently become available (1991), and was a considerable improvement on its predecessors. It offered support for access to up to 16 MBytes of system memory through the DOS Protected Mode Interface (DPMI) specification. This took advantage of the protected mode of the Intel 80286 and higher chips. Memory was now accessed through a selector handle which pointed to a memory pointer held in a selector table. This enabled memory to be transparently reallocated and reordered, without affecting the calling program. The 64 kB data segments remained however, meaning that inefficient (slow) 32-bit "huge" memory pointers were still required to access memory arrays of more than 64 kB (such as most images).

The Windows environment also promised to increase the portability of the program dramatically. The previously directly hardware mapped graphical display was replaced by a logical device context. This is effectively a virtual graphics device of extremely high pixel resolution and colour display capacity. The Windows graphical display interface (GDI) then maps graphical operations from this logical device to the physical hardware device. The advantage of this approach is that the executing program does not need to take any account of the display hardware, and can equally draw to the screen or a hard copy device such as a laser

printer or pen plotter. Pointer devices such as mice, light pens and graphical tablets are also well supported.

Unfortunately, the Windows Application Programming Interface (API) is complex (around 1000 functions and increasing with each new version of Windows), and entails a considerable learning curve. The structure of the program had to be completely re-written. This is because Windows programs simply act to respond to messages sent by the user interacting with the program. These messages can range from menu option selection to mouse movement within the drawing area of the window. In effect, the program is just a very small loop of code, for accepting and then parsing messages passed to it by the system. Each message is then handled by a section of code which can interact further with others. This is illustrated in Figure 24. The effect of this programming regime tends to be to increase the size of the source code of a program, compared to one of equal functionality written for MS-DOS. Conversely, the executable size of the code often decreases, as considerable functionality is already provided by the environment, for example graphical and communication port functions.

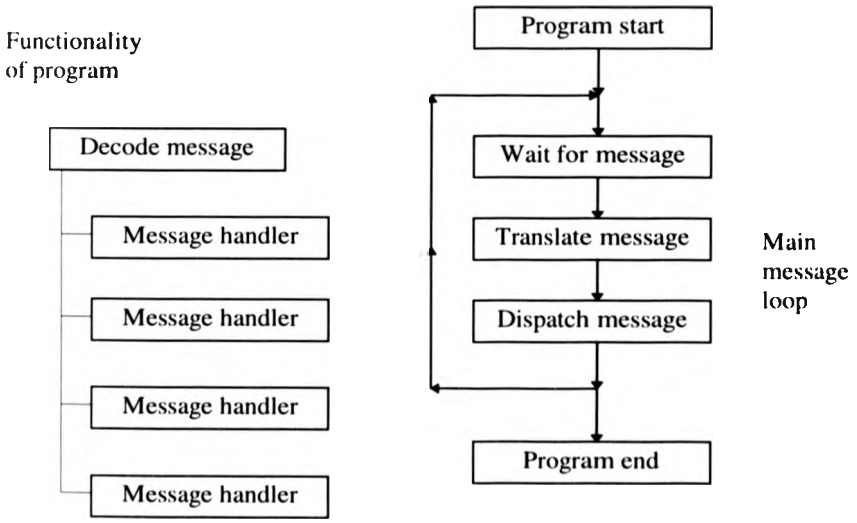

Figure 24. Overview of PIV Windows Program Structure

Windows also complicates the interface to the other hardware processing systems. Under MS-DOS, the frame grabber was memory mapped, i.e. it was accessed as simply another area of memory. However, the Windows protected memory manager intercepts all memory accesses,

and re-directs them. This makes normal memory mapping impossible. The usual solution is to write a Windows device driver to interface to the hardware device. Unfortunately, writing a device driver is a difficult and specialised task. The implemented solution was to use a different frame grabber which allowed access through input/output (I/O) registers rather than through memory mapping, and thus avoiding the problem.

VISIFLOW has been written to fully exploit the features of Windows 3.1, an upgrade which offers increased performance and robustness (less likely to crash), and scaleable (TrueType) fonts. More PC memory can also be accessed. In addition, common dialogue boxes are used, which offer a standard and consistent user interface for options such as opening, saving and printing data files.

VISIFLOW functionality

The VISIFLOW program can be broken down into two main areas: analysis routines and post-processing routines. The analysis routines allow choice of the image type, display of the live flow image itself, calibration for velocity and magnification, choice of the analysis method, and a variety of other options concerned with the actual PIV processing of the image. The post-processing routines provide data validation and other operations on the analysed vectors.

VISIFLOW image types

The type of image to be analysed can be selected from photographic, video and TIFF options. The photographic analysis option uses the traverse controller, video camera and microscope lens to analyse small sub-image segments of a high resolution transparency. The analysis origin co-ordinate and the size of the total analysis area can be chosen by the user. The magnification of the microscope lens can be adjusted to select different sizes of interrogation region, thus enabling different scales of flow behaviour to be examined. The choice of image magnification affects the analysis accuracy, and also the number of vectors generated for a particular flow image. The translation stages move the transparency in a raster pattern, thus scanning the whole image area. The majority of processing time is spent in analysing a particular sub-image from a larger negative, and so the time spent in traversing the negative becomes largely irrelevant. The multi-tasking nature of Windows enables the negative to be traversed while the numerical analysis is underway.

The video analysis option again uses the video camera but now in an on-line analysis configuration. The camera can be pointed at the flow, and the live PIV image observed. When required, the VISIFLOW system can be instructed to grab a video frame, store it in memory, and then process it. The frame acquisition can be initiated by the user, or electronically by the presence of an external trigger signal. The frame grabber can grab a number of consecutive video frames (up to 9 at 768 x 512 pixel resolution within the free space of the 4 MB grabber auxiliary buffer) with a variable time separation (down to 1 frame or 0.04 s). This enables a time varying flow to be captured and then studied.

The TIFF analysis option uses a previously digitised image file (saved in the Tagged Image File Format) as the source of the flow data. This file can be generated in a number of ways, including using commercially available photographic scanners. These work by scanning a line sensor down the illuminated photographic, and gradually building up the digitised image. They offer excellent geometric linearity, and the resolution currently available varies from 300 dpi (dots per inch) for mainstream A4 document scanners, to 4000 dpi for the more specialised (and expensive) 35 mm film negative scanners. The PIV photograph would need to be printed onto A4 paper for the standard document scanner to achieve the necessary digitised resolution, but could be scanned directly by the film scanner. The TIFF file generated could either be in a 1 bit black and white binary format, or in an 8 bit grey scale format. The advantage of the black and white format over the grey scale format is that it occupies much less disk storage space as it can be efficiently compressed using a run length encoding compression scheme. For examples, a PIV image of 768 x 512 pixels occupies 390 kB as a grey-scale TIFF file, but typically around 30 kB as a compressed binary TIFF file.

A recent alternative, not available at the time the system was designed, is to use a commercial service (such as Kodak PhotoCD) to process the undeveloped film and archive the images to a CD-ROM. Here the film images are scanned and stored on the disk, permitting convenient access at a variety of digitised resolutions.

VISIFLOW methods of analysis

The method of analysis can be selected from auto-correlation, particle tracking, and manual analysis.

Auto-correlation;

The auto-correlation analysis method, the principle of which was described earlier, first divides the image down into sub-images, or segments. The size (N x N pixels) of these segments can be adjusted by the user from 32 x 32 pixels to 512 x 512 pixels. It is shown later that the error in measuring particle displacement is roughly the same, when expressed as a fractional pixel error. Thus, using higher resolution interrogation areas (effectively smaller pixels) results in higher accuracy. This adjustable range of interrogation areas was used because below 32 x 32 pixels, (bias) errors in measuring particle displacement are high due to the large size of the pixels. At 512 x 512 pixels and above, accuracy is sufficient, while computational processing time continues to increase. Prasad et al [68] discuss the effect of the interrogation area resolution on these bias errors.

The spacing between the interrogation segments can be varied, but is usually set to give an overlap of half of the segment size. This is x 2 oversampling. The segment pixel data is then passed to the array processor where an N x N 2D real FFT is computed. The FFT is computed by using a 1D FFT algorithm, working on first the rows, and then the columns of the array. The 1D FFT algorithm is hand coded in DSP native assembler language, and uses separately computed trigonometry and "twiddle factor" data tables for maximum possible processing speed. The square of the magnitude of the resulting complex data array is then computed, giving real data once again.

Another 2D FFT is computed on the results of the first computation, and the square of its magnitude again computed. This is then the auto-correlation of the initial data array. The positions of the major signal peaks within the auto-correlation array are then determined. The highest peak is always at the centre of the 2D array, and represents the zero-order or d.c. correlation spatial frequency. It is a measure of the image correlated with itself, with no shift in position, and is proportional to the overall image intensity. This peak is then removed from the array using a circular mask with an adjustable size. A simple maximum value search is then performed on the array, and the co-ordinate position of the highest peak is found. This gives the spatial frequency of the most dominant correlation within the image, and hence the most likely value for the average velocity of the image segment being analysed.

An optimising algorithm can then be applied in an attempt to increase the accuracy of the identification of the location of the correlation peak. The peak position is known initially only to the nearest array grid point. Two algorithms were developed, based on Gaussian fitting and centre of gravity. The Gaussian algorithm fits a two dimensional Gaussian function to the peak, using the surrounding 5 x 5 grid points. The centre of gravity algorithm determines the centroid of the peak were it to be a solid volume. The Gaussian option is potentially more accurate, as a particle image theoretically has this intensity distribution, but the centre of gravity option often gives better results when the correlation peaks have a distorted shape, as is sometimes the case for noisy images or when there is a strong velocity gradient[68].

This correlation peak is then masked out as before, and the maximum value search repeated twice more. The sizes of the deletion masks can be adjusted by the user, so that the peaks are fully removed without also removing any other potential peak data. The positions of the three highest correlation values are determined and recorded together with their height (the degree of correlation) in the disk based analysis file.

Particle tracking;

Auto-correlation computes the average velocity of the seed particles recorded in a rectangular segment of the flow image. Conversely, the particle tracking method follows the movement of the seed particles directly. This method first identifies the position of each of the particle sub-images (or objects) within the main image. The x and y co-ordinates are determined, together with the size of the particle (its image area) in pixels. The particle images are identified using an 8-way connectivity rule, shown in Figure 25.

If an image pixel associated with a particular object is adjacent to another pixel, then that pixel is also included with the object. The object identification algorithm works by tracing around the border of the object using the connectivity rule, and thus fully identifying all of its boundary pixels. The extents of the object are now known. The area of the object is computed, together with the co-ordinates of its centre of gravity, or centroid. The centre of gravity, x_g, y_g for an object containing N pixels is computed using:

$$x_g = \frac{1}{N}\sum_{i=1}^{N} x_i \qquad (36)$$

$$y_g = \frac{1}{N}\sum_{i=1}^{N} y_i \qquad (37)$$

where x_i, y_i are the co-ordinates of each pixel in the object. Once the object has been identified, it is masked out and the algorithm then searches for the next object. Once completed, the list of particle centroids (sorted in ascending order) is then processed further.

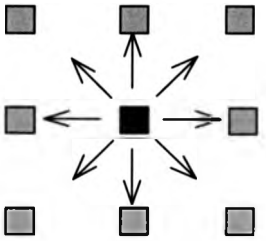

Figure 25. Eight-way connectivity rule used in particle tracking

Particles with an area below or above a certain user-specified value are deleted, as representing noise in the image. Film grain noise tends to produce many single noise pixels, while flare caused by unwanted reflections from the illuminating laser sheet tends to cause large continuous areas of noise pixels (several hundreds or thousands of pixels).

A simple nearest neighbour algorithm was initially used to match the appropriate multiple particle images together. Although efficient, this was found to give poor results when the seeding density was high enough so that nearest images did not always result from the same particle. Thus, a method was developed to restrict the direction and possible spacing searched that a particular particle image could be matched to. This algorithm is described below.

The image is broken into a number of regions and a predicted velocity magnitude and angle is then computed for each region. This prediction is done by analysing each particle in turn and computing all possible associated velocity vectors by matching it with all of its neighbours within a radius defined by a pre-defined maximum tracking range. The angle and magnitude of each possible vector is then added to a histogram, a separate one for each. This is illustrated in Figure 26. The modal averages of the histograms are then used to give the most probable values of the magnitude and angle of the average velocity of the region.

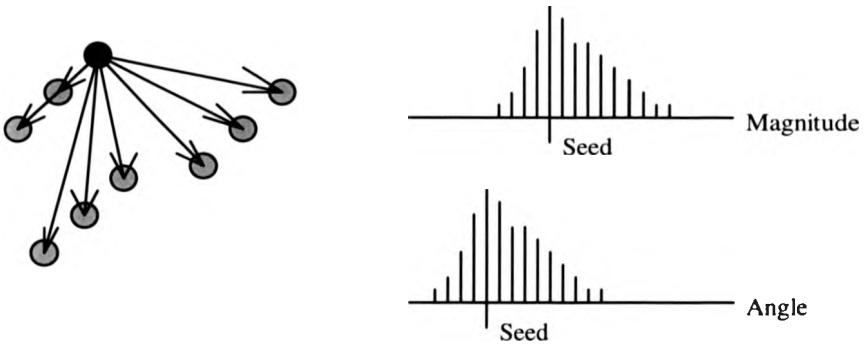

Figure 26. Particle tracking prediction process

The average velocity angle and magnitude and their standard deviations are then used to improve (seed) the main matching process which follows. Each particle is matched to the other particles within the maximum tracking range. The pre-computed velocity angle and magnitude are used to limit the possible ranges of matched vector magnitudes and angles, as shown in Figure 27.

The matched particles with the smallest separation, and yet fulfilling the other conditions are chosen to define the velocity vector. An option allows the user to specify the maximum number of particles to search for during the match. If more than two laser pulses are recorded during the camera exposure, this can be used to increase the reliability of the matching process, as a genuine particle track has to extend over several images. Once matched, the particle objects are removed from the centroid list.

This algorithm has been found to give good results with a variety of flow images. The size of the prediction region needs to be adjusted for each flow image, so that it is large enough that many particle images are present (to give representative statistics), but small enough that the flow velocity is similar across the area. Clearly, if the flow velocity has a high gradient and there are few particle images, then this approach is unsuitable.

The matched velocity vectors differ from correlation derived vectors in that they have random positions rather than being spaced on a regular grid. The correlation technique is best when the flow image is noisy, usually as a result of unwanted reflections or film grain noise. Noise in the spatial domain tends to be spread evenly in the frequency domain, and thus not influence the dominant frequency component search. However, the correlation technique requires

several particle pairs inside each interrogation area, and thus requires a uniformly high seeding density. Where the seeding rate is lower, particle tracking is often preferable, as each particle pair produces a separate velocity vector.

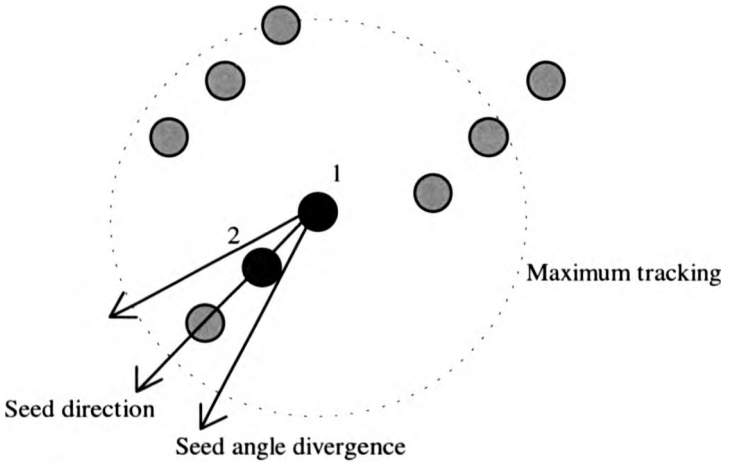

Figure 27. Illustration of the tracking algorithm

Manual analysis;

In addition to the two automated techniques, a simple manual analysis option enables the user to mark particle pairs by "dragging" an on-screen cursor from one particle image to another. This option is provided for flow images where the quality is too poor for automated analysis, and only a few vectors need to be produced.

VISIFLOW post processing

The post-processing routines are equally as important as the analysis routines. This group of routines offers velocity vector display, data validation, velocity interpolation, flow scalar variable computation, data filtering, printing, and a number of other options concerned with the user interaction with the previously processed data.

When performing auto-correlation analysis, occasionally an incorrect vector is generated. This is usually the result of a strong correlation being found between adjacent particles, rather than between the multiple images of a single particle. This case of spurious correlation was described earlier. If there are only two particles within the interrogation area, each with two

images, then there will be two equally strong correlation values. The vector can be corrected by substituting one of the other two correlation peaks which were saved during analysis along with the strongest peak. In the majority of cases, this was found to produce the correct value. However, occasionally when the spurious correlations are particularly strong, the vector needs to be deleted completely. This validation of the analysed velocity vectors can be performed fully automatically.

The validation algorithm compares the magnitude and angle of each vector to the weighted average of its neighbours (those vectors within a certain user-defined radius). If the velocity differs by more than a user-defined percentage amount, then the next correlation peak is substituted and the comparison repeated. This continuity test takes advantage of the fact that most incorrect vectors have a significantly different magnitude and angle to the surrounding (assumed) good data. An absolute vector magnitude and angle test can also be performed as part of the comparison. Here, if the vector falls outside a user specified range of values, then it fails. If the second correlation peak fails, the third is substituted. If the third correlation peak also fails the comparison, then the vector is marked as temporarily deleted. When the algorithm has passed through the whole data set, if there are any vectors which are marked as deleted, then the algorithm passes through the data again. This is repeated for a maximum of six iterations, or until there are no more deleted vectors. This algorithm was found to give good results for a majority of PIV datasets.

When the validation algorithm has been performed, it was found that there are sometimes regions of the dataset that remain deleted. This is usually the result of there being a low seeding density in those particular areas of the flow image. The iterative validation algorithm cannot substitute a vector when there are no neighbouring vectors to compare with. These gaps in the vector field can sometimes make the interpretation of the dataset more difficult. An interpolation algorithm was developed to fill in these gaps using the surrounding data. The interpolation algorithm works by searching through the dataset looking for co-ordinate positions where a vector should be, but is deleted. When it finds such a position the weighted average of the surrounding vectors is generated. This average is computed from all vectors within a user specified radius of the position. The average is weighted according to how far the vector is away from the position. Further vectors get a lower weight than adjacent vectors. The weight is set as a user specified (negative) power of the distance away from the position.

Setting a more negative value of the weighting power reduces the influence of more distant vectors relative to local vectors. This polynomial interpolation algorithm can also be used for limited extrapolation, but the validity of its results decrease rapidly as the position of interest moves further outside the main extents of the dataset.

The success rate of the validation algorithm is variable, depending on the flow image. The algorithm is most successful where only a few vectors are incorrect, and the average of the surrounding vectors can thus be relied on. In this case, a high degree of success in determining incorrect vectors can be achieved. Where many vectors are incorrect, the validation algorithm becomes unreliable, replacing good vectors with incorrect values, and better results are obtained by manually inspecting each vector and checking its value using a priori flow knowledge. Where appropriate the second or third correlation value can be substituted.

A basic test of the performance of the validation algorithm was performed. A uniform vector dataset was generated numerically. For a certain percentage of the vectors, the "correct" vector value was moved to the second or third correlation peak. For the other correlation values of each vector, random velocities were generated. The dataset was then validated using the continuity test. A validation radius of 3 vector separations was used, and several levels of allowed deviation from the neighbourhood mean were tried. A graph of the validation performance is shown in Figure 28. As can be seen, when the level of incorrect vectors is low, the algorithm is very successful at removing incorrect vectors. This reduces as the percentage of incorrect vectors increases, and the measured neighbourhood mean becomes less representative of the true neighbourhood mean. The maximum deviation allowed also has a significant effect on the success of the algorithm. For a uniform dataset such as this, very small values of allowed deviation can be used. In a flow with velocity gradient, then a larger value of maximum deviation will be necessary to avoid rejecting too many correct vectors.

The interpolation algorithm can also be used to convert the irregularly positioned vectors resulting from particle tracking analysis to a regular grid, more suitable for comparison with numerical codes. In this case, the entire dataset becomes interpolated, as typically no irregular vectors will lie exactly on the regular grid positions.

When the data had been interpolated, fluctuations due to noise could be smoothed out using a filtering algorithm if desired. The filtering algorithm works by applying a 5 x 5 filtering kernel

kernel to each velocity vector. The 25 kernel values can be entered manually by the user, or a default Gaussian filter used. The kernel values are weighted so that the average contribution from the original and surrounding vectors remains unity.

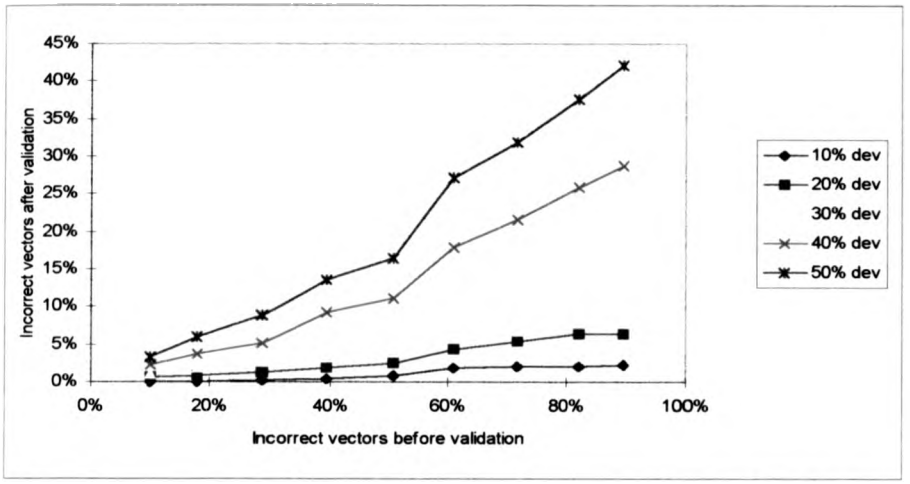

Figure 28. Validation performance

Additional flow information can be obtained from the final post-processed data set, by observing flow variables as vorticity. Vorticity, ω is a fundamental characteristic of turbulence. It is computed from the vector curl of the velocity, **v**:

$$\omega = \nabla \times \mathbf{v} \tag{38}$$

Two dimensional velocity data in a plane allows determination of only the out-of-plane component of vorticity,

$$\omega_z = \frac{1}{2}\left(\frac{\partial v}{\partial x} - \frac{\partial u}{\partial y}\right) \tag{39}$$

where (u, v) are the in-plane velocity components. This is evaluated by computing the circulation, Γ, around a closed contour surrounding the point,

$$\Gamma = \int \mathbf{u} \cdot d\mathbf{l} \tag{40}$$

and invoking Stokes' theorem to relate the circulation per unit area to ω_z

$$\omega_z = \lim_{A \to 0} \left(\frac{\Gamma}{A} \right) \tag{41}$$

The numerical approximation to (41) is implemented with a closed contour defined by the eight points surrounding the node at which the vorticity is to be evaluated.

The total auto-correlation processing time for a single velocity vector, using the DT2878 array processor and a 128 x 128 pixel interrogation region, and all relevant data transfer and display is approximately 0.4 seconds. This processing time can be adjusted by varying the auto-correlation resolution from 32 x 32 up to 512 x 512.

3.3 Numerical validation

Before use with real flow images, the VISIFLOW software was tested on computer generated data. A routine was written to generate simulated particle image fields with a specified angle and spacing between the pairs of images. Velocity gradients were not considered, but a number of other workers have looked at such cases, e.g. [68]. The images were then analysed normally to give velocity data. This analysed data could then be compared against the original, known data to determine the performance of the software.

3.3.1 Method

The particle image generation routine and consequent analysis was called a number of times from a program loop. Both angle and spacing were varied - the former from 0 to 175 degrees in steps of 5 degrees, the later from 1/10th to 1/3 the size of the interrogation area, in 5 steps. This gave a total dataset of 180 values. The test was repeated for different sizes of interrogation area. Particles with a Gaussian-like intensity distribution were used, with intensities computed according to,

$$I(x) = I_0 \exp\left[\frac{-(x - x_0)^2}{2\sigma^2} \right] \tag{42}$$

where the particle has an effective radius of σ. The particle diameter was adjusted for the different interrogation area, to give the same relative size between tests. The seeding density was set to give 10 particle pairs per interrogation area.

3.3.2 Results

Results are shown for auto-correlation, both without and using Gaussian interpolation in the correlation peak finding algorithm. Results are expressed for 256x256 pixel interrogation areas as a fractional pixel error. The pixel error was computed using the following equation;

$$\text{Error} = \sqrt{(x_a - x_m)^2 + (y_a - y_m)^2} \tag{43}$$

where (x_a, y_a) are the co-ordinates of the predicted correlation peak, and (x_m, y_m) are the co-ordinates of the measured correlation peak. Figure 29 shows the non-interpolated errors. Figure 30 shows the Gaussian interpolated errors.

The pixel error graphs show that errors are always less than one pixel. The non-interpolated data shows no apparent trend to the data. The apparent randomness of the errors indicates no systematic error is present in the correlation routines.

The interpolated data clearly shows a lower overall error in the data, as is hoped. However, error spikes are present in both the x and y data for certain values. At these points, the convergence of the Gaussian fitting routine in one or both directions failed, and the original data was instead used. The reason for these spikes is not known - it is possible that there is some kind of rounding error in the array processor FFT or Gaussian calculations.

The mean and standard deviation of the pixel error for 64x64, 128x128 and 256x256 pixel auto-correlations is shown in Table 1. The non-interpolated data shows an approximately constant mean error of around 0.4 pixels. The interpolated data shows a lower mean error of around 0.2 pixels.

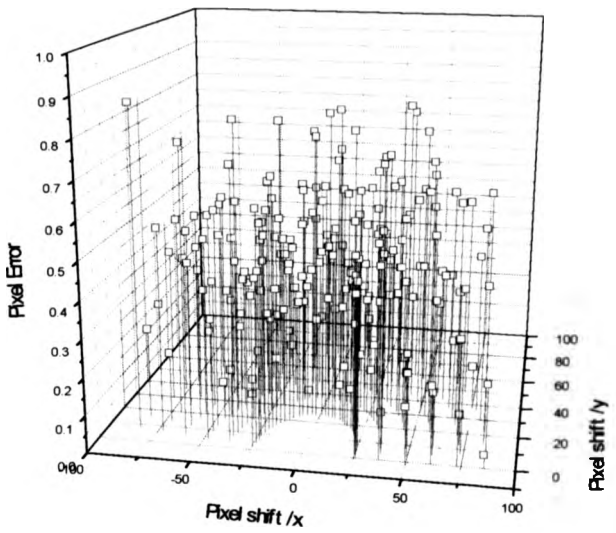

Figure 29. Correlation error in pixels - no interpolation

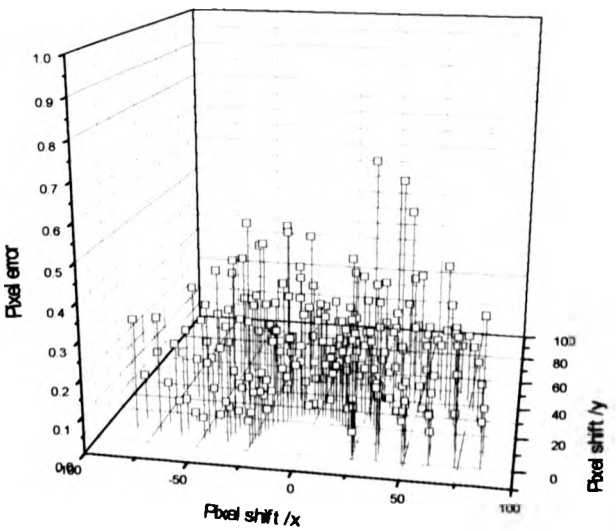

Figure 30. Correlation errors in pixels - Gaussian interpolation

These calculated velocity errors of fractions of a pixel are not thought to be significant, as virtually all PIV correlation calculations are done with an expected particle separation of several, usually tens of pixels. Here, the fractional pixel error is usually negligible when computing the total particle displacement.

Interrogation area size	Particle diam. /pixels	Mean pixel error	Standard devn. of pixel error
64 x 64	4	0.421	0.176
64 x 64 - GS interpolated		0.188	0.142
128 x 128	8	0.424	0.207
128 x 128 - GS interpolated		0.172	0.104
256 x 256	16	0.407	0.177
256 x 256 - GS interpolated		0.182	0.144
512 x 512	32	0.423	0.190
512 x 512 - GS interpolated		0.202	0.119

Table 1. Auto-correlation pixel errors

3.4 Experimental validation

Once implementation of the modified processing hardware and software had been completed, and basic testing of the PIV software completed, a flow study was made in order to assess the general validity of the PIV technique, and the suitability of the VISIFLOW system in particular. This PIV study was part of a larger experiment for improving understanding of the flow of liquid coolant within the cylinder block of an automotive engine. This larger experiment was undertaken at the same time, and this allowed several data-sets to be compared.

The conflicting legislative and performance requirements of the modern automotive engine dictates the detailed optimisation of all features of the design. With this impetus, increasing attention is being given to the coolant system where the requirements are for minimum coolant volume and uniform flow distribution.

Optimisation of the complex three dimensional coolant system by means of conventional design iteration has proven extremely difficult. Laser sheet imaging, particle image velocimetry and laser Doppler anemometry techniques were applied to a particular four cylinder engine

cylinder engine block, giving qualitative and quantitative flow field data [74]. This flow data was then compared to a CFD predicted flow field [75]. The main aim of these laser measurements was to validate the CFD model by comparing against experimentally derived data. This would indicate the engineering value and accuracy of the model calculations to the relevant design engineers. There was in addition, the equally important aim of validating the whole-field PIV diagnostic data against the more established LDA and numerical data.

3.4.1 Experimental Rig

A production 1.6 litre four cylinder gasoline engine was used as the basis for a transparent acrylic cold flow model, shown in Figure 31, together with NdYAG laser for LSI and LDA fibre probe and computer. The geometry of the model replicated the principal dimensions, flow entry and exit positions, bore spacing and minimum coolant jacket thicknesses of the production engine.

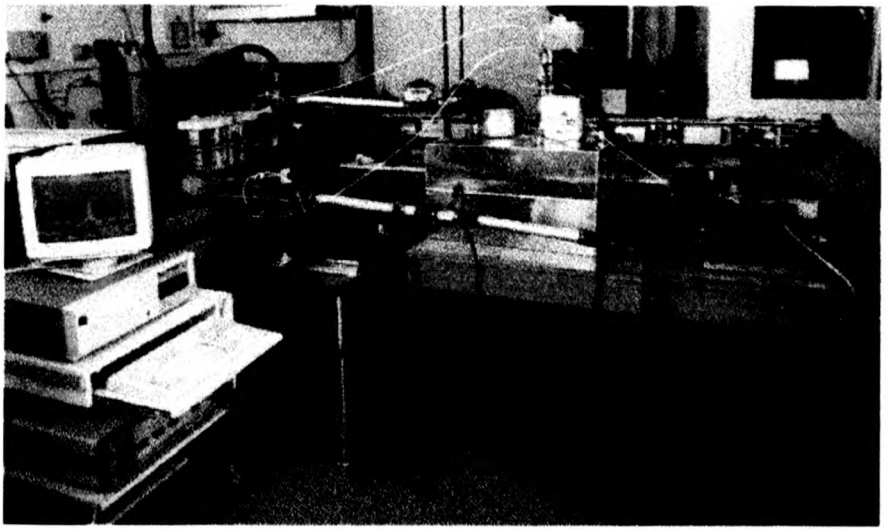

Figure 31. Engine Cooling Flow Rig

The model was simplified by encapsulating the inner bore geometry within a rectangular box. The enclosed cylinders were modelled by a moulded acrylic insert. The simplifications used provided the following advantages:

- Good optical access allowing the whole flow field to be observed and measured.

- Simplified construction of the CFD mesh without losing the principal geometric features that dictate the flow field.

- Simplified manufacture of the physical model.

Flow was delivered to the model from a 740 W external pump via a single pipe of sufficient length as to eliminate the pump flow effects to a single entry at the lower left hand corner of the model. Flow was removed from the model via eight rectangular holes in the top of the block. These fed into "legs" which fed a collector which returned the fluid to a plenum which in turn fed the pump which drives the flow. These legs were elongated to allow measurement of the pressure drop from the model inlet to each leg. The flow restrictions imposed by the cylinder head gasket were not included in the model. The whole system produced a closed circuit, Figure 32. The coolant flow rate was measured with a Hydrill turbine flow meter inserted into the feed pipe. The pressure losses between the inlet and each exit leg were measured with a Scharitz differential pressure transducer.

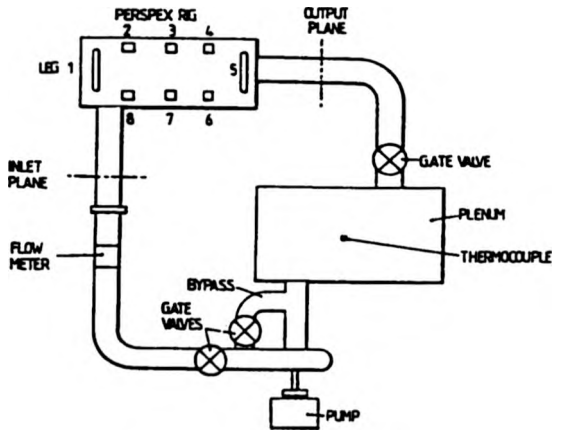

Figure 32. Schematic of the engine coolant flow rig

3.4.2 LDA study

LDA measurements were undertaken to measure two components of velocity in a single plane on the cooling water inlet side of the engine block and midway between the outer walls of the cylinders and the inside of the block wall. A photograph of the experimental arrangement is shown in Figure 33.

Instrumentation and set up

The LDA system employed was a TSI 2-component backscatter fibre optic system. A 4 W Coherent Argon Ion laser was used as the light source. The beam was split into two beams of different wavelengths (488 and 514.5 nm). These beams were each divided into two coherent in-phase beams. One beam of each wavelength was passed through an acousto-optic Bragg cell. This was used to impart a frequency shift of 500 kHz between the two beams. The effect of the frequency shift can be thought of as creating a moving fringe pattern in the intersection volume, thereby biasing the recorded burst frequencies . The frequency shift was used to bias the velocity measurements by an amount greater than the maximum reverse velocity present. During later analysis, this known shift was subtracted from the measured burst frequency, giving the true burst frequency, thereby enabling reverse velocities to be measured with the otherwise velocity sign insensitive LDA technique.

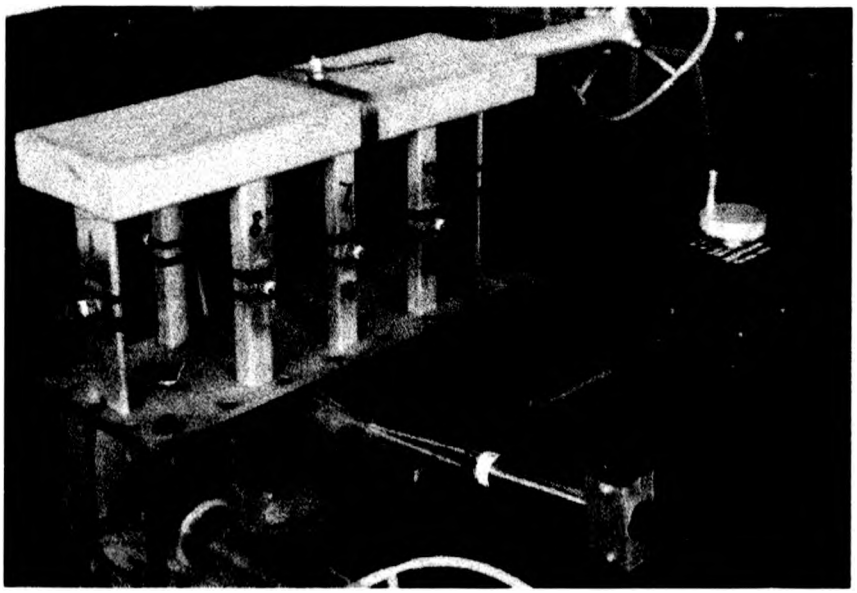

Figure 33. Engine coolant flow LDA experimental arrangement

The dimensions of the measurement volume were determined by the optics within the fibre optic probe. The small exit diameter of the outer probe lens meant that the initial separation of the four beams was small and hence the probe intersection volume was fairly wide and long - 2.7 mm long, with a diameter of 140 μm, at a working distance of 135 mm from the

end of the physical probe. The fringe spacing was calculated to be 4.92 μm for the green beam, and 4.68 μm for the blue beam.

Signals were processed using TSI IFA750 processors controlled by a 25 MHz 386 AT micro computer. The IFA750 processors used high speed digital Fourier transform hardware accelerators to compute a high resolution auto-correlation signal for each Doppler burst. This auto-correlation was then analysed to give the dominant velocity component. The LDA processors were designed for high accuracy and high data rate collection even in high noise environments. The processors were designed to trigger on the signal to noise ratio, rather than the signal amplitude. This increased the analysis accuracy and improved automatic validation of the data being acquired. The bandwidth of the processor was 90 MHz, and therefore the maximum measurable velocity was more than adequate for this study.

The LDA processors were controlled by TSI FIND software, which provided a flexible menu driven user interface. The raw velocity data was stored on the host computer's hard disk as it was collected. The software analysed the raw data off-line, providing comprehensive information on flow statistics, and generating velocity profiles for each line of probe traverse.

The fibre optic probe was mounted on an XYZ traverse stage which was under full computer control by the AT-PC also performing the data acquisition. Traversing was undertaken over as large a region as practicable, the spacing between measurement points being set to 10 mm in both the horizontal (X) and vertical (Y) directions. The main obstacle to acquisition being the inlet pipe itself which was in the path of the traversing stage at one end of its travel. This was overcome by tilting the LDA probe downwards slightly (10°) so that the traverse did not come into contact with the pipe. The vertical velocity component was then scaled to correct for this non-perpendicular angle. The traverse resulted in a measured grid of 12 x 31 (total 372) data points, defined as in the schematic of Figure 34.

Seeding

Various seeding materials were tested for suitability in this application, from 1 μm diameter latex particles, through to 5 μm ZrO_2 particles. The best results (highest consistent data rate at different locations) were obtained without seeding at all, but relying on natural sediment in the somewhat murky mains water employed in the rig.

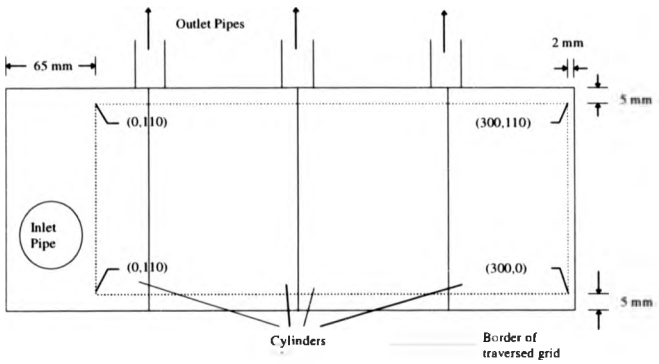

Figure 34. Engine coolant flow LDA measurement grid

Measurements

Following setting up and testing, LDA data was acquired over a two day period. Each of the twelve 31 point horizontal traverses were undertaken separately and the data stored after each point was measured. The optical alignment and the quality of the data was checked at a few points prior to each acquisition of a 31 point data set. A maximum of 5000 burst signals were processed at each point, or as many as were received in 50 seconds. Typically, time-out occurred with 1000-2000 signals being acquired at each point, although this varied considerably from point to point. At only a few locations did scattering of the laser beams within the inside model surfaces prevent valid data being obtained.

The temperature of the circulating water was found to gradually increase as the pump continued to operate and produce heat. After about three hours of running, the water reached an equilibrium temperature of approximately 30 °C.

3.4.3 LSI study

This was carried out in two phases. The first phase was a relatively simple white light imaging (WLI) study. This used a 1 kW tungsten filament halogen lamp, masked by a slot to produce a 2.0 mm thick sheet of light which was used to illuminate the plane of interest. The flow was observed by fitting a simple bubble generator, consisting of a matrix of 32 x 0.5 mm diameter holes fed by compressed air, to the model inlet. The small bubbles acted as scattering centres and allowed the flow to be visualised. For the flow rates described later, best results were obtained by using black and white 2.25 inch format 400 ASA film with a shutter speed of

1/60th second. This first phase was used as a foundation feasibility study for the later PIV, LDA and numerical work. A single plane was studied, the same as for the LDA work.

The second phase was more sophisticated and used a dual oscillator NdYAG laser as the illumination source. This was the customised design described in the previous chapter. Five planes were studied, as shown in Figure 35. Both video and photographic cameras were used to record the flow images. The video recordings were intended for visualising the main characteristics of the flow, while the photographic images were recorded for later quantitative PIV analysis.

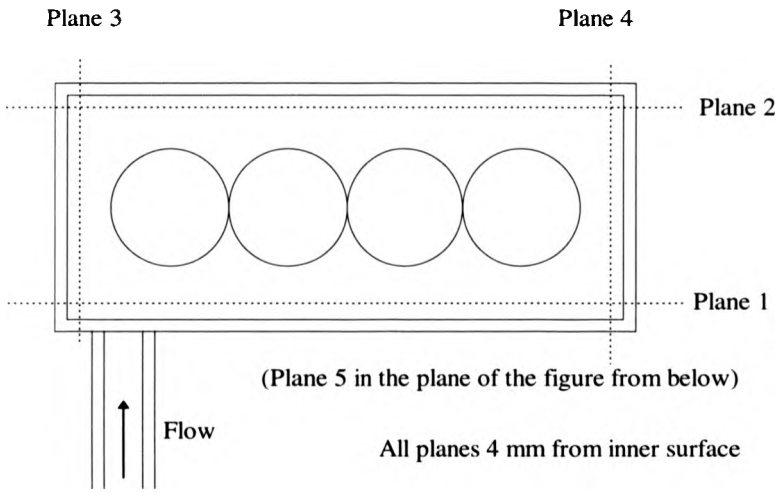

Figure 35. Engine coolant flow LSI measurement planes

LSI image recording

Photographic recording was carried out using a Nikon FM2 35 mm SLR camera. This was a manual design, but with electronic metering to aid setting the correct exposure. A focal plane shutter enabled synchronisation to the NdYAG laser pulse, giving a minimum exposure of 4 ms. This relatively short exposure meant that unwanted ambient light could be reduced, and the contrast of the particle images thus increased. A 55 mm MicroNikkor macro lens was used to image the flow, at 0.8 m giving a magnification of approximately 0.16 in the image plane. The lens was operated at f/4 and f/8, giving near to diffraction limited resolution [76]. Kodak

TMAX 400 ASA black and white film was used to record the images. It was conventionally processed, and its resolution was quoted at approximately 120 lines/mm [77].

Video imaging was made using a Sony XC77RRCE video camera. The MicroNikkor lens was again used, together with an adapter enabling the Nikon lens "F mount" bayonet lens fitting to attach to the video camera "C-mount" fitting. The composite video output from the camera was recorded by a JVC BR-S811E S-VHS tape recorder. The S-VHS format provides a recording resolution of approximately 400 lines. A microphone was used to record experimental details onto the audio track of the tape as the flow images were recorded. Later, this commentary aided efficient retrieval of desired flow sequences.

An interface unit was constructed to synchronise the pulsed laser to the video camera. The vertical blanking video output signal was extracted from the camera. This TTL level signal gave a pulse at the end of every field (50 Hz) - each video frame being made up of two such interlaced fields. This 50 Hz signal was buffered up to 15 V by the interface, and the frequency then divided by two to give two signals of 25 Hz, each pulse alternating with the other. This was done because the laser oscillator was incapable of the full 50 Hz repetition rate. One of the 25 Hz signals was used to trigger the first laser oscillator. The second laser oscillator was then either triggered from the first oscillator after a set delay, giving two pulses per video frame (for PIV), or triggered from the second 25 Hz signal, giving one pulse per video field (for higher repetition frequency visualisation).

LSI seeding

Polystyrene beads (Shell Styrocel) were used to seed the water flow for the LSI and PIV measurements. 400-500 μm diameter beads were used in the case of the video recordings and 200-300 μm beads were used in the photographic work. The beads have a density only slightly greater than water and so remain buoyant in the flow. The larger beads were found to gradually settle out of the liquid over a period of an hour or so, although remaining fully suspended while the rig was being operated. The low flow speed and relatively gentle flow gradients meant that the beads could be assumed to be following the flow adequately.

The seed particles were added to the overflow water tank above the pump. This gave rapid entrainment into the main flow. The seed was added gradually until the particle number density was sufficient. Particle concentration equilibrium was reached approximately 30 seconds are

adding seed. A higher number density was used for the quantitative photographic recording than for the video recording. This was because for correlation analysis, it is important that there was at least one particle image pair for each processed segment of the recorded image. For the video recording, a lower density of seeding was preferred, so that individual double particle images could be easily resolved from neighbouring particles, and often they could be tracked from one frame to another.

When switching between the different sizes of seed particles, the seed was flushed from the system with mains water. In addition, particles of rubber from a gasket in the pipework tended to contaminate the water after a number of hours of running. Considerable flushing time was needed to ensure all particles were removed.

LSI measurements

Four different optical arrangements were required for the four side planes that were studied. Measurements of a fifth plane, a horizontal plane at the base, and viewed from underneath the model, were attempted but abandoned as a result of poor data caused by obscuration caused by sediment that had settled in the model. The acrylic rig was suspended using rope so that optical access was easy from all directions. Some of the light sheet optics were mounted on a trolley so that they could be easily adjusted for the next plane to be measured.

Photographic recordings were designed for post processing by the VISIFLOW analysis system to obtain velocities. Double images of particles were captured by operating the laser in dual pulse mode. The separation of these pulses was varied between 1 and 20 ms to obtain the optimum displacements of particle images. Video recordings were undertaken with the laser operating in single pulse 50 Hz mode, and in dual pulse 25 Hz mode, in both cases synchronised with the video camera.

The time separations between the double pulses was varied from one plane to another, to compensate for the difference in global velocities experienced. The time separations were made such that clear double particle images could be seen by eye while the experiment was being set up. The time separations are listed in Table 2.

Plane measured	Photographic recording laser pulse time separations / ms	Video recording laser pulse time separations / ms
1	0.5, 1, 2	2, 5
2	2, 4, 8	2, 5
3	0.5, 1	1
4	1	5

Table 2. Details of PIV recording parameters for engine model cooling flow

3.4.4 Computational model

A three dimensional computational mesh of the coolant flow model was constructed, Figure 36. The model employed 50,000 computational cells with a mean cell volume of 75.7 mm^3. This mesh density was considered to be that which would be most appropriate for the analysis of the complete coolant flow geometry, given limited analysis time and moderate CPU availability. The fluid properties input to the simulation were for water at 20 °C, giving a density of 998.2 kg/m^3 and laminar viscosity of 1.005 x 10^{-3} NS/m^2. An inlet flow rate of 2.46 x 10^{-3} m^3/s (147.3 l/min) was specified. The inlet turbulence intensity was set at 1 % with a mixing length of 10 % of the inlet pipe diameter. On the exit, a back pressure of 1.0 bar gauge was specified. No heat transfer was specified for any of the boundary faces.

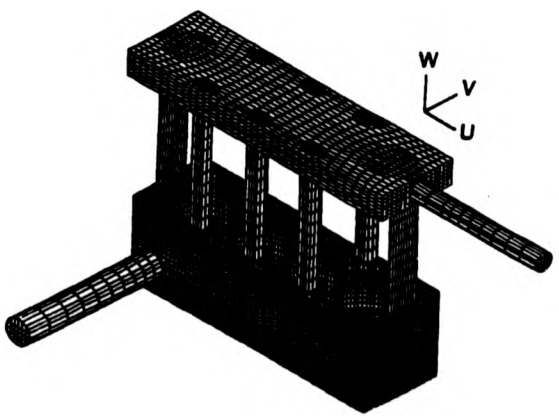

Figure 36. Engine coolant flow CFD mesh

The flow problem was solved using the STAR-CD [78] analysis package. A full upwind differencing scheme was employed, and calculations proceeded until the normalised global residuals reduced to less than 1.0×10^{-3}.

3.4.5 Experimental results

LDA

The raw LDA data is shown in Figure 37 - Figure 40. Theses graphs plot the twelve horizontal profiles, respectively, of mean horizontal velocity, horizontal standard deviation, mean vertical velocity, and vertical standard deviation.

A few points were found to be invalid in the raw LDA data (marked as circled in the graphs). The corrupted points were easily visible from the pronounced difference in magnitude of one or both of the velocity components, compared to the neighbouring data. Inspection of the velocity histograms of the corrupted data revealed very narrow distributions centred on the value of the 500 kHz frequency shift applied to the beams. It was thus deduced that the processors were triggering on stray scattered light. Indeed, the spatial positions of the few corrupted points were found to correspond to the fixing screws in the top and bottom acrylic plates and the centrelines of the internal acrylic cylinder geometry, where surface scattering would be expected to be strongest.

The LDA velocity dataset was then transferred to the VISIFLOW analysis software in order to present it as a two-dimensional, two component velocity map. The software was modified to allow import of the ASCII format LDA data, rather than the normal binary format PIV data. The result is shown in Figure 41 for the raw data, although edited to remove the few clearly corrupted data points, described previously. This vector method of velocity data presentation is clearly much easier to comprehend than the previous profile graphs. Figure 42 then shows the result of filling the gaps using interpolation. Although a complete map is preferable for viewing purposes, the data values interpolated in this way should be treated with caution. It is possible to 'smooth' this data but this is considered inappropriate in the case of data acquired using LDA, where the value is already the average of perhaps several thousand samples taken over a long time period.

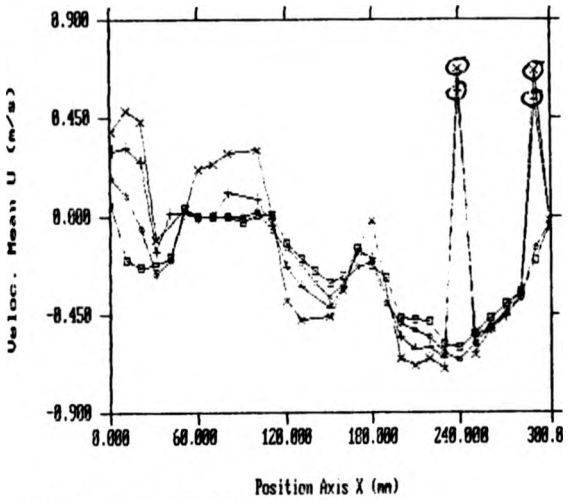

Plot 1 = □ : Row 9 (y=80)
Plot 2 = ◇ : Row 10 (y=90)
Plot 3 = + : Row 11 (y=100)
Plot 4 = X : Row 12 (y=110)

(a)

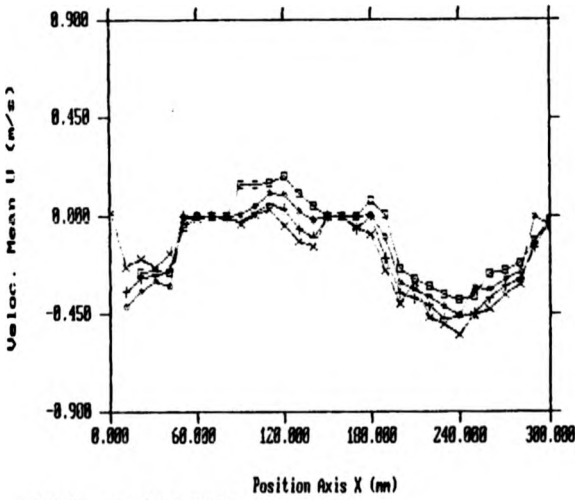

Plot 1 = □ : Row 5 (y=40)
Plot 2 = ◇ : Row 6 (y=50)
Plot 3 = + : Row 7 (y=60)
Plot 4 = X : Row 8 (y=70)

(b)

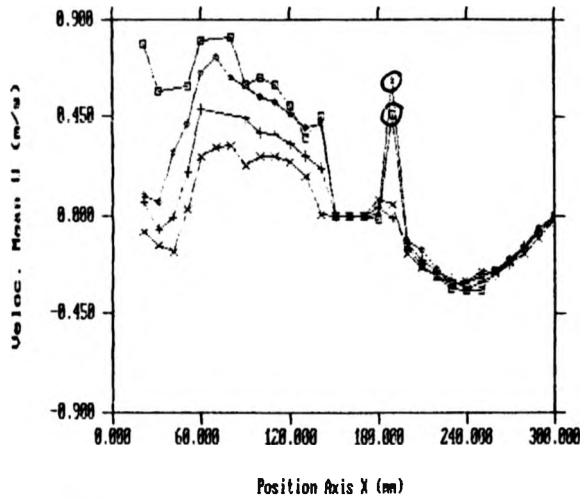

(c)

Figure 37. Engine coolant LDA horizontal mean velocity

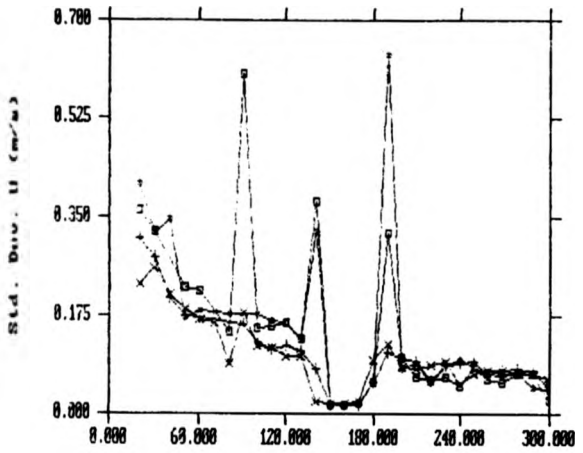

Plot 1 = □ : Row 1 (y=0)
Plot 2 = : Row 2 (y=10)
Plot 3 = + : Row 3 (y=20)
Plot 4 = × : Row 4 (y=30)

(a)

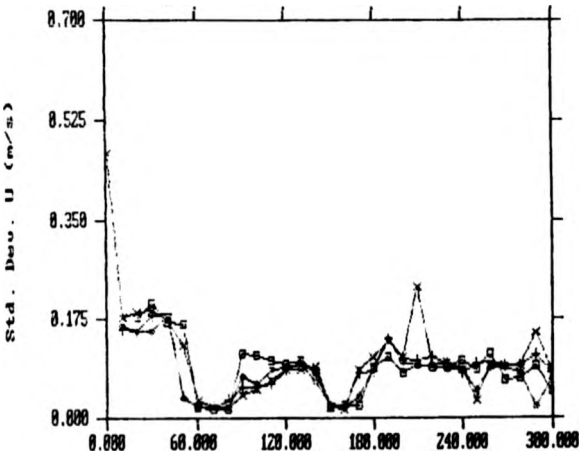

Plot 1 = □ : Row 5 (y=40)
Plot 2 = ◇ : Row 6 (y=50)
Plot 3 = + : Row 7 (y=60)
Plot 4 = × : Row 8 (y=70)

(b)

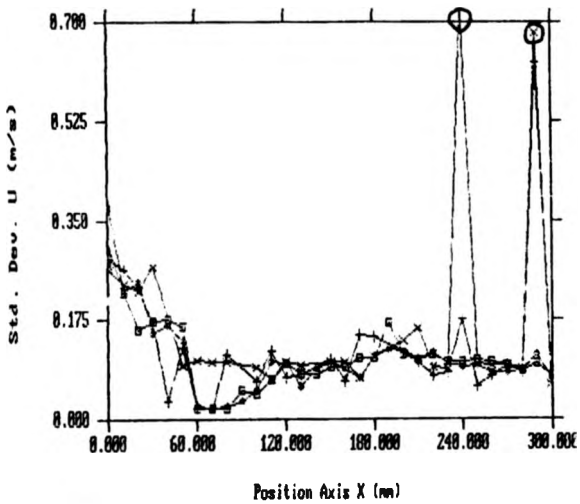

(c)

Figure 38. Engine coolant LDA horizontal velocity standard deviation

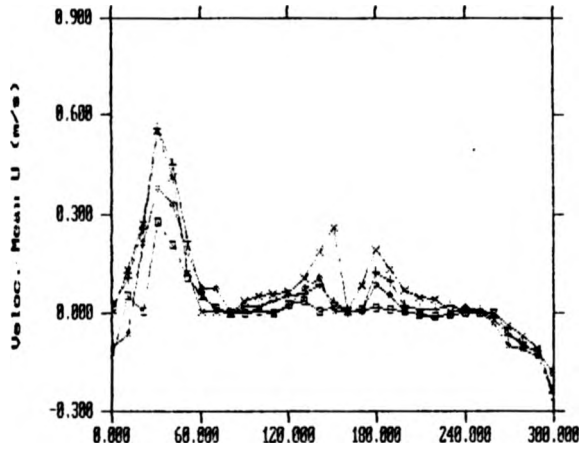
0.900
0.600
0.300
0.000
-0.300
0.000
60.000
120.000
180.000
240.000
300.000
Position Axis X (mm)
Plot 1 = : Row 1 (y=0)
Plot 2 = : Row 2 (y=10)
Plot 3 = : Row 3 (y=20)
Plot 4 = : Row 4 (y=30)

(a)

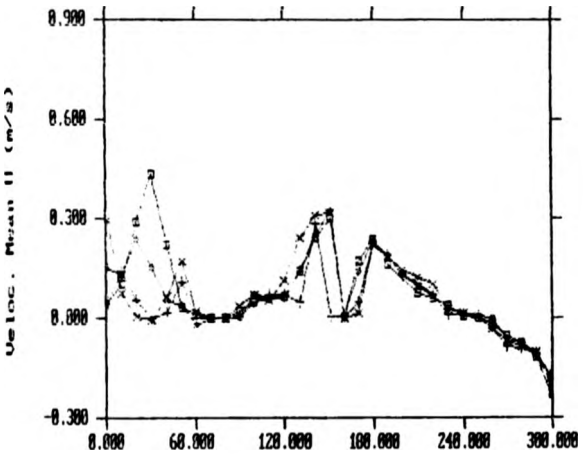
0.900
0.600
0.300
0.000
-0.300
0.000
60.000
120.000
180.000
240.000
300.000
Position Axis X (mm)
Plot 1 = : Row 5 (y=40)
Plot 2 = : Row 6 (y=50)
Plot 3 = : Row 7 (y=60)
Plot 4 = : Row 8 (y=70)

(b)

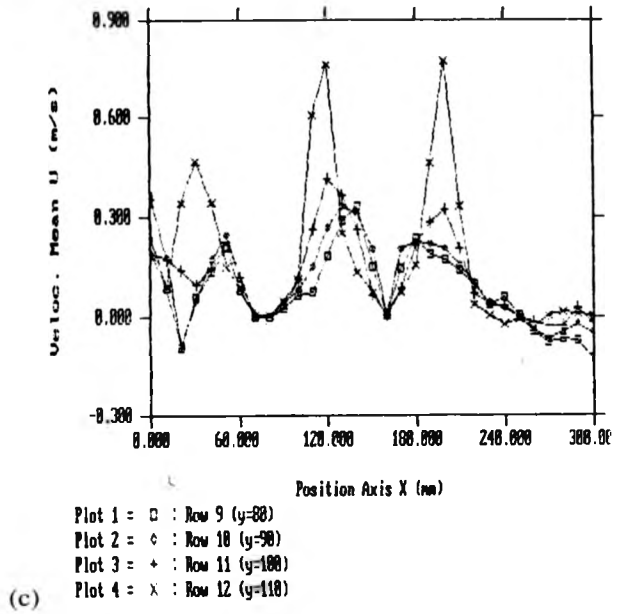

(c)

Figure 39. Engine coolant LDA vertical mean velocity

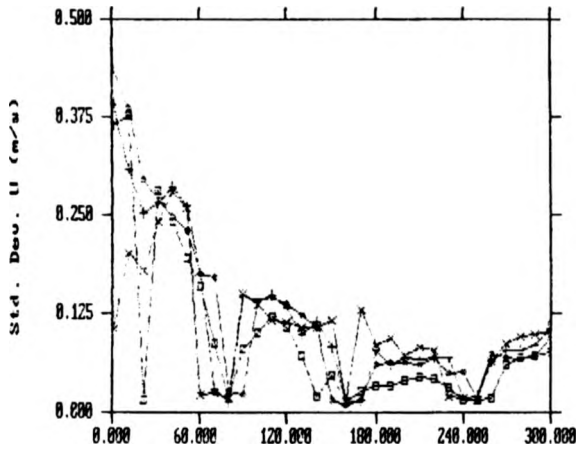
0.500
0.375
0.250
0.125
0.000
Std. Dev. U (m/s)
0.000
60.000
120.000
180.000
240.000
300.000
Position Axis X (mm)
Plot 1 = : Row 1 (y=0)
Plot 2 = : Row 2 (y=10)
Plot 3 = : Row 3 (y=20)
Plot 4 = : Row 4 (y=30)

(a)

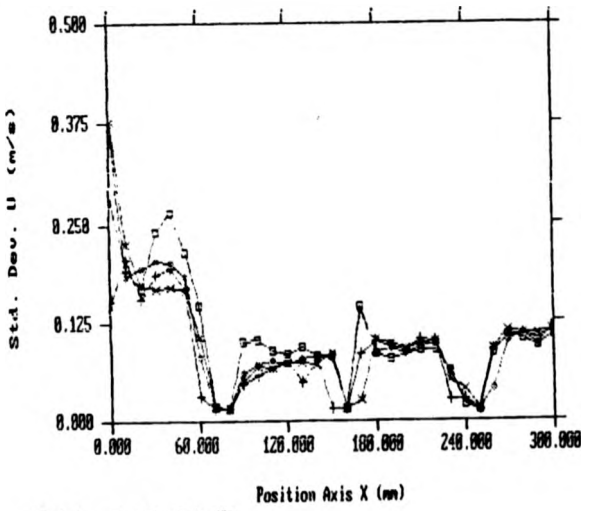
0.500
0.375
0.250
0.125
0.000
Std. Dev. U (m/s)
0.000
60.000
120.000
180.000
240.000
300.000
Position Axis X (mm)
Plot 1 = : Row 5 (y=40)
Plot 2 = : Row 6 (y=50)
Plot 3 = : Row 7 (y=60)
Plot 4 = : Row 8 (y=70)

(b)

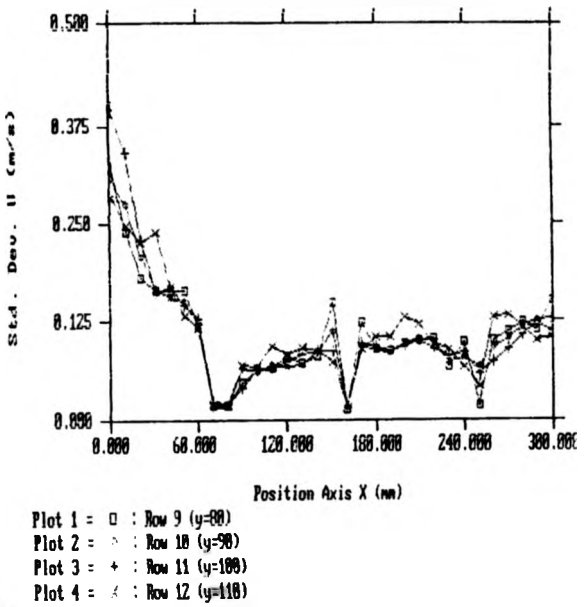

(c)

Figure 40. Engine coolant LDA vertical velocity standard deviation

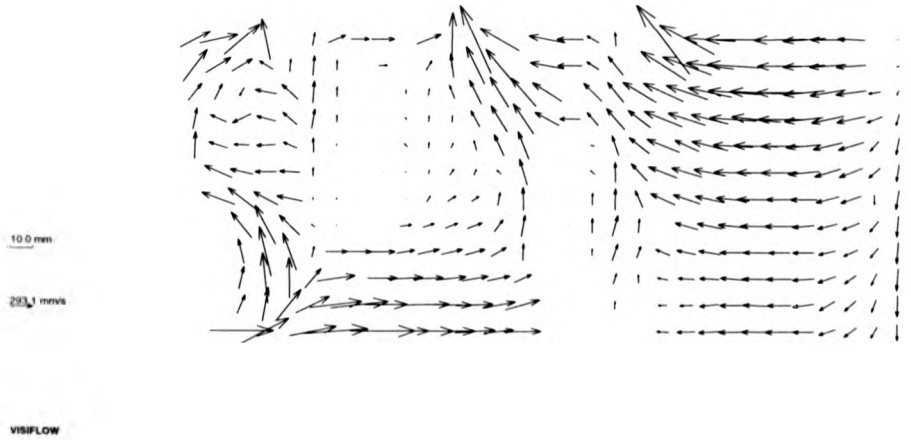

Figure 41. Engine coolant LDA gridded dataset

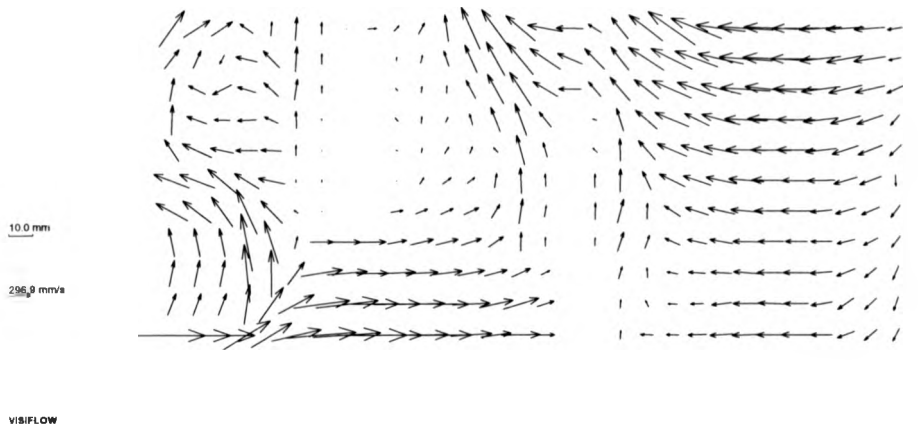

Figure 42. Engine coolant LDA interpolated dataset

The magnitude of the velocity vectors was found to vary between 0 and 1 m/s. No recirculations are seen, but a relatively large area of flow stagnation is evident below and between two of the outlet pipes.

LSI

The video recordings were not designed for later quantitative analysis, in the way that the photographic data were, but only to reveal the basic flow patterns which exist. Yet they do contain important and potentially valuable information about the velocity field as well as both the temporal and spatial behaviour of the flow.

Of the 36 photographs taken of each of the four planes, one was selected for PIV analysis. These photographs are shown in Figure 43 - Figure 46.

Figure 43 shows the photograph selected for analysis from plane 1. This plane is the same as studied using LDA and the computational model.

Double images of particles are observed at almost all parts of the flow. The velocities extracted, by VISIFLOW using auto-correlation are given in Figure 47. The reasons for the several gaps are either lack of double images or ambiguous determination of the velocity component usually because of different particles at the same location moving in different directions or widely different velocity magnitudes. These invalid vectors were removed using

the automatic validation algorithm, followed by manual removal of the few remaining clearly invalid vectors. This variation of magnitude and direction across an interrogation region is often a feature of high turbulence flows, and where high velocity gradients exist. Figure 48 takes this raw data and fills the gaps using the previously described interpolation algorithm. Figure 49 further smoothes this data though application of a 5 x 5 Gaussian filter kernel to each vector.

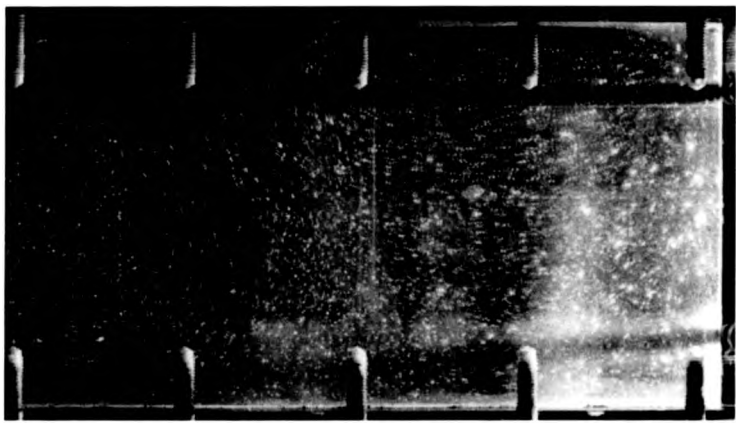

Figure 43. Photograph of Engine Coolant LSI flow plane 1

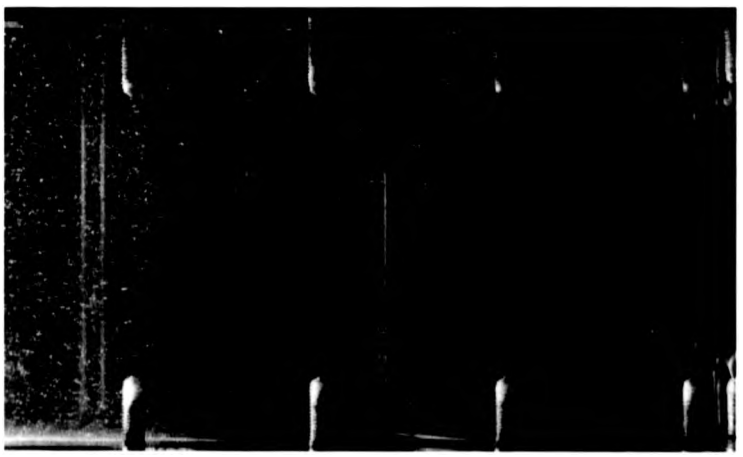

Figure 44. Photograph of Engine Coolant LSI flow plane 2

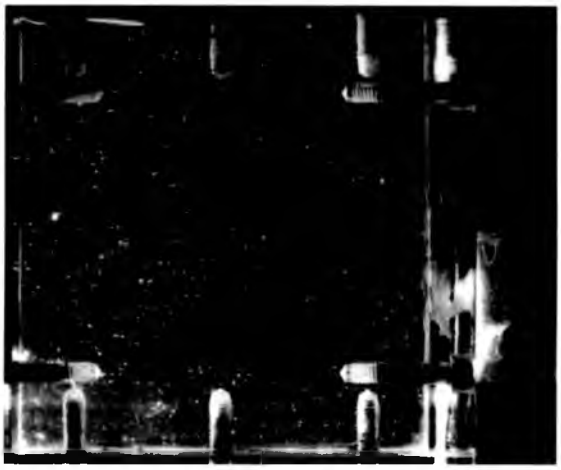

Figure 45. Photograph of Engine Coolant LSI flow plane 3

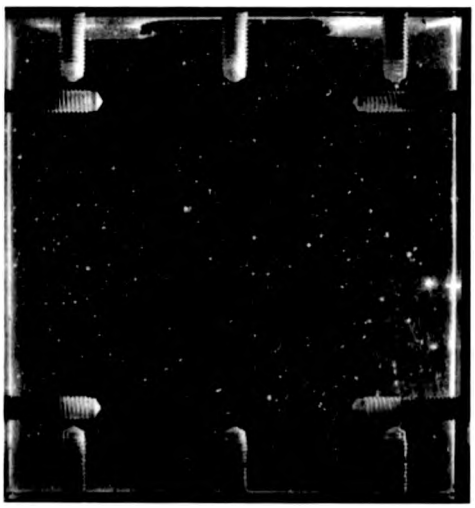

Figure 46. Photograph of Engine Coolant LSI flow plane 4

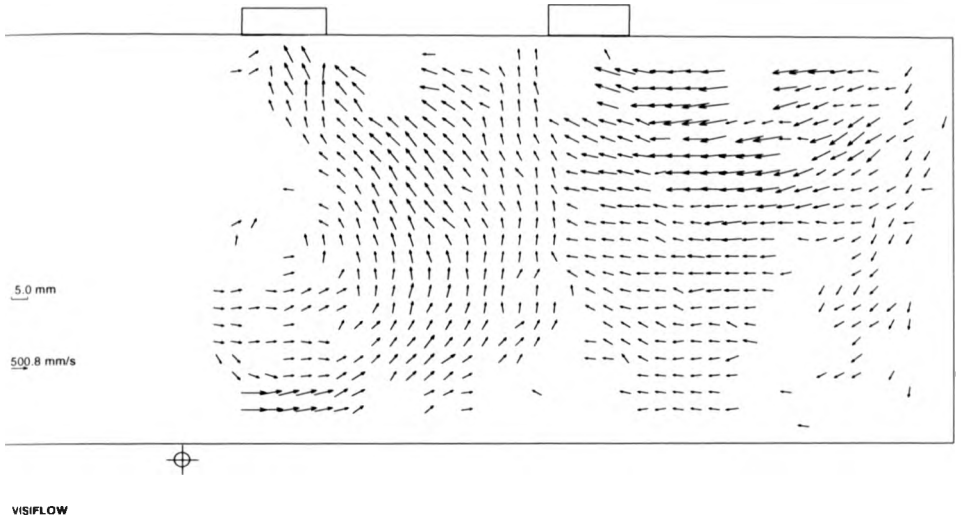

Figure 47. PIV data for plane 1 of the engine coolant flow

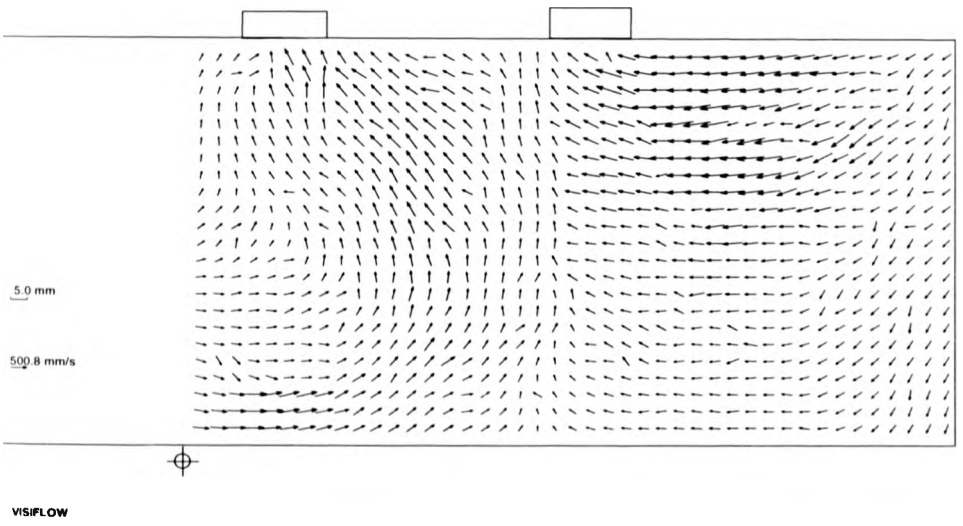

Figure 48. Interpolated PIV data for plane 1 of the engine coolant flow

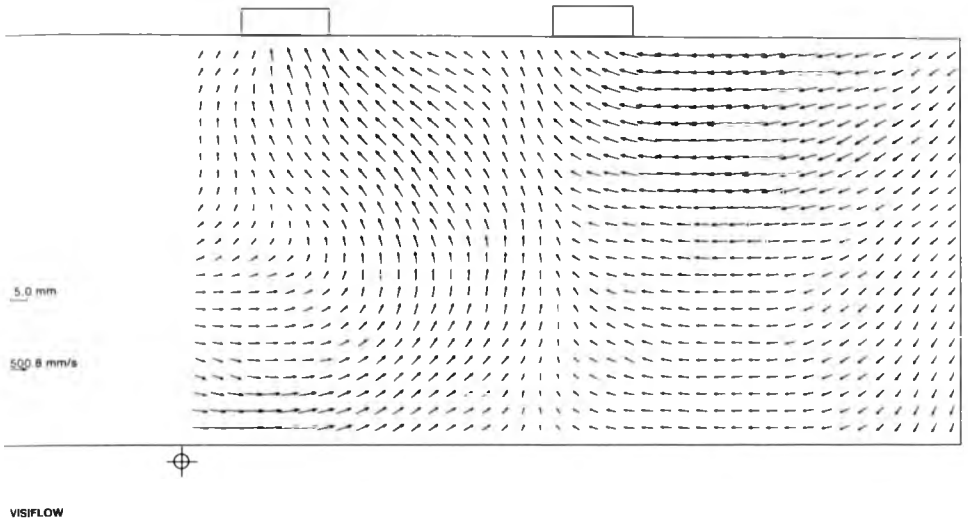

Figure 49. Smoothed PIV data for plane 1 of the engine coolant flow

The same process was applied to a photograph of plane 2, Figure 44, to produce the velocity maps shown in Figure 50 - Figure 52.

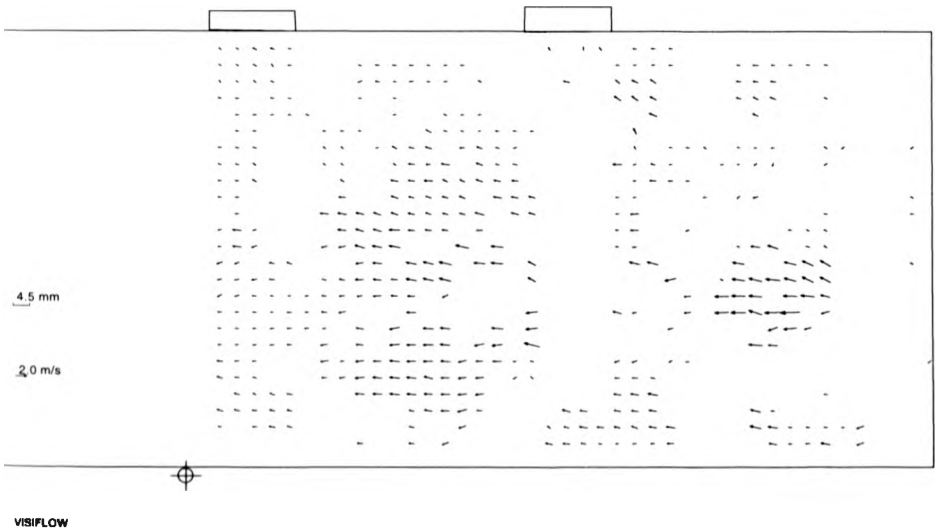

Figure 50. PIV data for plane 2 of the engine coolant flow

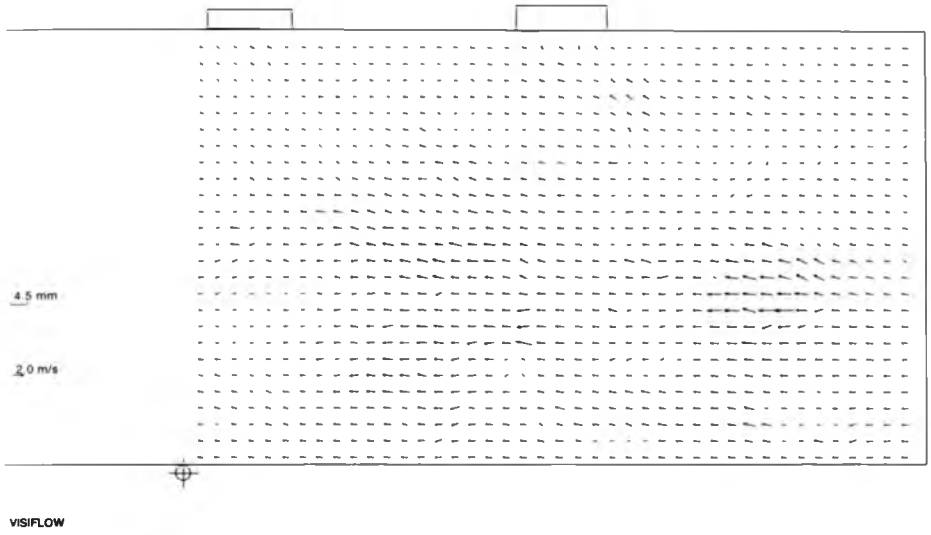

Figure 51. Interpolated PIV data for plane 2 of the engine coolant flow

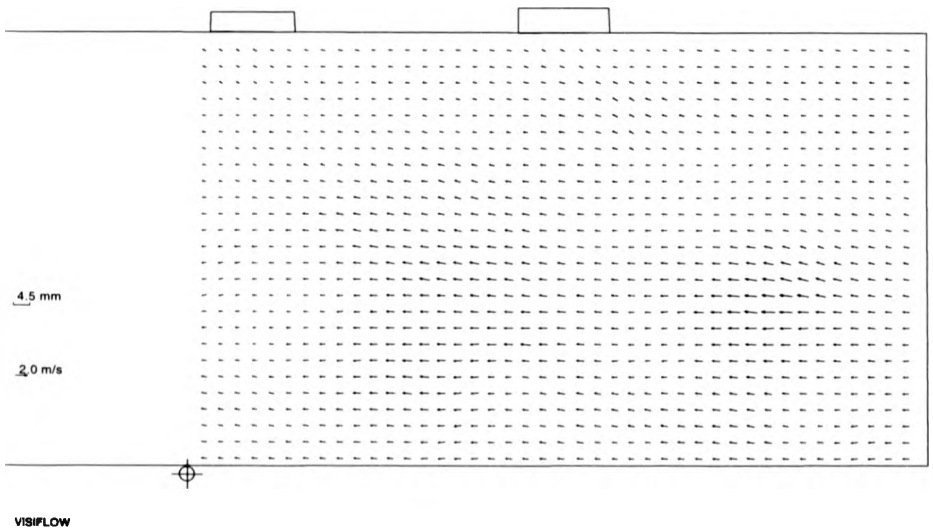

Figure 52. Smoothed PIV data for plane 2 of the engine coolant flow

Figure 45 shows the photograph selected for analysis from plane 3. As well as showing double images of particles within the block, double images are also captured in the inflow pipe. The

raw processed data velocity map, and the interpolated and smoothed versions of this are shown in Figure 53 - Figure 55, respectively.

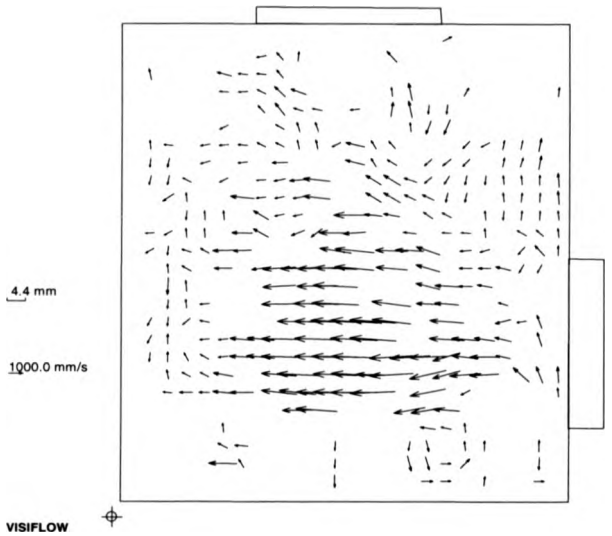

Figure 53. PIV data for plane 3 of the engine coolant flow

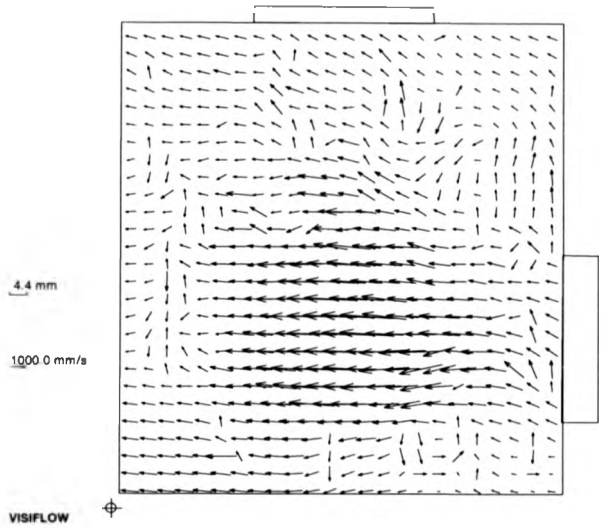

Figure 54. Interpolated PIV data for plane 3 of the engine coolant flow

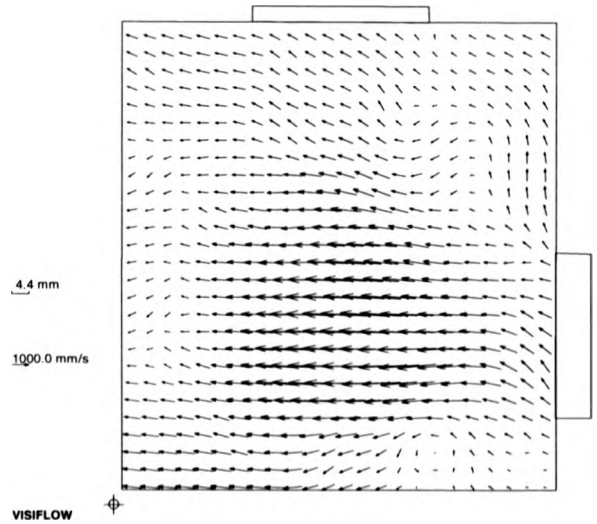

Figure 55. Smoothed PIV data for plane 3 of the engine coolant flow

Correlation analysis of the photograph of plane 4, Figure 46, resulted in far more gaps than data, due to the low seeding density, and for this reason it was analysed using the previously

described particle matching algorithm with the results shown in Figure 56. Figure 57 shows how this was fitted to a standard rectangular grid, again using the interpolation algorithm. Figure 58 then shows the smoothed version.

3.4.6 Discussion of results

Figure 59 shows a comparison of the predicted and measured flow fields for plane 1. Due to the obstruction from the inlet pipe, LDA and PIV results are restricted to a region to the right of the inlet. The PIV results are further restricted by the field of view of the analysed photograph. The PIV results shown are the basic data, without interpolation or smoothing. Consequently, there are gaps between these data points. The quantitative comparison between predicted and observed flow fields is good with recirculations A, B and C being correctly identified. Quantitative comparison of predicted and measured U and V velocities for sections 1, 2 and 3 are presented in Figure 60, Figure 61 and Figure 62.

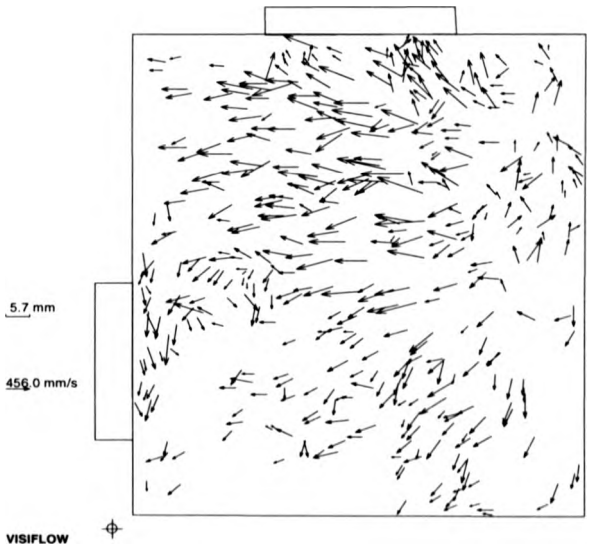

Figure 56. PIV data for plane 4 of the engine coolant flow

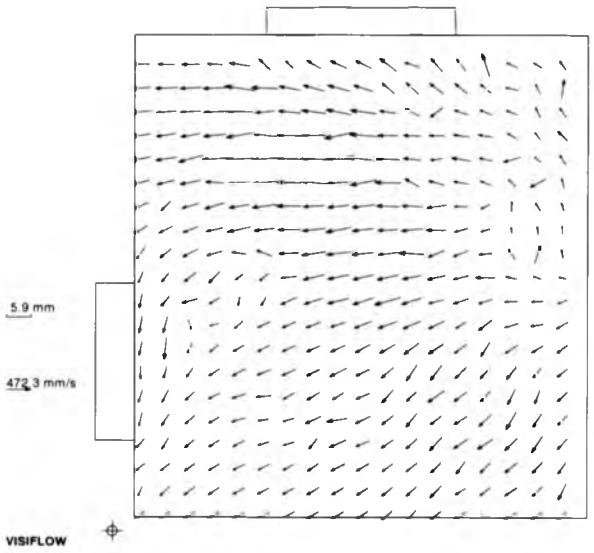

Figure 57. Interpolated PIV data for plane 4 of the engine coolant flow

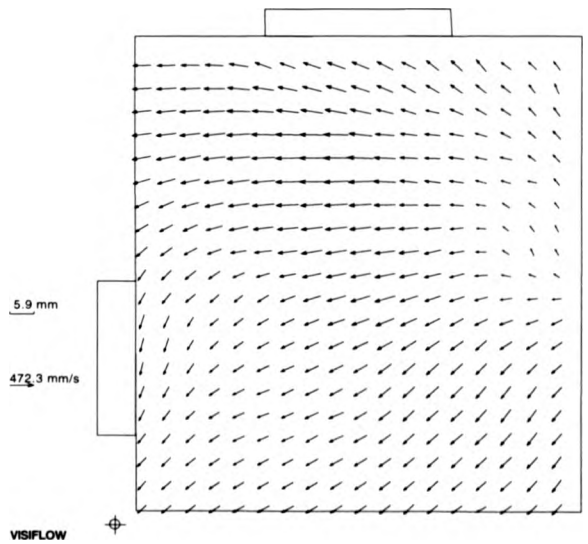

Figure 58. Smoothed PIV data for plane 4 of the engine coolant flow

For section 1, the overall comparison is good with the velocity magnitudes being accurately predicted. The difference in U velocity at around 250 mm suggests that the position where the

leftward and rightward flows stagnate, flow feature D is being predicted at a position 40 mm to the right of the measured position. The difference in V velocity near the right wall suggests that the magnitude of flow feature E on this section is under predicted. The difference is however not repeated on the other sections. The most significant difference between the LDA and CFD in the V velocity is near the inlet. This difference suggests that flow feature B is physically positioned lower than that predicted.

For section 2 the overall comparison is again good with the peak magnitudes of velocity being accurately predicted. The most significant differences in velocity occur at around 220 mm, where the predicted U and V velocities are low. It is not clear as to which flow feature is causing this difference.

There is excellent comparison between predicted and LDA U and V velocity on section 3. This shows the magnitude of upward velocity beneath each of the block legs to be accurately predicted. The PIV results show the same periodic structure, but show a smaller range in the oscillating V values, giving peak values approximately two thirds of the LDA data. This may be a result of the local averaging implicit in the correlation method of analysis.

Figure 63, Figure 64, and Figure 65 presents a comparison of PIV and CFD results for planes 2, 3 and 4 respectively. Due to the absence of significant large eddies, LDA results were not recorded for these planes. Also, experiment data acquisition time was limited, and the LDA measurements were particularly time consuming. Qualitative comparison between the CFG and PIV data are reasonable, but not as good as for plane 1.

There is clear resemblance between the PIV generated velocity map and that obtained using LDA. Yet it must be remembered that the PIV map reveals the velocity field at the instant the photograph was recorded, and that in any turbulent or unsteady flow situation, this will change from one image to another. That the flow does vary becomes very evident on viewing the video recording of the flow. Thus, it is not valid to attempt a direct accuracy measurement by comparing the CFD and PIV results.

In the case of plane 4, the reason why the conventional auto-correlation analysis scheme resulted in few valid vectors suggests a region of turbulence which is higher than studied elsewhere in the model. That turbulence is high in this region is clearly seen in the initial

velocity map shown in Figure 56. In such a situation, it may be difficult to justify the validity of an instantaneous velocity map, let alone interpolating and smoothing the data.

3.4.7 Conclusions on developing a PIV analysis system

PIV and LDA measurements have been successfully undertaken for the engine flow model. Velocity data was also obtained from a numerical model and the results compared to the experimental data. The three data sets were found to be similar, and therefore each technique was validated by the others. Confidence was highest in the LDA data, although it took the longest time to acquire (approximately 48 hours), being a point measurement technique. The numerical data was obtained relatively easily, although the time for the setting up of the problem and its computation was not insignificant.

The acquisition of the PIV data was rapid, although its analysis was not carried out at the same rate. The initial LSI pictures provided by the technique give rapid initial visualisation and characterisation of a flow, with the PIV analysis able to give numerical results if the flow is of sufficient interest. The coolant flow results show that the VISIFLOW PIV analysis system can provide valid results from an experimental flow, when compared to other flow data, both experimental and numerical. However, a full comparison between the quantitative results provided by VISIFLOW and those of LDA and CFD was not attempted. This was due to the vastly different sampling times of the effectively instantaneous PIV and the time averaged LDA and CFD.

The PC hardware based processing system has been shown to provide sufficient performance to realise rapid analysis of PIV images. Both film and video images can be processed. Film gives highest resolution and a compact method of archiving the images. Video is convenient and allows on-line processing, and the ability to acquire easily sequences of images to track the temporal development of a flow, but spatial resolution is lower than for film.

The VISIFLOW software package has proved to be easy to use, with its mouse-driven graphical interface. The output data of the software is easy to interpret and readily exportable in a number of formats. For example, the vector images shown in this chapter are Windows metafiles. The software is now in use with a number of research groups around the world, working on a variety of flow applications, ranging from wind tunnel aerodynamics to studying the flow of air around insect wings in flight.

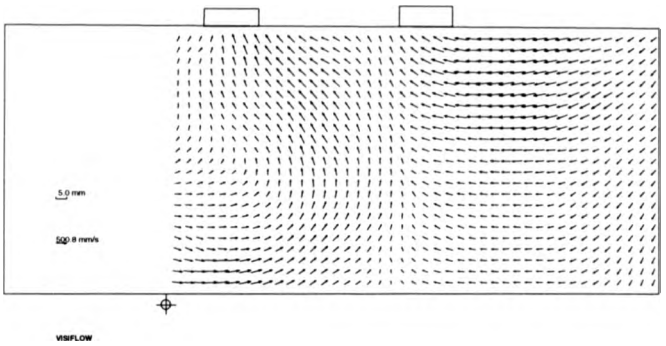

(a) PIV

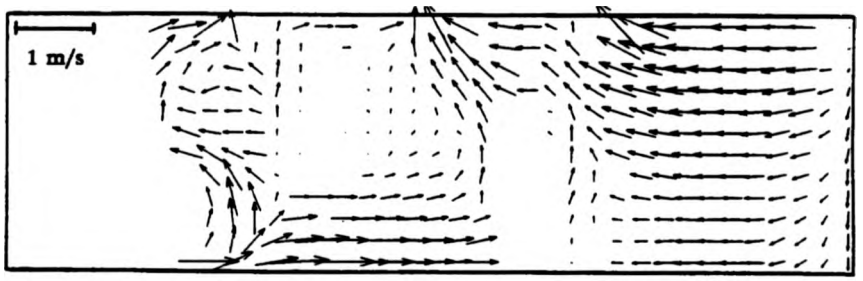

(b) LDA

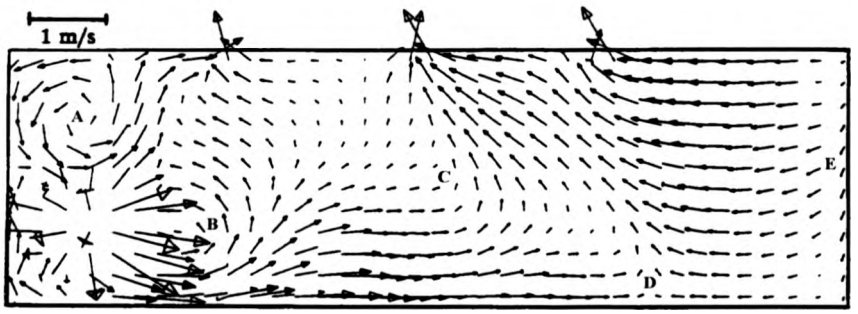

(c) CFD

Figure 59. Comparison of predicted and measured flow fields for plane 1

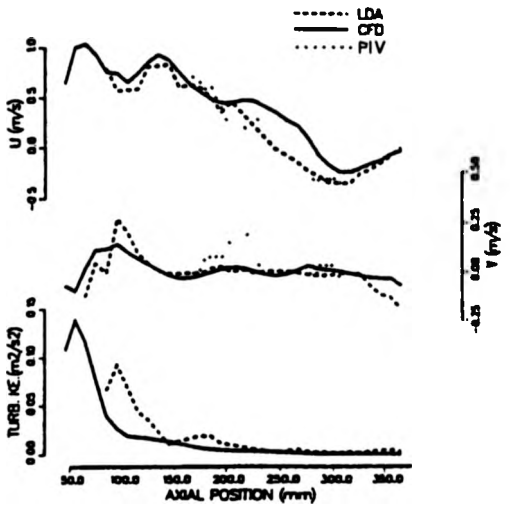

Figure 60. Comparison of predicted and measured velocities for section 1

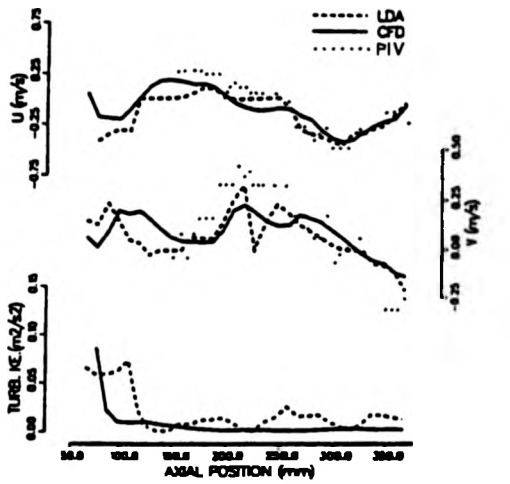

Figure 61. Comparison of predicted and measured velocities for section 2

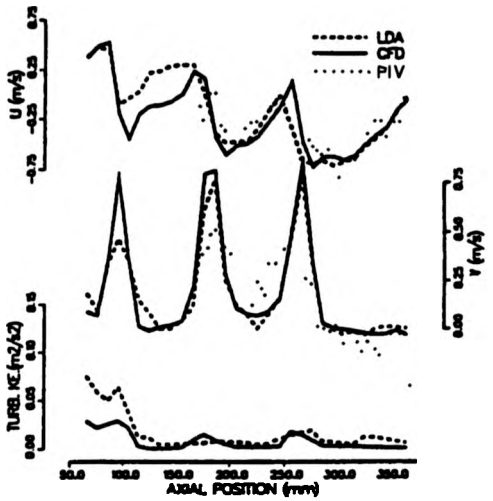

Figure 62. Comparison of predicted and measured velocities for section 3

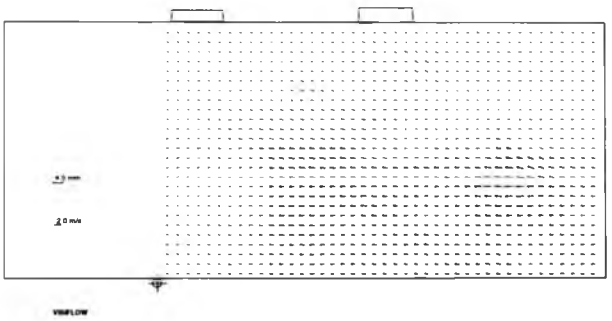

(a) PIV

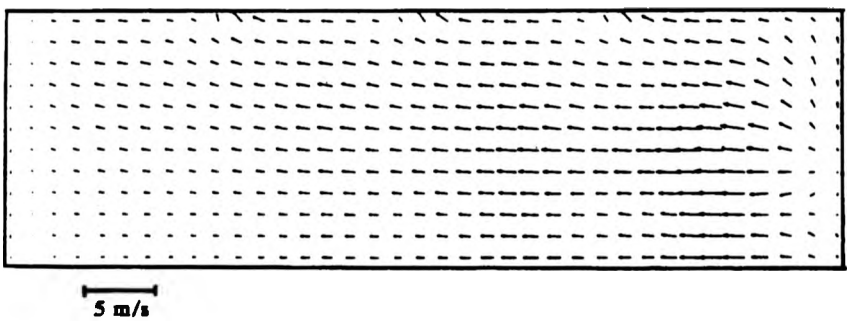

(b) CFD

Figure 63. Comparison of PIV and CFD results for plane 2

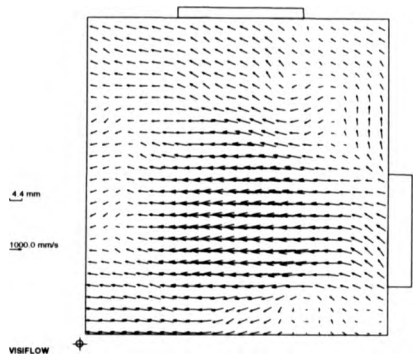

(a) PIV

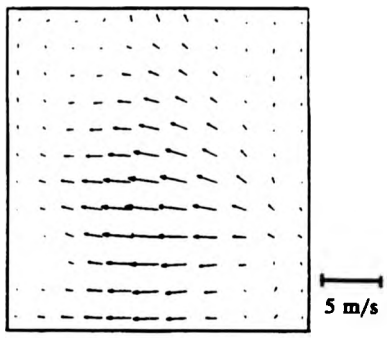

(b) CFD

Figure 64. Comparison of PIV and CFD results for plane 3

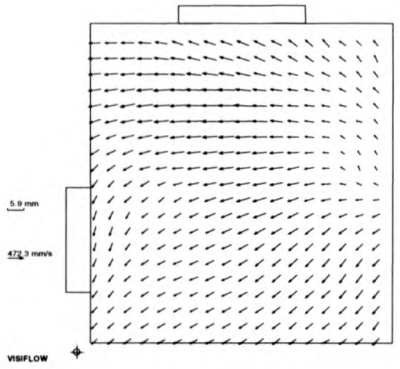

(a) PIV

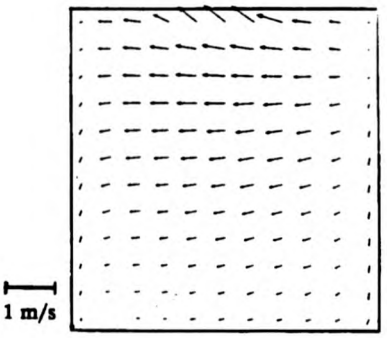

(b) CFD

Figure 65. Comparison of PIV and CFD results for plane 4

4. Global Diagnostics Applied to Diesel Sprays

This chapter discusses application of global methods developed for visualising the initial atomisation and wall impingement of an automotive diesel spray [79], as well as describing the development and implementation of global techniques suitable for wall liquid film thickness measurement of an impinging spray.

An overview of the experimental apparatus developed and used is given initially. The experimental work on the spray is then described. The near nozzle region is discussed first, followed by the developing spray. The behaviour of the spray as it impinges against a surface is then discussed, followed finally by the behaviour of the surface film generated by the spray.

4.1 Diesel fuel properties

Diesel fuel is a liquid consisting of a complex mixture of heavy petroleum distillation products, in the fraction between paraffin and residual oil. However, the exact constitution of fuel varies considerably from batch to batch, and from one source of crude oil to another. Consequently, the major characteristics of diesel fuel such as density, sulphur content, volatility and viscosity are variable [87]. Diesel is characterised by its *cetane number*, which is a measure of the ignition quality of the fuel. The higher the cetane number, the greater the tendency of the fuel to undergo self ignition on compression.

For the measurements described in this thesis, a model fuel was studied. This gave the advantage of a clearly defined mixture of compounds, which ensured repeatability and allowed studies by a number of workers to be compared.

The model fuel consisted of n-decane. This mixture was chosen because of its similar physical properties to typical diesel fuels. The combusting characteristics were not important here, as no burning of the fuel took place in these studies.

4.2 Experimental apparatus

4.2.1 TIFOSI injection system

A prime requirement for diesel spray measurements is a flexible and controllable means of generating the injection event. For this work, the TIFOSI system [80] was used. This large

car/small van scale diesel system consists of a fuel injection pump driven by a variable speed electric motor. The pump drive shaft is instrumented with an optical shaft encoder to measure the rotational speed.

An electronic system was used to control a standard fuel pump supplying fuel to the injector. For convenience when making laser measurements, the system was designed to allow single injections. This was necessary as injections were either into the open air, or into un-purged confined spaces. The single injections meant that spray did not build up from previous injections, which would otherwise obscure much image detail.

The injection pump runs continuously so a solenoid by-pass valve was situated close to the injector. When the valve is open, the pressurised fuel returns directly to the fuel tank. When the valve is closed, injections take place. The opening and closing of the valve was carefully timed by the control electronics so that single injections could be selected. This timing was adjusted so that the pressure history for the single injection was very similar to that for the continuous injection. The single injection was found to be very repeatable, with only very small shot-to-shot fluctuations observed.

Peak pressures were monitored by a piezoelectric gauge in the fuel supply pipe and the system could be adjusted to give up to approximately 1500 bar. A standard automotive needle lift injector was used, with a single hole exit nozzle of 0.32 mm diameter. The fuel spray was directed to impinge vertically onto a flat glass plate, at a distance from the nozzle of 50 mm. The glass plate was adjustable for impingement at different angles. The transparent plate permitted viewing of the spray cross section from all directions. An ordinary automotive diesel fuel was used.

All of the measurements described here were made using the same setting of the TIFOSI system. A pump speed of 500 rpm was set with a stroke setting of 10.5 mm. The pressure trace indicated a peak pressure of approximately 500 bar. This setting gave an injection quantity of 20 mm^3. This standard setting was also used by co-workers at collaborating laboratories to ensure results were comparable.

4.2.2 High pressure cell

A high pressure cell was used to simulate the conditions found inside a combustion chamber. The Harwell "small" HP cell was used for these studies. A photograph of the cell together with the NdYAG laser and a 35 mm photographic camera, is shown in Figure 66. A schematic of the cell when configured for LSI is shown in Figure 67. The cell was certified for pressures of up to 30 bar. The gas used inside the cell was nitrogen, supplied by a large palette of linked gas cylinders. An electric coil was used to pre-heat the pressurising gas, allowing the cell and its contents to be heated up to 420 °C. Thermocouples were attached at various points inside and outside the cell, enabling temperatures to be verified.

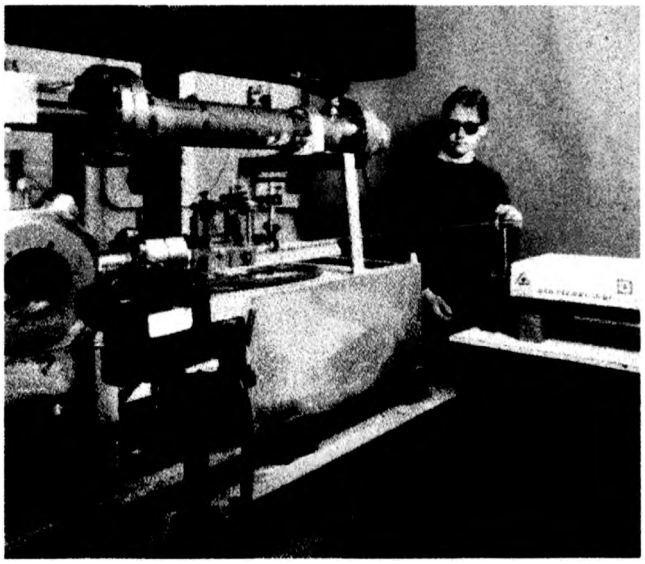

Figure 66. Photograph of the Harwell small HP cell

The inert nature of the pressurising gas ensured that combustion of the injected spray did not take place, which would otherwise occur at these elevated pressures and temperatures.

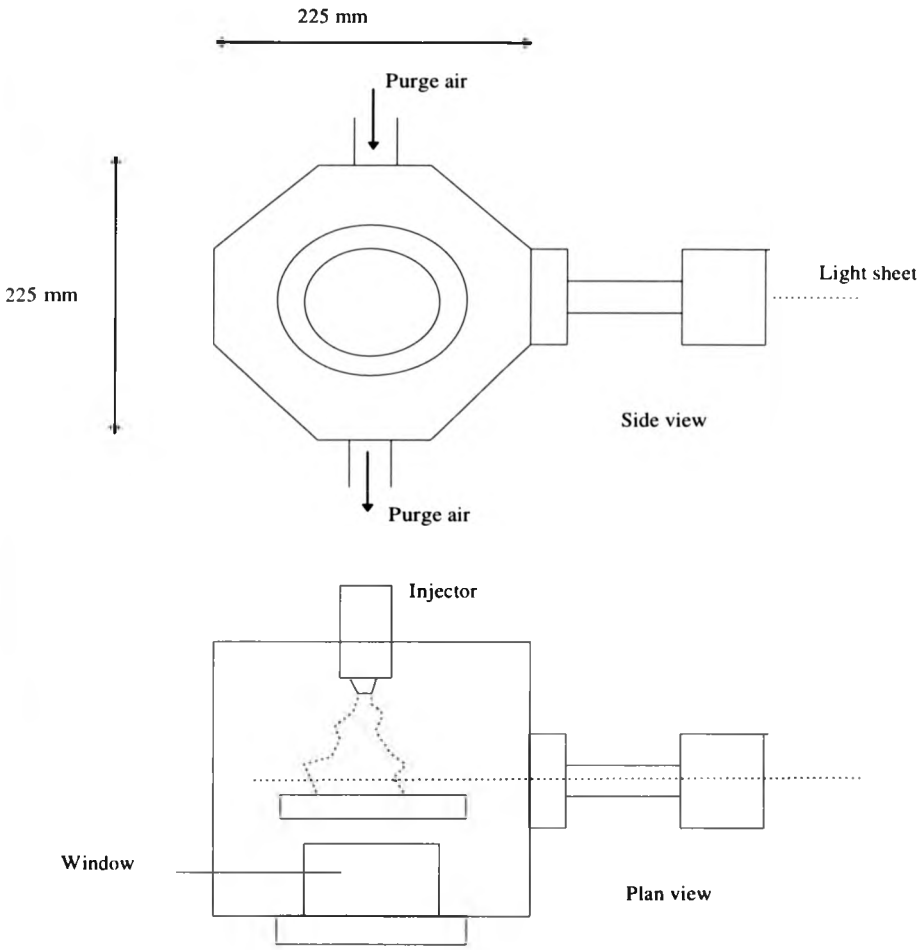

Figure 67. Schematic of the Harwell small HP cell configured for LSI

4.2.3 Cameras

Holographic camera

A holographic camera was constructed for convenient exposure under ambient background lighting. The camera consists of a 100 mm diameter electromagnetic leaf shutter linked to a 4x5" sprung-back via a flexible bellows (for isolation from any shutter vibration). The camera back accepted standard double backed plate holders into which the glass holographic plates were first inserted (in a darkroom). The plate holders could also accept cut film sheets. The fastest shutter speed was measured to be approximately 100 ms.

The shutter has a minimum fully open time of about 100 ms. Fogging of the film from ambient light was found to be negligible over this time period as a result of the slow holographic emulsions used. In practice, the camera was found to be very useful, allowing easy setup of the holographic optics, and convenient recording of plates.

High-speed camera

For high-speed imaging, a new design of drum camera was used. The Cordin LaserCam consists of a 0.32 m diameter hollow metal drum, mounted with its axis horizontal. A high-speed electric motor rotates the drum at up to 18000 rpm. A 1 m long strip of 35 mm photographic film is fixed so that it is pressed against the inside of the drum. A lens and mirror optical system transmits an image of the flow onto the film against the inside of the drum.

When the drum rotates, the camera acts in "streak-mode", with a linear film speed of up to 300 m/s. At this high rotation speed, the air inside the drum becomes very turbulent, causing mechanical instability, and damage to the film. To avoid this, the air is removed using a vacuum pump before recording an image sequence. The camera can then be run up to speed - this takes approximately 5 minutes.

If a copper vapour laser is used as the light source for the camera, it generates sharp images without any need for a rotating prism system as used in most high-speed cameras. The pulsed laser itself acts as the framing mechanism. This has several advantages - the image quality is higher, and the transmission optics are cheaper. The resolution of the camera is set by the 35 mm film used, and is therefore superior to a conventional 16 mm camera.

When the drum of the camera has reached the rotation speed, the mechanical camera shutter can be opened. The laser then produces a burst of pulses, synchronised to the shutter opening. The length of the pulse burst is set to exposure the film for exactly one revolution. At the end of the laser burst, the camera shutter is closed. This produces a sequence of around 28 full frame (or more reduced frame) images, which can then be processed as with conventional 35 mm cameras.

4.3 Study of the near nozzle region

Two types of LSI were used to view the near nozzle flow field. Normal LSI using a 532 nm NdYAG was used to visualise the position of fuel droplets in the spray through direct

scattering. Fluorescent LSI was then used to view the distribution of fuel droplets and any associated fuel vapour surrounding the spray.

4.3.1 "Normal" LSI

The injector was positioned to spray directly downwards. A plastic container was placed below the injector at a distance of approximately 300 mm to catch the issuing spray. It was found that a considerable quantity of the spray was reflected from the container back into the air. This was inconvenient as the delicate imaging camera (and its operator) were situated nearby. The diesel fuel mist and vapour were considered harmful if inhaled, and posed something of a fire risk. To minimise the level of fuel in the atmosphere, the container was lined with plastic foam. This acted to damp the impingement, ensuring the majority of the spray was captured by the container. An extraction fan and nozzle were used to remove the remaining fuel vapour. This combination was found to be entirely satisfactory when making a number of spaced, single shot injections. However, continuous injecting was not possible (or indeed necessary for these measurements) due to the extra spray generated.

The TIFOSI system was synchronised to the shutter contacts of the Nikon SLR camera. The electric motor and pump were run continuously, with the injector solenoid set to bypass normally. When an injection was commanded, the solenoid de-energised causing an injection. The time delay between the switch press and the actual injection event varied, depending on the position of the pump in its cycle. To overcome this, the camera was used as the master synchronisation with an open shutter period of 0.25 seconds, long enough to encompass any possible injection delay.

When the camera contacts closed, the TIFOSI fired. The pump shaft encoder of the TIFOSI was then used to trigger the NdYAG laser after a variable delay set by the TIFOSI controls. An interface unit was used to convert and buffer the 5V (TTL) output from the TIFOSI to the 15 V, higher current input of the laser. A delay of approximately 200 µs then occurred between the trigger and the emitted light pulse, as a result of the finite duration of the pumping flash lamp emission, and the consequent Q-switching delay. This laser delay was constant and was easily corrected for by minor adjustment of the main TIFOSI delay.

Using the pump shaft encoder as the trigger source for the laser was found to give a very repeatable illumination of the issuing spray. The trigger pulse delay could be varied while repeatedly injecting, allowing the full range of the injection event to be observed.

For all of the studies, the previously described Nikon FM2 SLR camera was used, with a 105 mm MikroNikkor macro lens. 100 or 400 ASA Kodacolor film was used to record the images, because automated colour film processing was readily available in the laboratory, and a short record-develop-view results cycle was necessary. Apertures in the range f/4 to f/11 were used, depending on the intensity of the scattered light.

4.3.2 Fluorescent LSI

The fluorescent LSI was performed in the same way as the normal LSI, but the NdYAG laser was converted to frequency tripled operation, giving 355 nm light. This wavelength was found to cause strong fuel fluorescence. The fluorescence was nevertheless considerably weaker than the previously measured direct scattered 532 nm light, and required a larger lens aperture.

Setting up of the experiment was considerably harder than before, as the UV laser light was invisible to the eye. To overcome this, a piece of white paper was used as a target to view the laser spot. It was found that the white dye in the paper fluoresced strongly, giving a highly visible blue spot and allowing the optics and injector to be aligned. A UV filter was placed over the camera lens to ensure that direct scattered UV light did not contribute to the film exposure.

4.4 Impingement visualisation

4.4.1 LSI

LSI was then applied to study the impingement of the spray against a glass surface. As before, injections under ambient temperatures and pressures were performed with illumination parallel to the axis of injection. Study was also made of injections under more realistic conditions in the high pressure cell described previously. Here the limited access and space inside the HP cell meant that cross-sectional sheet illumination was necessary.

Axial LSI

For the LSI study, converging and cylindrical lenses were used to produce a light sheet through selected cross-sections of the spray. The sheet thickness was estimated to be approximately 200 µm. The optical configuration is shown in Figure 68. A Nikon FM2 35 mm camera with a 105 mm MicroNikkor lens was used to record the scattering from the illuminated plane within the spray. Magnifications of up to approximately 1:1 could be obtained. Standard 100-400 ASA Kodacolor print film was used together with Kodak TMAX-400 ASA black and white film.

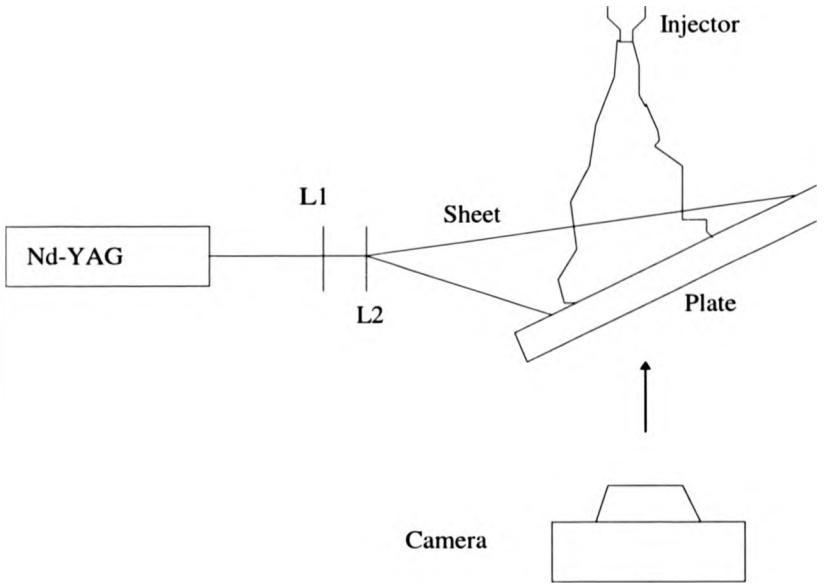

Figure 68. Optical configuration for the axial LSI of the diesel spray

A flat circular glass plate with a diameter of 120 mm was used as the impingement surface. Glass was chosen for the plate material as it transmitted the illuminating light sheet, thereby reducing scattering from the surface over the area of the impingement. The reduced extraneous scattering improved the quality of the LSI images obtained. The plate was mounted so that it could be adjusted to give different angles of impingement. The spray injector was set to spray directly downwards. The distance between injector and surface was

set to 50 mm. This distance is typical of injector/piston surface distances commonly found in automotive engines.

The quantity of spray scattered off the plate was found to be greatest in the direction of its tilt. The imaging camera, mounted nearby, but perpendicular to this direction did not therefore suffer greatly from diesel contamination. As a precaution however, a low cost glass filter (ultra-violet absorbing) was mounted on the front of the lens to protect its coatings from any possible damage.

Cross-sectional LSI

Cross sectional LSI was used to image the spray impingement in the high pressure cell. The limited space inside the cell meant that the injector had to be mounted horizontally. A steel adapter was made to replace one of the cell windows, and the injector attached through it. A glass plate was drilled with two mounting holes and fixed in a vertical plane, at a distance of 50 mm to the injector, and just inside the opposite cell window. The mounting holes and their associated bolts were sited so that they did not cast an appreciable shadow on the LSI image. A 35 mm camera was placed next to this window on its other side, viewing through the impingement plate.

The geometry of the high pressure cell meant that the optical path from the sheet optics to the injector was long, and the position of the sheet consequently very sensitive to the alignment of the pointing optics. It was also found to be very difficult to make fine and precise adjustment of the separation of the grazing or near grazing sheet to the impingement plate. Therefore a pair of Wollaston prisms were added at the end of the sequence of optical components. The optical configuration is shown in Figure 69. One of the prisms was mounted on a fine pitch translation stage, allowing fine adjustment of the separation of the prisms and thus the position of the light sheet relative to the glass plate.

In use, the prisms were found to allow easy and stable alignment of the light sheet. The sheet position was adjusted carefully so that the surface was just illuminated, giving a grazing light sheet.

Unwanted reflection of the light sheet within the cell was initially a problem. The polished steel surface, and confined volume acted to greatly reduce the contrast of the illuminated spray

against the background. The problem was solved by using a candle to deposit carbon black on the relevant surfaces. This coating was found to be sufficiently robust to survive the cloud of fuel droplets, but was easy to remove after the experiment was completed.

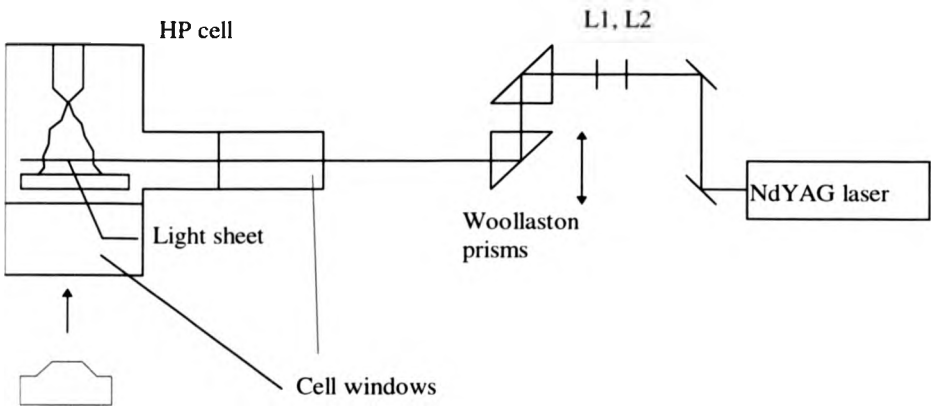

Figure 69. Optical configuration for the cross-sectional LSI of the diesel spray (plan view)

A flow of the pressurising gas was maintained through the HP cell during measurements. This was done to prevent a build up of fuel drops in the confined space of the cell interior, which would otherwise obscure the LSI images and reduce the contrast of the illuminated spray. Even so, it was found to be necessary to occasionally open the cell and clean the light sheet entry and camera imaging windows. This caused considerable inconvenience, as the cell had to then be re-pressurised and brought back up to operating temperature over a period of about one hour.

Another problem encountered was that the fairly thin glass impingement plate tended to break occasionally during measurements. The reason for this was thought to be stresses induced by the change in cell temperature, and consequent disparity in the coefficients of expansion of the metal and the glass. The problem was not considered significant as the plates were low cost, being made of standard window glass. However, the need to open the cell, replace the plate and then to re-pressurise meant that it was inconvenient. The problem was overcome by replacing the mounting bolts with spring loaded versions, which could accommodate small changes of position.

4.4.2 Holography

For the holography work, etalons and apertures were added to the NdYAG laser to improve the coherence length to approximately 40 cm. This was sufficient for the small size of the spray impingement. The laser pulse energy available was reduced then to approximately 30 mJ. Both in-line and off-axis optical configurations were employed.

A dielectric coated beam splitter was used to produce the two beams and concave lenses and mirrors were employed to form a collimated reference beam. The off-axis optical configuration is shown in Figure 70. The path lengths of the object and reference rays were matched to make best use of the available laser coherence. Ilford SP695 blue/green sensitive 4 x 5" high resolution photographic plates were used to record the holograms. Ilford specifications suggest a resolving power of approximately 5000 lines/mm.

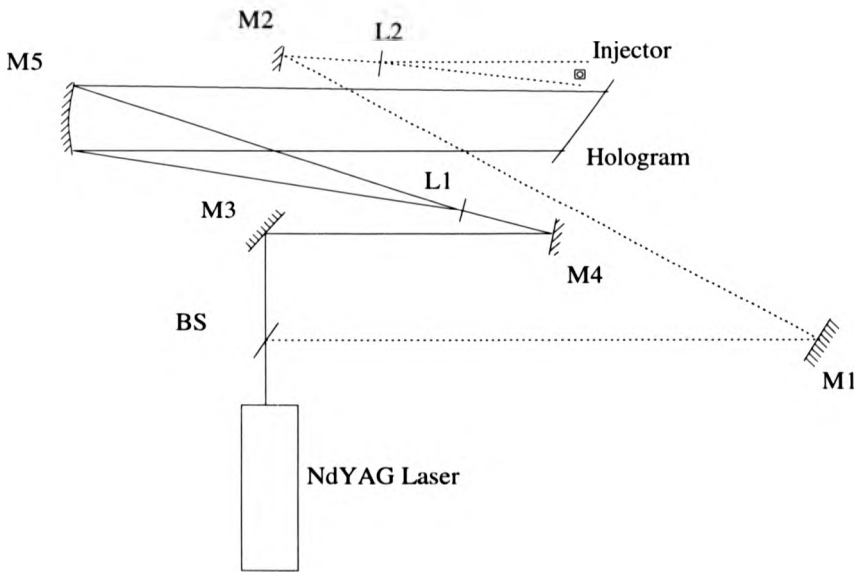

Figure 70. Off-axis holographic configuration for the diesel spray

Figure 71 shows a photograph of a reconstructed holographic image of the impingement. The object beam was concentrated on the lower part of the spray where it is interacting with the surface. A reflection of the spray in the glass plate surface can be seen. The film plate was

approximately 10 cm from the spray. The off-axis configuration was used, with a reference/object beam ratio of approximately four.

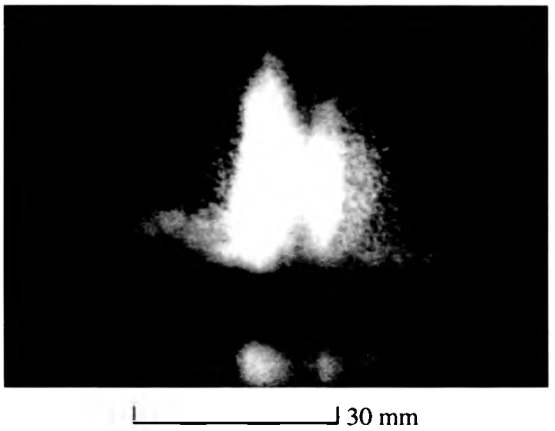

Figure 71. Reconstructed hologram of diesel spray impingement

In-line holograms were also taken, but the reconstructions were not very successful. Only the extreme edges of the spray were visible in the reconstructed image. This was because the high optical density of the spray significantly affected the reference beam. Indeed, a shadow of the spray was visible on the hologram plate.

The holographic reconstruction in Figure 71 shows the impingement clearly. A cloud of larger droplets surrounds the impingement, with smaller particles moving away parallel to the plate. The large particles were sized by using the image processor to count the number of pixels within the area of their focused image. Sizes in the range 30-100 microns were measured. The small particles moving horizontally were not resolved but the sizes were less than 10 microns. This resolution limitation could be overcome using a converging lens to magnify the image before recording the hologram, at the expense of a reduced field of view, and a reduced depth of field.

Fingers of spray are visible in the three dimensional image. The causes of this asymmetric structure are not fully understood but a link with a pulsed or banded structure visible within the main spray is thought likely. A likely cause of this behaviour is cavitation within the injector nozzle, although the reason for this is also unclear.

4.4.3 Backlighting

The main disadvantage of all of the studies described above is the lack of time resolution. The temporal evolution of the spray can certainly be studied, but only by looking at a number of discrete spray events. Ideally, a single spray event should be studied, with a temporal resolution fine enough to resolve its development. Only the copper-vapour laser offers a high enough framing rate. Unfortunately, the individual pulse energy (up to approximately 2 mJ) is insufficient for the 90° scattering required by LSI. Consequently, backlighting was used, with its more efficient use of light.

For the backlighting work, a fibre delivery system was used to expand the Cu-vapour laser beam to a diameter of approximately 30 cm. A white card was placed behind the fuel injector and positioned at 45 degrees to scatter the light into the camera. The optical configuration is shown in Figure 72. The large size of the expanded beam ensured that only the centre region was imaged, thereby improving the uniformity of the background. Lengths of Kodak TMAX-400 black and white film were used. The short coherence length (less than 5 cm) of the Cu-vapour laser ensured that speckle on the backlit screen was minimised.

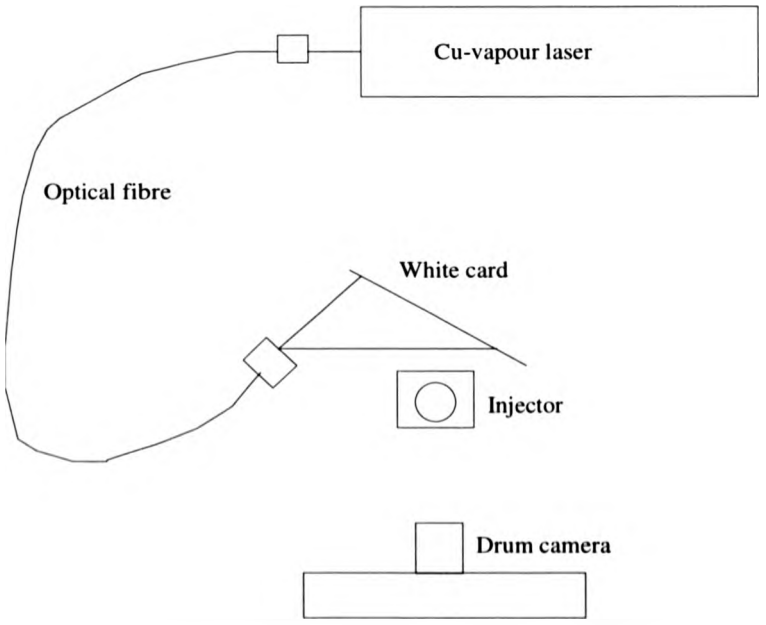

Figure 72. Optical configuration for backlighting the diesel spray

4.4.4 Impingement visualisation results

The LSI photographs reveal great detail in the impingement region. However, the fuel droplets are very small and the number density high such that individual droplets are difficult to resolve. Droplets around 20 μm and larger are resolved in these LSI photographs.

Figure 73 shows a vertical spray impinging onto a surface inclined at 30 degrees. A curl up vortex is clearly visible on the higher side of the slope. On the other side, the spray is moving across and away from the surface, and slowly diverging. The curl feature has been found to develop with time and increase in size in consecutive photographs as the injection timing is varied.

Figure 74 shows the impinging spray illuminated with UV laser light. The image shows the droplets in a light blue colour - the centre wavelength of the fuel fluorescence band. The edges of the structure are much more diffuse as a result of the vapour phase being excited in addition to the liquid. Further work is being done to resolve the different fluorescence characteristics of the two phases, thereby differentiating between them.

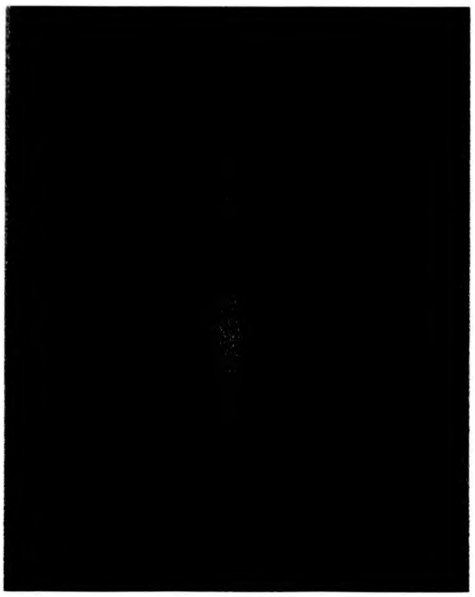

Figure 73. Diesel impingement onto surface inclined at 30 degrees

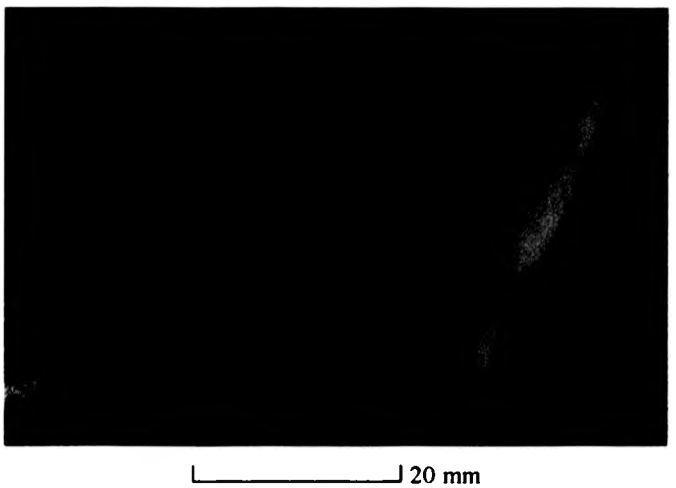

Figure 74. Diesel spray impingement illuminated with UV light sheet

Figure 75 (a), (b) and (c) shows the time evolution of a normally incident spray (130 μs, 300 μs and 1.1 ms after injection respectively), viewed through the glass plate. The light sheet was

positioned to graze the surface. A complex droplet distribution is visible. The small central disk shows the cross section of the incident spray before impact. Radial tracks can be seen together with a lip of fluid towards the edge of the larger impingement disk.

Figure 76 shows a sequence of backlit images with the spray impinging normally onto the surface. The field of view is such that only one half of the impingement is visible. The time separation between these images was approximately 60 μs.

The backlit images in Figure 76 show good correlation of features from one record to the next. This enables velocities to be easily determined. The image quality of the backlit film images was poorer than the LSI images, but considerable spray detail could still be observed. It was estimated that flow features greater than about 50 microns could be resolved.

The photographs were registered to give accurate frame-to-frame alignment and imaged onto a video camera, using the PIV film acquisition system described in Chapter 3. The registration could not be done conventionally using the sprocket holes of the 35 mm film, as the drum camera/laser framing mechanism did not use these. Instead, a reference mark within the picture was chosen, and each frame was manually aligned with respect to it. The video pictures were digitised and binarised to produce a black and white image. A simple search algorithm then located the tip of the spray. This was then repeated for the rest of the image sequence. The tip of the spray was measured to have a vertical velocity of approximately 250 m/s before impact. Previous frames indicated a deceleration from the nozzle exit. After impingement, the spray tip moved in a horizontal direction with a fairly constant speed of approximately 40 m/s.

The tip velocity for the illustrated sequence is plotted in Figure 77. Frame-to-frame timing uncertainty was estimated to be only a few tens of ns (resulting from copper vapour laser jitter), so the major unknowns in this velocity determination were thought to be in the location of the exact spray tip, and knowledge of the precise image magnification. Tip uncertainty was estimated to be smaller than 5 screen pixels (about 2 mm). A velocity accuracy of better than 5 % was estimated. The measured tip velocities compare well to PDA measurements of diesel spray impingement made by Coghe et al [19].

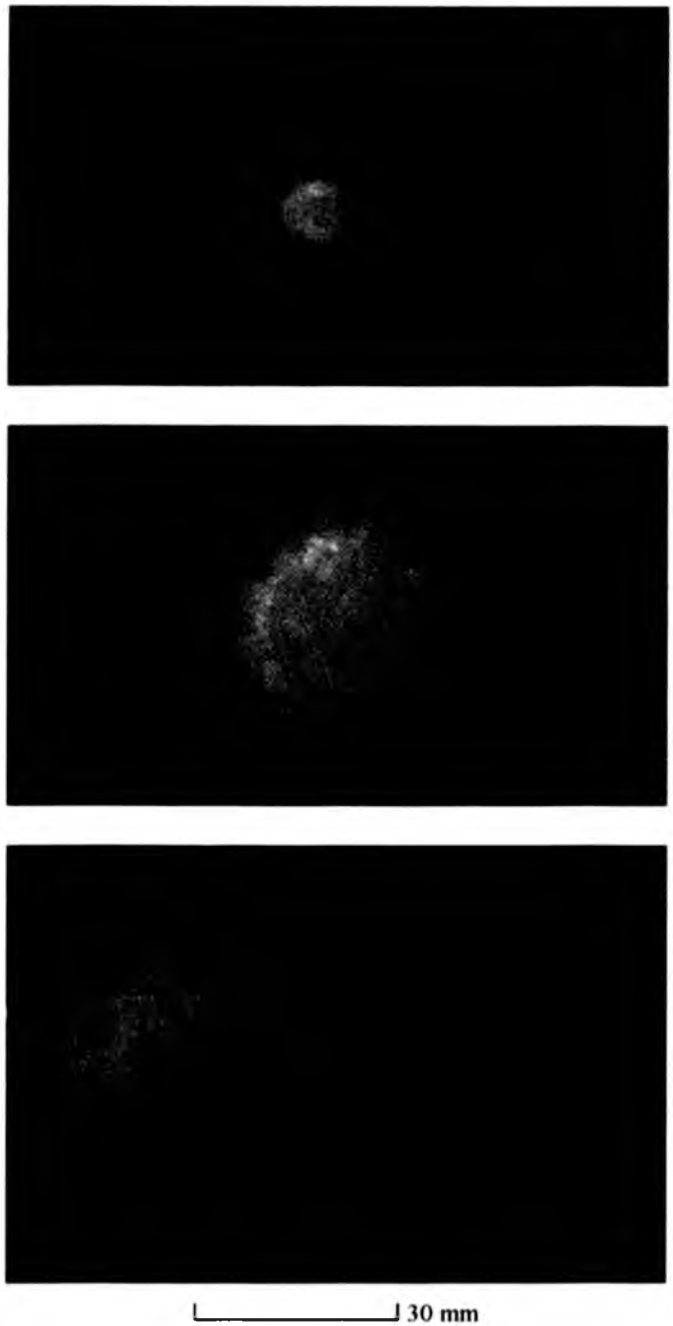

Figure 75 Time evolution of diesel spray impingement

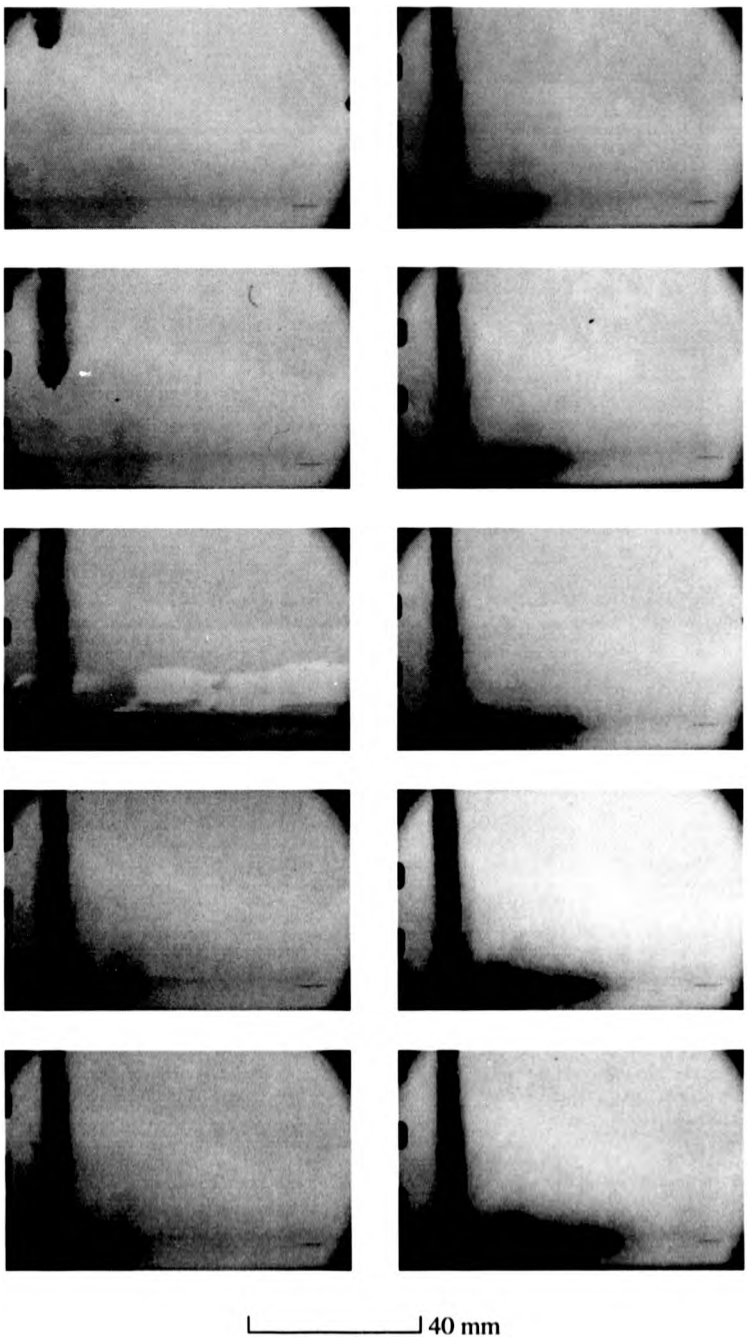

Figure 76. Sequence of backlit diesel spray impingement

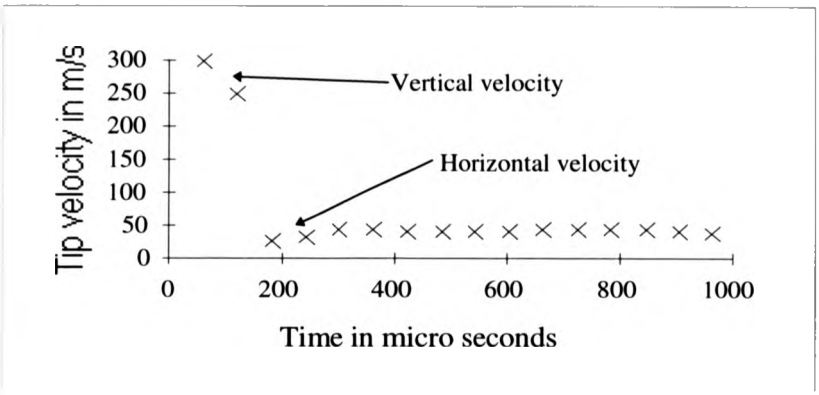

Figure 77. Graph of impinging diesel spray tip velocity against time

The jet model [9] mentioned in Chapter 1 seems to most closely describe the behaviour of the spray impinging normally onto the surface. The majority of the droplets shown in Figure 76 appear to move in a direction roughly tangential to the surface. However, a number of droplets do regain height from the surface. Thus the spray does not follow the jet model exactly, but is a hybrid with the other models. This is to be expected, as the computational impingement models are necessarily a simplification of the true behaviour.

Photographs of the spray footprint under conditions of 20 bar pressure and 206 °C are shown in Figure 78, Figure 79 and Figure 80 for early, middle, and late parts of the injection respectively. The light sheet was aligned to give grazing incidence. These and other photographs show an interesting wave-like annular structure. A small initial footprint is seen which expands to a diameter of about 10 mm at most. This is the cross-sectional area of the spray itself. After this, a concentric ring structure is seen with radial streaks of liquid or possibly dense droplets. This is assumed to be a vortex spreading out across the plate as the injection progresses. It is also clear that the impinging film is far from uniform, with some areas having what appears to be a thick film, and some areas having no film at all. This accentuates the problem of where to measure the film thickness when using a point measurement technique such as the length of line approach.

Representative cross-sectional images recorded in the HP cell were measured to give the diameter of the footprint for a number of cell temperatures and pressures. The footprints are plotted against time (crank angle degrees) in the graph of Figure 81.

The graph shows that the dominant parameter affecting the spray penetration is pressure. As the cell pressure increases, so the spray penetration and hence the footprint reduces rapidly. However, at a constant pressure , changing the temperature of the cell atmosphere appears to make very little difference. This pressure dependence of the footprint diameter can be explained by the change in atmospheric resistance seen by the spray as it emerges from the injector nozzle. This causes retardation of the spray at high pressure.

The Wollaston prisms were then adjusted to move the light sheet position away from the impingement surface and further photographs were taken for separations of 2 and 4 mm. To investigate the footprint at the different separations, the diameter of the spray was again measured from the photographs. The footprint graph is shown in Figure 82.

By studying the graph, it is clear that under atmospheric conditions, the spray footprint is largest at the plate surface and then decreases away from the plate. However, at 20 bar and 200 °C this phenomenon appears to be reversed. That is, the spray footprint is larger 4 mm away from the plate than at the plate surface. One possible explanation for this would be the existence of a vortex at the edge of the footprint with a radius of 4 mm or greater. The best way to confirm this would be to make axial LSI measurements within the HP cell. Unfortunately, as previously explained, the geometry of the cell precludes this. However, the previous axial LSI photographs taken in open atmosphere do indeed show a vortex feature in the impingement cloud.

4.5 Film thickness measurement

When the film thickness measurement program was started, the thickness of a typical diesel spray impingement film was uncertain. A simple model for the film measurements was constructed, consisting of a horizontal aluminium channel down which liquid could flow. The channel could be blocked to enable different static thickness layers of liquid to be set up.

Chapter 1 describes a variety of techniques available for film thickness measurements. Optical film thickness techniques were chosen for these studies due to their non-intrusive nature. They also have the potential for high temporal and spatial resolution.

Figure 78. Early diesel spray footprint, 131.6 CAD, 20 Bar, 206 °C

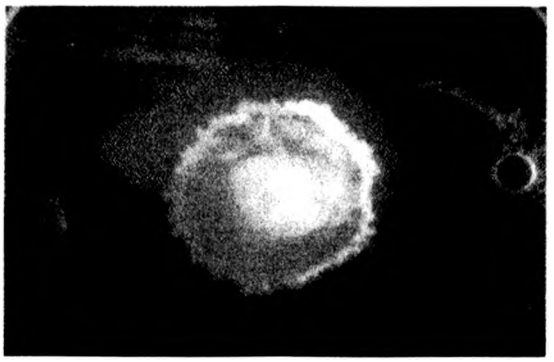

Figure 79. Middle diesel spray footprint, 133.5 CAD, 20 Bar, 206 °C

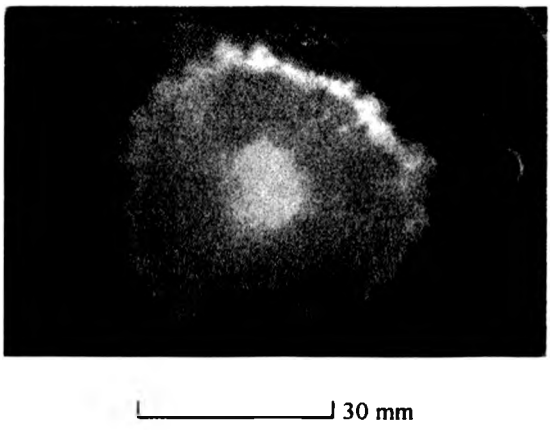

Figure 80. Late diesel spray footprint, 134.7 CAD, 20 Bar, 206 °C

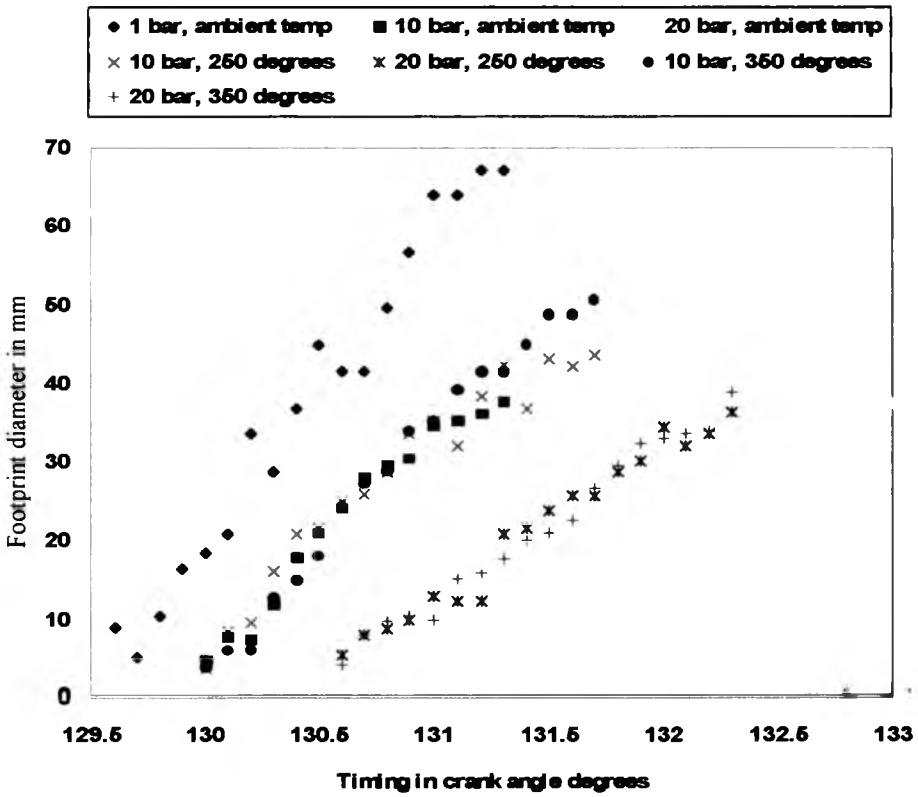

Figure 81. LSI footprint diameter against time for different HP cell conditions

The LIF techniques previously described assume that fluorescence intensity is only dependent on film thickness. However, in practice, laser induced fluorescence is also dependent on temperature. This temperature dependence is studied in the next section.

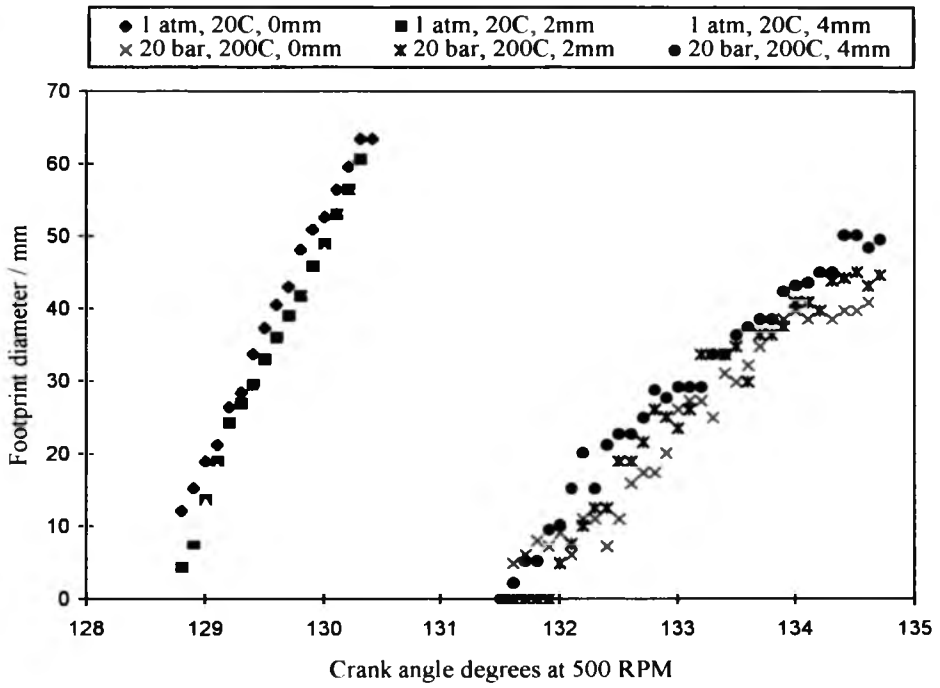

Figure 82 LSI footprint diameter against time for different HP cell conditions

4.5.1 Fluorescence behaviour of the model fuel

In a real diesel fuel, the presence of aromatic compounds provides a strong fluorescence. In the model fuel, the absence of these compounds means that laser induced fluorescence is weak. To increase the fluorescence response, Bis-MSB dye was added to the model fuel. This laser dye (p-Bis (o-methylstyryl)-benzene) gives a peak fluorescence at approximately 420 nm when excited at 355 nm [81]. For all studies, the dye was used at a concentration of 0.00296 mol/l. This was found to give a strong fluorescent response.

The fluorescence spectra and temperature response of laser induced fluorescence for the model fuel/Bis-MSB mixture was studied [82]. A sample of the fuel was transferred to a silica ampule which was sealed and placed into a 100 mm diameter furnace tube. A pulsed NdYAG beam, frequency tripled to 355 nm, operating at 10 Hz and providing a pulse energy of 0.4 mJ was passed through a bulk sample of the fuel. The dye exhibited good fluorescence but only minimal attenuation and therefore linear behaviour. Spectra were recorded as an

average over 100 laser pulses, that is over a 10 second period, at selected temperatures whilst the furnace was being heated. The heating rate of the furnace was about 1 °C/minute so that temperature variation of the sample during spectrum acquisition was negligible. All spectra were recorded using the detector on fixed gain.

Figure 83 shows spectra recorded at 100 - 150 °C. Peak fluorescence was found to be at around 420 nm. Figure 84 shows the temperature dependence of spectrum amplitude at 420 nm. As can be seen, there is a clear temperature effect, with the fluorescence intensity in general reducing with increasing temperature. Unfortunately, the intensity does not return to the previous ambient level upon subsequent cooling; this almost undoubtedly being the result of breakdown of the dye by the heating.

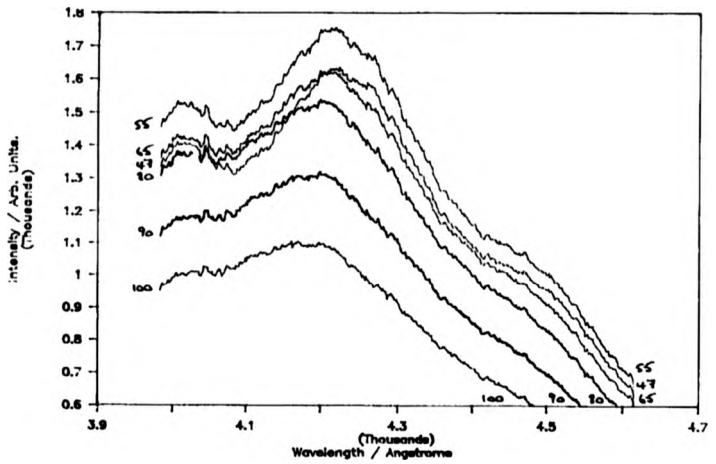

Figure 83. Diesel fuel UV laser induced fluorescence spectra

The basic LIF film thickness technique will thus give misleading results when surface temperature gradients exist, as the LIF intensity measured can vary due to changes in either temperature or thickness.

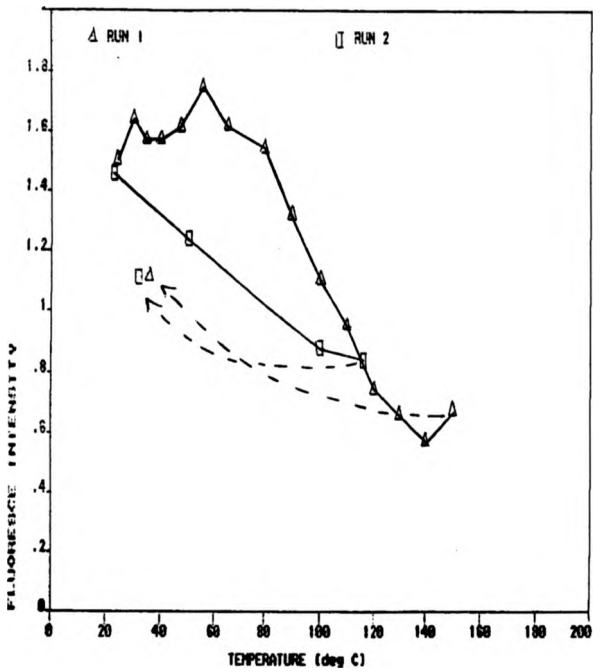

Figure 84. Temperature dependence of laser induced fluorescence spectrum

Length of line LIF film thickness measurement

A technique was proposed to overcome the temperature dependence of the fluorescence, by a modification to the LIF technique. This modification is to measure the actual length of the fluorescing path of the laser beam through the liquid rather than simply its intensity. The length of this path is clearly proportional to the film thickness. The intensity of the fluorescence is not important, so the technique should be unaffected by temperature. This technique is known as the "length of line" technique. The optical system was designed and optimised by a number of workers at Harwell [83]. A schematic of the optics is shown in Figure 85. The optical system images the fluorescing line onto a 512 pixel linear CCD sensor, which produces an analogue output signal. The processing system developed to yield film thickness data from CCD camera output is described briefly below.

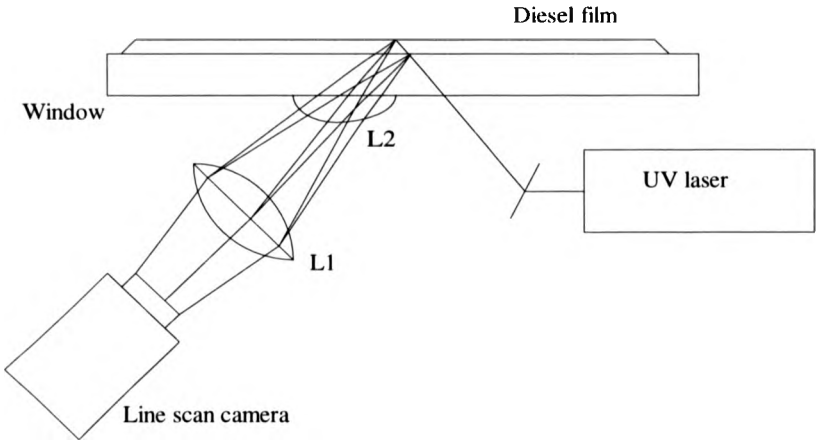

Figure 85. Schematic of "length of line" film thickness measurement technique

The linear CCD output took the form of a signal peak of variable width, representing the line length (and thus film thickness). The data rate of the signal was 10 MHz, giving a scan rate (and hence film thickness measurement) of up to approximately 19 kHz. This signal was input into a Yogagawa digital oscilloscope with a storage capacity of 1 MB and a maximum sampling rate of 100 MHz. A 386 PC was connected to the oscilloscope via a GPIB interface. MS-Windows based software (GraphIt) was written to acquire the signal, and process it to yield line length. A simple algorithm was written to measure the width of the signal peak above a specified threshold value.

The system was calibrated with diesel films of known thickness. A number of approaches were tried to generate films of a known repeatable thickness. The technique finally adopted was to attach a micrometer to the plate and trap a small amount of diesel between the silica surface and the micrometer plate. The micrometer enabled thicknesses down to 20 µm to be defined.

In use, the system proved capable of resolving changes in film thickness over the period of the impingement. Figure 86 shows typical output from the program, recording a room temperature impingement in the high pressure cell (20 bar). The data show that the initial film build up is very rapid, almost a step function - however the thickness never exceeds 30 µm. This was below the 30 µm resolution limit measured for the optical system (using a ruled glass slide), so absolute thickness data was unreliable.

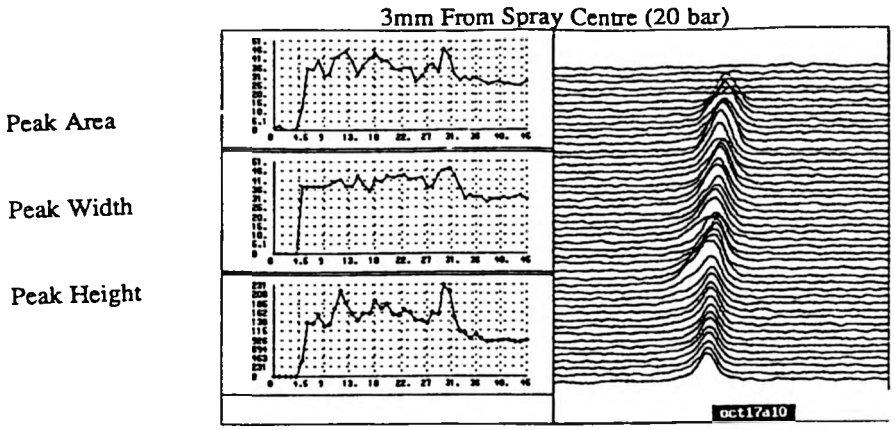

Figure 86. GraphIt program output

The length of line technique was found to be rather difficult to set up, owing to the need for precise focusing and alignment. The system also proved not to be sensitive enough for measuring the films actually encountered. The TIR technique was thus developed to overcome these problems.

TIR experimental procedure

The theory behind the technique is described in Chapter 2. Transmission of ultra-violet light is poor through normal glass. A special optical plate was therefore designed and manufactured from fused silica to ensure good transmission of the UV. The geometry of the plate was computed to give illumination across a large surface area, with an incident angle slightly greater than the critical angle. A schematic of this plate is shown in Figure 87. In considering its design, the refractive index of diesel fuel was taken to be 1.41.

A frequency tripled NdYAG pulsed laser was used to generate the UV illumination. The laser produced 10 mJ pulses of 355 nm light, with a pulse duration of 15 ns. The maximum pulse repetition rate was 40 Hz, although used here for single pulses. The laser was expanded using negative cylindrical and spherical lenses to form an approximately collimated beam of dimensions 7 x 2 cm. The beam then entered the angled end facet of the plate.

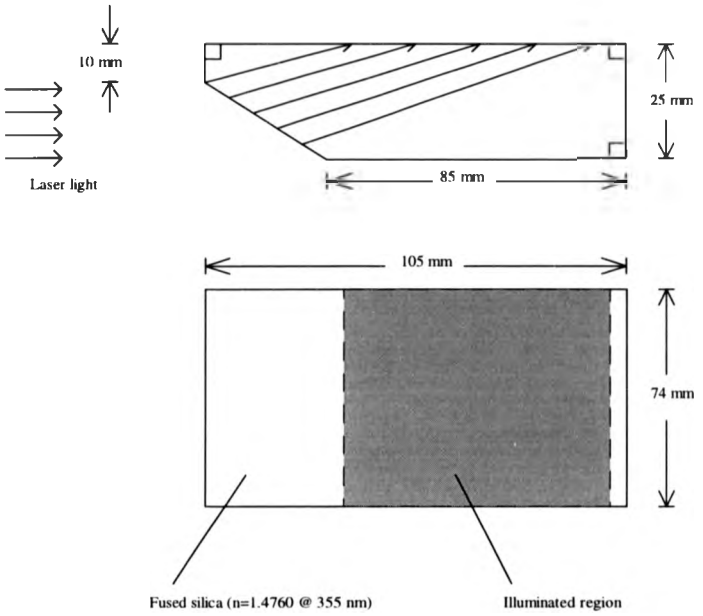

Figure 87. Schematic of TIR impingement plate

A high resolution CCD camera (768 x 576 pixels) was used with a 16 mm lens (and 2 mm extension ring) to view through the plate. The video signal was passed to a PC-based image processing system and thus displayed. The electronic gain of the camera was fixed so that screen pixel intensity was proportional to original image intensity.

A single hole diesel injector (0.25 mm nozzle diameter) was mounted horizontally and as before, positioned 50 mm from the surface of the vertically held plate. The injector was connected to a diesel pump capable of reaching a pressure of 2000 bar. A solenoid valve was used in conjunction with the TIFOSI electronic control system to allow single injections.

The TIFOSI system was used to synchronise the injection with the laser and image processing systems. This enabled a single video frame of a single injection event to be acquired. This was then saved on the computer hard disk as a 256 grey-level TIFF (tagged image file format) file. The experimental apparatus is shown in schematic in Figure 88.

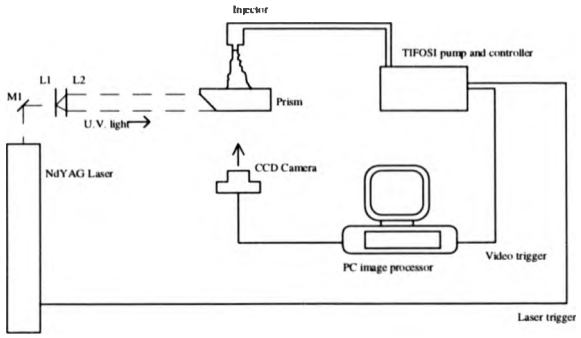

Figure 88. Schematic of TIR experiment

TIR calibration tests

The measurement system was first calibrated using known thicknesses of diesel fuel. As before, a micrometer was used to measure the calibration films.

Data were taken of various thicknesses of film from 10 - 300 microns. The camera aperture was adjusted to ensure the video image was not saturated. Four measurements were recorded for each film thickness to allow any laser shot-to-shot fluctuation to be averaged.

Captured images were analysed for their average intensity across the micrometer plate area. This was then normalised taking account of the camera aperture. Pixel intensity is plotted against film thickness in Figure 89. An exponential best fit line is shown, with the data demonstrating good agreement with what is expected from applying Beer's law as explained below.

The intensity of light passing through an absorbing liquid film can be expected to obey Beer's law:

$$I = I_0 e^{-kx} \tag{44}$$

where I is the intensity of the laser light passing through the absorbing liquid film, I_0 is the incident intensity, x is the distance travelled into the film, and k is an absorption constant.

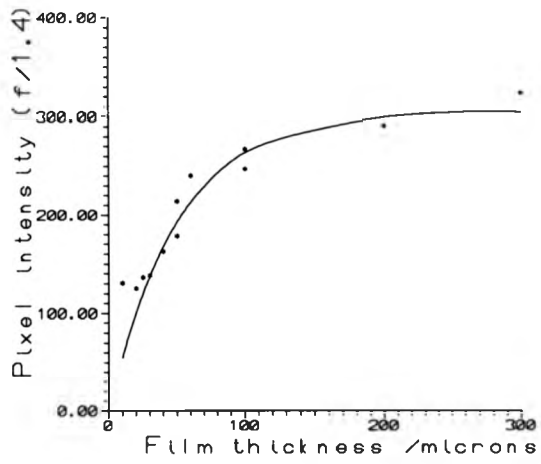

Figure 89. Graph of TIR pixel intensity against mechanically measured film thickness

If the fluorescence intensity at a point is proportional to the laser intensity, then the total fluorescence F from an illuminated line of length z is:

$$F = \int_0^z I.dx = \frac{I_0(1-\exp(-kz))}{k} \qquad (45)$$

Thus an exponential relationship between fluorescence intensity and film thickness is expected, and this appears to be confirmed by the calibration data with the best fit line giving I_0=6.1x10^6 pixel grey levels and k=20000 m^{-1}. It can be noted that the absorption constant for the laser light is very high with a consequent significant tail off in measurement accuracy for thick films. Only small increases in intensity occur for films thicker than approximately 100 microns. This strong absorption is confirmed by previous work.

TIR measurements and results

The imaging system was set up to be fully automatic in operation. The only operator involvement was the initial injection trigger. Four images were recorded at each of a number of delays between injection and laser trigger. A large quantity of image data (40 MB with 0.25 MB per image) was thus saved to disk. The plate surface was wiped clear after each injection - this removed virtually all of the adhering film and any remaining was not detected by the camera. The period of time around the onset of impingement was studied in greatest detail

(time resolution of 0.2 crank angle degrees (CAD)), although images were recorded for as late as 170 CAD after impingement. All measurements were made with the pump operating at 500 rpm and set for a delivery of 20 mm^3 of fuel each injection. Note that 1 CAD ≡ 333 μs at 500 rpm.

The laboratory lights were dimmed while collecting data. This prevented background light from causing spurious image features. The camera had an electronic shutter which would normally have been used to eliminate stray light, except that it has the effect of switching the image acquisition to field mode (half the vertical resolution of frame mode) and was therefore not used in this way.

Good quality images were obtained for all the injections measured. The images shown in Figure 90 - Figure 95 are video prints of the TIFF image files for times t = 0, 130, 400, 600, 1500 and 9800 μs (about 30 CAD) from initial impingement. This thickness data is derived from the calibration curve shown in Figure 89, using the best fit values for I_0 and k. Intensity information was extracted from Figure 93 using a coarse image sampling grid (averaging over 20 x 20 pixel blocks), and is presented as a film thickness graph in Figure 96.

Absolute accuracy of this thickness data is difficult to determine, due to the difficulty of calibrating the technique to known very thin films. The TIR data gives similar values to those from the capacitance technique [20], with films in the range 5-20 μm measured.

From Figure 90 - Figure 95 it can be seen that the size of the "footprint" does not increase in size significantly with time after impingement. The footprint diameter increases rapidly just after the onset of impingement and then grows slowly. This is in contrast to LSI footprint measurements which show a steadily increasing diameter with time. For comparison, a typical LSI footprint image in shown in Figure 97. The structure of the TIR footprint is much simpler than for the LSI images, with no droplets or rings evident. The difference between the results of LSI and TIR is due to the ability of the TIR technique to image the film alone, whereas LSI reveals all near surface fuel, whether film or droplets close to the surface. This makes it a superior technique for film thickness visualisation and measurement.

Figure 90. TIR image of impingement film for t=0 μs

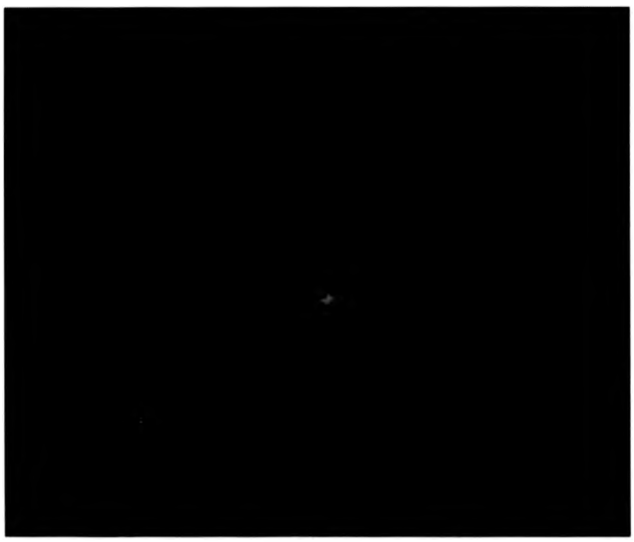

Figure 91. TIR image of impingement film for t=130 μs

20 mm

Figure 92. TIR image of impingement film for t=400 μs

Figure 93. TIR image of impingement film for t=600 μs

20 mm

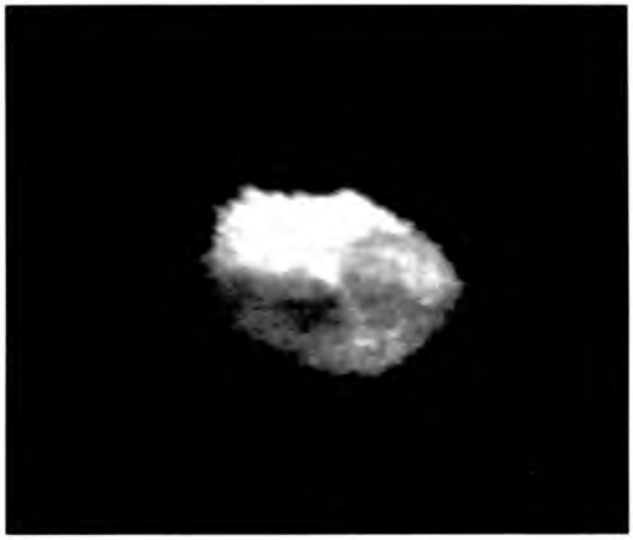

Figure 94. TIR image of impingement film for t=1500 μs

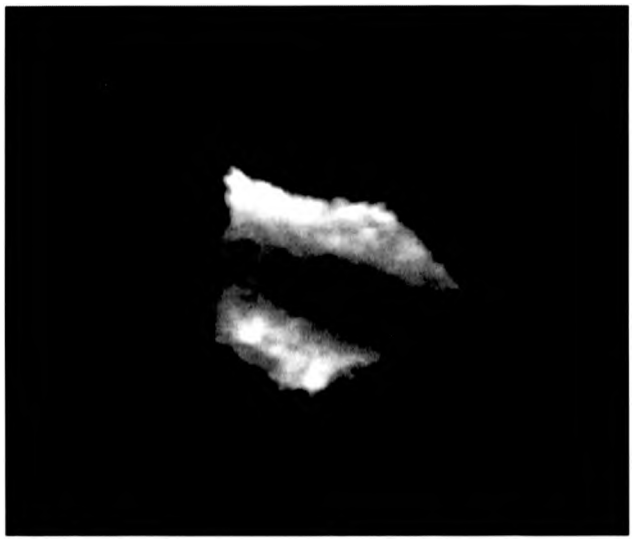

Figure 95. TIR image of impingement film for t=9800 μs

20 mm

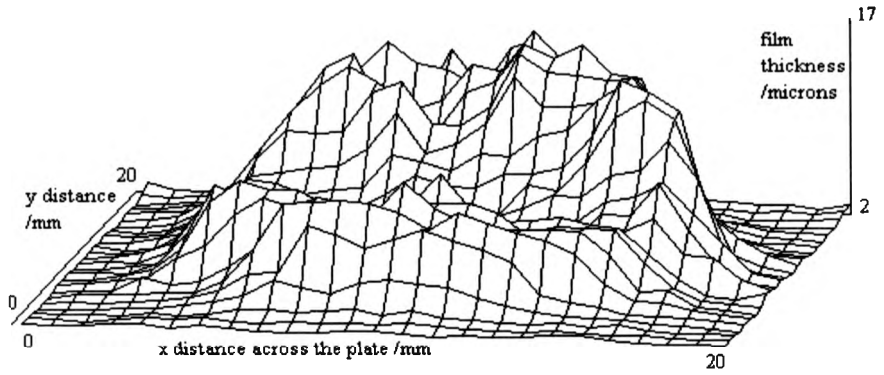

Figure 96. Graph of film TIR thickness at t=600 μs

Discussion of TIR results

From the limited TIR results gained so far, it appears that the conical spray, on hitting the plate, immediately produces a small circular footprint with a size equal to the spray cross-section. The majority of the spray then rebounds and an expanding cloud of droplets is produced. Small quantities of liquid remain attached to the surface and cause the film footprint to grow slowly, until the end of the injection. The film then disperses gradually under gravity over a period of many seconds.

The quality of the data could be improved using delay timing direct from a needle lift sensor or by detecting the first emergence of the spray from the injector. This would improve the repeatability of the injection time and reduce any shot to shot variation. Also, improving the time resolution of the measurements at the onset of injection to 0.1 CAD or better would be useful in investigating the development of the film.

The spatial resolution gained using the CCD camera to capture images was fairly limited. Perhaps detailed structure exists within the film, but this would only be revealed by higher magnification and/or moving to photographic film as a means of recording data. A higher magnification would lose the advantage of measuring the entire footprint at one time, while photographic recording would reduce the convenience of the rapid results provided by the video. Similarly, the current method does not allow the temporal development of the film resulting from an individual injection to be investigated. This would demand the use of high

speed photography synchronised with a high repetition rate laser - it is possible but requires further development.

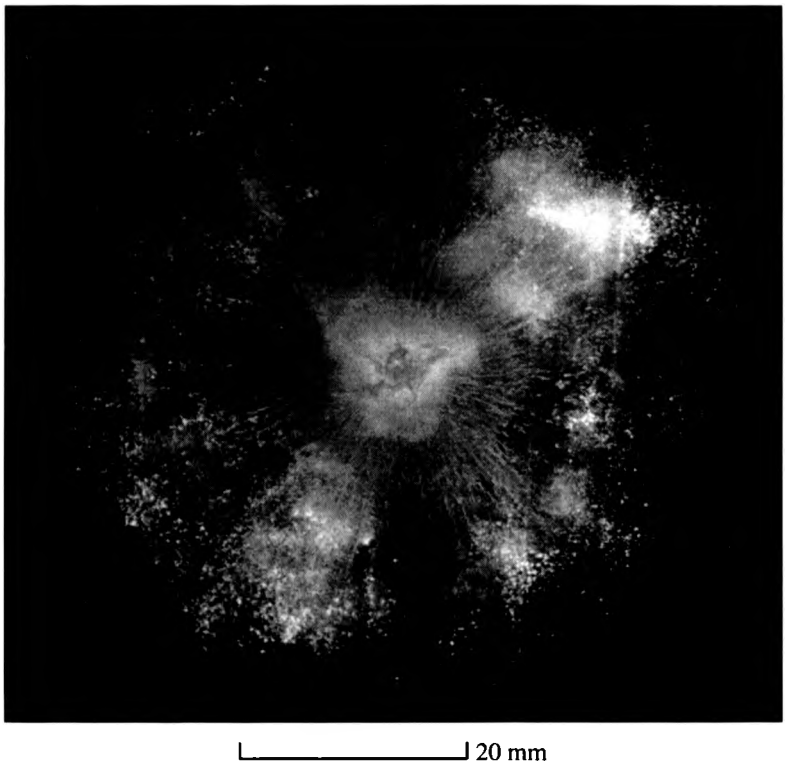

Figure 97. Typical LSI diesel spray impingement image

It is also possible that, with careful design of optical windows and imaging optics, the TIR technique could be employed with more realistic wall geometries than just the flat wall described in this report. Studies within high temperature high pressure environments should be relatively easy compared to the requirements of measurement techniques previously designed and employed in such environments.

The standard UK-sourced diesel fuel used was found to be highly suitable for the measurement of the thin films typically produced, with strong fluorescence and appreciable absorption within a few tens of µm's. Dilution of this diesel with a less fluorescent fuel, or use of a model fuel, may aid calibration of the technique considerably. A less absorbing fuel would also allow much thicker films to be investigated with the same technique.

TIR conclusions

Global diesel film visualisation and thickness data have been obtained using a novel technique based on total internal reflection of light at a glass/air boundary when in the absence of a film and transmission in one's presence. Fluorescence from the diesel film produced from illumination by UV radiation reveals the whole of the spray 'footprint' in contact with a wall. The technique additionally ensures that *only* fuel in contact with the wall is measured. Calibration of the fluorescence intensity is straightforward and enables relatively accurate fully quantitative measurement of film thickness across the entire footprint.

Data have been acquired for a single nozzle injector placed 50 mm from a wall and impinging normally for several different time delays from initial impingement through to well after the injection. Excellent results were achieved which identify the potential for accurate thickness measurement over the entire film. Following calibration against films of known thickness, two-dimensional maps have been generated which identify typical film thickness less than 20 μm, in good agreement with work previously undertaken using other techniques.

4.6 Conclusions on measuring diesel sprays

The LSI results clearly provide considerable information on the global behaviour of the spray near the surface. This information is useful in its own right and also for characterising the flow for possible further investigation by point measurement techniques. The footprint LSI images reveal the complexity of the impingement structure.

The holographic technique stores much greater information about the spray, including droplet size and velocity information. It is particularly useful for studying complex flow structure which cannot be adequately recorded by a planar technique.

The backlighting technique provides the ability to see the full temporal evolution of a single spray event. The others can only capture the spray at an instant in time, and require multiple injections to be studied at different delays for the spray development to be recorded. The backlit image sequence of the spray impingement seems to suggest that the jet impingement model bears the most close resemblance to physical reality.

The techniques provide useful flow visualisation and in conjunction with image processing can provide valuable quantitative data. The techniques described offer convenient and robust

diagnostics in this difficult flow application, and offer the possibility of measurements under realistic high pressure and temperature conditions, such as those found in a real engine.

The TIR technique shows great promise as a new and powerful method for analysing liquid films, able to characterise films rapidly and quantitatively. The technique also provides the opportunity, with relatively little in the way of further development, to measure the temporal development of diesel films (via rapid recording techniques) and to investigate the fine spatial structure and behaviour of such films.

As yet, only a basic experimental feasibility study of the TIR technique has been undertaken. The initial results are excellent, yet there are still several improvements which are able, and which are advised, to be made prior to its use for detailed diesel film investigations. These improvements concern calibration and spatial resolution of the technique, together with some attention to the injection timing. The amount of work involved with these is small. Further improvements to the accuracy and temporal resolution of the measurement may then wish to be considered, as well as adaptation of the technique to more realistic wall geometries. The latter are optional and will all involve additional development.

The TIR technique has already provided valuable, whole-field, quantitative film thickness data which agrees well with the necessarily limited data obtained by electrical measurements, and has been used to optimise the design and validate the output of a capacitance based *in-situ* engine cylinder diesel film thickness instrument [20] now undergoing trials.

5. Global Diagnostics Applied to Coal Furnaces

5.1 Optimisation of techniques for measurement in coal furnaces

This chapter discusses global optical methods developed to study coal combustion, and charts their application to a number of coal furnaces, increasing in size from laboratory to semi-industrial scale and the consequent difficulties encountered in making the optical measurements.

The main problems with using global optical techniques such as LSI for the study of industrial coal furnaces are the high combustion luminosity, the high particle loadings, and the lack of good optical access in many facilities. Consequently, optical measurements in coal furnaces have proved to be difficult - Baker et al [84] attempted to use LDA for measurements in a 2 m square furnace, but results were disappointing, probably due to the relatively unsophisticated optical and signal processing systems available at the time. For several years following this, no similar work was reported. Recently however, improvements in measurement technology (primarily improved LDA signal processing) have begun to make measurements feasible, and accounts of several successful applications of LDA to coal flames have been published [85] [86].

Point measurement techniques such as LDA are generally the most suitable for the hostile environment of a coal furnace, due to their high noise immunity. However, they are somewhat inflexible in use, requiring long acquisition times, while maintaining an expensive to run furnace facility at constant flow conditions. There is a need for more global, imaging based techniques such as LSI, to enable rapid characterisation of a particular furnace configuration, and evaluation of several running conditions in a short space of time.

LSI and laser backlighting are applied here to several furnaces of different sizes, and the resulting problems and limitations explored. Prior to the measurements described here, very little (if any) application of global techniques such as LSI to coal furnaces has been made. As previously described, Trolinger et al [39] applied holography to the study of individual coal particles. The shape and size of the particles was recorded at different stages through their combustion. However, the technique was applied to study a small volume (approx 8 cm^3) of a small flat-flame laboratory burner at close range. In larger furnaces, the larger working

distances and much stronger refractive index gradients would make the technique unfeasible. It was thus decided to concentrate on LSI, a more robust technique in this harsh environment. Much of the described work was of an exploratory nature, moving on to the next step once problems had been solved.

5.1.1 Coal fuel properties

Coal is predominantly carbon, with a variable percentage of other materials, such as sulphur. The precise chemical composition varies with geographical origin [87]. Grimethorpe coal, used for many of the measurements described here, has been assayed and its chemical composition is shown in Table 3.

Moisture	% air-dry	3.6
Volatile matter	% dry	32.8
Ash	% dry	10.3
Total carbon	% dry	75.1
Total hydrogen	% dry	4.6
Total sulphur	% dry	1.73
Total chlorine	% dry	0.21
Gross calorific value	kJ/kg	30380

Table 3. Chemical composition of Grimethorpe coal

The coal fragments produced by the milling process typically have a wide size distribution, with a range of around 1 - 100 microns. The crystalline nature of coal means that the particles cleave to give flat surfaces. Thus the pulverised particles are often faceted and thus highly non-spherical.

Optically, coal is black and rough, with a low reflectance and a high absorption across the visible wavelength range. Faceted coal particles can produce specular reflections, yielding unpredictable scattering.

5.1.2 Optical problems in coal furnaces

Combustion luminosity

Combustion luminosity is a significant problem when attempting to use imaging techniques such as LSI and backlighting. In the visible spectral region, coal flame luminosity is comprised primarily of chemiluminescent emissions and the grey/blackbody continuum from coal and other particulates[88], with the latter tending to dominate. A camera imaging the flow has to be able to differentiate the laser light scattered from the flow particles from the background light resulting from combustion. This problem increases rapidly as the size and consequent power of the coal burner increases.

Two main approaches were used to reduce the effect of combustion luminosity on imaging techniques, so as to improve the contrast of laser scatter against the background. The first is to reduce the exposure time of the imaging sensor. Clearly, the quantity of luminosity recorded is integrated with time, thus giving a linear relationship between combustion image intensity and exposure time. However, if the laser illumination is continuous, reducing the exposure time reduces the laser image intensity recorded as well, thus having no effect on image contrast. If instead a pulsed laser is used - the exposure duration can be reduced considerably: a typical Q-switched laser has a pulse duration of the order of a few nano seconds.

The second technique is to exploit the monochromatic nature of laser illumination. Combustion luminosity is blackbody radiation from incandescent coal particles, and its energy is thus spread across a wide wavelength range. It's effect can thus be reduced by using a narrow bandpass filter centred on the laser wavelength. This blocks most of the combustion radiation, while absorbing little of the laser light.

As discussed earlier, combustion luminosity has significant components in the visible and near infra red regions and unfortunately video and photographic cameras have high sensitivity in these spectral regions.

Particle loading

In the burner quarl (area around the mouth of the burner) region, the coal particle loading is high. In fact, in the immediate vicinity of the injection gun, the flow has to be considered to be two-phase, with the coal a significant volume fraction of the inlet air. This high density of

particle loading poses problems for optical techniques. The black coal particles readily absorb illuminating laser light, and light is also lost from scattering in directions away from the required direction. When the particle loading is sufficiently high, multiple scattering occurs - this is where light scattered from one particle then goes on to scatter off further particles.

Successful application of light sheet illumination relies on a low probability of particle scattering, so that individual photons scatter off one particle at most. If a light sheet is set up to illuminate a plane along the centre line of the furnace, the high particle density attenuates the illuminating laser beam before it reaches the measurement region. The light sheet is then likely to have a reduced intensity, with possible intensity variations along its length as a result of non-uniform particle concentration.

The obvious way to combat attenuation by the particle field is to use higher laser power, so that a significant intensity is present in the sheet. However, there is a limit to the laser power that can be applied - above a certain level, light absorption will cause breakdown/ignition of the highly combustible coal particles to occur, thereby removing the non-intrusive nature of the laser illumination. This laser induced particle breakdown has been observed when using similar, although more highly focused, pulsed laser beams for CARS thermometry in coal furnaces [89].

If the particle density is high within the illuminated plane, absorption and excessive scattering can occur there also. This has the effect of particles throwing shadows onto other particles in the sheet region, see Figure 98.

Finally, if there is a high particle density between the light sheet and the imaging camera, the image of the flow itself will be obscured.

Optical access

Obviously, any laser based flow diagnostic requires optical access to be available in the furnace geometry. In many furnaces, this is the main barrier to using these diagnostics. Most furnaces are built with a thick layer of refractory bricks, to insulate the furnace, and reflect radiation back into the interior to support further combustion. Point measurement techniques, particularly back-scatter LDA, have an advantage here over imaging techniques in the degree of optical access required. Even so, measurements are generally restricted to furnaces

modified to allow optical diagnostics, with the exception of the LDA study described by Ereaut and Gover [90] in a normally running 2 GW coal fired power station. However, this is not usually a problem, as most other combustion research, such as computational flow modelling, is also performed with well-characterised research reactors.

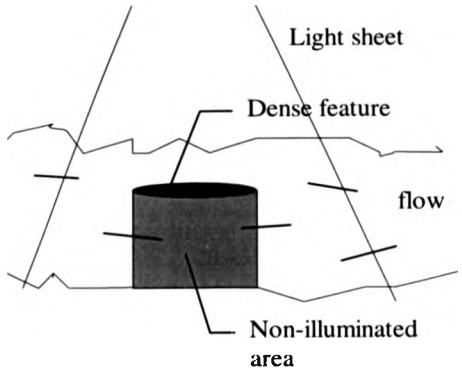

Figure 98. Effect of dense particle loading on LSI image quality

Imaging techniques require large apertures in a furnace (one for introducing the light, and the other for viewing the flow), and to prevent escape of combustion gases, these ports should be enclosed, using windows. Low expansion glasses such as Pyrex are necessary, to avoid fracture caused by the large thermal gradients. The particle loading inside a furnace is high, and windows may suffer from deposits, thereby obscuring the view. This may mean a purging air flow is necessary to keep them clear. The high radiant flux from a large furnace can damage sensitive optics and cameras, so air or water cooling of these components may be required.

Where optical access is limited, innovative means of introducing laser beams may be needed. These could include fibre-optics or directing light beams along existing pipes within the furnace geometry. Optical fibres are subject to damage from high power laser beams, and so are generally unsuitable to carry the pulsed laser beams (peak powers are often tens of MW) necessary for LSI and PIV, unless used in parallel in a fibre bundle. The focusing quality of the laser beam exiting from such a fibre bundle is usually poor when used in a light sheet.

Refractive index gradients

A serious restriction on the application of all optical techniques in large furnaces is the presence of significant time dependent refractive index gradients. These are caused by the strong temperature variations within the furnace, which give consequent variations in gas density.

Hong et al [91] have investigated refractive index gradients in relation to LDA where the beams cross a temperature interface and have identified two distinct effects. The first, termed the "phase effect", is due to the changing phase difference in the laser light between the two beams. The second, termed the "Schlieren effect" is due to deflection of the incoming beams (beam steering). Both of these effects are random about zero. For LSI measurements, only the second effect is relevant.

Hong et al support their work with experiments on a small flame for which the apparent LDA velocity error due to refractive index changes was found to be negligible. For larger flames, beam steering is more complex, since beams encounter a succession of hot and cool gas pockets.

In LSI measurements, the beam steering effect will cause deflection and mis-focusing of the light sheet, and distortion of the scattered light from the illuminated flow field. Distortion of the light sheet and flow image will increase as thermal power and hence refractive index gradients increase, and as furnace size and hence optical path lengths increase.

5.2 Laboratory coal burner study

A laboratory burner was developed specifically for the evaluation of various laser techniques on pulverised coal flames by Abbott [92]. The burner was sized to allow the laser techniques to be tested on a convenient small scale flame. A major influence on the design was the need to allow unlimited optical access and so the flame was not enclosed. In the absence of a refractory lining, and hence radiative heat transfer, the coal flame is not self-supporting. Additional heat was supplied by a pre-mixed propane-air flame which surrounds the coal jet. A schematic for the burner is shown in Figure 99.

Grimethorpe coal, supplied ready-milled by Marchwood Engineering Laboratories was used in all the measurements. The coal was sieved through a 75 μm mesh and the burner was operated

at a coal feed rate of up to 0.5 g/min. The resulting flame was approximately 250 mm long, reasonably symmetric and stable for periods of up to one hour before refilling of the fluidised bed coal feeder was necessary.

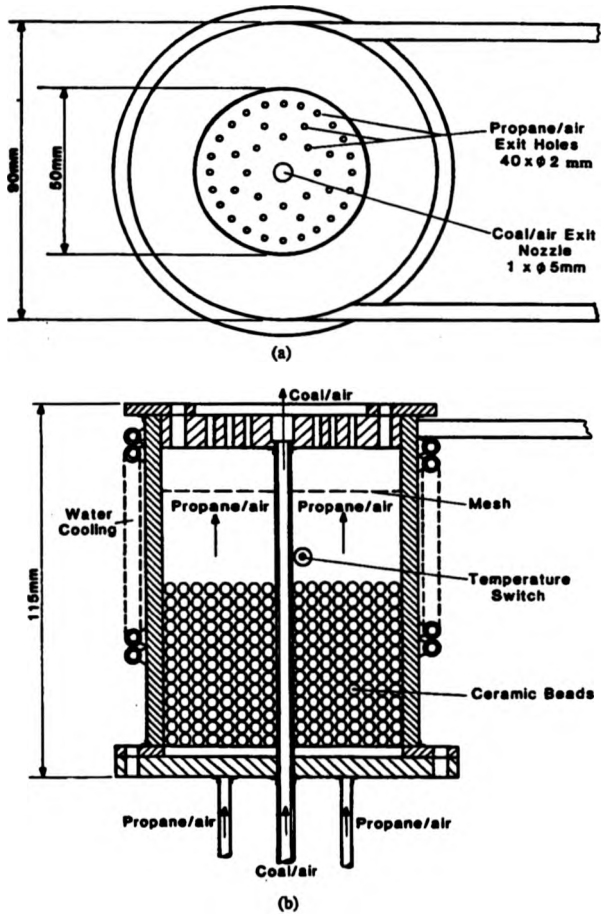

Figure 99. Schematic of laboratory coal burner

At first, an Argon ion laser, together with a rotating octagonal faceted mirror, was used to provide a light sheet [93]. Recordings of scattered light were made using a CCD camera and analysed later using an image processor. Light sheet flow visualisation was applied to an isothermal coal jet and the gas supported coal flame. The light scattered by coal particles in the flame was swamped by the combustion luminosity and so the latter was removed with a

narrow band pass filter. The filter used was a 25 mm diameter, 1 nm width (FWHM) band pass interference filter, originally intended for use with an LDA system.

The NdYAG laser described previously was then applied to the flame, and produced improved images. In order to study in more detail the structure of the gas flow, titanium dioxide (TiO_2) particles (approximate diameter of 1 μm) were introduced into the coal jet. These particles are white and scatter light well, while following the flow well. They are low cost and readily available due to their use as an ingredient of many paints. The seeding rate of these particles was adjusted independently of the main flame flow parameters, to allow the seeding density to be optimised for visualisation. Figure 100 shows a typical image. This successfully reveals the large scale structures resulting from the interaction between the coal jet and the surrounding propane flame.

Figure 100. LSI image of the laboratory-scale coal flame with TiO_2 seeding

The interface unit described in the previous chapter was used to enable the laser to be run synchronously with the framing rate of a Siemens K211 CCD video camera at 25 Hz. This

allowed the main temporal development and fluctuations of a flow to be monitored in a convenient way, even through the spatial resolution (500 x 582 pixels) was considerably less than the photographic film used previously.

The NdYAG laser was then used to provide two closely spaced laser pulses, so that PIV images could be recorded. These were analysed manually, as automated PIV software such as VISIFLOW was not available at this time. The photographic image was magnified and the pairs of particle images matched together by hand. Figure 101 shows a typical two-pulse image, with its associated velocity vector map shown in Figure 102. External seed particles were not added here, as the coal particles themselves provided sufficient seeding. The PIV velocity can be compared with detailed LDA velocity data for the burner, obtained by Abbott [94], and velocities show good qualitative agreement. As previously discussed, direct comparison is not easy as the LDA data is time averaged over a period of approximately 1 minute, while the PIV data is effectively instantaneous.

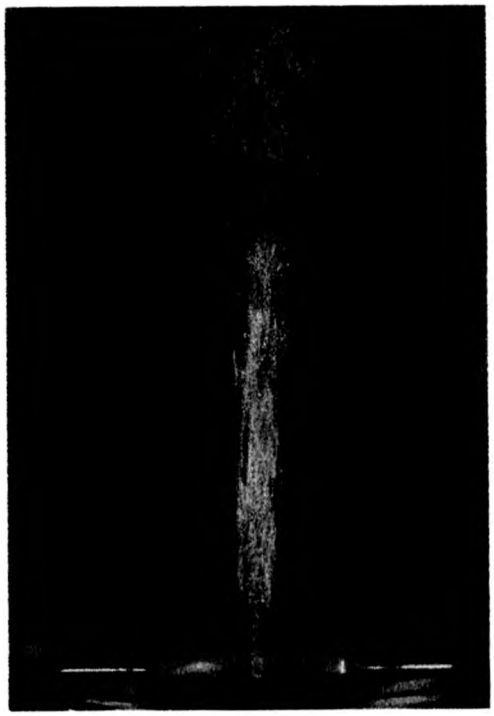

Figure 101. PIV image of the laboratory-scale coal flame

The particulate number density was dependent on the coal feed rate. At low and medium feed rates, individual coal particles were visible in the low resolution video images, while for the highest feed rates (0.5 g/min), individual particles could only be identified in the outer edges of the flame.

The video signal was input into a B&M Spektronik image processor, which digitised the image to a resolution of 640 x 512 pixels. The image processor allowed a number of frames to be added together, to produce a summed image. Normalisation of the intensity of this image yielded an averaged image for the measured time period of 100 frames (4 seconds).

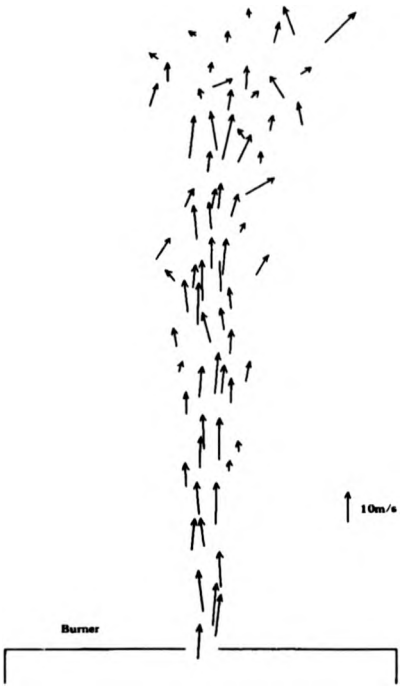

Figure 102. PIV vector map of the laboratory-scale coal flame

Computation of pixel intensity along particular line profiles provided a valuable measure of the distribution of average particle intensity. If the coal particles each scatter light identically, and light absorption is negligible, then the pixel intensity can be related directly to particle concentration [95]. Figure 103 shows pixel intensity compared with LDA data rate along a profile. The two curves compare well - LDA data rate is usually proportional to particle

concentration, so it can be deduced that light sheet intensity is also proportional to particle concentration here.

5.3 Small scale isothermal burner model

The small, laboratory-scale of the above measurement study was then extended to a more realistic, larger, geometry. The isothermal flow rig at NEI International Combustion in Derby was studied [96].

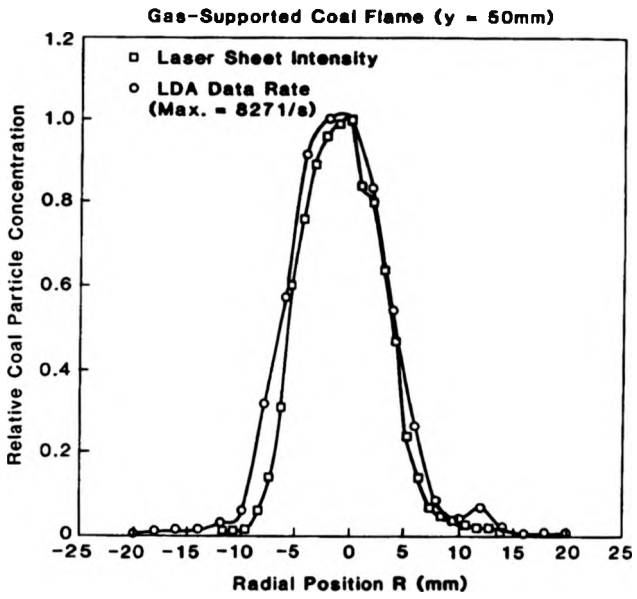

Figure 103. Comparison of LSI pixel intensity with LDA data rate

5.3.1 Experimental apparatus

The NEI flow rig consists of a wooden chamber of rectangular cross-section. A 40 hp fan is used to drive particle-laden air through the burner geometry and into the chamber. Large acrylic plastic windows give good optical access into the chamber. Figure 104 shows a schematic of the isothermal flow rig.

The flow rig is used to test one-third scale burner designs, scaled with respect to the Froude number [97]:

$$Fr = \frac{U_0}{\sqrt{gL}} \tag{46}$$

where U_0 is the flow speed, L is a typical dimension such as the diameter of the burner inlet, and g is the acceleration due to gravity. An annular burner design, often used in full-size furnaces was studied here. Figure 105 show a schematic of the burner design.

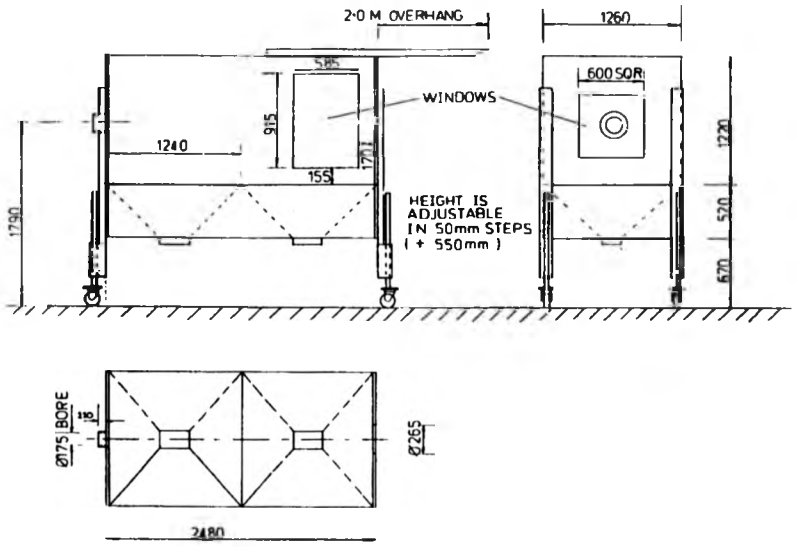

Figure 104. Schematic of NEI isothermal flow rig

Various seeding materials were considered to simulate pulverised coal particles, although the choice was limited due to the need for large quantities. Available materials were sawdust and flyash (obtained from Castle Donington power station). The sawdust had an estimated size distribution of 10 - 1000 μm. The flyash was finer, with 90 % (weight) less than 38 μm in size (measured by sieving). The seed material was fed into the inlet airstream using a vibrating plate feeder. The quantity was estimated by collecting the material over a set time interval, and then weighing it. Sawdust was introduced at rates of 51, 326 and 716 g/min. The flyash was introduced at 190 g/min.

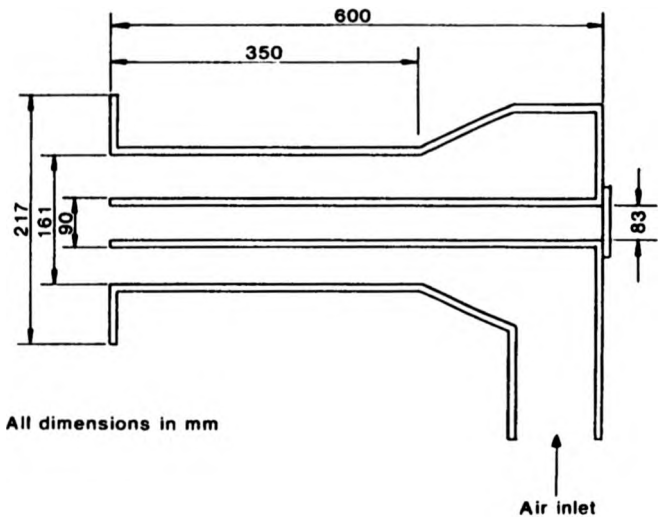

Figure 105. Schematic of NEI isothermal burner

5.3.2 Measurements and results

The NdYAG laser was used to provide a light sheet, introduced into the flow with two configurations;

(i) along the flow centreline, to illuminate a vertical section.

(ii) across the face of the burner, to illuminate a cross-section of the flow.

These two configurations were chosen to give a good characterisation of the flow of the two main planes of a flow expected to be axially symmetric.

The light sheet thickness was estimated to be approximately 1 mm. The laser beam had to travel up to 2.5 m before illuminating the portion of the flow being studied, and then the scattered light travelled approximately 1 m before collection by the imaging camera.

Laser pulse separations of 50, 100 and 200 μs were used, and PIV photographs were recorded using a 35 mm Pentax SLR camera, mounted orthogonally to the laser sheet. LSI visualisation was recorded with the Siemens video camera, previously described, and a VHS video recorder. Here the NdYAG laser was synchronised to the camera at 25 Hz.

5.3.3 Results

It was found that when running the rig with flyash, the exhaust fan was unable to draw out the seed rapidly enough, and the chamber became filled with a cloud through which the laser light could not penetrate. In addition, the windows became obscured, and so entailed cleaning the rig after a short period of operation. A typical LSI image is shown in Figure 106. This shows that the highest particle concentration is at the outer surface of the burner annulus, and that the distribution is highly irregular.

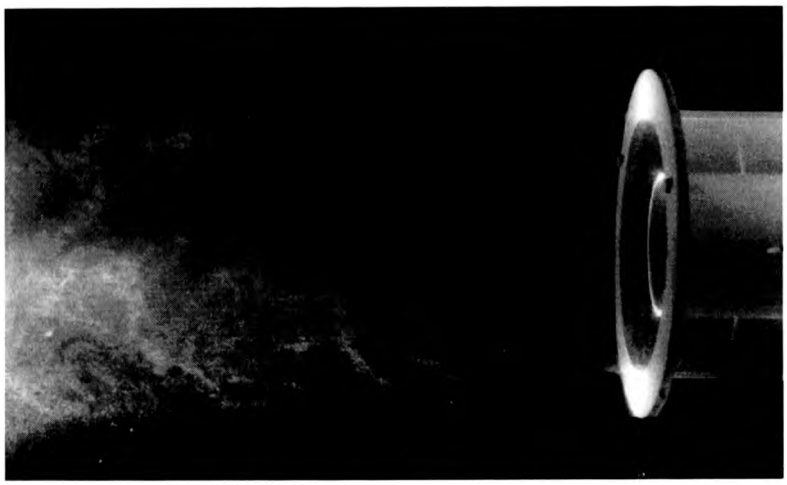

Figure 106. LSI image of NEI isothermal burner model seeded with flyash

Running with sawdust gave clearer images as the particles were larger, and individual particles could be easily distinguished in the recorded images. Figure 107 shows an image, recorded with two laser pulses, spaced at 100 μs. Again, it can be seen that most of the seed exits from the outer surface of the burner. This was thought to be due to unexpected swirl in the inlet air, forcing the particles outwards. Video images show that the flow exhibited a pulsating nature - this was likely to be due to roping within the supply pipework. However, the video framing rate of 25 Hz was insufficient to fully track the development of the flow.

Automated PIV analysis of Figure 107 was attempted with the then HarPIV system. The image showed a wide range of particle trajectories, even within relatively small areas. This is due to the extensive size and momentum ranges of the sawdust particles. This resulted in severe interference of the optically generated Young's fringe patterns, giving many invalid

vectors. Consequently, the most satisfactory velocity map was obtained manually. An example of this is shown in Figure 108. Since the pipework itself was transparent, it is possible to measure the velocities of particles in the burner pipework. These velocities can be seen to be slightly higher in the lower (denser) part of the pipe.

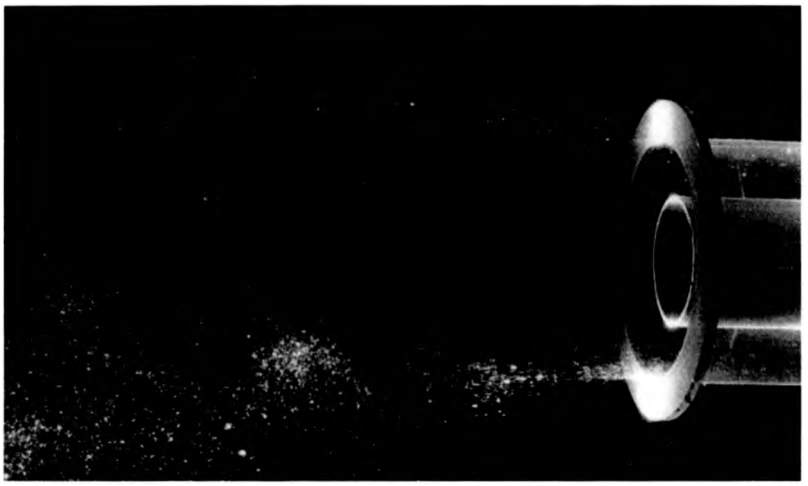

Figure 107. PIV image of NEI isothermal burner seeded with sawdust

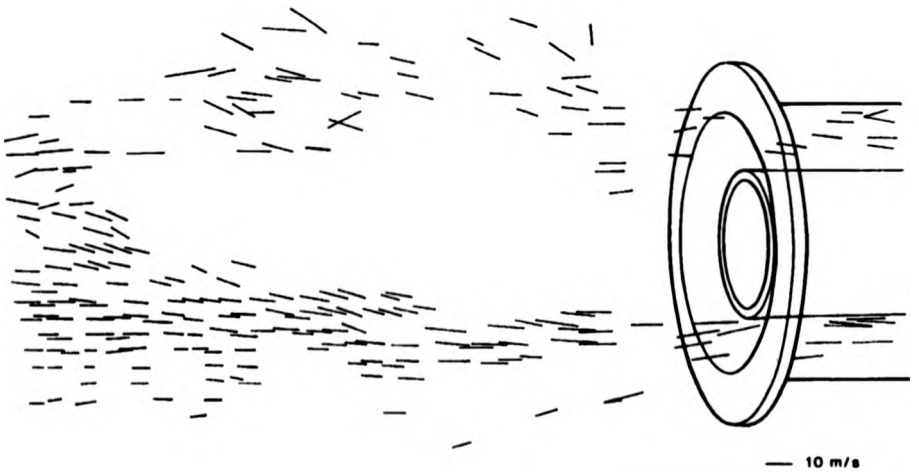

Figure 108. PIV vector map of NEI isothermal burner model

In general, particles in the lower part of the flow have well-defined velocities and trajectories. In contrast, the upper part of the flow appears to have a fairly random distribution of velocities, indicating a region of higher turbulence. It is thought that the presence of the flue in the top surface caused a disturbance in the flow, thereby increasing the turbulence here.

A reduction of velocity magnitude was found to occur along the axis and outwards along the diameters. This was expected as the flow expands from the small area of the nozzle to fill the larger volume.

This study showed the viability of using lasers for measurements on larger flow geometries, and the value of on-line video visualisation for rapid characterisation of the flow. The shortcomings of the basic HarPIV analysis system with uneven seeding density were exposed, and effort was therefore expended in improving this aspect.

5.4 Small propane burner

The laboratory scale burner and isothermal work above showed the feasibility of using laser sheet illumination for studying a combusting flow. A combusting flow was now studied in more detail, and measurement and analysis methods were optimised for PIV recording [98]. Photographic and video images were recorded to study the velocity field and spatial and temporal fluctuations of the flame front respectively.

5.4.1 Experimental apparatus

The burner design used in this study was the same as that which has been used for a number of previous studies [99] [100]. The burner has a turbulence-generating, perforated plate situated 21 mm from the exit and an outlet diameter of 35 mm. A photograph of the burner is shown in Figure 109. Propane (commercial grade) and compressed air are metered and mixed before entering the burner. Within the burner, the flow is smoothed before exiting through the turbulence-generating plate and nozzle. The resulting turbulent flame is stabilised onto the rim of the burner by a ring of propane pilot flames. A portion of the air flow was seeded prior to mixing with the propane. Monodisperse silicone oil droplets (approximately 1 μm diameter) from a spray atomiser providing seeding in the unburnt region of the flame. These droplets evaporate in the flame front and provide an indication of the position of the local flame front. However, they are unsuitable for seeding the burnt gas region.

In order to enable double particle images to be generated in the burnt region, solid particles are required. Titanium dioxide, as used for the laboratory coal burner visualisation, was considered first as a suitable material. However, Witze and Baritaud [101] describe a reduction in scattering efficiency from titanium dioxide resulting from exposure to high temperatures. They were making LDA measurements in an internal combustion engine, and observed a large reduction in measured burst signal data rate in the burnt gas region of their flow. They postulated that partial melting and de-agglomeration occurred at the high temperatures present at the flame front, reducing the effective size of the TiO_2 seed particles; titanium dioxide has a melting point of 2100 K. They recommended instead zirconium oxide (ZrO_2) for combustion measurements, and this was used in this study. This material has a high temperature stability (melting point of 3000 K) and they found only a small reduction in the scattering cross-section when burnt.

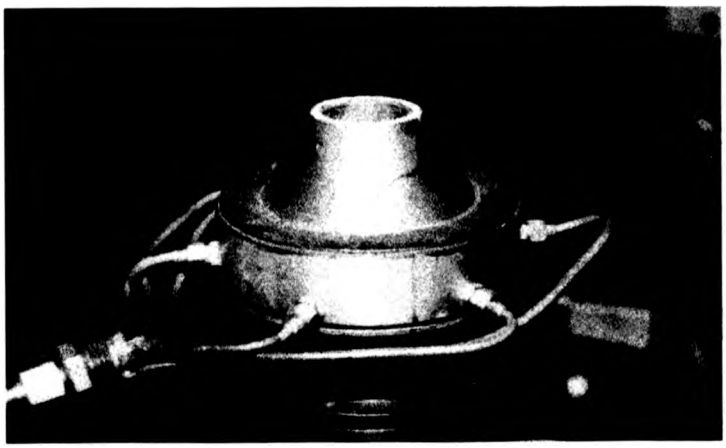

Figure 109. Photograph of propane burner

ZrO_2 particles (approximate diameter of 5 μm) were dried in a dessicator and then introduced into the air flow prior to its mixing with the propane gas, using a Pallas RGB1000 seeding generator. This device uses a motorised piston to push a container of seed particles against a rotating brush. These seed particles are then dispersed into a venturi, which gives a high speed air stream. A divertor pipe loop was used to allow the amount of air flowing through the seeder to be varied, without changing the total quantity of air supplied to the burner. Brush and piston travel speed could be adjusted independently to give fine control of the quantity and subsequent seeding density of the particles in the air stream.

The burner was mounted in an isolated combustion enclosure for safety reasons, together with the associated laser, optics and cameras. This particular design of burner was used because it offered a precisely controllable flow, which has been previously characterised, and it allowed good optical access from all directions. Seeding of the inlet air was also easily adjusted.

Seeding density is important in PIV and in this two-component flow a compromise was reached where the density was maintained high enough in the burnt region to determine velocity without speckle occurring in the unburnt region. A complicating factor here is the significant expansion of the seeded gas as it is burnt - this acts to reduce the seeding density in the burnt region.

The NdYAG laser was used to illuminate the flame. Double pulses were generated with a time interval of 50 or 100 μs, dependent on the flow speed. A light sheet was generated using spherical and cylindrical optics, giving a thickness of approximately 300 μm at its waist. For photographic recording, a Nikon FM2 camera and 105 mm MicroNikkor lens were used to image the particle laden flow field onto the 35 mm film. This camera was chosen as it offered a fast 4 ms focal plane shutter speed, which acted to reduce the background exposure from combustion luminosity. Faster shutter speeds (down to 0.25 ms) were available - however these were not suitable for LSI as they were achieved only by closing the second shutter blade while the first blade was still closing. This gave the effect of a moving slit - see Figure 110.

The MicroNikkor lens was optimised for near field subjects, giving good resolution and a flat field. A magnification from light sheet to image plane of approximately 0.5 was achieved. A Siemens CCD camera was used to obtain video images, which were recorded using a JVC S-VHS video recorder. The CCD camera had a resolution of 640 x 580 pixels, although the vertical resolution was halved in practice, as one field of the video interlace signal was redundant. Figure 111 illustrates the sychronisation of the laser pulses to the video signal.

The S-VHS recording had little effect on the quality of the camera image, as it has a specified resolution of over 400 lines. Combustion luminosity was less than for the laboratory coal burner, as the propane-air flame has only a faint bluish colour.

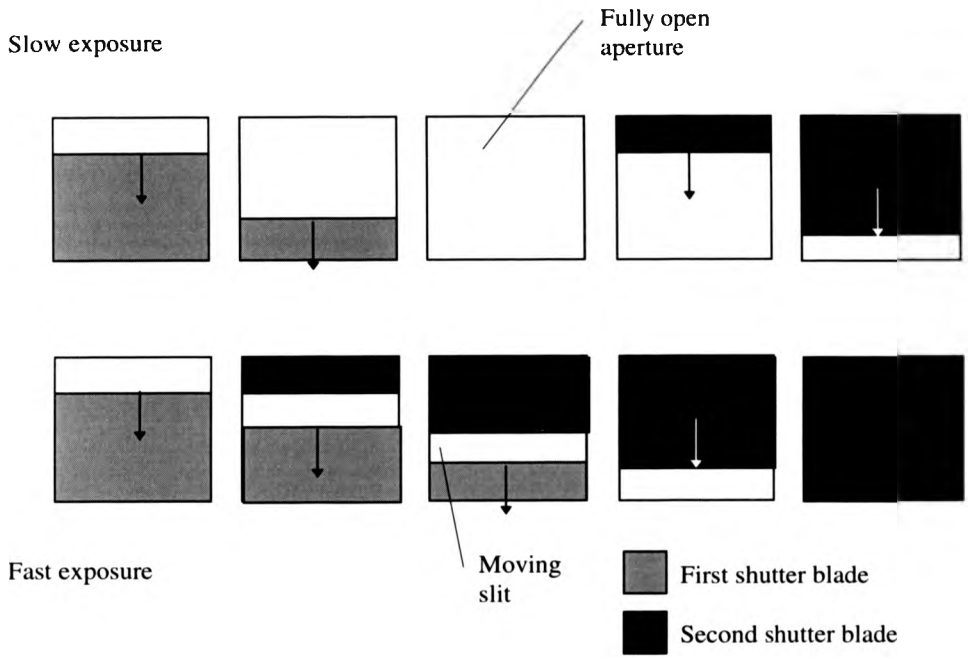

Figure 110. Focal plane shutter behaviour

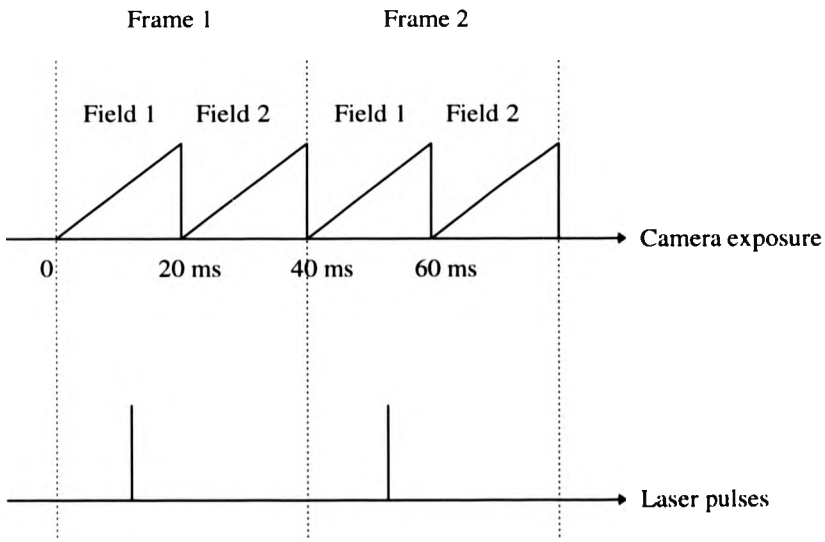

Figure 111. Laser synchronisation to alternate video fields

The bandpass filter described previously was used initially. However, it was found that some image vignetting was produced. This resulted from masking of the image by the small physical size of the filter, combined by a restriction of the acceptance angle of the image light rays. This effect was not seen for the laboratory coal flame, as a small format CCD camera was then used, together with a fairly long focal length imaging lens, requiring only a narrow acceptance angle.

An interference filter experiences a shift in its peak transmission wavelength when the incidence angle is shifted away from perpendicular. A multi-layer dielectric interference filter is effectively a stack of Fabry-Perot interferometers. The wavelengths of the transmission peaks for each interferometer are governed by the angle of incidence of the incident light ray. The wavelength of peak transmission at small angles of incidence for the whole interference filter can be shown [102] to be,

$$\lambda = \lambda_{\max} \sqrt{1 - \left(\frac{n_o}{n_e}\right)^2 \sin^2 \phi} \qquad (47)$$

where n_o is the refractive index of the external medium (n_o =1 in air), n_e is the "effective refractive index" of the filter material, and ϕ is the angle of incidence of the image light ray on the filter surface. The difference, λ_{max}-λ, is the "angle shift". This wavelength transmission shift with angle manifests itself in this application as a strong reduction in the intensity of the monochromatic laser light scattered from the flow, at the edges of the camera image, where the incidence angle is higher.

To overcome these filter problems, a new filter was specified and then applied. This was a 10 nm bandwidth (FWHM), 50 mm diameter interference bandpass filter. The filter was modified to allow it to mate to the 52 mm filter thread of the Nikon lens. The 10 nm bandwidth gave three advantages over the 1 nm filter used previously; the physical diameter was larger, the acceptance angle was greater, and also the blocking efficiency was found to be considerably higher outside the pass band. This acted to improve the illuminated particle image contrast considerably. The previous 1 nm and new 10 nm filter designs are compared in Table 4.

Bandpass/nm	Peak transmission	Background transmission	Capture angle

10	50 %	10^{-6}	34°
1	60 %	10^{-4}	11°

Table 4. Comparison of characteristics of 1 and 10 nm bandpass interference filters

The film chosen for this work was Kodak TMAX black and white film. The camera shutter contacts were used to trigger the NdYAG laser, via a pulse generator. Positive contact prints of the recorded negative images were made onto Kodak 2415 Technical Pan film. As previously explained, this was done to reduce the d.c. component of the auto-correlation function. The effect can also be achieved using image processing to invert the colours of the image.

5.4.2 Analysis of images

PIV analysis was performed using the VISIFLOW software, described previously. Here silicone oil droplets were used as the seeding material. Autocorrelation was used for analysis of 256 x 256 pixel areas (representing flow regions of approximately 1 mm^2). Each interrogation area was overlapped by 50% with its neighbours. The theoretical accuracy of 0.5 pixel for correlation displacement measurement was increased further to potentially sub-pixel resolution by computing the centre of gravity of the located auto-correlation peaks. In this way, the correlation error in determining velocity was small relative to other sources of experimental error, such as velocity averaging over the interrogation area, particle slip, non-linearity in the imaging optics (distortion) and laser pulse jitter.

It was however not possible to measure the actual cumulative error for this experiment, as the theoretical flow model was not understood sufficiently. Conventional CFD models provide time averaged velocities measured at discrete points, while correlation PIV such as described here provides instantaneous velocities, averaged over the interrogation area.

A typical photographic image, Figure 112, was analysed to give a grid of 35 x 54 vectors. These 1890 vectors took approximately 1 hour to compute (around 2 seconds per vector) using the DT2878 array processor.

The raw analysed data was then post-processed to replace incorrect correlation first velocity choices with second or third choices where the noise level and consequent chance of mis-correlation was high. This post processing or validation, was carried out automatically. For

each vector, the algorithm computes the average velocity magnitude of the surrounding vectors. If the vector magnitude is more than 30 % different to this average value, then the second choice is chosen. If this is also too different to the average, then the vector is temporarily blanked. This process is repeated for each vector, and then repeated for the entire vector set. This iterative process is continued until the number of suitable vectors is maximised. Five iterations were found to be produce convergence for this dataset.

Figure 113 shows the vector plot obtained from the central region of the flame. The high seeding density gives auto-correlation peaks with a high signal to noise ratio, as a result of the large number of image pairs in each interrogation region. Consequently, over 95 % of the correlation first choice peaks were validated. The remaining vectors were taken from the correlation second choice peaks. The vector field appears to have uniform velocity, although this is not so.

Figure 114 shows the same vector field as Figure 113, but with the global mean velocity (7.3 m/s) subtracted from each vector. This is equivalent to viewing the flow with a moving reference frame. If the now small fluctuations about this mean are magnified, large-scale structures are now apparent in the flow field - these appear to have similar sizes from one to another, approximately 2 mm in diameter. These fluctuations can possibly be explained as remnants of the turbulence induced by the 4 mm perforated plate within the burner. The size of these fluctuations would be expected to reduce with increasing distance from the burner, although the resolution of the PIV fluctuations is insufficient to show this.

Reuss et al [103] describe finding similar structures in PIV data obtained from an IC engine. They caution that the finite size of the correlation area associated with each vector means that any smaller turbulent structures will remain unresolved.

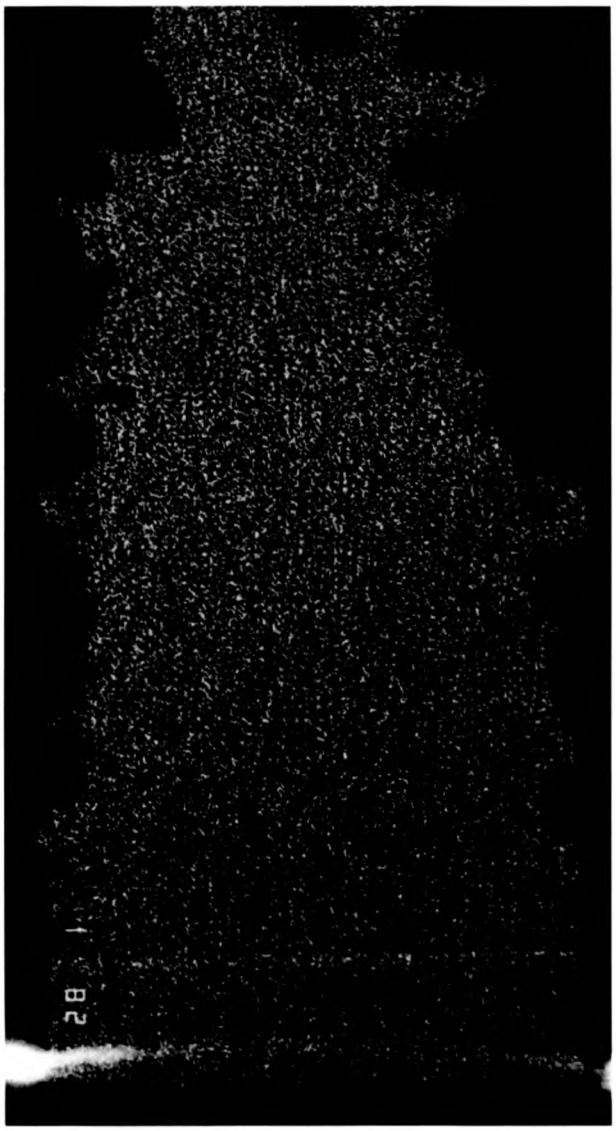

Figure 112. PIV photograph of the small propane burner

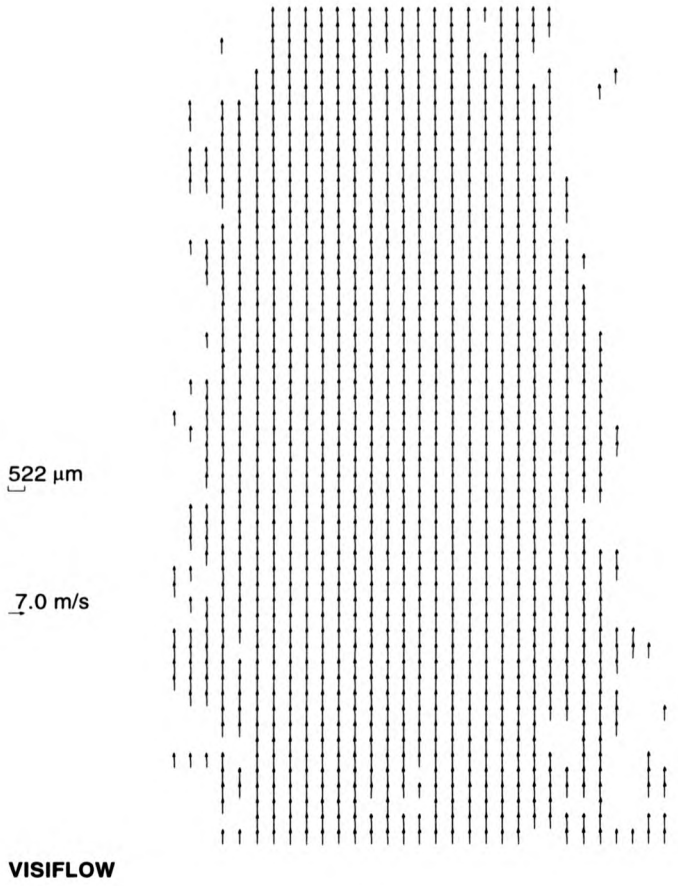

Figure 113. PIV vector map of the small propane burner

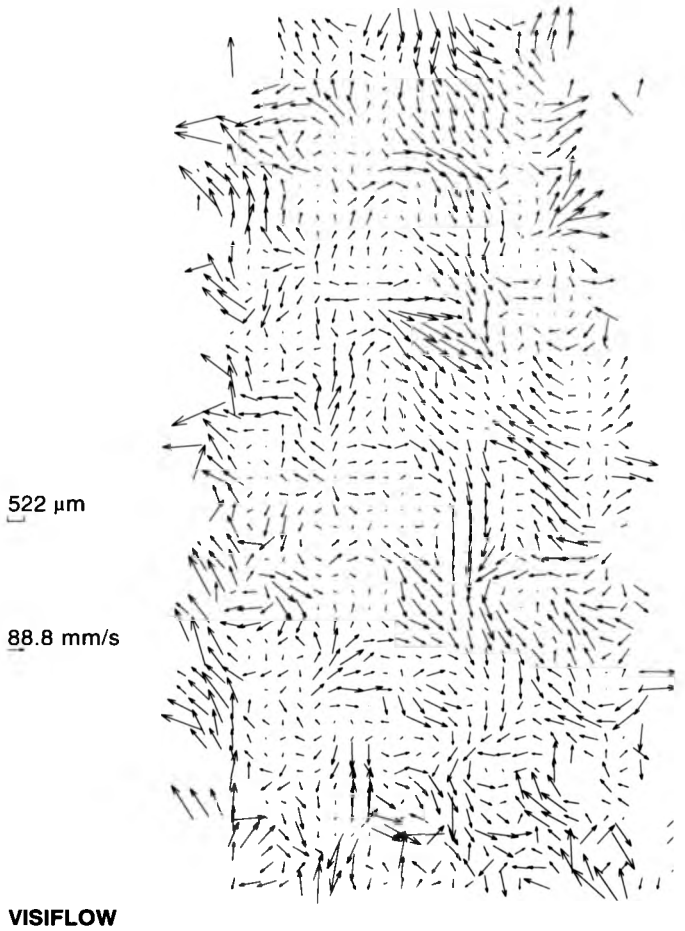

Figure 114. PIV vector map of the small propane burner with global mean subtracted

5.5 Intermediate industrial test furnaces

The studies described above showed the potential of global laser diagnostics for mapping combusting coal flows. The LSI technique was now applied to larger scale furnaces. An initial study was carried out as an addendum to other laser diagnostic work at a larger furnace, with a rated output of approximately 1.5 MW. This furnace was considerably larger than the laboratory coal burner, and a number of problems were encountered. Aspects of the LSI experimental technique were then optimised and further work was undertaken on a smaller furnace, of approximately 0.8 MW thermal output power.

5.5.1 1.5 MW water cooled furnace

The first furnace studied was situated at the same NEI facility as the isothermal burner rig. This was a 1.5 MW test furnace, running on a coal/water mixture (CWM), prepared and supplied by British Coal's Coal Research Establishment. The CWM contained 65 % of solids (Grimethorpe coal), with a mean particle size of 30 μm. The furnace was cylindrical in shape and horizontal, approximately 4 m in length and 1 m in diameter. The furnace was surrounded by a 20,000 litre water cooling bath as it did not have the traditional refractory lining, used for insulation and radiant heat absorption and re-radiation. Consequently, it was necessary to support the coal flame with a coaxial propane gas flame at all times. A schematic of the furnace is shown in Figure 115.

Optical access was limited for this furnace, with one window at the flue end, along the centre-line, and a couple of windows along the side of the furnace. The light from the previously described NdYAG laser (100 mJ pulses) was formed into a sheet, and was introduced along the centre-line of the furnace through one window, and a photographic or video camera viewed through one of the side windows. The furnace was already running when the experimental study began, which made the initial optical alignment somewhat harder. Imaging was difficult as the thick water blanket necessitated viewing through a long narrow tube in the side with a window at one end. A telephoto lens (105 mm) was thus used to make the best of the viewing conditions.

Both photography and video recordings were attempted [104], but with only limited success. The shortest shutter exposure of the FM2 photographic camera (4 ms) still allowed considerable combustion luminosity through to the recording film, and coal particles were found not to be visible against the bright background of the developed image. Similar problems were evident with the video recording. The Siemens CCD video camera suffered from severe "blooming". This is a spurious image artefact caused when infra-red radiation penetrates deeply into the silicon surface of the CCD sensor, and causes charge to diffuse from one charge pit to another, thus causing blurring and saturation of the image produced. Use of the narrow bandpass filter helped somewhat, but image contrast was still much too poor for coal particles to be distinguished against the intense combustion radiation background. An infra-red blocking "heat filter" from a slide projection system was also tried in conjunction with the narrow line filter, but was found to have only a minor effect.

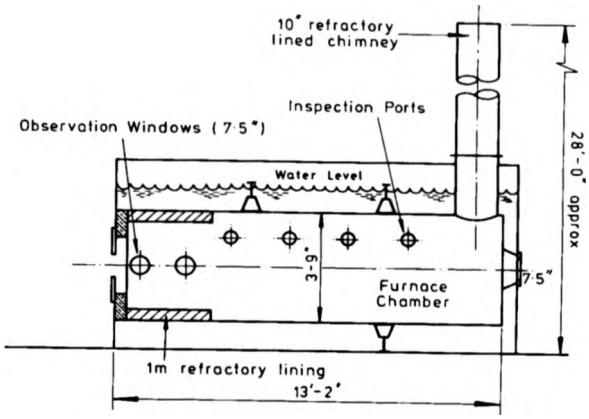

Figure 115. Schematic of NEI 1.5 MW furnace

Problems were also encountered with the high thermal loading on the imaging cameras. The conducted heat from the furnace structure, and the radiative heat from the combusting coal caused the cameras to heat up significantly. It was thus only possible to record images for short periods, before a suitable shield was interposed. It was found that the glass window in the observation port tended to become coated with a fine layer of slag and ash after a period of a few minutes, when running at high coal supply pressures. It was estimated that light transmission was reduced by about 50 % in this case. This necessitated frequent cleaning of the windows, which also suffered frequent cracking resulting from the high thermal stress.

The combusting coal particles were finally detected by using the "raw" NdYAG beam, i.e. without forming it into a light sheet. Now the much higher light intensity was sufficient for the scattered laser light to be detectable against the combustion background. Measurements of the beam size impinging on the furnace quarl surface indicated an approximate diameter of 5 mm. A beam waist of approximately 350 μm would have normally been expected from the beam focusing optics (assuming a Gaussian beam intensity profile). The increase in beam diameter was caused by beam steering within the furnace. The main consequences of this thicker sheet are the reduced spatial definition of the position of the plane, and a reduction in illuminating intensity by approximately 14 times.

The main conclusions that were drawn from these first LSI measurements in a large scale coal furnace are that beam steering from density gradients causes the intensity of the focused light

sheet to be reduced considerably and that imaging is difficult from ports that are not well designed. The success of the "raw" beam visualisation indicates that LSI measurements in coal-fired furnaces are possible but that the laser power required is greater than for measurements in isothermal flows of similar dimensions. Comparison with the isothermal rig images indicates much greater laser power is necessary.

Unfortunately, increasing the NdYAG laser power by a large amount is not readily achievable at present, and is unlikely to be for some time. Another approach that could be used would be to use a different type of pulsed laser. Ruby lasers readily provide up to 10 J of light, but the repetition rate is then only a few pulses per minute, making video imaging impractical. Also, the longer wavelength (697 nm against 532 nm for NdYAG) gives less scatter from particles. In addition, thermal background radiation at longer wavelengths is likely to be considerably higher, making filtering more difficult. Excimer lasers can provide several 100's of mJ at high repetition rates at a variety of wavelengths in the ultra-violet. Scattering from particles is considerably enhanced. However, sheet optics and camera imaging lenses must be transparent to the ultra-violet light. This usually entails making them from fused silica. Special CCD coatings are also needed to increase the camera sensitivity at these wavelengths, and even then, only the near ultra-violet can be conveniently detected. The beam quality and divergence of excimer lasers is also considerably inferior to NdYAG, making light sheet formation more difficult.

The solution then lies with improving the ability to remove background radiation by filtering and shuttering at the camera end of the technique. Improving video camera technology promised exposure time reduced to 100 μs from the 40 ms duration of the Siemens camera used here.

5.5.2 800 kW coal-fired test furnace

The thermal efficiency of a furnace and its pollutant emission are very dependent on the temperature, species concentration, combustion residence time and mixing characteristics of each part of the flow field. The flow characteristics of the furnace thus have a strong effect on the efficiency of combustion. The furnace flow field is affected by many parameters, particularly the furnace geometry and the design of the burner. Consequently, increased understanding of the particulate distribution and the flow velocity map with its associated

recirculations is most important. LSI appears to be the only technique capable of rapidly and conveniently mapping particulate distribution, and of visualising its fluctuations.

A laser measurement programme was planned at the International Flame Research Foundation (IFRF) in IJmuiden, Holland. This facility has a number of furnaces of different sizes, each well instrumented for experimental measurements with thermocouples, flow meters, pressure sensors and various combustion gas concentration meters. Many different flow conditions can be set, simulating a wide range of furnaces used in industry. Conditions are known to have a high degree of repeatability, from the results of other experimental diagnostics. The furnace geometries are considered as international standards for combustion research work, with many experimental and computational studies carried out.

Before this experimental measurement programme, modifications were designed for the apparatus previously used for the NEI LSI measurements, and then implemented, to improve the capability of the technique in large furnaces.

Experimental equipment

The IFRF No. 2 furnace was used for this study, together with a cylindrical pre-combustion chamber. This was adopted to give the necessary optical access for LSI. Figure 116 shows a photograph of the pre-combustor on the No. 2 furnace. The chamber has an internal diameter of 0.88 m and a length of 2 m. The flame thermal input was in the range of 400 to 800 kW.

A small slot was cut in the top metal wall and refractory material was removed, parallel with the axis of the chamber, to allow the introduction of a light sheet to illuminate a central vertical plane within it. When tilted, the light sheet illuminated the complete region of interest, including a significant part of the burner quarl. Several observation ports were cut into the side of the chamber to allow observation of the light sheet at an angle of nearly 90°, shown in Figure 117.

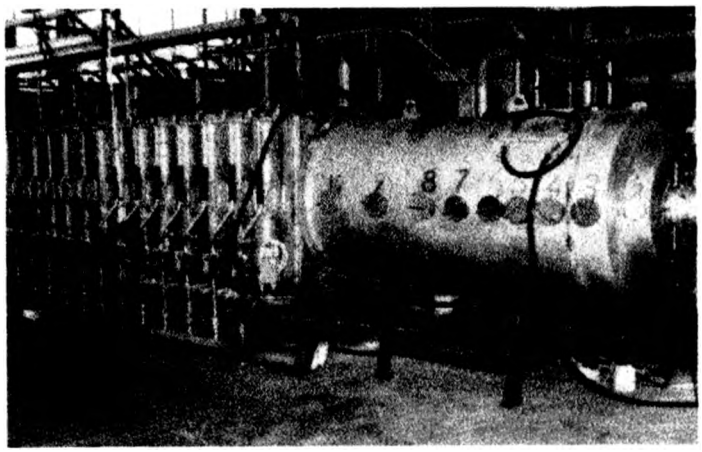

Figure 116. IFRF No. 2 furnace

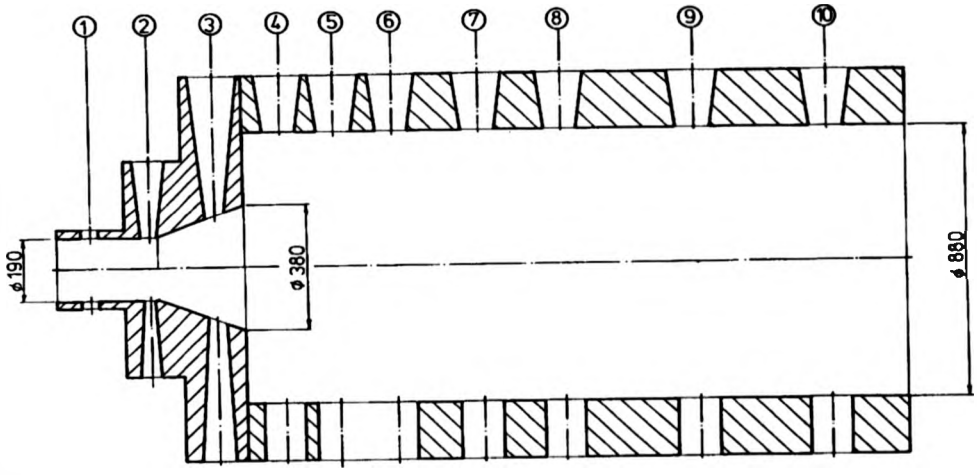

Figure 117. Viewing ports in the IFRF No. 2 furnace

LDA, CARS and LSI were the laser techniques employed [105], although only the LSI work is discussed here [106]. An argon ion laser (from the LDA system) and the previously described NdYAG system were employed for the LSI measurements.

A JAL 916G CCD camera was substituted for the previous Siemens design. This camera has a variable exposure gating facility, allowing a shutter speed as short as 100 μs to be selected. This is an exposure duration considerably shorter than previously available from video (20 ms)

or film cameras (4 ms), and promised improved combustion luminosity suppression than before. The camera has a resolution of 760 x 640 pixels and was fitted with a 12.5 mm f/1.4 lens, giving a field of view of about 600 mm in the axial dimension. The camera was angled slightly towards the quarl region in order to capture the burner near field region. When measuring in flames, the camera was shielded from the heat by wrapping it in aluminium foil.

Both Argon and NdYAG lasers were used with the same light sheet generating optics, consisting of spherical and cylindrical lenses. The two different designs of laser were used in order to compare their performance and determine the most suitable for this type of measurement.

The lasers were situated in an air conditioned clean room, and the beams deflected over to the furnace using mirrors. Plastic pipes were used to enclose the extended beam paths to protect the experimental staff. The light sheet optics were mounted on brackets welded to the top of the furnace. A single converging lens (f = 1 m) was used to produce a beam waist of approximately 200 μm at the furnace centreline. Two cylindrical lenses (f = -12.7 and -25.4 mm) were used together to form a light sheet, diverging away from the entrance slot. Uncoated lenses were used, in an attempt to ensure durability in the high temperature and dusty conditions near the furnace. Viewing through one of the side ports allowed the orientation of the light sheet to be optimised by checking the scattered line of light on the quarl wall.

The video camera automatic gain control (AGC) was disabled for this study, so that video image intensity was fully proportional to scattered light intensity. A JVC BR610S S-VHS recorder was used to record the camera output. The AGC of the video recorder was also disabled. Lens aperture and video recorder gain were adjusted to ensure that image intensity was not saturated, but instead made best use of the recording dynamic range available. The 400+ lines of resolution of the S-VHS recorder was more than sufficient, as the image quality was limited by thermal refractive index gradients. Image noise was also higher than optimum. This was thought to due to increased dark current in the CCD sensor, due to the camera temperature being higher than that recommended in the specifications.

Photographic images were recorded using the FM2 camera, previously described and a 35 mm f/2 lens. This lens was used to provide a field of view comparable to the acceptance angle of

the viewing port. The lens was used mainly at f/8, giving an acceptable image quality. Kodak TMAX film (3200 ASA) was used, in order to accommodate the fast shutter speeds and the low light levels available. The film was processed using TMAX developer, and yielded about 60 lines/mm resolution.

The 10 nm bandpass filter described earlier was used over the camera lens. Slight image vignetting was found for the 12.5 mm video lens, but this was not a problem as the limited field of view of the port through the thick furnace refractory wall insulation obscured the edges of the image.

Measurements

Altogether, over 250 different flow conditions were studied, comprising isothermal (cold) flows, and gas and coal flames with different injection gun designs, gun positions, primary and secondary swirl levels, and for isothermal and gas flames, different seeding particles. These parameters were chosen to show the various different extremes of operating conditions that can occur in industry for this type of furnace. The variation of parameters is shown in Table 5.

Parameter	Variations tested			
Injection gun	Central hole	Annular	Spray head	Four jet
Gun position/mm	0	65	130	
Secondary swirl number	0.0	0.7	1.4	
Primary swirl	none	co-swirl	contra-swirl	
Seed particle	small	large		
Coal flow rate/kg/h	25	50		

Table 5. IFRF No.2 Furnace parameter variation

The measurements were made over a three week period, with one week each for isothermal flows, gas flames and coal flames. The furnace operating conditions were changed over the period, to make the LSI measurements gradually harder. This was done in an attempt to assess the full potential of the technique for this application. For the combusting runs, the furnace was ignited first thing in the morning each day, and allowed to run up to an equilibrium temperature for several hours before commencing measurements. The measurement procedure for each flow condition consisted of starting the video tape recorder and synchronising laser

pulse illumination, removing the viewing port cover (used to shield the imaging optics from the heat), and then switching on the seeding (if used). The flow was then typically recorded for approximately one minute, allowing any fluctuations to be captured.

The furnace running conditions are summarised in Table 6. These were kept constant throughout the measurements.

Secondary air input	M_s=1200 kg/h V_s=17 m/s at 20 °C
Gas input at 400 kW	M_g=40.2 kg/h V_g=32.3 m/s at 20 °C
Primary cold air input	M_a=65.2 kg/h V_a=19.9 m/s at 20 °C

Table 6. IFRF No.2 Furnace running conditions

Measurements in the isothermal flows were designed to investigate the injection patterns for different conditions and in addition, the effect of primary co- and contra-swirl on primary/secondary air mixing. Measurements in gas flames had the objective of investigating the interaction between the primary jet and the near burner flow field. The effect of particle size, primary momentum and the burner injector gun position in both well-mixed and diffusion gas flames were all studied. The programme culminated with measurements in 25 and 50 kg/h coal flames with minimal gas support.

The cold flows and gas flames were seeded with particles to provide the scattering medium necessary for LSI visualisation. The coal flames were not seeded, because the coal particles themselves acted as suitable scattering centres. Zirconium oxide was chosen as the seed material due to its previously described good performance at elevated temperatures. The seed powder was available in two size ranges, 0.5 - 5 µm and 5 - 90 µm. Most measurements were made using the smaller size range. The larger particles do not follow the flow accurately and were used only to assess the extent of particle slip, by comparing the jet characteristics of small and large sized particles. Micro-balloons were also tried in cold flows. These are hollow glass spheres, with a size range of 20 - 100 µm and a low density of 0.15 kg/l. The low density of the particles gives an aerodynamic diameter of about three times smaller than their physical size, and they can therefore be expected to follow the flow reasonably well.

Both the primary air or gas stream and the secondary air stream could be seeded, and seeding could be steady or pulsed. Preliminary measurements indicated that seeding the secondary air stream did not reveal contours of the internal or external recirculation zones very well and so these measurements were obtained by seeding the primary air or gas stream only.

The effect of fuel injector design was studied by using a central hole gun, an annular gun and a four hole gun. The inlet swirl level was set at S_0=0, 0.7 and 1.4. Here, S is the *swirl number* of the furnace flow, and is defined [107] by

$$S \equiv \frac{\Omega}{R \cdot L} \tag{48}$$

where Ω is the axial flux of momentum, R is the radius of the flow cylinder and L is the axial flux of linear momentum. Equation (48) can be expanded, giving,

$$S = \frac{\int_0^R \rho\left(r\bar{U}_\theta\right)U_z 2\pi r\,\mathrm{d}r}{R\int_0^R \rho\bar{U}_z^2 2\pi r\,\mathrm{d}r + R\int_0^R \bar{P}2\pi r\,\mathrm{d}r} \tag{49}$$

where ρ is the fluid density, (U_r, U_θ, U_z) are the fluid velocity components, and P is the fluid pressure. Here, the pressure term from the linear momentum is excluded, giving $S = S_0$.

The gun position was positioned either at the quarl throat (GP=0), or pushed to the middle of the quarl (GP=130). The swirl number and burner gun position values described here were calibrated for the furnace previous to these measurements. The effect of swirl on the primary jet was also investigated for the central hole gun by swirling the jet in the co- and contra-direction relative to the secondary swirl. The effect of the various burner design parameters was investigated in cold flows, gas flames and coal flames.

The c/w Argon laser offered the possibility of recording true averaged image intensities, by extending the image recording duration. This enabled the average particle density field to be recorded. When using the Argon ion laser, photographs were taken for each flow setting, with fast (0.5 - 2 ms) and slow (0.1 - 1 s) shutter speeds. The fast shutter speed photographs showed instantaneous structures of the flow, while the slow shutter speed photographs showed the time-averaged contours of the jet.

The Argon laser supplied 4 W of light, against 80 mJ for each NdYAG light pulse. Thus for a 20 ms exposure duration, both lasers contributed the same energy to the camera image (80 mJ), and thus were equally suitable for making LSI measurements. For a 100 µs exposure duration, the Argon laser supplied 0.4 mJ, against the same 80 mJ energy from the NdYAG laser. Therefore, the Argon laser was not really suitable for recording combusting flows, as the exposure time of the camera could not be reduced to remove the combustion background, without excessive reduction of the illuminated particle intensity. Initial measurements confirmed this - only the flame could be seen in the recorded images. If the exposure level was increased in an attempt to view the scattered laser light, the combustion radiation then saturated fully the recording.

A Pyrex glass window was fitted to the observation port in an attempt to protect the camera from the heat of the furnace. In addition, a cold air flow was directed at the camera to cool it further. Even so, it was found that after extended exposure to the radiant flux of the furnace, the camera surface temperature rose considerably, and on one occasion caused partial melting of the (unfortunately black) camera case. The best solution found was to interpose a thick metal shutter between measurements. The small slot in the top of the furnace was not covered, so furnace differential pressure was made slightly negative to give a small air in-flow to minimise contamination of the light sheet optics. This air flow also acted to cool the LSI optics. Even so, the optics still had to be cleaned occasionally to prevent adhering coal and ash particles from causing damage to the lenses exposed to the high pulsed laser power.

Discussion and interpretation of LSI results

Cold flows

Both Argon and NdYAG lasers were found to be equally successful for the isothermal flow measurements. Micro-balloons were used briefly and gave interesting results. The large diameter (approx. 50 µm) of these particles resulted in a strongly scattered signal, and streak lines could be observed for individual particles when illuminated by the c/w laser. However, the seeding injection rate was necessarily high for this large scale flow and only very limited quantities of this seed material were available. The results shown were therefore made using zirconium oxide (zirconia) powder as a seed.

The use of the smaller zirconia particles meant that individual particles could not be distinguished in the LSI video images. This was due to the high seed density and relatively low resolution of the video image. Consequently, PIV with its requirement of matching multiple particle images on a single frame was not possible. It was also not possible to track flow movement from one image frame to another due to the low framing rate of the video camera (25 Hz). Therefore, only the global particle distribution could be visualised.

The on-line nature of the video LSI images was found to be most useful, as the flow conditions could be varied and the effect immediately visualised in real-time. The global visualisation of particle distribution enabled rapid characterisation of the flow without the traditional and time consuming intrusive sampling techniques.

Central hole gun

The schematic in Figure 118 shows the position of the gun, quarl and light-sheet in the subsequent LSI images.. Figure 119 shows instantaneous photographs of the flow from the central hole gun, for three swirl levels and two gun positions. The flows were illuminated by the NdYAG laser, and recorded by the CCD camera. A Mitsubishi CP100B dye sublimation video printer was used to produce colour paper copies of selected video frames from the recorded S-VHS tape sequence. The LSI images reveal a wealth of information about the flow field.

The effect of swirl level:

At S_0=0, the jet shows a long cylindrical core followed by vortices which are carried downstream with the main flow. The region between the core and the boundaries of the jet envelope can be defined as the mixing region. At S_0=0, the jet envelope is long and narrow. At S_0=0.7 and 1.4, the jet envelope appears to be shorter and wider than in the non-swirling flow. Observation of the video recordings using pulsed seeding shows that a large fraction of the eddies issued from the jet are recirculated back towards the injection gun. This interaction between the jet and the swirl-induced recirculation contributes towards higher mixing in the radial flow direction. The effect of swirl on the flow is indicated in Figure 119.

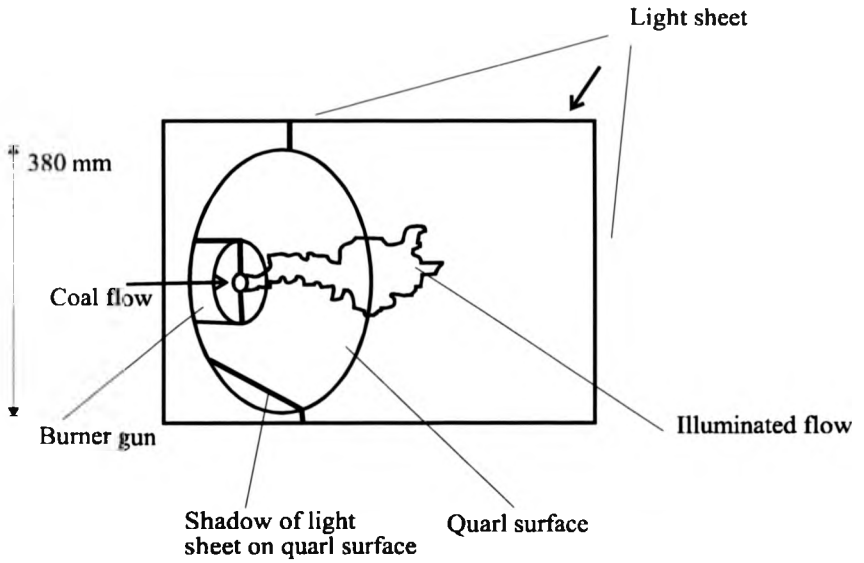

Figure 118. Schematic of LSI view in IFRF No.2 furnace

The effect of gun position:

When the flow has swirl and the gun is positioned at the quarl throat, the jet does not reach the quarl outlet. Eddies are recirculated towards the gun before they break up and disperse with the secondary air. The light sheet reveals a higher particle concentration along the quarl walls than downstream of the jet. This indicates that the primary jet is entrained by the secondary air. Moving the gun to GP=130 increases the penetration distance of the jet and decreases the width of the jet envelope. This indicates that pushing the gun into the quarl delays mixing between primary jet and secondary air. For GP=130, particles are not entrained by the secondary air along the quarl wall and are dispersed downstream of the jet in the centreline region.

The effect of primary swirl:

The effect of primary swirl on the central hole jet was studied for two levels of secondary swirl (S_0=0.7 and 1.4). When the primary jet was swirled, the jet appeared very turbulent and showed very large fluctuations in the radial flow direction. The light sheet was parallel to the flow direction so it was not possible to assess whether the flow was rotating or not. For S_0=0, swirling of the primary jet reduced the length of the jet potential core and caused large erratic fluctuations of the eddy direction. The jet envelope shape appeared to be the same with primary swirl in both co- and contra-directions to the secondary swirl.

GP=0 GP=130

$S_0 = 1.4$

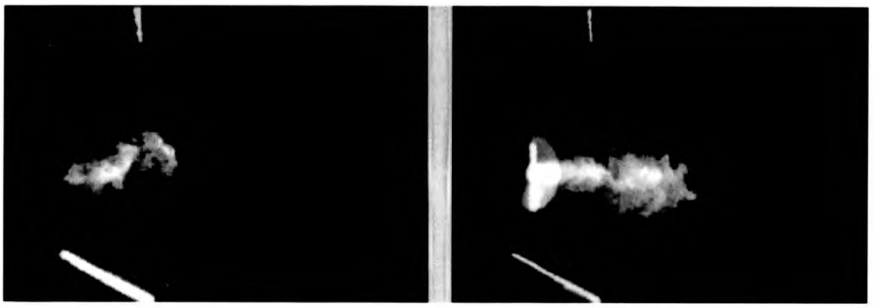

$S_0 = 0.7$

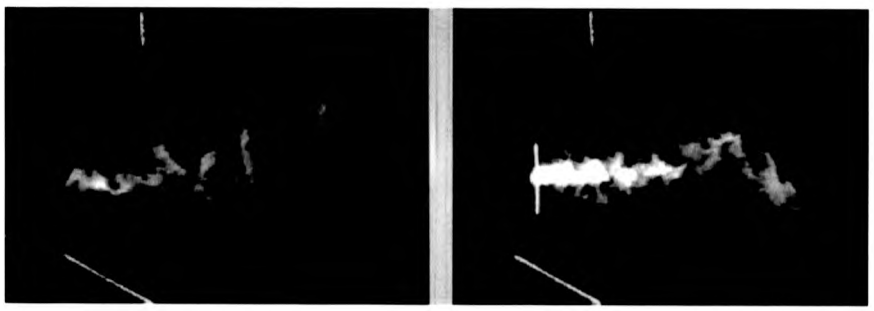

$S_0 = 0.0$

Figure 119. LSI images of isothermal flow from the IFRF No. 2 Furnace central hole gun

Annular gun

Figure 120 shows instantaneous photographs of the annular jet for three swirl levels and two gun positions. Although the central hole gun and the annular gun jets had identical momenta and velocities, the jet mixing patterns appear completely different. At S_0=0, the particles injected with the annular gun are entrained and dispersed in the wake of the gun. For S_0=0.7 and 1.4, the centrifugal forces acting on the flow entrain the seed particles away from the axial centreline and along the quarl wall. Only a small fraction of the eddies are entrained into the downstream region of the flow. The particle concentration in the centreline area is very low, especially when the gun is pushed further into the quarl. The effect of gun position does not appear very pronounced in the case of cold flows from the annular gun, and does not modify the entrainment of particles along the quarl wall in the main secondary stream.

GP=0 GP=130

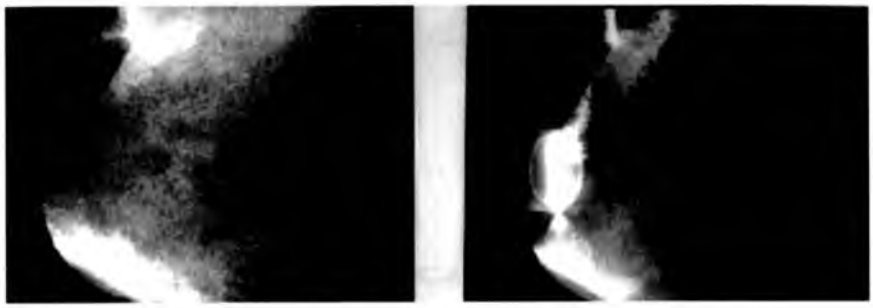

$S_0 = 1.4$

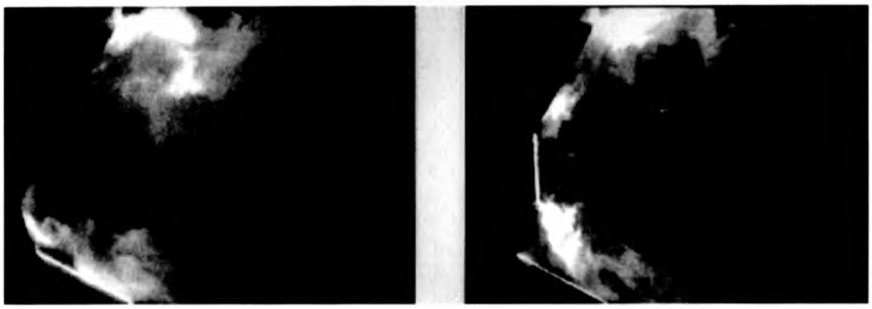

$S_0 = 0.7$

$S_0 = 0.0$

Figure 120. LSI images of isothermal flow from the IFRF No. 2 Furnace annular gun

Four hole gun

Figure 121 displays instantaneous and time-averaged photographs of the four hole gun jets for S_0=0 and 0.7 at GP=130. The gun was placed so that two holes were illuminated by the vertical laser sheet. At S_0=0, the jets have long and thin cores, followed by a mixing region in the wake of the gun. The width of the mixing region is about one gun diameter. For S_0=0.7, as a result of the action of the centrifugal forces, the mixing region becomes shorter and wider. The estimated length and width of the mixing zone are about one and two gun diameters, respectively. Observation of the video recording sequence shows that the jets behave as fully independent jets and do not impinge on each other. Eddies are entrained in the wake of the gun and in the secondary air stream along the quarl wall. The final particle dispersal occurs along the quarl wall.

Gas flames

Although the c/w Argon laser was mostly satisfactory, only the pulsed NdYAG laser, in conjunction with the shuttered video camera, was capable of overcoming completely the background combustion radiation. The gas flame luminosity was fairly low, but visible as a bright background on the images recorded with the Argon laser. However, the image quality when using the NdYAG laser and gated camera together was somewhat lower than when the camera was operated in non gated mode (effectively open shutter). This was because in gated mode, only one of the two image fields was exposed by the illuminating laser, pulsing at 25 Hz. Thus the vertical resolution was halved to 312 lines (625/2). The second image field only received light from the combustion background. This allowed easy switching from viewing one field to the other, enabling comparison of the scattered image intensity against the combustion radiation background. It was not possible to increase this resolution by illuminating both fields with the same laser pulse. This was due to the necessarily short gating time, which meant that each field was exposed separately.

Well mixed gas flames were produced with the radial gas injector located upstream of the quarl. The flame thermal input was 300 kW and the corresponding average temperature in the quarl zone can be estimated between 700 and 900 °C. The purpose of using the gas flames was to produce a combusting flow, and to use the same jet inputs (same momentum and

velocity, 0 36 N and 20 m/s) as in the cold flows. This method allowed comparison of the jet penetration and mixing patterns in cold and combusting flows.

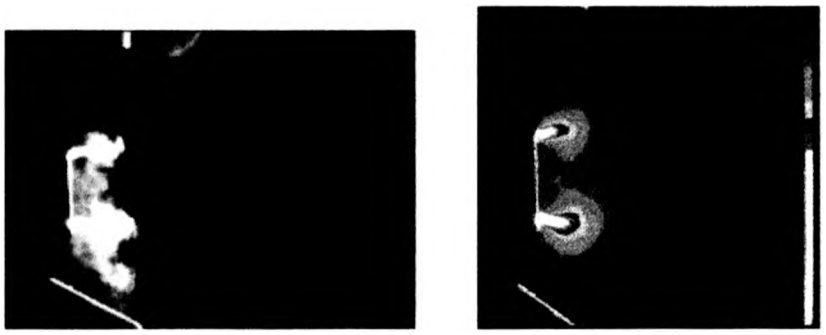

$S_0 = 0.7$

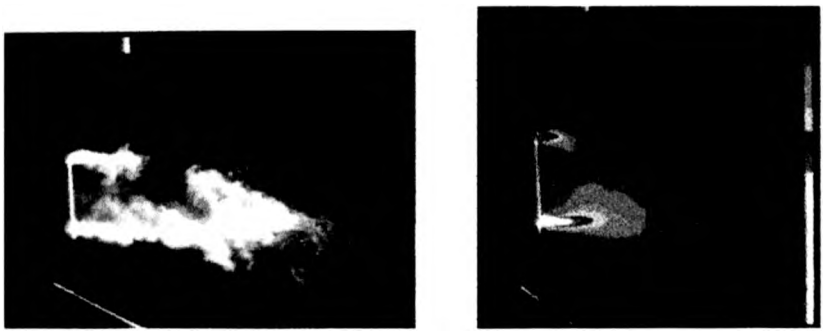

$S_0 = 0.0$

Figure 121. LSI images of isothermal flow from the IFRF No. 2 Furnace four hole gun

Central hole gun

Figure 122 displays instantaneous photographs of the central hole jet for three swirl levels and two gun positions. Comparison of these flows with the cold flows of Figure 119 does not reveal any major differences. The shape and size of the jet envelopes are similar in cold and combusting flows. A closer comparison shows that for combusting flows with GP=130, the jet vortices penetrate further downstream in the axial centreline region. This process (again verified by pulsing the seeding, and observing the video recording image sequence) can be explained by the weaker internal recirculation zone in the case of the combusting flows [108]. The weaker reverse flow contributes to an easier jet penetration in the recirculation zone. The

The weaker reverse flow contributes to an easier jet penetration in the recirculation zone. The evidence of a weaker recirculation zone in the case of a hot flow can be seen for S_0=0.7, 1.4 and GP=130. The photographs show that fewer eddies are recirculated towards the gun and more are entrained downstream of the centreline region than in the corresponding cold flows.

Annular gun

Figure 123 displays instantaneous photographs of the annular jet for two swirl levels at GP=130. At S_0=0, the flow pattern is similar to the cold flow case, with particle dispersion in the wake of the gun. At S_0=0.7, the mixing pattern exhibits differences from the cold flow case with less particle entrainment in the secondary region. These differences can again be attributed to the weaker recirculation strength in combusting flows, as described in the previous section.

Coal flames

The burner was not originally designed for coal, so the coal flames had to be sustained with a 400 kW well-mixed gas flame to ensure flame stability. The coal flow rate was normally set to 25 kg/h, which corresponded to a thermal input of about 250 kW. The transport air flow rate was 50 kg/hour. The coal jet output velocity and momentum was 15.5 m/s and 0.32 N respectively.

Central hole gun

Figure 124 displays instantaneous photographs of the central hole jets for three swirl levels and two gun positions. Observation of the video recordings and photographs show that for GP=130, jet penetration is long and there is little mixing in the radial direction. Comparison of the coal jets with the gas flame flows, Figure 122, shows that the coal jet penetrates further into the recirculation zone than the air jet. The transport air momentum and velocity of the coal jet are lower than the momentum and velocity of the well-mixed gas flame air jet. The higher penetration of the coal jet even with a lower transport air momentum and velocity indicates that the coal loading increases the jet penetration substantially.

GP=0 GP=130

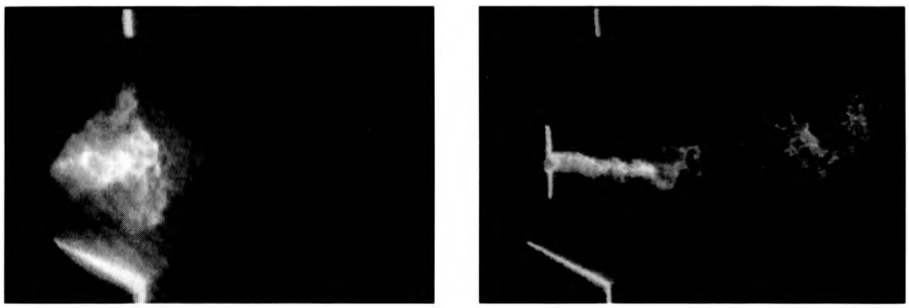

$S_0 = 1.4$

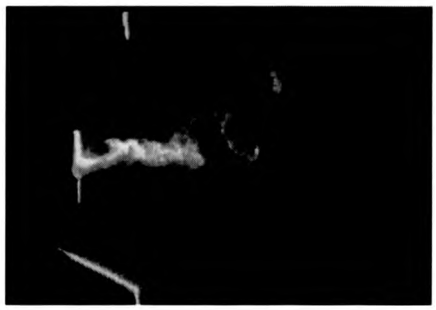

$S_0 = 0.7$

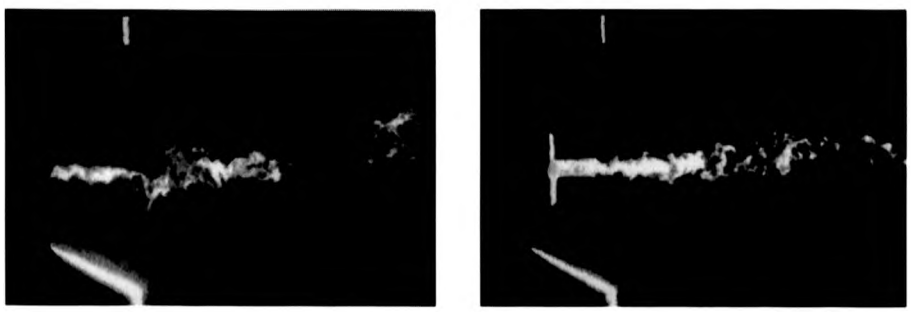

$S_0 = 0.0$

Figure 122. LSI images of a gas flame from the IFRF No. 2 Furnace central hole gun

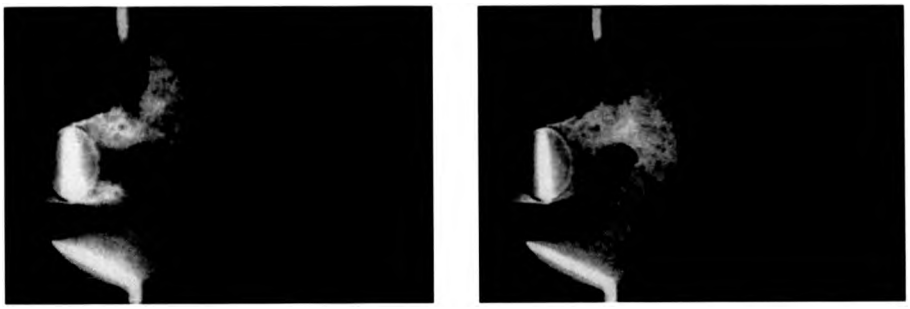

S_0=0.7 S_0=0

Figure 123. LSI images of a gas flame from the IFRF No. 2 Furnace annular gun

Observation of the instantaneous and time averaged (see later image processing) photographs of Figure 124 and Figure 125 shows that swirl has only a limited effect on increasing mixing in the radial direction and does not reduce the penetration distance. When the gun is located at the quarl throat, mixing in the radial direction is larger and is more sensitive to swirl level.

The effect of primary swirl on the central hole coal jet was studied for two secondary swirl level (S_0=0.7 and 1.4) and two primary swirl directions, co and contra to the secondary swirl direction. As in the cold flows, swirling the primary jet caused large fluctuations in the jet direction and made visual observation of a representative flow difficult. The jet envelope shape was similar for primary swirl in co- or contra-swirl direction to the secondary swirl. Figure 126 shows time averaged photographs of the coal jet for S_0=0.7 and 1.4 and with primary swirl in contra-direction to the secondary swirl. Comparison can be made with Figure 125 which shows the same cases without primary swirl. When primary swirl is applied to the jet, it's envelope becomes smaller, wider and indicates a much faster radial mixing and dispersion of the coal particles. The main effect of primary swirl is to spread the particles away from the centreline in a region of higher turbulence and tangential velocities which further enhances mixing in the radial direction.

GP=0 GP=130

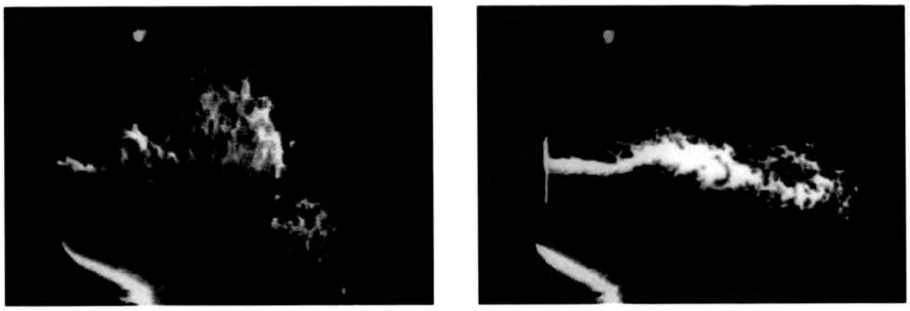

$S_0 = 1.4$

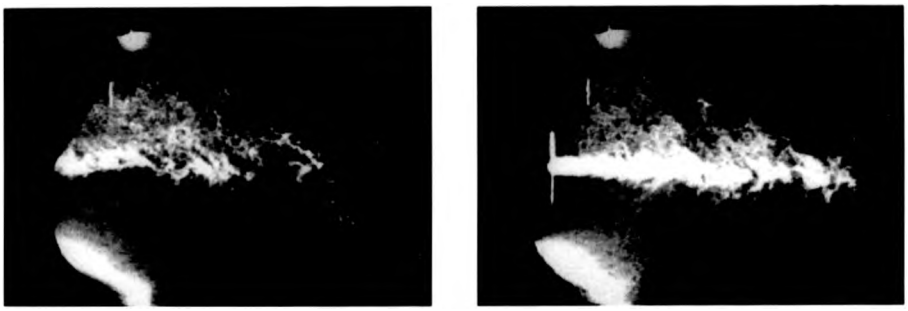

$S_0 = 0.7$

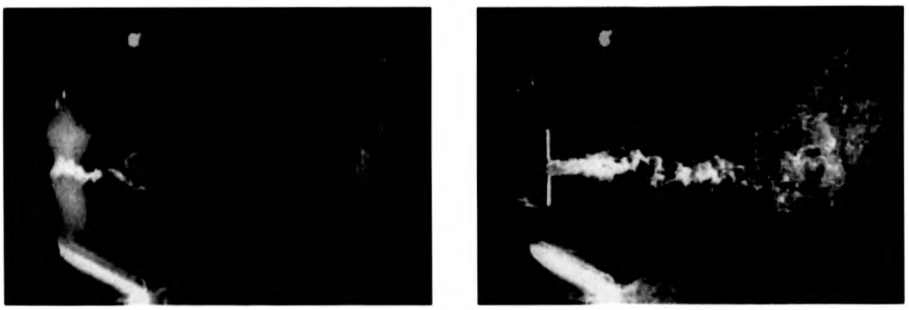

$S_0 = 0.0$

Figure 124. LSI images of a coal flame from the IFRF No. 2 Furnace central hole gun

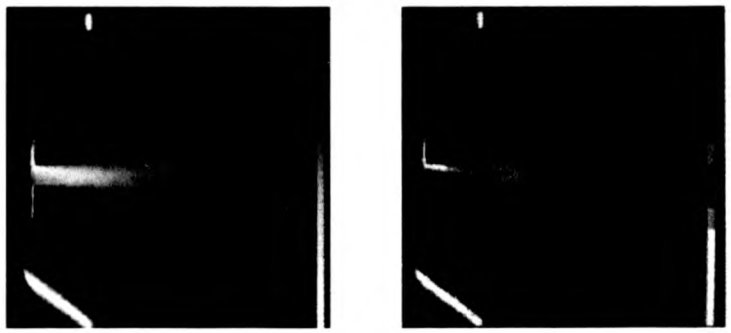

$S_0 = 1.4$

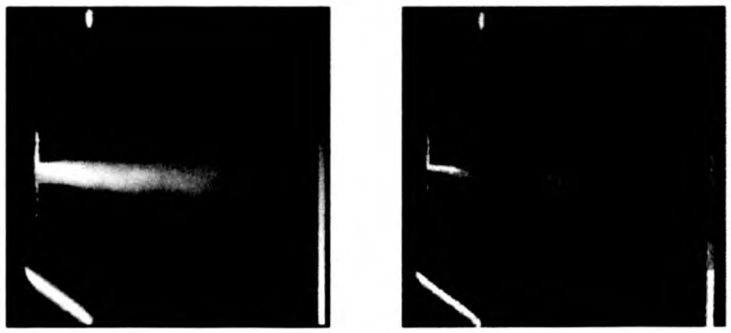

$S_0 = 0.7$

Figure 125. Time-averaged LSI images of a coal flame from the IFRF No. 2 Furnace central hole gun

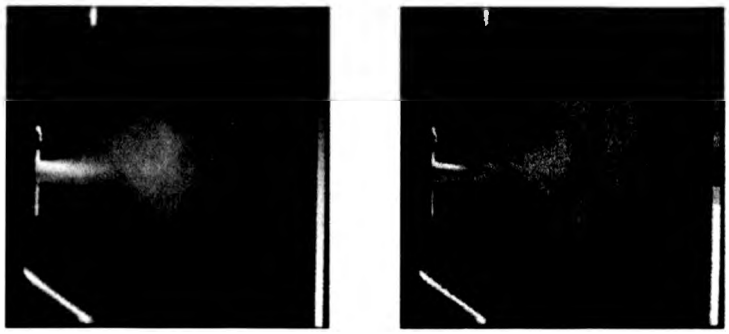

$S_0 = 1.4$

$S_0 = 0.7$

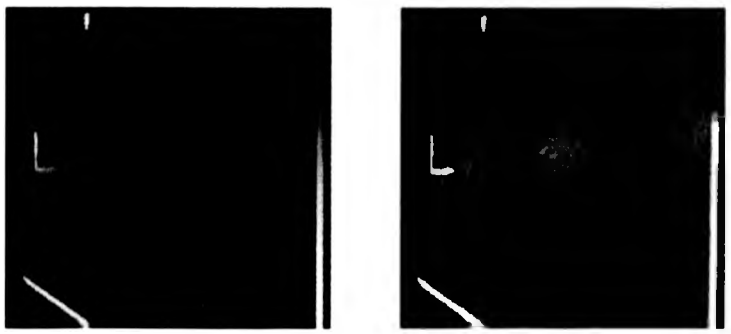

$S_0 = 0.0$

Figure 126 Time-averaged LSI images of a coal flame from the IFRF No. 2 Furnace central hole gun, S_0=0.7 and S_0=1.4. Primary swirl in the contra-direction

Annular gun

Figure 127 displays instantaneous photographs of the annular coal jet for two swirl levels and two gun positions. The difference in the jets at the top and bottom of the image resulted from a partial blockage of the gun. The blockage was caused by the narrow annulus of the gun, which had been designed for gas injection. At S_0=0, the coal particles are entrained in the centreline region over a longer distance than in the gas flames. At S_0=1.4, observation of the video recordings show a broad mixing region downstream of the quarl for both gun positions. At GP=0 and S_0=1.4, the injection pattern appears different from the previous cold flows and gas flames, which showed particle entrainment in the secondary stream along the quarl wall and low particle concentration in the centreline region. The less pronounced effect of secondary air entrainment on the coal jet may be due to the higher inertia of the coal particles and the gas combustion in the quarl inlet.

Four hole gun

Figure 128 displays instantaneous photographs of the four hole gun coal jet for two swirl levels at GP=130. The coal flow rate was increased for these cases to 50 kg/h. The photographs show dark spots which are due to large pockets of coal absorbing the laser light. The light absorption at high particle loads indicates a possible limit on the use of laser sheet illumination in large coal flames. The coal injection pattern at GP=130 is similar to the pattern observed in the gas flames. The parallel jets are surrounded by a long mixing region whose size is not significantly affected by the swirl level.

Summary of LSI results

It is thought that these images are the first such measurements made of particle distribution in isothermal and combusting semi-industrial scale coal furnaces. These results show the NdYAG laser sheet illumination technique with the gated CCD camera to be successful even in the largest coal flames (approximately 0.8 MW) with the various delivery guns. The combustion luminosity was removed at all times to a sufficient degree, with at least 3-4 f-stops difference between the collected laser light and the flame radiation. These measurements required the minimum 100 μs gating period of the CCD camera. A possible limitation of the LSI technique was revealed when studying flows with the highest coal feed rates - significant absorption of the laser light can occur, obscuring the image.

GP=0 GP=130

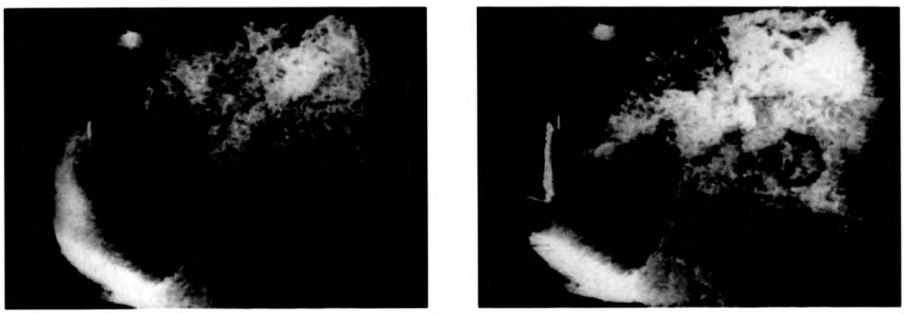

$S_0 = 1.4$

$S_0 = 0.0$

Figure 127. LSI images of a coal flame from the IFRF No. 2 Furnace annular gun

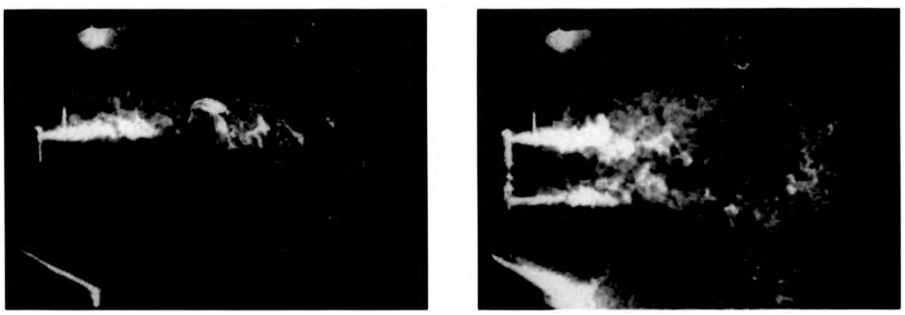

S_0=0.7 S_0=0.0

Figure 128. LSI images of a coal flame from the IFRF No. 2 Furnace four hole gun

5.6 Image processing of LSI images

Digital image processing offers the possibility of extracting quantitative or semi-quantitative data from the flow image recordings [109][110]. As previously described, it can be used to modify the image data for a number of reasons; including noise reduction, contrast improvement, enhancement of specific features, and addition of false colours.

False colours were added to some of the images to enhance the pixel intensity variation, and make it easier to compare the different particle distribution shapes. The instantaneous images were also converted to more representative time averaged images by summing a sequence.

A sequence of 100 consecutive LSI flow images from the IFRF No. 2 furnace, corresponding to four seconds of recording, were processed using a number of algorithms to derive additional information. The furnace conditions were 25 kg/hour coal feed rate, S_0=0.7 and GP=130. The image processing system was that described previously for PIV analysis. This four second time period was chosen as being long enough to average out any short term flow fluctuations, allowing a good representation of the mean flow to be obtained. Longer sequences were avoided, to reduce computation times and to allow the summed image to be stored in the available 16 bit data buffer.

Time averaging was achieved by adding the 100 flow images, giving Figure 129. If the recorded image intensity is not saturated, it can be assumed that image pixel intensity (grey-scale) is proportional to scattered light intensity, and hence particle concentration. Although not attempted in these studies, quantitative concentration profiles could be obtained by graphing pixel intensity, and using another measurement method, such as physical sampling, to obtain spot concentration calibration.

The time averaged image was then remapped using discrete false colours to show iso-intensity contours, Figure 130. The ten colour levels, extending from white, red, green, blue and black were set to normalise the image grey levels. The pseudo-colours clearly increase the contrast and enhance features present in the image. White was set on the brightest area on the jet near the quarl, and black was set on the darkest area of the furnace. The other colours were then divided between these two extremes. This normalising of the light intensity levels made it possible to compare jet shape and penetration distance for different flow sequences, when recording exposure parameters may otherwise have varied slightly.

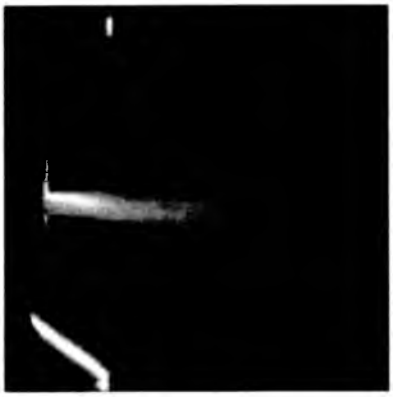

Figure 129. Time-averaged LSI image of a coal flame from the IFRF No. 2 Furnace central hole gun

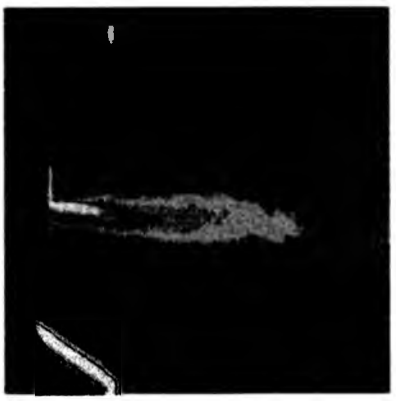

Figure 130. Time-averaged LSI image with false colours of a coal flame from the IFRF No. 2 Furnace central hole gun

Figure 131 shows the standard deviation of the previous summed image, again colour enhanced. The PC array processor was used to accelerate this large-scale computation. It can be seen that there are some regions where the intensity is much greater than others. This is where the intensity variation from frame to frame is greatest and can be related to regions of flow instability or to mixing effects.

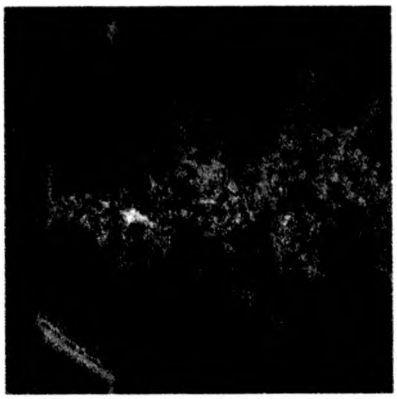

Figure 131. Standard deviation of time-averaged LSI image with false colours of a coal flame from the IFRF No. 2 Furnace central hole gun

Figure 132 shows the previously summed (mean) image, with contour lines added to enhance the intensity variation. The contours were spaced at 32 grey-level intervals. Five contour lines cover the intensity range present across the coal jet.

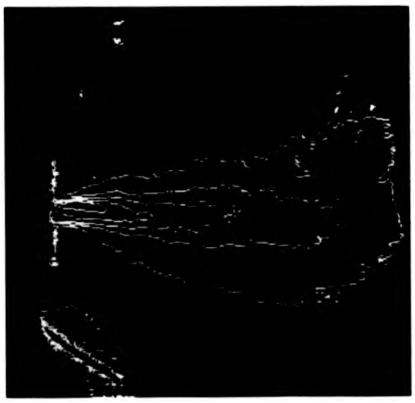

Figure 132. Time averaged LSI image with contour lines of a coal flame from the IFRF No. 2 Furnace central hole gun

5.7 Larger test furnaces

The IFRF No. 2 furnace study showed the potential of the LSI technique for large coal furnace measurement, and provided results enabling detailed characterisation of the various operating conditions. The technique was now explored further to find its full capabilities, and

attempt to discover any limitations. Two further furnaces were studied, both of larger scale than previously measured.

5.7.1 IFRF No. 1 furnace measurements

Experimental equipment

The first of the larger furnaces studied was the No. 1 furnace at the IFRF. This furnace is larger than the No. 2 furnace, allowing considerably bigger flames. The furnace is of square cross-section with internal sides of 2 m, wall thickness approximately 0.5 m, and 6.25 m in length. A single variable swirl annular type burner was positioned on the central axis at one end of the combustion chamber. A schematic of the furnace is shown in Figure 133.

This time only the NdYAG laser and gated video camera were used. The combustion luminosity was much higher than could be studied using conventional photography. The double oscillator laser was used with both oscillators firing simultaneously, giving twice the output intensity. As before, the CCD camera was used with a shutter gating time of 100 μs. Video sequences (typically 10 s in duration, that is 250 individual images) were recorded onto S-VHS tape.

The NdYAG laser was installed in a clean room at one end of the furnace house. Mirrors were used to direct the laser beam towards the furnace. For safety reasons, the laser beam was enclosed in a two inch diameter steel pipe extending from the laser room to the light sheet slot.

The light sheet optics were mounted on brackets welded to the top side of the furnace. Providing suitable optical access for introducing the light sheet was difficult. The furnace had a number of attached sensors on the outside surface which precluded perpendicular access to the illuminated axial centre-line plane of the flow. A small slot was cut into an upper corner of the furnace wall and parallel to the furnace axis. A single 1 m focal length converging spherical lens was used to reduce the beam diameter in the furnace to a waist of approximately 1 mm. The light sheet was produced by a combination of two negative cylindrical lenses (focal length -12.7 and -25.4 mm). Simple uncoated optics were used. The laser sheet was introduced through a 50 cm slot located at 40 ° above the horizontal plane. The illuminated area extended to about 1.5 m from the furnace front wall. The path length of the laser sheet inside the furnace was estimated to be approximately 3 m.

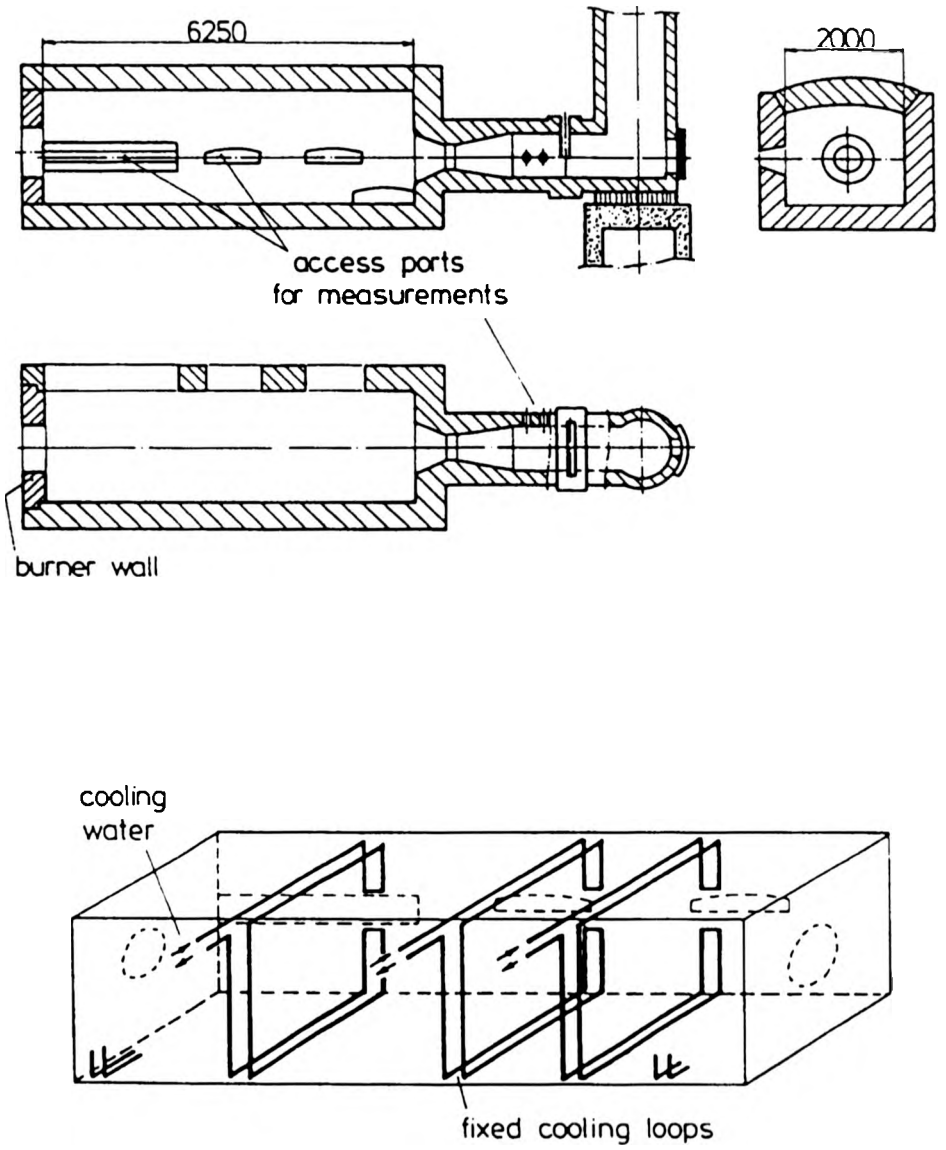

Figure 133. IFRF No. 1 furnace schematic

The optics mounted directly on the furnace surface suffered slightly from vibration induced by the normal operation of the furnace (fuel feeding, main air flow and flue extraction). The optics were sufficiently large that the position of the beam did not deviate significantly from optimum positions on the mirrors and lenses. This vibration caused the generated light sheet to

move correspondingly. The maximum sheet movement was estimated to be 2-4 mm by viewing the light impinging on the quarl surface under cold running conditions. Here it was possible to physically enter the furnace and observe the light scattered from the surface at close quarters. A somewhat larger source of sheet displacement was caused by refractive index gradients within the combusting flow. This was harder to measure, but observations through the port window indicated that it was 4 cm at most. The total sheet displacement was considered acceptably low, when compared to the relatively poor spatial resolution of the video camera.

The illuminated plane of the flow was viewed through ports in the side of the furnace which were only opened for short periods to prevent damage to the camera by radiative heating. As before, cooling was supplied to the sheet optics and camera using compressed air. Even so, some degradation of the video image was noticeable, with noise levels somewhat higher as a result of the thermal shot noise in the CCD sensor.

The experimental programme was designed to perform LSI in a number of different burner configurations including different fuel injector designs, swirl levels and gun positions. The effect of fuel injector design on jet mixing was studied in cold flows and gas flames by using a gas gun with different injection modes. The coal gun was of the type used for the IFRF aerodynamically air staged burner (AASB).

A schematic of the AASB burner used in this study is shown in Figure 134. This low-NOx coal burner has been extensively tested at the IFRF [111]. For visualisation in cold flows and gas flames, the coal gun was replaced by a gas gun. The gas gun featured three different injection modes which resulted in flames with different mixing characteristics. Gas could be injected through 12 radial holes, through an annulus or through a central hole.

Both the primary jet and the secondary air could be seeded. The seeding systems were based on the cyclone design described by Glass and Kennedy [112].

Measurements undertaken

The large size of the furnace gives a consequently high running cost, and it was necessary to "piggyback" the LSI study [113] onto an existing LDA measurement programme (AP20). The furnace required many hours to attain operating temperature, so measurement runs had to be

carefully planned. Access to the furnace was only possible after the LDA measurement period, so this entailed doing all of the LSI work at night. Unlike before, coal flames were now fully self-supporting once operating temperature had been established. This was due to the large size of the furnace, and the correspondingly large thermal power giving sufficient re-radiation from the refractory lining to maintain coal combustion.

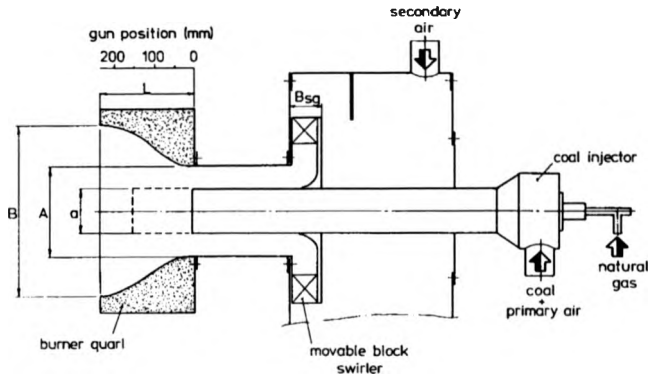

Figure 134. Schematic of the AASB burner

The inlet swirl number was varied between 0 and 1.2. The gun position was either at the quarl throat (GP=0) or pushed close to the middle of the quarl (GP=100). The experiments were carried out in four night shifts.

Table 7 and Table 8 list the detailed burner input conditions used for cold flows, gas and coal flames.

Secondary air flow	M_s=3000 kg/h T=270 °C V_s=46 m/s
Pilot flame	20 kg/h gas through D 300 kg/h air through E V=60 m/s
Primary gas input configuration 1	radial injection 180 kg/h through A V_p=53 m/s

	T=20 °C
Primary gas input configuration 2	radial and central injection 90 kg/h through A, V_{pA}=26.5 m/s 90 kg/h through B, V_{pB}=266 m/s
Primary gas input configuration 3	annular injection 180 kg/h through C Vp=103 m/s

Table 7. Gas burner inputs

Secondary air flow	M_s=2800 kg/h T=270 °C
Primary air flow	M_p=500 kg/h, T=70 °C M_{coal}=280 kg/h V_p=19 m/s

Table 8. Coal burner inputs

The viewing window was not ideal, with the angle of view rather restricted by the thick refractory layer. In addition, the aperture became further reduced when running with coal, due to slag deposition.

Discussion of results

Again, isothermal flows and gas flames were studied as well as coal flames, this time with thermal powers up to 3 MW. The gun position and swirl number were varied for coal feed rates between 200 and 300 kg/hour.

LSI of the isothermal flows and gas flames was again completely successful. On the other hand, video recordings of the largest coal flames, although revealing the penetration and spread of the coal jet, show less detailed structure than in the No. 2 flames. This was partly because of the oblique optical geometry. Combustion radiation was a greater problem than in the previous work, although laser scattered light could still be detected against the brighter background. The schematic in Figure 135 shows the position of the gun, quarl and light-sheet in the subsequent LSI images.

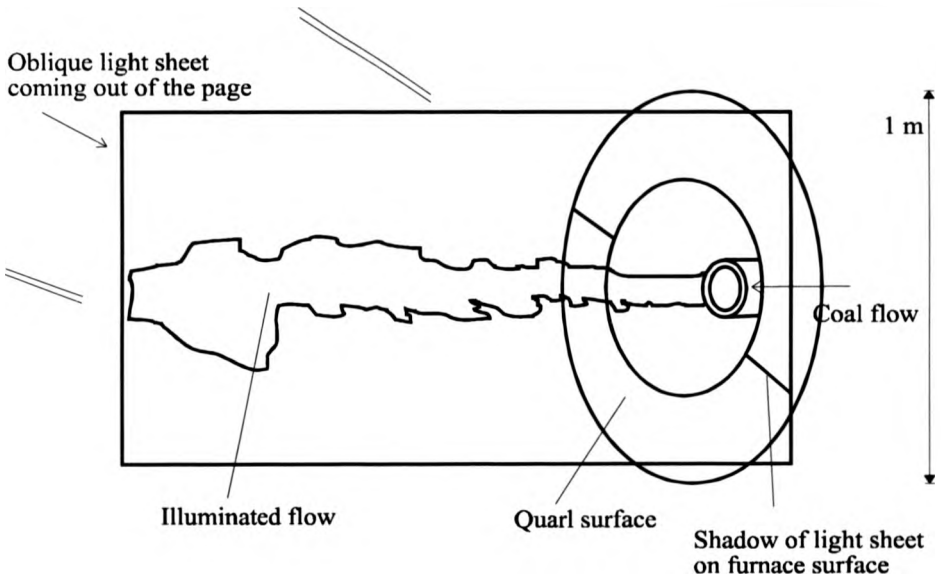

Figure 135. Schematic of LSI view in IFRF No.1 furnace

Cold flows;

Figure 136 shows the primary jet issuing from the annular injector for two secondary air swirl levels (S_0=0 and 1.4). The jet flow rate and outlet velocity were 260 kg/h and 103 m/s. The two photographs of this figure were taken a few seconds after seeding was switched on, and represent a stationary, developed jet. The bottom photograph (S_0=0) shows a long and narrow primary jet with little mixing in the radial direction. Vortices issued from the jet are entrained downstream with the main flow, and the video recording shows that part of the jet fluid is eventually recirculated in the external recirculation zone.

The top photograph shows the primary jet for a secondary air swirl level S_0=1.4. The swirling flow results in axial and radial pressure gradients which cause the annular jet to expand radially in the secondary air stream immediately after leaving the gun. The dark unseeded region inside the jet indicates the internal recirculation zone established by the strongly swirling flow. Observation of successive frames shows eddies shedding from the jet and recirculating towards the gun into the internal recirculation zone.

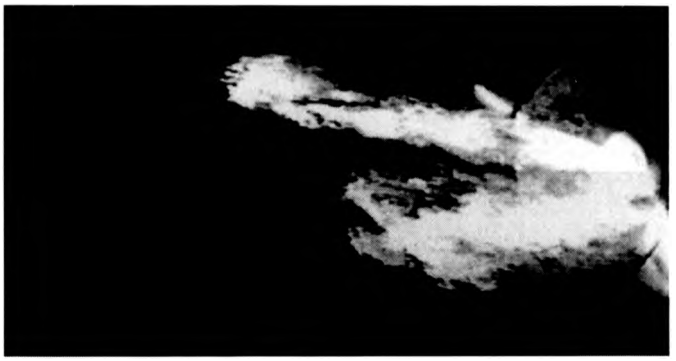

S_0=1.4

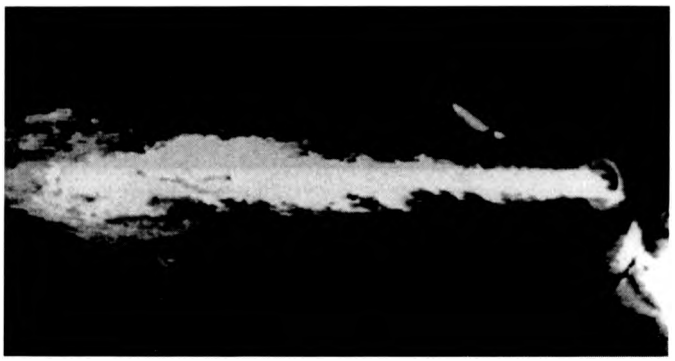

S_0=0.0

Figure 136. LSI images of isothermal flow in IFRF No. 1 Furnace

Figure 137 displays a narrow columnar flow observed in many of the cold swirling flow configurations. This visualisation was achieved by continuously seeding the secondary air stream until the entire furnace was filled with scattering particles. The uneven light intensity of the rapidly expanding light sheet can be seen. The dark column at the furnace centreline is thought to represent a recirculating stream coming from as far away as the flue chimney. The video recordings provide an animation of this column, which is seen to oscillate slowly around the furnace centreline and persist over several video frames. This persistent column implies a slow reverse velocity and weak turbulent exchange with the surrounding flow. This columnar flow, also known as a Prudman-Taylor column, is a well-documented feature of swirling flows and has been previously described by Hagiwara and Bortz [114].

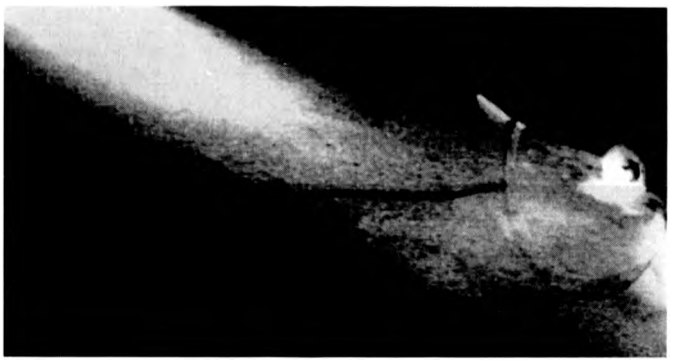

Figure 137. LSI image of isothermal columnar flow in IFRF No. 1 Furnace

Gas flames;

The three photographs of Figure 138 show that pulsing the seeding in the secondary flow can reveal different aspects of the flow. This figure shows 2.5 MW swirling gas flames produced with the radial injector. The top photograph, which was taken immediately after seeding was switched on, shows that the secondary stream issued from the quarl is concentrated along the quarl wall. The dark (unseeded) area within the secondary air stream reveals the stagnant central recirculation zone attached downstream of the gas injector. The middle photograph, taken a few seconds later, shows the centreline region filled with particles, as a result of the internal recirculation flow. The bottom photograph was taken after the seeding was stopped. The boundary between the external recirculation zone still full of particles, and the unseeded flow issuing from the quarl is clearly visible. These zone contours could be observed for 10 to 20 seconds, indicating the long particle residence time in the external recirculation zone. It was also observed that the average particle residence time in the external recirculation zone depended on the swirl level and was shorter at high swirl than in non-swirling flows.

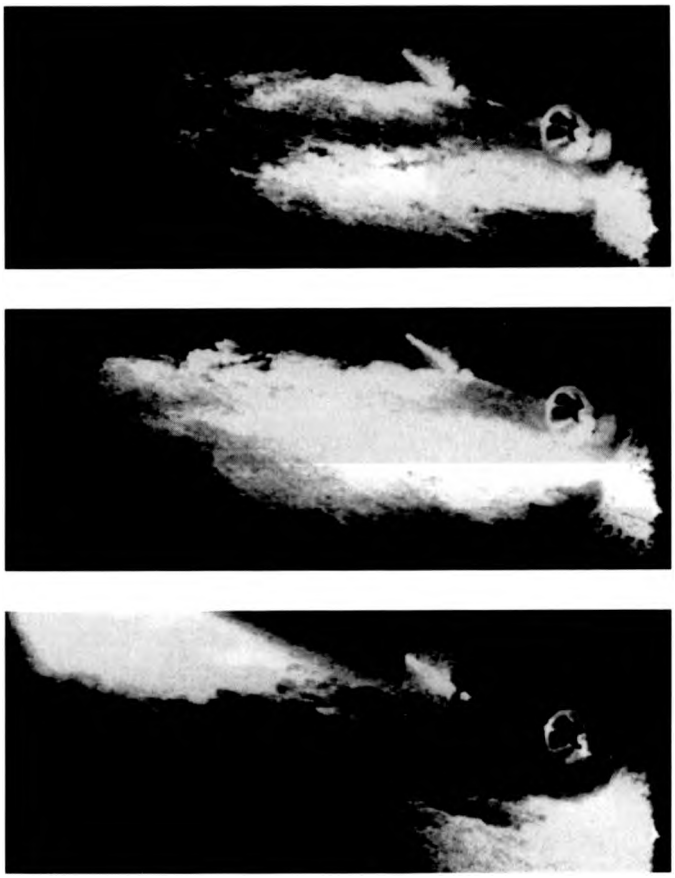

Figure 138. LSI image sequence of a gas flames in IFRF No. 1 Furnace

Coal flames;

LSI in coal flames was seriously restricted by the very high particle loading, which strongly absorbed the laser light. Figure 139 shows two examples of illuminated coal flames with the injector located at the quarl throat or pushed inside by 150 mm. As previously, the very bright area on the left side of the top photograph is the result of the uneven light sheet intensity scattering from particles in the external recirculation zone. The poor image quality is a result of strong absorption of the laser sheet, causing resultant non-uniform illumination of the flow. It is only possible to distinguish in the photograph that the maximum coal concentration is located along the quarl wall, indicating that the coal jet is entrained by the secondary air.

Pushing the injector inside the quarl (bottom photograph) resulted in still higher particle loading which acted to absorb the light sheet completely. This can be observed from the lack of laser light scattering from the right side of the quarl surface. The grey cloud issuing from the burner is caused by residual flame radiation, indicating that the camera exposure of 100 μs is not short enough to fully suppress radiation from these very luminous flames.

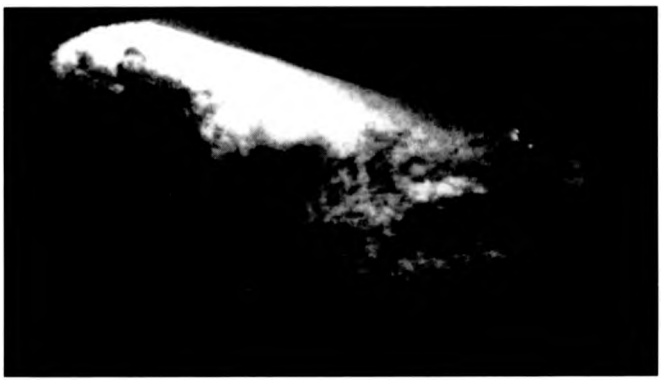

GP=0

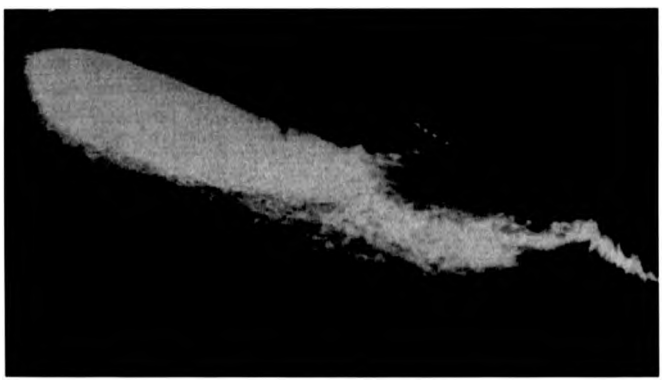

GP=150

Figure 139. LSI images of coal flames in IFRF No. 1 Furnace

The limitations to the success of the LSI technique for combusting measurements were caused mainly by the large size of the furnace. This had several effects, the first being the need for greatly expanded and consequently less intense laser illumination. In conjunction with the brighter combustion radiation background, this caused the visibility of the coal particles to be

significantly reduced. The second effect was that the necessarily long optical path lengths combined with the high density of the coal particle field caused considerable absorption and multiple scattering of the laser light. It was found that even the un-expanded NdYAG laser beam failed to penetrate the coal jet at times. This caused the approximately constant intensity profile illuminating light sheet to be degraded severely, and additionally to partially or fully obscure the illuminated plane from the imaging camera.

The first limitation, insufficient illuminating intensity, could certainly be overcome, by using a higher power laser. This would increase the visibility of the illuminated particles against the combustion background. However, this would be expensive, and the larger size of laser would reduce its portability and hence flexibility. Most importantly, a larger laser would probably necessitate using a lower pulse repetition rate, due to pumping flash lamp energy restrictions. A lower pulse rate would remove the convenience of real-time 25 Hz video recording.

The second limitation, the high optical absorption and multiple scattering, is more restrictive. Using more laser power would simply mean that more light is absorbed, with no real improvement in image quality. Improvements in the technique and extension to even larger coal flames are therefore only likely to be possible by inserting the beam into the centre of the flame using some form of water cooled probe similar in design to that used by Ereaut and Gover [90] for LDA furnace measurements. The probe would protect the beam from absorption, ensuring a high intensity in the measurement plane. The probe diameter would be necessarily large, to contain the water cooling system and optical lenses. It is unlikely that fibre optics could be used to reduce the size of the optics as there is currently no fibre that can transmit the high peak laser power without rapid destruction. This physical probe solution removes one of the big advantages of optical measurement, the non-intrusiveness of the technique.

5.7.2 RISØ furnace measurements

The IFRF No. 1 measurements revealed two limitations to the LSI technique for large coal furnace measurements. These were now explored in a further experimental study, and further optimisations made to the LSI experimental equipment in an attempt to overcome them.

Experimental equipment and measurements undertaken

The No. 1 furnace was somewhat inflexible in use, and so the research furnace at the RISØ national laboratory in Denmark was chosen for this further work. The running costs and availability were also superior to the No. 1 furnace. The RISØ furnace is rated at 2 MW and was designed specifically for laser measurements. The furnace is a horizontal cylinder, 4.5 m long and 1.2 m in internal diameter with a small sudden contraction near the end, see Figure 140. Optical access was much easier than for the previous furnace measurements. The furnace has a number of horizontal access ports, each water cooled, and several vertical slots. An air-purged and water cooled window was mounted on the particular port being used for flow imaging.

Both isothermal and combusting flows were studied; the furnace was fitted with an experimental swirl stabilised burner, giving a rated power of 1.4 MW. The furnace facility was fully instrumented and computer controlled, enabling a constant flow condition to be accurately maintained. Flyash was available to seed isothermal flows, and although the feed rate from the seeder was sufficient, the small supply reservoir required frequent refilling. Pulverised coal was therefore injected through the gun for most isothermal runs, using the same handling equipment as for normal combustion. In these cases, however, the supply was limited to periods of 10-20 seconds in order to lessen the risks of ignition in the preheated air flow. In addition, after a longer time period, isothermal coal particle concentration reached a level where attenuation of the laser beam became excessive.

As before, the NdYAG laser and video recording were used. However, a new camera was now employed, a Sony XC-77/RR-CE model. This new camera had two advantages. The first was that it was a remote-head camera, with a small imaging sensor and separate electronics and power supply. This made it easier to get it closer to the furnace, and its small size meant a smaller thermal capacity so that air cooling was much easier. The second and more significant advantage was a 1 μs shutter gating facility. This gave an improvement of over three f/stops in image/background intensity ratio over the JAI camera. However, the short gating interval increased the demands on the laser synchronisation unit, and some modifications had to be made to increase stability so that the 15 ns laser pulse remained consistently within the 1 μs gating period, throughout the duration of the measurements.

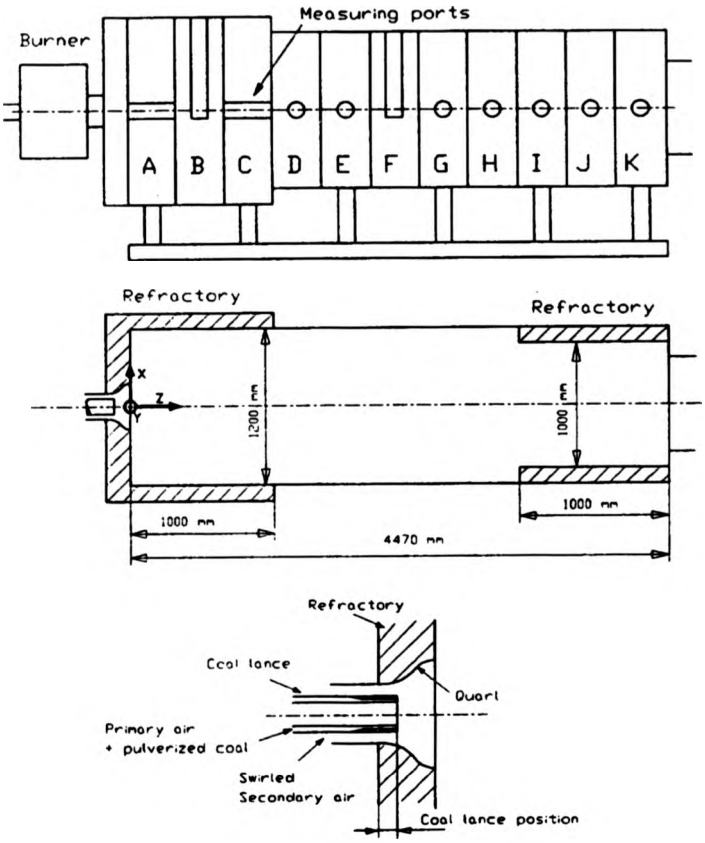

Figure 140. RISØ furnace schematic

The laser/video synchronisation unit was further modified to provide two output signals, each of 25 Hz, but with differing phase. Each signal was synchronised to one field of the video image, and then used to trigger one of the oscillators of the laser. Thus the 25 Hz double oscillator laser was able to supply a 50 Hz output, thereby doubling the temporal resolution of the technique. No video resolution was lost, as previously one of the interlaced fields was not used. As before, Figure 141 illustrates the sychronisation of the laser pulses to the video signal.

Laser backlighting was attempted for this study in addition to LSI. As described previously, a pulsed laser is used to back-illuminate particles which are then captured on film onto a CCD camera. The form of each particle image captured is a sharp silhouette of an object against a bright background. Use of a high magnification lens results in a limited field of view but the

ability to capture high resolution images of individual particles. A new imaging lens was employed for this study.

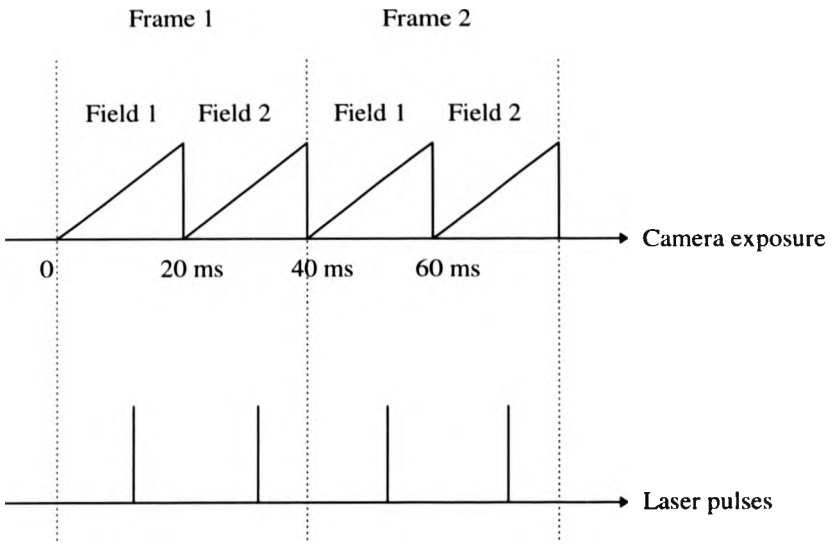

Figure 141. Laser synchronisation to both video fields

The previous 12 mm lens was used for all of the LSI work, while an Infinity Corp. K2 long range microscope lens was used for the backlighting. This K2 lens was used as it gives high magnification (X 0.9), but with a long working distance (1 m). A high magnification is needed to resolve the actual shape of the particle. Conventional LSI images only have sufficient resolution to show a single illuminated pixel for each particle. The large furnace diameter precluded use of conventional macro lenses which have a working distance of only a few mm's. Tests [115] indicated that at a working distance of 1 m, the effective focal length was 584 mm with a depth of field of 0.95 mm. The main disadvantage of this lens was its small effective aperture, and consequently slow f/number (f/38) in comparison to the conventional lenses. This meant that high intensity back illumination was needed to obtain sufficient contrast in the backlit image.

Backlighting was carried out by expanding the NdYAG laser beam with a spherical diverging lens and directing it onto a white diffusing screen placed close to a port on the opposite side of the furnace to the viewing port. The screen was made of 3 mm thick opalescent plastic, which gave a good diffusion of the incident light, thereby providing even backlit illumination. In

initial trials the plastic suffered from softening and consequent distortion as a result of heating by the intense furnace radiation, so air purging was used to cool the screen. A schematic of the backlighting optics is shown in Figure 142.

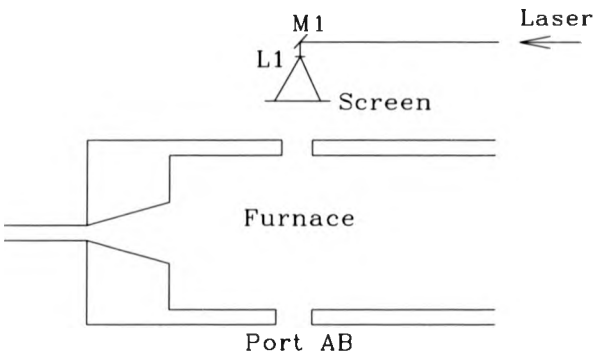

Figure 142. Schematic of backlighting in the RISØ furnace

For some of the LSI measurements, as before, the laser beam was steered into the furnace from above, through a small slot cut through the refractory lining. Cylindrical optics were placed into an air purged tube which was lowered slightly into the furnace to increase the field of illumination.

The previous work with the No. 1 furnace indicated that strong absorption and scattering of the light sheet before reaching the measurement zone was a problem. A new method of introducing the light sheet was thus attempted. The laser beam was guided down the burner centre-line through an aperture in the burner used for inserting the flame ignitor. The beam was then expanded into a sheet just before the mouth of the annular gun. Initial attempts at aligning the light sheet were unsuccessful due to the need to remove the LSI optics for flame ignition on combustion start-up. When re-inserted, it was difficult to determine the optical alignment with the bright flame visible. A probe tube was therefore designed to guide the laser beam and to hold the optics close to the mouth of the gun. The tube was machined to accurately fit the aperture, and allowed precise and repeatable optical alignment. The two optical geometries employed are shown in Figure 143. The design of the tube is shown in Figure 144.

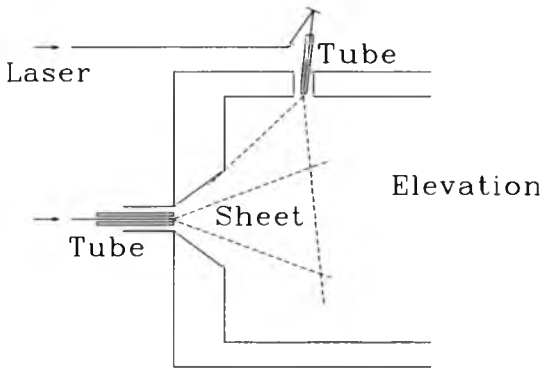

Figure 143. LSI optical configurations in the RISØ furnace

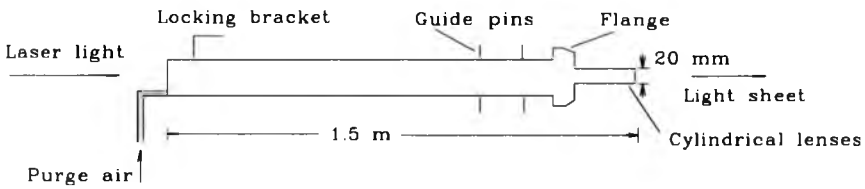

Figure 144. Design of RISØ optics for insertion into the burner

Discussion of results

The schematic in Figure 145 shows the position of the gun, quarl and light-sheet in the following LSI images.

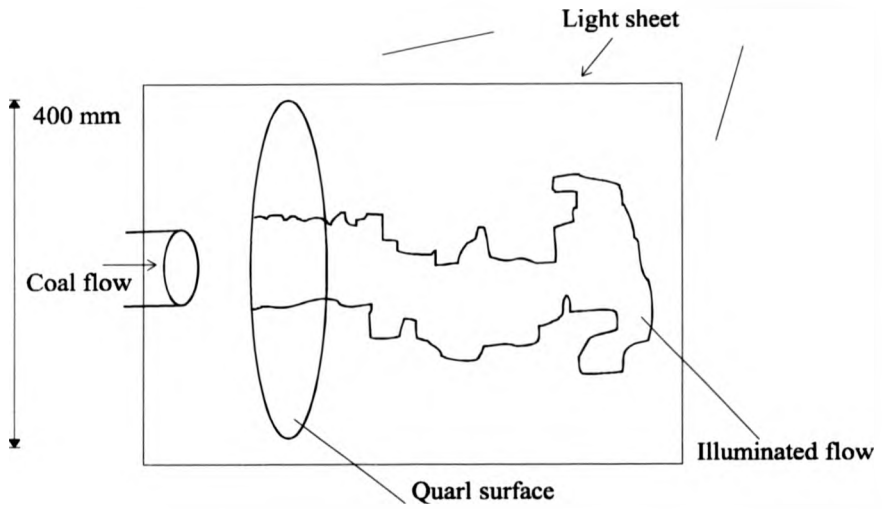

Figure 145. Schematic of LSI view in RISO furnace

Isothermal flows;

In a series of experiments the coal gun was pushed 70 mm forward into the furnace and the swirl level set to zero. The laser sheet was introduced through the top of the furnace. Figure 146 shows a still video picture. A long jet can be seen emerging from the coal gun. The particles leave the gun as an annulus but "internal" mixing occurs rapidly, quickly forming an apparently solid jet. Further downstream "external" mixing takes place by large vortices (several tens of cm's in diameter), indicating turbulence at large length scales. When the swirl level of the secondary air is raised to 0.08, the jet is preserved, Figure 147. At a level of 0.34 the jet is observed to become unstable and fluctuates strongly, Figure 148. At a higher level of 0.7, a broad jet leaves the quarl and then almost immediately disperses, Figure 149.

Figure 146. LSI image of isothermal flow in RISØ furnace, S_0=0

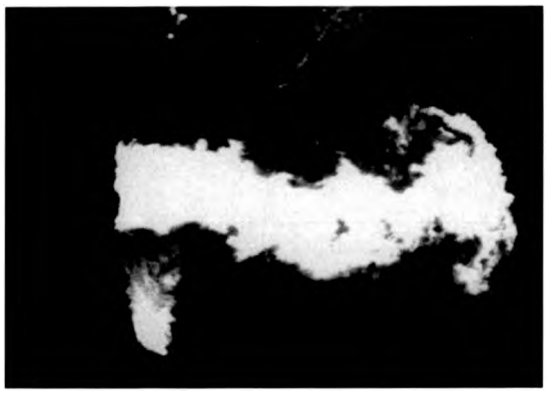

Figure 147. LSI image of isothermal flow in RISØ furnace, S_0=0.08

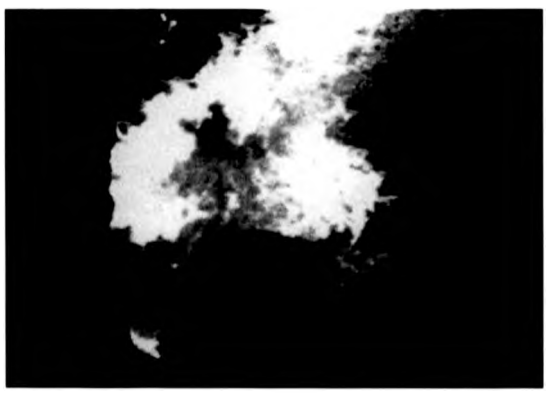

Figure 148. LSI image of isothermal flow in RISØ furnace, S_0=0.34

Figure 149. LSI image of isothermal flow in RISØ furnace, S_0=0.7

Further "isothermal" measurements were taken with the secondary air heated to 200 °C. Swirl level was varied with the coal gun at a position of +35 mm. A swirl level of 1.16 corresponds to the standard running conditions, Figure 150. In this case the particles are very well distributed in the entire quarl area. It can be seen from the very first introduction of seeding that the particles disperse into the recirculation zone of the flow.

Figure 151 shows the effect of the through-gun illumination. The illumination in the immediate quarl area is more intense, allowing the extent of the particle field to be easily determined. The high particle density tends to absorb and scatter the illumination rapidly though.

Figure 150. LSI image of isothermal flow in RISØ furnace, S_0=1.16

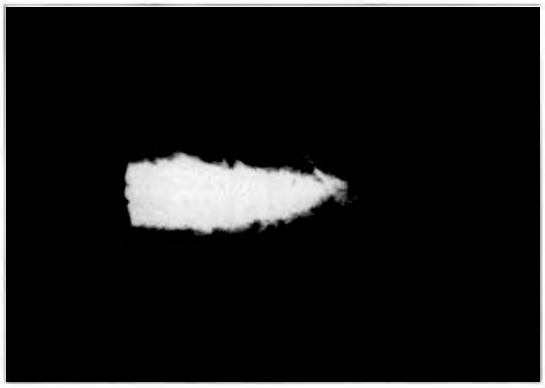

Figure 151. LSI image of isothermal flow in RISØ furnace with through-gun optics, S_0=0

Backlighting was found to be suitable only in locations where attenuation from the particle loading was somewhat less than the maximum possible. Because of the restricted depth of field of the K2 lens, only relatively few coal particles images were captured. Yet as a basic technique for capturing high resolution images of individual particles in flight, the method worked extremely well and a number of good quality images were recorded. One of these is shown in Figure 152, obtained in this case from an isothermal zero swirl flow with GP=+35 mm. Particle size estimated from this image is a highly irregular 50 μm. Measurements over several particles indicate typical dimensions of approximately 20 μm, but with occasional particles being much larger.

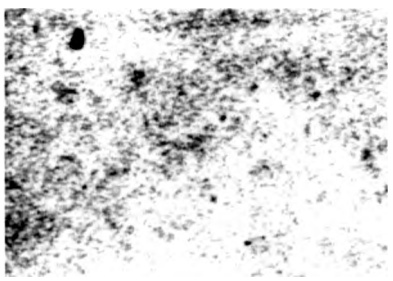

Figure 152. Backlit image of a coal particle in the RISØ furnace

Flame measurements;

LSI measurements were successfully performed in the 1.3 MW coal flame at standard running conditions, the coal seeding supply was not pulsed as for the isothermal runs, but continuous.

The laser sheet itself and subsequent camera view of it suffered from considerable attenuation due to the increased particle loading.

The distribution of coal particles, Figure 153 looked very similar to the isothermal experiments at the same running conditions, Figure 150. When the swirl was lowered to 0.34, Figure 154, the entire quarl exit area was still filled with particles but of variable density and areas with particle loading can be observed, maybe corresponding to coal ropes. Sheet attenuation is particularly high in this image, but the top and right hand edges of the coal distribution can be seen. By visual inspection, a very large "fluffy" flame is seen. When the swirl number is further lowered to 0.18 a clearly defined jet of particles can be seen, Figure 155. Absorption of the laser sheet can be clearly seen from the reduction in brightness from the top to the bottom of the jet.

The through-the-gun optics were again used, but were found to be much less successful than for the isothermal work. The sheet appeared to penetrate only a short distance (a few cm) into the coal jet. This was thought to be due to the increased particle loading under combusting conditions.

Figure 153. LSI image of coal flame in RISØ furnace, S_0=1.16

Figure 154. LSI image of coal flame in RISØ furnace, S_0=0.34

Figure 155. LSI image of coal flame in RISØ furnace, S_0=0.18

No backlighting images could be obtained under combusting conditions. The higher particle loading absorbed considerably more light, resulting in a dim image. No particle images could be discerned. This was thought to be due to the high refractive index gradients in the hot air causing severe distortion of the imaging wavefront. The K2 lens is particularly sensitive to such effects due to its high magnification.

5.8 Conclusions on measuring in coal furnaces

The above studies have shown that laser sheet visualisation is a powerful method for studying the primary jet mixing with the secondary air, and the interaction with the internal recirculation zone. The method was used to observe the jet length, shape and its fluctuations. The fast and global view of the flow obtained from LSI makes this technique a very valuable complement to

the more detailed but time-consuming LDA technique for furnace measurement. The LSI technique seems to be limited ultimately by the furnace particle loading, which causes absorption of the laser illumination, and obscuration of the resulting flow field image.

Useful information was obtained for the near burner fuel distribution in pulverised coal flames up to 1.3 MW. It is thought that this is approaching the practical limit for LSI based visualisation in pulverised coal furnaces. Above this burning rate, the effects of laser attenuation become severe, while combustion luminosity is less of a constraint. However, for furnaces with lower particle loadings, such as oil or gas, this attenuation is not a problem and it is expected that the technique could be used in higher power furnaces.

Image processing has shown itself to be useful for extracting more quantitative information from LSI images. Regions of flow instability and significant mixing were identified.

Backlighting of isothermal and combusting flows was attempted. For the former, images of individual coal particles were successfully recorded. The presence of refractive index gradients in the combusting flows caused sufficient distortion of the image wavefront that no particle images could be discerned.

The attenuation problems inherent with the LSI technique could be reduced through the use of shielding to limit the input beam exposure to the particle field. This could take the form of a water cooled probe similar to that used for large scale LDA furnace studies, although care would need to be taken to minimise the physical intrusiveness of such a probe.

It has thus been found that LSI in coal furnaces gives best results where the flow is dispersed (away from the immediate burner outlet), and where absorption is relatively low. LSI has been shown to be particularly useful when seeding can be pulsed and applied to separate streams within a flow. This can reveal large scale recirculations and can enhance boundary features that may be present in a flow.

6. Conclusions and recommended areas for future research

Before final conclusions and recommendations are made, the following section describes developments occurring recently in some of the measurement techniques discussed, and some developments expected in the future.

6.1 Future developments

Global optical diagnostics such as particle image velocimetry are currently being researched by a large number of groups around the world, and consequently are developing rapidly. Particular effort is being focused in certain areas, these being increasing the spatial and temporal resolution of imaging, increasing the speed, degree of automation and robustness of automated analysis, and looking at three dimensional behaviour, rather than just two. The following sub-sections describe improvements to VISIFLOW made since the experiments described previously, and new global techniques which show promise.

6.1.1 VISIFLOW

The VISIFLOW PIV software continues to undergo changes, and is now considerably more powerful than described previously. A cross-correlation analysis option has been added to the auto-correlation and particle tracking options already present.

Cross-correlation allows the easy resolution of directional ambiguity, and also extends the dynamic range of PIV beyond that possible with single-frame analysis, due to the much smaller particle displacements that can be measured. Particle displacements of less than one pixel between the two frames can now be easily measured. The analysis time for cross-correlation is slightly longer, due to the need for three 2-D FFTs rather than two for auto-correlation.

Program code has also been added to allow use of a faster array processor (Alacron FT200). This gives a performance of up to 200 MFLOPS, allowing 128 x 128 pixel area auto-correlation analysis to be computed in about 0.05 seconds per vector. This is approximately ten times faster than previously achieved. The new array processor also has a digital input interface which allows connection of a slow scan CCD camera, such as the 2048 x 2048 pixel Kodak MEGAPLUS 4.2. This camera gives near photographic quality images at a 2 Hz

framing rate. The combination of the fast processor and high resolution camera gives an on-line capability to the system, allowing results to be obtained in near real-time.

The VISIFLOW software has also been modified to support connection of a TWAIN scanner. This is a document or film scanner controllable through a standard (TWAIN) interface. Now, printed photographs or original film strips can be scanned directly via the software, making the analysis process more convenient.

The post-analysis part of the software has also been improved. Animation of a sequence of vector datasets allows the temporal development of a flow to be visualised. Flow streamline plotting has also been added. The streamlines are computed by placing one or more imaginary particles into the flow and mapping their progress by computing the local velocity experienced by them as they move.

Most recently, a 32 bit version of VISIFLOW has been written. This allows native operation under the new Microsoft Windows NT and Windows 95 operating systems. The advantage of the 32 bit code is that analysis performance is more than twice as fast, and multi-tasking is considerably smoother.

6.1.2 Doppler global velocimetry

In 1991, Komine et al [116] developed a new laser Doppler velocimeter. Instead of using heterodyne detection as for LDA described previously, Komine used the edge of an absorption line in iodine vapour as an optical frequency discriminator to provide a direct measure of the Doppler frequency. Adjusting the laser frequency to the midpoint along the edge, the scattered light from a stationary object in the laser beam would be attenuated 50 % as it passed through the Iodine vapour cell. If the object were moving through the laser beam, the scattered light would be attenuated more (or less if the direction of travel were reversed) by the iodine vapour since the Doppler effect would change the frequency of the scattered light. The greater the velocity, the greater (or less) the attenuation.

This technique is known as Doppler global velocimetry (DGV). The technique measures the velocity of an entire illuminated plane. There is the potential for instantaneous velocity measurement using a pulsed laser source, or mean velocity measurement using a c/w laser and an integrating detector. The simple processing requirements of the technique compares

favourably to PIV where considerable post-processing is necessary. Development of DGV may result in fully real-time whole-field velocimetry. In addition, discrete seed particle images are not needed as they are for PIV, only that sufficient light is scattered from the flow to trigger the detector.

The simplicity of the DGV optical configuration is attractive, and images do not need to resolve individual particles unlike PIV. The technique is most suitable for fast flows, where the Doppler shift is significant, i.e. typically 10's of m/s or more. The DGV technique has now been applied to a number of flows, e.g.[117] [118].

A short feasibility study has been carried out by the author[119], regarding the suitability of the technique for the measurement of sprays such as the diesel sprays discussed here. The study concluded that DGV is a potentially valuable technique for application to industrial flows due to its robust nature.

One disadvantage found is the need for a single, extremely narrow and stable laser wavelength. This was readily achieved using the previously described Argon laser with its etalon. However, achieving long-term stability of a single mode was difficult, and a robust implementation would require active stabilisation of the laser cavity and mirrors. The lack of laser stability also made calibration of the technique difficult due to the need to remain precisely at the same point on the iodine absorption spectrum.

6.1.3 Three dimensional global diagnostics

Many flows are best studied using fully three dimensional flow diagnostics. These are flows that have a significant out of plane component, for example, a swirling flow. Two dimensional diagnostics such as PIV can only view a projection of the flow into the measurement plane.

Some work has been done using conventional PIV to measure three component velocities e.g. [120] [121] [122]. Methods used often encode the sheet in some way, i.e. with an intensity or colour change across its waist, or use multiple camera views (stereoscopy). However, three component velocities are still only measured within a single plane in the flow.

True three dimensional techniques such as holography are needed to measure three component particle velocities throughout an entire volume in the flow. Pulsed holography is already widely used to visualise gas density fluctuations and particle field distributions. A number of

problems need to be overcome however, before holographic velocimetry becomes fully practicable. The main two problems are

1. The need for a hardened and preferably simplified image recording and replay system, comprising laser, automatic camera, film development and reconstruction optics.

2. The lack of fast, robust processing algorithms for determining three dimensional vectors across a three dimensional field.

A number of research groups are working in this area, e.g. [123] [124]. The ultimate in velocimetry, time-resolved three dimensional measurement is also coming closer. Holographic cinematography is already viable [125], and quantitative velocimetry will follow as analysis algorithms improve.

6.2 Conclusions

The use of global diagnostics for combustion applications has been explored. Laser sheet illumination in particular, has been shown to be a powerful tool for visualising flow behaviour under difficult environments similar to those found in industrial applications.

For diesel sprays, pulsed LSI has revealed the complex flow field where the spray impinges against a surface. This spray-surface interaction is a common occurrence in diesel engines. The combination of a drum camera and high repetition rate pulsed laser has allowed the temporal development of an individual spray event to be studied. The flow images suggest that the spray impingement seems to behave according to the jet impingement model [9]. Visualisation of diesel films resulting from spray impingement onto a surface has revealed a complex distribution of material and shown its temporal development.

LSI has been applied successfully, for what is thought to have been the first time, to the visualisation and measurement of semi-industrial scale coal flames. The combination of a short gated video camera and pulsed laser successfully overcame significant combustion luminosity to reveal particulate distribution in flames of up to 2.5 MW thermal power. Larger flames than this are thought to be inaccessible with current LSI methods, due to the problems of excessive light absorption and scattering in the dense flow. However, it may prove possible to study larger flames using some form of cooled probe, at the expense of flow intrusion and a reduced field of view.

For PIV analysis, a hardware system based on a PC, capable of accepting photographic and video images has been developed. A software package (VISIFLOW) has been developed to work with this system. It is believed that the software has eased the application of the rapidly developing PIV technique considerably.

The author considers that global techniques will continue to develop, becoming the mainstays of flow measurement, where the lack of flow disturbance and/or harsh environmental conditions necessitate non-invasive diagnostics. Expected advances in laser, video and computer technology will benefit whole-field diagnostics considerably.

6.3 Recommendations

For PIV, high resolution video imaging should be implemented, together with software that increases ease of use, and provides more intelligent, automatic, post-processing to further reduce incorrect data. Three dimensional velocimetry analysis algorithms need considerable effort, to increase their efficiency and robustness when processing detailed flow images. In conclusion, it is recommended that additional research investment be put into global optical diagnostics to further improve their suitability for application to realistic combustion flows.

6.4 References

1. Frankl G., Barker B.G. and Timms C.T., "Electronic unit injectors for direct injection engines", Diesel Fuel Injection Systems, I Mech E Seminar, MEP, London, (1989).

2. Rao K.K., Winterbone D.E. and Clough E., "Combustion and emission studies in high-speed DI diesel engines", I Mech E Paper C448/070, (1992).

3. Wachters L.H.J. and Westerling N.A., "The heat transfer from a hot wall to impinging water drops in the spheroidal state", Chem. Eng. Sci., **21**, pp1047-1056, (1966).

4. Cumo M. and Farello G.E., "Heated wall-droplet interactions for two-phase flow heat transfer in liquid deficient region", Proceedings of Symposium on Two Phase Flow Dynamics, Eindhoven, pp1325-1357, (1967).

5. Zhang S. and Gogos G., "Film evaporation of a spherical droplet over a hot surface: fluid mechanics and heat/mass transfer analysis", J.Fluid Mech., Vol. **222**, pp. 543-563, (1991).

6. Wachters L.H.J., Bonne H. and van Nouhuis H.J., "The heat transfer from a hot horizontal plate to sessile water drops in the spheroidal state", Chem. Eng. Sci., **21**, pp923-936, (1966).

7. Dimitrov D.S. and Ivanov I.B., "Hydrodynamics of thin liquid films. On the rate of thinning of microscopic films with deformable interfaces", J. Colloid Interface Sci., **64**, pp97-106, (1978).

8. Pandit A.B. and Davidson J.F., "Hydrodynamics of the rapture of thin liquid films", J. Fluid Mec., **212**, pp11-24, (1990).

9. Naber J.D. and Reitz R.D., "Modelling engine spray/wall impingement", SAE Paper 880107, (1988).

10. Wang D.M. and Watkins A.P., "Numerical modelling of diesel spray wall impaction phenomena", International Journal of Heat and Fluid Flow, **14** (3), pp 301, (1993).

11. Goldstein R., "Fluid mechanics measurements", Springer-Verlag, Berlin (1983).

12. Durst F., Melling A. and Whitelaw J.H., "Principles and practice of laser Doppler velocimetry", Academic, New York, (1976).

13. Barlow S.M., "Laser Doppler anemometry measurements in a large gas fired furnace", 1st Symposium on the Application of Laser Anemometry to Fluid Mechanics, Lisbon, (1982).

14. Thompson D.H., "A tracer particle fluid velocity meter incorporating a laser", J.Phys. E:Sci. Instrum. **1**, pp.929-32, (1968).

15. Durst F. and Zaré M., "Laser Doppler measurements in two phase flows", Proceedings of LDA Symposium, Copenhagen, pp.403-429 (1975).

16. Bachalo W.D. and Houser M.J., "Phase/Doppler spray analyser for simultaneous measurements of drop size and velocity distributions", Optical Engineering, **23**, pp. 583-590, (1984).

17. Dodge L.G., Rhodes D.J. and Reitz R.D., "Drop size measurement techniques for sprays: comparison of Malvern laser-diffraction and Aerometrics phase Doppler", Applied Optics, **26**, No. 11, (1987).

18. Eckbreth A.C., "Laser diagnostics for combustion temperature and species", Abacus Press, Tunbridge Wells, UK, (1988).

19. ed. Binder K., "Interaction of jets with walls", CEC Report JOUE-0012-D, (1990).

20. Gover M.P. and Ereaut P.R., Period Report for April 1991 to November 1991 for CEC Project "Diesel Combustion", (1991).

21. Ozdemir I.B., "Correlation between the size characteristics of the wall jet and the dynamics of the unsteady film formed after the impingement of an unsteady two-phase jet", Proc. 6th Symposium on the Application of Laser Anemometry to Fluid Mechanics, Lisbon, (1992).

22. Ting L.L., "Development of a laser fluorescence technique for measuring piston ring oil film thickness", Transactions of ASME, Journal of Lubrication Technology, **102**, 165-171, (1980).

23. Hoult D.P., Lux J.P., Wong V.W., and Billian S. A., "Calibration of laser fluorescence measurement of lubricant film thickness in engines", SAE paper 881587, (1988).

24. Richardson D.E. and Borman G.L., "Using fibre optics and laser fluorescence for measuring thin oil films with application to engines", SAE paper 912388, (1991).

25. Lux J.P., Hoult D.P. and Olechowski M.J., "Lubricant film thickness measurements in a diesel engine piston ring zone", Journal of STLE, **47**, 5, 353-364, (1991).

26. Shaw B.T., Hoult D.P. and Wong V.W., "Development of engine lubricant film thickness diagnostics using fibre optics and laser fluorescence", SAE paper 920651, (1992).

27. Sanda S., Saito A., Konomi T. and Nohira H., "Development of scanning laser-induced-fluorescence method for analysing piston oil film behaviour", IMechE paper C465/014/93, (1993).

28. ed. Yang W.J., "Handbook of flow visualisation", Hemisphere Publishing, New York, (1989).

29. ed. Véret C., "Flow visualisation IV", Hemisphere Publishing, New York, (1987).

30. Adrian, R.J., "Scattering particle characteristics and their effect on pulsed laser measurements of fluid flow: speckle velocimetry vs particle image velocimetry", Applied Optics, **23** (11), pp.1690-1691, (1984).

31. Adrian R.J., "Particle-imaging techniques for experimental fluid mechanics", Annual Review of Fluid Mechanics, Vol. **23**, pp.261-304, (1991).

32. Lourenco L.M. and Krothapalli A., "Particle image displacement velocimetry measurements of a three-dimensional jet", Physics of Fluids, Vol. **31**, pp.1835-1837, (1988).

33. Pickering C.J.D. and Halliwell N.A., "Speckle photography in fluid flows:signal recovery with two-step processing", Applied Optics, **6** (8), pp.1128-1129 (1984).

34. Gabor D., "A new microscopic principle", Nature, **161**, pp. 777-778, (1948).

35. Cartwright S.L., Dunn P. and Thompson B.J., "Particle sizing using far-field holography: new developments", Optical Engineering, **19** (5), pp.727-733, (1980).

36. Bryanston-Cross P.J. and Gardner J.W., "Holographic visualisation of a combustion flame", Opt. and Lasers in Eng., **9** pp.85-100, (1988).

37. Thompson B.J., Ward J.H. and Zinky W.R., "Application of hologram techniques for particle size analysis", Applied Optics, **6** (3), pp.519-526, (1967).

38. Schuster P.R. and Wagner J.W., "Holographic velocimetry for flow diagnostics", Experimental Mechanics, Vol. **28** (12), pp. 402-408, (1988).

39 Trolinger J.D. and Heap M.P., "Coal particle combustion studied by holography", Applied Optics, **18** (11), pp.1757-1762, (1979).

40. Desgroux P., Domingues E. and Cottereau, "Measurements of OH concentration in flames at high pressure by two-optical path laser induced fluorescence", Applied Optics, **31** (15), pp.2831-2838, (1992).

41. Gross K.P., McKenzie R.L. and Logan P., "Simultaneous measurements of temperature, density and pressure in supersonic turbulence using laser induced fluorescence", Experiments in Fluids, **5**, pp.372-380, (1987).

42. Andresen P., Bath A., Gröger W., Lülf H.W., Meijer G. and ter Meulen J.J., "Laser induced fluorescence with tunable excimer lasers as a possible method for instantaneous temperature field measurements at high pressures: checks with atmospheric flame", Applied Optics, **27** (2), pp. 365-378, (1988).

43. Lee M.P., Paul P.H. and Hanson R.K., "Quantitative imaging of temperature fields in air using planar laser induced fluorescence of O_2", Optics Letters, **12,** pp.75-77, (1987).

44. Shand A.M., "The use of fluorescence and total internal reflection to investigate diesel wall films", UKAEA Report, AEA-EE-0463, (1993).

45. van de Hulst H.C., "Light scattering by small particles", Dover Publications, New York, (1981).

46. Adrian R.A. and Yao C.S., "Pulsed laser technique application to liquid and gaseous flows and the scattering power of seed materials", Applied Optics, Vol. 24, No. 1, pp44-52, (1985).

47. Hjemfelt A.T. and Mockros L.F., "Motion of discrete particles in a turbulent flow", Appl. Sci. Res., **16**, pp149-161, (1965).

48. Basset A.B., "Treatise on hydrodynamics" Vol. II, Deighton, Bell and Co., London, (1888).

49. Hinze J.O., "Turbulence" (Second Edition), McGraw-Hill, (1975).

50. Melling A. And Whitelaw J.H., "Optical and flow aspects of particles", Proc. LDA Symposium, Copenhagen, (1975).

51. Kodak T-MAX Technical Datasheet.

52. Kodak MEGAPLUS 1.4 Technical Specifications.

53. Joyce-Loebl Ltd., "Image Analysis: Principles and Practice", Gateshead, UK, (1989).

54. Strickland R.N. and Aly M.G., "Image sharpness enhancement using adaptive 3x3 convolution masks", Optical Engineering, Vol. **24**, No. 4, pp683-686, (1985).

55. Westergaard C.H. and Buchhave P., "PIV: Comparison of three autocorrelation techniques", Proc. SPIE Vol. **2052**, Laser Anemometry Advances and Applications, pp.535-541, (1993).

56. Keane R.D. and Adrian R.J., "Theory of cross-correlation analysis of PIV images", Journal of Applied Scientific Research, Vol. **49**, pp.191-215, (1992).

57. Ramirez R.W., "The FFT: Fundamentals and concepts", Prentice-Hall, (1985).

58. Dudderar T.D. and Simpkins P.G., "Laser speckle photography in a fluid medium", Nature, **270** (5632), pp.45-7 (1977).

59. Meynart R., "Instantaneous velocity field measurements in unsteady gas flows by speckle velocimetry", Applied Optics, Vol. **22**, pp.535-40, (1983).

60. Ansari F. And Ciurpita G., "Automated fringe measurement in speckle photography", Applied Optics, Vol. **26** (9), pp.1688-1692, (1987).

61. Huntley J.M., "An image processing system for the analysis of speckle photographs", J. Phys. E: Sci. Instrum., Vol. **19**, pp.43-49, (1986).

62. Coupland J.M. and Halliwell N.A., "Particle image velocimetry: rapid transparency analysis using optical processing", Applied Optics, Vol. **27** (10), pp.1919-1921, (1988).

63. Jacobsen, M.L. and Buchhave, P., "PIV Processing: Parallel processing with optical correlators", Proc. 5th Symposium on the Application of Laser Anemometry to Fluid Mechanics, Lisbon, (1990).

64 Mao Z.Q., Halliwell N.A. and Coupland J.M., "Particle image velocimetry: high-speed transparency scanning and correlation-peak location in optical processing systems", Applied Optics, **32** (26), pp.5089-5091, (1993).

65. Pickering C.J.D. and Halliwell N.A., "Particle image velocimetry: improving fringe signal-to-noise ratio with a two-step photographic process", J. Opt. Soc. Am., Vol. **2**, No. 4, pp.610-615, (1985).

66 Willert C.E. and Gharib M., "Digital particle image velocimetry", Experiments in Fluids **10**, pp.181-193, (1991).

67 Keane R.D. and Adrian R.J., "Optimisation of particle image velocimeters. Part 1: Double pulsed systems", Meas. Sci. Technol. **1**, pp.1202-1215, (1990).

68 Prasad A.K., Adrian R.A., Landreth C.C. and Offlut P.W., "Effect of resolution on the speed and accuracy of particle image velocimetry interrogation", Experiments in Fluids **13**, pp.105-116, (1992).

69. Adamczyk A.A. and Rimai L., "2-Dimensional particle tracking velocimetry (PTV): Technique and image processing algorithms", Exp. In Fluids, Vol. **6**, pp.373-380, (1988).

70. Hassan Y. and Blanchat T., "Full-field bubbly flow velocity measurements by digital image pulsed laser velocimetry", Exp. In Fluids, Vol. **11**, pp.293-301, (1991).

71. Ramer R. and Shaffer F.D., "Automated analysis of multiple-pulse particle image velocimetry data", Applied Optics, Vol. 31, No. 6, pp.779-784, (1992).

72. Bryanston-Cross P.J., Judge T.R., Quan C., Pugh G. and Corby N., "The application of digital particle image velocimetry (DPIV) to transonic flows", Prog. Aerospace Sci., Vol. **31**, pp.273-290, (1995).

73. Wernet M.P., "Fuzzy logic particle tracking velocimetry", Proc. SPIE, Vol. **2005,** Optical Diagnostics in Fluid and Thermal Flow, pp.701-708, (1993).

74. Ereaut P.R., Shand A.M., Sandford M. and Postlethwaite I., "Experimental and numerical investigation of engine cooling flows", IMechE paper C465/039/93, (November 1993).

75. Sandford M. and Postlethwaite I., "Engine coolant flow simulation - A correlation study", SAE Paper 930068, (1993).

76. Nikon MicroNikkor 55 mm lens technical specifications.

77. Kodak TMAX film technical paper.

78. STAR CD Version 2.11 User Manual, Computational Dynamics Ltd., (1991).

79. Shand A.M., "Full-field visualisation of fuel spray impingement", FED-Vol **128**, Proceedings Symposium on Experimental and Numerical Flow Visualisation, ASME Annual Conf., Atlanta, (1991).

80. TIFOSI operation manual.

81. Furumoto H. and Ceccon H., J. Appl. Phys., **40**, 4204, (1969).

82. Astill A., "Temperature effects of bis-msb fluorescence (solution in model fuel)", UKAEA Test Measurements, (1990).

83. Gover M.P., Ereaut P.R., Whiteman P.R., Old C.F. and Azzopardi B.J., "Film thickness measurement techniques", CEC Report JOUE-0029-D, (1993).

84. Baker R.J., Hutchinson P. and Whitelaw J.H., "Preliminary measurements of instantaneous velocity in a two metre square furnace using laser anemometry", J. Heat Transfer, Vol. **96**, p410 (1974).

85. Pröbstle G. and Wenz W., "Velocity measurements in a swirl driven pulversied coal combustion chamber", Combustion and Flame, Vol 72, p193, (1988).

86. Abbott M.P., "Two phase velocity and turbulence measurements in a 0.5 MW pulverised coal fired furnace", Proc. 9th Members Conf., International Flame Research Foundation, Noordwijkerhout, (1989).

87. Francis W. And Peters M.C., "Fuels and fuel technology" (Second edition), Pergamon Press, Oxford, UK, (1980).

88. Gaydon A.G., "The spectroscopy of flames", Chapman Hall, London, UK, (1974).

89. Beiting E.J., "Multiplex CARS temperature measurements in a coal fired MHD environment", Applied Optics, **25**, p.1684, (1986).

90. Ereaut P.R. and Gover M.P., "LDA measurements of flame velocities in a 2000 MEe coal-fired power station", J. Inst. Energy, September, (1991).

91. Hong N.S., Jones A.R. and Weinberg F.J., "Doppler velocimetry within turbulent phase boundaries", Proc. Roy. Soc. London A, Vol. **353**, p.77 (1977).

92. Abbott M., "The development of a laboratory scale pulverised coal burner to evaluate laser measurement techniques", UKAEA Technical Report AERE-R-12929, (1987).

93. Ereaut P.R., "The application of laser light sheets to a laboratory coal flame", UKAEA Technical Report AERE-R-1300 (1987).

94. Abbott M.P., "Laser Doppler anemometry applied to gas expansion flows and industrial coal flames", PhD thesis, University of Wales (1989).

95. Schon J.R., "New techniques for flow visualisation measurement of velocity and concentration", VKI lecture series 1986-09; Flow visualisation and digital image processing, (1986).

96. Ereaut P.R. and Shand A.M., "Laser sheet visualisation of an isothermal burner test rig at NEI", UKAEA Technical Report AERE-R-13338 (1988).

97. ed. Emrich R.J., "Methods of experimental physics", Vol. **18B**, pp830, Academic Press, New York, (1981).

98. Armstrong N.W.H., Shand A.M., Bray K.N.C. and Ereaut P.R., "PIV applied to premixed turbulent flames", Proceedings Optical Methods and Data Processing in Heat and Fluid Flows IMechE Conference, London (1992).

99. Chew T.C., Britter R.E. and Bray K.N.C., "Laser tomography of turbulent pre-mixed bunsen flames", Combust. Flame, Vol. **75**, pp 165-174, (1989).

100. Kostiuk L.W., Bray K.N.C. and Chew T.C., "Premixed turbulent combustion in counterflowing streams", Comb. Sci and Tech., Vol. **64**, pp 233-241, (1989).

101. Witze P.O. and Baritaud T.A., "Particle seeding for Mie scattering measurements in combusting flows", Sandia Technical Report, SAND85-8912, (1986).

102. Melles Griot Optics Guide, Melles Griot Inc (1990).

103. Reuss D.L., Adrian R.J., Landreth C.C., French D.T. and Fansler T.D., "Instantaneous planar measurements of velocity and large-scale vorticity and strain-rate in an engine using particle-image velocimetry", SAE paper 890616, (1989).

104. Ereaut P.R., Brown A.B. and Shand A.M., "Laser light sheet measurements in a 1.5 MW furnace at NEI, Derby", UKAEA Technical Report AERE-R-13611 (1989).

105. ed. Sykes J., "Harwell Coal Combustion Programme. Final report", UKAEA Technical Report, (1992).

106. Dugué J., Ereaut P.R., Horsman H. and Shand A.M., "Laser sheet visualisation in cold flows and gas and coal flames in the IFRF Furnace No. 2", IFRF Doc. No. F/72/y/19, (1990a).

107. Syred N and Beer J.M., Combustion and Flame, **23**:143, (1974).

108. Dugué J., Weber R. and Horsman H., "The effect of combustion on swirling flows expanding in a medium confinement furnace. Results of the NFA 4-1 investigation", IFRF Doc. No. F/59/y/7, (1989).

109. Shand A.M., "An image processing system for fluid studies", UKAEA Technical Report AERE-R-13283, (1988).

110. Shand A.M., "LSI image processing for coal flames", UKAEA Technical Report AERE-EE-0079, (1990).

111. Morgan M.E. and Dekker J.S.A., "Effects of coal quality on the performance of low Nox burners", IFRF Doc. No. F 088/a/9, February (1989).

112. Glass M. and Kennedy I.M., "An improved seeding method for high temperature laser Doppler velocimetry", Combustion and Flame, **29**, pp 333-335, (1977).

113. Dugué J., Ereaut P.R., Horsman H. and Shand A.M., "Laser sheet visualisation in cold flows and 2.5 MW gas and coal flames", IFRF Doc. No. F/72/y/20, (1990).

114. Hagaiwara A. and Bortz S., "Studies of the near field aerodynamics of swirl burners. Results of the NFA 1 investigation", IFRF Doc. No. F 259/a/1, November (1984).

115. Dowling J., "Infinity Corp. K2 lens - resolution tests", UKAEA Test Measurements, (1990).

116. Komine H., Brosnan S., Litton A.B. and Stappaerts E.A., "Real time Doppler global velocimetry", AIAA Paper 91-0337, January (1991).

117. Bloom S. H., Searcy P. A., Choi K., Kremer R. and Korevaar E., "Helicopter plume detection by using an ultranarrow-band noncoherent laser Doppler velocimeter", Optics Letters, **18** (3), pp. 244-246, (1993).

118. Meyers J. F., Lee J. W., Cavone A. A. and Suzuki K. E., "Investigation of the vortical flow above an F/A-18 using Doppler global velocimetry", Proc. SPIE, Vol. **2052**, Laser Anemometry Advances and Applications, pp 633-640, (1993).

119. Shand A.M., "Doppler global velocimetry for sprays. A feasibility report", UKAEA Technical Report AEA-InTec-1675, December (1993).

120. Arroyo M.P. and Greated C.A., "Stereoscopic particle image velocimetry", Measurement Science Technology, **2**, pp.1181-1186, (1991).

121. Prasad A.K. and Adrian R.J., "Stereoscopic particle image velocimetry applied to liquid flows", Proc. 6th Symposium on the Application of Laser Anemometry to Fluid Mechanics, Lisbon, (1992).

122. Willert C.E. and Gharib M., "Three-dimensional particle image velocimetry with a single camera", Experiments in Fluids, **12**, pp.353-358, (1992).

123. Coupland J.M. and Halliwell N.A., "Particle image velocimetry: Three dimensional fluid velocity measurements using holographic recording and optical correlation", Applied Optics, **31**, pp.1004-1008, (1992).

124. Bryanston-Cross P.J., Funes-Gallanzi M., Harris A.E., Quan C. And Judge T.R., "Holographic particle image velocimetry (PIV)", Proc. 6th Symposium on the Application of Laser Anemometry to Fluid Mechanics, Lisbon, (1992).

125. Lauterborn W., Judt A. And Schmitz E., "High-speed off-axis holographic cinematography with a copper-vapour-pumped dye laser", Optics Letters, **18** (1), pp.4-6, (1993).